

UNCLASSIFIED

AD NUMBER

AD523087

CLASSIFICATION CHANGES

TO: unclassified

FROM: confidential

LIMITATION CHANGES

TO:

Approved for public release, distribution unlimited

FROM:

Distribution authorized to U.S. Gov't. agencies only; Test and Evaluation; Oct 1972. Other requests shall be referred to AFWL [LRT], Kirtland AFB, NM 87117.

AUTHORITY

AFWL ltr, 24 Dec 1974; AFWL ltr, 4 Jun 1976

THIS PAGE IS UNCLASSIFIED

CONFIDENTIAL

AFWL-TR-72-28

(Unclassified Title)

AFWL-TR-
72-28

HYDROGEN FLUORIDE LASER TECHNOLOGY STUDY

F. Mastrup

E. Broadwell

J. Miller

T. A. Jacobs

TRW Systems Group

TECHNICAL REPORT NO. AFWL-TR-72-28

October 1972

Classified by AFWL (LRT)
EXEMPT FROM GENERAL DECLASSIFICATION
SCHEDULE OF EXECUTIVE ORDER 11652
EXEMPTION CATEGORY 3
DECLASSIFY ON: Indefinite

AIR FORCE WEAPONS LABORATORY

Air Force Systems Command

Kirtland Air Force Base

New Mexico

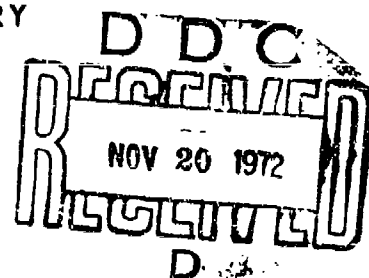
SPECIAL HANDLING REQUIRED
NOT RELEASABLE TO FOREIGN NATIONALS
The information contained in this document will
not be disclosed to foreign nationals or their
representatives.

This document contains information affecting the national defense of
the United States within the meaning of the Espionage Laws (Title 18,
U.S.C., sections 793 and 794), the transmission or revelation of which
in any manner to an unauthorized person is prohibited by law.

Distribution limited to US Government agencies only because of test
and evaluation (Oct 1972). Other requests for this document must
be referred to AFWL (LRT), Kirtland AFB, NM 87117.

CONFIDENTIAL

AD 523087



AIR FORCE WEAPONS LABORATORY
Air Force Systems Command
Kirtland Air Force Base
New Mexico 87117

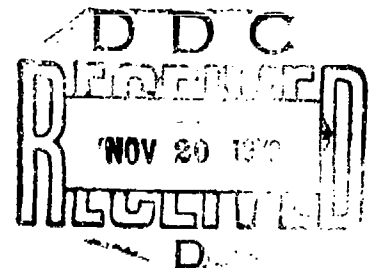
This report is classified Confidential, Group 3 because of chemical laser test and evaluation data contained herein.

WARNINGS

This material contains information affecting the national defense of the United States within the meaning of the Espionage Laws, Title 18, USC, sections 793 and 794, the transmission or revelation of which in any manner to an unauthorized person is prohibited by law.

SPECIAL HANDLING REQUIRED--NOT RELEASABLE TO FOREIGN NATIONALS.

When U. S. Government drawings, specifications, or other data are used for any purpose other than a definitely related Government procurement operation, the Government thereby incurs no responsibility nor any obligation whatsoever, and the fact that the Government may have formulated, furnished, or in any way supplied the said drawings, specifications, or other data, is not to be regarded by implication or otherwise, as in any manner licensing the holder or any other person or corporation, or conveying any rights or permission to manufacture, use, or sell any patented invention that may in any way be related thereto.



DO NOT RETURN THIS COPY. RETAIN OR DESTROY.

CONFIDENTIAL

(Unclassified Title)

HYDROGEN FLUORIDE LASER TECHNOLOGY STUDY

F. Mastrup
E. Broadwell
J. Miller
T. A. Jacobs
TRW Systems Group

TECHNICAL REPORT NO. AFWL-TR-72-28

Distribution limited to US Government agencies only because of test and evaluation (Oct 1972). Other requests for this document must be referred to AFWL (LRT), Kirtland AFB, NM 87117.

CONFIDENTIAL

CONFIDENTIAL**FOREWORD**

This report was prepared by the TRW Systems Group, Redondo Beach, California, under Contract F29601-71-C-0070. The research was performed under Program Element 62301D, Project 1256, and was funded by the Advance Research Project Agency under ARPA Order number 1256.


Inclusive dates of research were 22 March 1971 through 22 October 1971. The report was submitted 18 August 1972 by the Air Force Weapons Laboratory Project Officer, Captain William E. Thompson III (LRT).

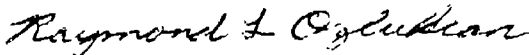
Classified information has been extracted from reference 8.


In addition to the authors, principal contributors to the report were G. S. Bell, D. L. Hook, J. V. Mageean, and A. S. Whiteman.

The authors wish to thank the following individuals for significant contributions to the program: J. Auguston, R. Barth, H. Bobitch, H. Ethington, R. Herrett, R. Kemp, D. Mansell, K. Mock, R. Rainer, and R. Wuerker.

This report has been reviewed and is approved.


WILLIAM E. THOMPSON III
Captain, USAF
Project Officer


RAYMOND L. OGLUKIAN
Major, USAF
Chief, Advanced Technology Branch


DONALD E. LAMBERSON
Colonel, USAF
Chief, Laser Division

(This page is Unclassified)

ABSTRACT

This report presents an in-depth discussion of performance and diagnostic testing of the TRW versions of all-chemical, combustion driven hydrogen-fluorine lasers. Emphasis is placed on engineering principles of combustor/injector operation and design; performance testing; spectroscopic measurements and infrared mapping of excited and ground-state molecular concentrations in the laser cavity flow field; and fluid mechanical observations of the flow field. The exceptionally high quality of the data has permitted several distinct and significant conclusions concerning the nature of the flow field and has indicated the direction for future chemical laser research. A sufficiently in-depth discussion is presented which may serve as a point of departure for future chemical laser technology efforts.

(Distribution Limitation Statement B)

CONTENTS

| <u>Section</u> | | <u>Page</u> |
|----------------|---|-------------|
| I | INTRODUCTION AND SUMMARY | 1 |
| | CL-II Design and Operating Characteristics | 4 |
| | Cavity Diagnostics | 10 |
| II | LASER CAVITY DIAGNOSTIC MEASUREMENTS | 33 |
| | Introduction : | 33 |
| | Laser Cavity Diagnostic Objectives | 34 |
| | General Cavity Diagnostics Measurements Technical Approach | 35 |
| | Cavity Diagnostic Techniques Description | 37 |
| | Experiment Parameters Summary | 74 |
| | Cavity Diagnostic Experiment Results | 96 |
| | Cavity Diagnostic Experimental Results Discussion | 141 |
| III | FLUID MECHANICAL ANALYSIS | 152 |
| | Cavity Flow Field Structure | 152 |
| | Nozzle Boundary Layer Analysis | 163 |
| IV | LASER PERFORMANCE | 179 |
| | Closed Cavity Power Performance Data and Correlations | 182 |
| V | CONCLUSIONS | 224 |
| | APPENDIX I TEST HARDWARE AND DATA REDUCTION PROCEDURES | 225 |
| | APPENDIX II CHEMILUMINESCENT SPECTRUM REDUCTION PROGRAM | 267 |
| | REFERENCES | 273 |

ILLUSTRATIONS

| <u>Figure</u> | | <u>Page</u> |
|---------------|---|-------------|
| 1 | CL-II Combustor/Laser Schematic | 4 |
| 2 | Combustor Injector Design Configuration | 5 |
| 3 | CL-II Combustor Injector | 5 |
| 4 | CL-II 1- by 7-inch Nozzle Array | 6 |
| 5 | Face-on View of CL-II 1- by 7-inch Multiple Slot Array Cavity Injector | 6 |
| 6 | Installation of 1- by 7-Inch Nozzle Array in CL-II Cavity Box | 7 |
| 7 | Effect of Cavity Fluorine Dissociation on Specific Power | 8 |
| 8 | Summary Comparison Between CL-I and CL-II Combustor Configurations | 8 |
| 9 | Schematic of Chemiluminescence Apparatus | 11 |
| 10 | Schematic of IR Scanner Apparatus | 13 |
| 11 | Schematic of Resonance Absorption/Gain Apparatus | 14 |
| 12 | Typical "Boltzman" Plot of Chemiluminescent Data: Baseline Flow (1-0) | 17 |
| 13 | Typical "Boltzman" Plot of Chemiluminescent Data: Increased Cavity Pressure (1-0) | 18 |
| 14 | Vibrational State Distribution vs Laser Cavity Station X; Baseline Flow | 20 |
| 15 | Vibrational State Distribution vs Laser Cavity Station X; Duct Pressure x 2 | 21 |
| 16 | Vibrational State Distribution vs Laser Cavity Station X; Duct Pressure x 4 | 22 |
| 17 | Vibrational State Distribution vs Laser Cavity Station X; Duct Pressure x 6 | 23 |
| 18 | Vibrational State Distribution vs Laser Cavity Station X; Flow Increased 50% | 24 |

ILLUSTRATIONS (Continued)

| <u>Figure</u> | | <u>Page</u> |
|---------------|---|-------------|
| 19 | Calculated Excited Species Concentrations, Lasing Case | 27 |
| 20 | Calculated Excited Species Concentrations, Nonlasing Case | 27 |
| 21 | Top View of Cavity Flow Field | 28 |
| 22 | Chemiluminescence Experiment: Apparatus Schematic | 40 |
| 23 | Chemiluminescence Experiment: Spectral Response | 41 |
| 24 | Chemiluminescence Experimental Apparatus - Photograph of Test Setup | 43 |
| 25 | Line Attenuation Factor for Self-Absorption vs Line Center Opacity | 49 |
| 26 | IR Scanner Experiment: Apparatus Schematic | 59 |
| 27 | IR Scanner Apparatus - Photograph of Radiometer and Mirror Drum | 59 |
| 28 | IR Scanner: Spatial Resolution Geometry | 60 |
| 29 | IR Scanner Real Time Oscilloscope Display: Amplitude Modulation | 66 |
| 30 | IR Scanner Real Time Oscilloscope Display: Intensity Modulation | 66 |
| 31 | Line-of-Sight Geometry in Chemiluminescence and Gain/Absorption Experiment | 68 |
| 32 | Resonance Absorption/Gain Experiment: Apparatus Schematic | 69 |
| 33 | Absorption/Gain Experiment Geometry | 71 |
| 34 | Doppler Profile Resonance Line Absorption: Line Attenuation versus Line Center Opacity | 73 |
| 35 | Typical Chemiluminescence Spectrum | 97 |
| 36 | Typical "Boltzman" Plot of Chemiluminescent Data: Baseline Flow (1-0) | 99 |

ILLUSTRATIONS (Continued)

| <u>Figure</u> | | <u>Page</u> |
|---------------|--|-------------|
| 37 | Typical "Boltzman" Plot of Chemiluminescent Data: Baseline Flow (2-1) | 100 |
| 38 | Typical "Boltzman" Plot of Chemiluminescent Data: Baseline Flow (3-2) | 101 |
| 39 | Typical "Boltzman" Plot of Chemiluminescent Data: Increased Cavity Pressure (1-0) | 103 |
| 40 | Typical "Boltzman" Plot of Chemiluminescent Data: Increased Cavity Pressure (2-1) | 104 |
| 41 | Typical "Boltzman" Plot of Chemiluminescent Data: Increased Cavity Pressure (3-2) | 105 |
| 42 | Vibrational State Distribution vs Laser Cavity Station X: Baseline Flow | 109 |
| 43 | Vibrational State Distribution vs Laser Cavity Station X: Duct Pressure x 2 | 110 |
| 44 | Vibrational State Distribution vs Laser Cavity Station X: Duct Pressure x 4 | 111 |
| 45 | Vibrational State Distribution vs Laser Cavity Station X: Duct Pressure x 6 | 112 |
| 46 | Vibrational State Distribution vs Laser Cavity Station X: Flow Increased 50% | 113 |
| 47 | Vibrational State Distribution vs Laser Cavity Station X: Helium Substitution | 114 |
| 48 | Vibrational State Distribution vs Laser Cavity Station X: Increased Combustor Temperature | 115 |
| 49 | Vibrational State Distribution Ratios | 118 |
| 50 | Typical Absorption/Gain Experimental Data: Attenuation for (1-0) P3, P5 Spectral Lines | 119 |
| 51 | Typical Absorption/Gain Experimental Data: Attenuation Gain Factors | 120 |
| 52 | Absorption/Gain Experimental Data for DF Laser Condition | 125 |
| 53 | IR Scanner: Oscilloscope Real Time Data Display: Test Flow Conditions I-IV | 127 |

ILLUSTRATIONS (Continued)

| <u>Figure</u> | | <u>Page</u> |
|---------------|---|-------------|
| 54 | IR Scanner: Oscilloscope Real Time Data Display: Test Flow Conditions I-IV | 128 |
| 55 | Infrared Chemiluminescent Intensity Display of Laser Cavity: Test Ia | 131 |
| 56 | Infrared Chemiluminescent Intensity Display of Laser Cavity: Test Ib | 132 |
| 57 | Infrared Chemiluminescent Intensity Display of Laser Cavity: Test IC | 133 |
| 58 | Infrared Chemiluminescent Intensity Display of Laser Cavity: Test Id | 134 |
| 59 | Infrared Chemiluminescent Intensity Display of Laser Cavity: Test II | 135 |
| 60 | Infrared Chemiluminescent Intensity Display of Laser Cavity: Test III | 136 |
| 61 | Infrared Chemiluminescent Intensity Display of Laser Cavity: Test IV | 137 |
| 62 | Relative Vibrational Species Population $\alpha_v(X)$ | 138 |
| 63 | Vibrational Species Population and Variations: Baseline Flows | 139 |
| 64 | Vibrational Species Population and Variations: Duct Pressure Increased x 6 | 140 |
| 65 | Cavity Flow Field, Top View, Run 182A | 153 |
| 66 | Cavity Flow Field, Top View | 154 |
| 67 | Cavity Flow Field, Side View | 155 |
| 68 | Cavity Flow Field, Side View, Run 182D | 156 |
| 69 | Cavity Flow Field, Side View Run 182A | 162 |
| 70 | Cavity Flow Field, Side View, Run 182J | 162 |
| 71 | Nozzle Flow with Boundary Layers | 163 |
| 72 | Contour of Wind Tunnel Test Nozzle and Its Analytic Approximation | 168 |

ILLUSTRATIONS (Continued)

| <u>Figure</u> | | <u>Page</u> |
|---------------|---|-------------|
| 73 | Boundary Layer Thickness and Exit Pressure vs Plenum Pressure | 176 |
| 74 | CL-II Boundary Layer Profiles at Nozzle Exit | 177 |
| 75 | Closed Cavity Power X_c Scan for Test 097 | 184 |
| 76 | Closed Cavity Power X_c Scan for Test 098 | 187 |
| 77 | Closed Cavity Power X_c Scan for Test 099 | 188 |
| 78 | Closed Cavity Power X_c Scan for Test 100 | 191 |
| 79 | Closed Cavity Power X_c Scan for Test 101 | 192 |
| 80 | Closed Cavity Power X_c Scan for Tests 103 and 112 | 193 |
| 81 | Specific Power vs Mixer Temperature for CL-I and CL-II Laser Tests | 196 |
| 82 | Effect of Incomplete Dissociation of Cavity Fluorine | 198 |
| 83 | Functional Relationship Between Specific Power and Cavity Fuel Flow | 199 |
| 84 | Effect of He Diluent Flow on Specific Power/Gram of Atomic Fluorine and Specific Power/Gram of Total Flow | 200 |
| 85 | Summary Comparison Between CL-I and CL-II Combustor Configurations | 202 |
| 86 | Closed Cavity Power X_c Scan for Test 151 | 203 |
| 87 | Closed Cavity Power X_c Scan for Test 152 | 206 |
| 88 | Closed Cavity Power X_c Scan for Test 153 | 207 |
| 89 | Closed Cavity Power X_c Scan for Test 154 | 208 |
| 90 | Closed Cavity Power X_c Scan for Tests 155 and 156 | 209 |
| 91 | Closed Cavity Power X_c Scan for Test 157 | 211 |
| 92 | Closed Cavity Power X_c Scan for Test 158 | 212 |

ILLUSTRATIONS (Continued)

| <u>Figure</u> | | <u>Page</u> |
|---------------|--|-------------|
| 93 | Closed Cavity Power X_c Scan for Test 159 | 213 |
| 94 | Closed Cavity Power X_c Scan for Test 160A and B | 214 |
| 95 | Closed Cavity Power X_c Scan for Test 160 | 215 |
| 96 | Closed Cavity Power X_c Scan for Tests 210 and 214 | 216 |
| 97 | Closed Cavity Power X_c Scan for Test 211 | 218 |
| 98 | Closed Cavity Power X_c Scan for Test 212 | 219 |
| 99 | Closed Cavity Power X_c Scan for Test 213 | 220 |
| 100 | Closed Cavity Power X_c Scan for Tests 215, 216 and 217 | 221 |
| 101 | Closed Cavity Power X_c Scan for Tests 218, 219 and 220 | 222 |
| 102 | CL-I and CL-II Combustor/Laser Schematics | 227 |
| 103 | Combustor Injector Design Configuration | 229 |
| 104 | Injector Assembly | 282 |
| 105 | CL-II Pre-Cavity Combustor Injector | 230 |
| 106 | Water-Cooled Combustor | 232 |
| 107 | Installation of Combustor and Injector in Test Configuration | 233 |
| 108 | Exploded Assembly View of CL-II Gas Cooled Plenum | 233 |
| 109 | CL-II Gas Cooled Plenum Design | 234 |
| 110 | Atomic Fluorine Temperature Dependence | 235 |
| 111 | Gas to Wall Temperature Profiles | 236 |
| 112 | Chemical Laser 1- by 7-Inch Nozzle Array | 240 |
| 113 | Installation of 1/2 by 7-Inch Nozzle Array in CL-II Cavity Box | 240 |

ILLUSTRATIONS (Continued)

| <u>Figure</u> | | <u>Page</u> |
|---------------|---|-------------|
| 114 | Installation of 1- by 7-inch Nozzle Array in CL-II Cavity Box | 241 |
| 115 | Face-on View of CL-II 1- by 7-Inch Multiple Slot Array Cavity Injector | 241 |
| 116 | 1- by 7-Inch 2D Slit Nozzle | 233 |
| 117 | High Power Water-Cooled Laser Mirrors | 242 |
| 118 | Manual Differential Micrometer Adjustments on CL-II Laser Mirrors | 244 |
| 119 | Remotely Operated Differential Micrometer Adjustments with Position Feedback on CL-II Laser Mirrors | 244 |
| 120 | Water-Cooled Mirror Assembly | 245 |
| 121 | Schematic of the TRW Chemical Laser Test Apparatus | 246 |
| 122 | Photograph of the TRW HF/DF Chemical Laser System with New Resonator Mount | 248 |
| 123 | Photograph of the TRW HF/DF Chemical Laser Viewed From the Rear External Mirror Mount | 249 |
| 124 | Transmission Curves for Sapphire Reflectors | 250 |
| 125 | Laser Burn Pattern Seen in Plexiglas Print | 251 |
| 126 | Laser Effects Laboratory | 253 |
| 127 | Laser Test Control Console | 253 |
| 128 | Chemical Laser Facility Feed System and Instrumentation Schematic | 254 |
| 129 | HEPTS Steam Ejector Pumping System | 256 |

TABLES

| <u>Table</u> | | <u>Page</u> |
|--------------|---|-------------|
| 1 | Test Operating Parameters Summary for Tests Series I-IV | 75 |
| 2 | Detailed Test Operating Parameters | 77 |
| 3 | Chemical Thermodynamic Properties and Molecular and Atomic Constants | 81 |
| 4 | Plenum Chamber Equilibrium Molar Flow Rates and Salient Gas Parameters | 82 |
| 5 | Laser Cavity Molar Flow Rates and Gas Parameters | 91 |
| 6 | HF Ground State Densities from Self-Absorption | 108 |
| 7 | Test Data Summary, Chemiluminescent and Resonance Absorption Experiment | 116 |
| 8 | HF Ground State Densities from Gain/Absorption Experiment | 122 |
| 9 | Cavity Heat Transport and Velocities | 143 |
| 10 | Comparison of Measured and Theoretical Nozzle Exit Mach Numbers for Low Reynolds Number Wind Tunnel | 175 |
| 11 | Test Program Milestones | 179 |
| 12 | Diagnostics Test Run Summary CL-II Combustor and 1 x 7 Nozzle | 180 |
| 13 | Target Diagnostic Test Conditions | 275 |
| 14 | Data Summary for Runs 97 Through 101 | 276 |
| 15 | Data Summary for Runs 103 Through 112 | 277 |
| 16 | Data Summary for Runs 151 Through 160 | 278 |
| 17 | Data Summary for Runs 210 Through 220 | 280 |
| 18 | Specific Energy Losses to the Plenum Walls | 235 |
| 19 | Comparison of Cavity Injector Design Characteristics | 239 |

TABLES (Continued)

| <u>Table</u> | | <u>Page</u> |
|--------------|--|-------------|
| 20 | HEPTS Data Acquisition and Recording Equipment | 258 |
| 21 | Laser Technology Experiments Summary of Measurement Uncertainty | 261 |

NOMENCLATURE

(U) Except where otherwise noted in the text, the symbols used have the meaning, value and units as given below.

| | | |
|-------------------------|---|---|
| a_o | Velocity of sound $\sqrt{\frac{\gamma RT}{\mu}}$ | cm/sec |
| A | Area of cross section or component | cm ² |
| B | Molecular rotational constant | cm ⁻¹ |
| C | Velocity of light (3×10^{10}) | cm/sec |
| e | Denotes the exponential function | |
| f | Degrees of freedom of the gas molecules | |
| $F_r(j)$ | Rotational term value $= B_v J(j+1)$ | cm ⁻¹ |
| e_{gi} | Electronic statistical weight for species i | |
| G | Vibration term value $= \omega_e (V+1/2) - \omega_e X_e (V+1/2)^2$ | cm ⁻¹ |
| h | Planck constant (6.62×10^{-27}) | erg sec |
| H | Static enthalpy | |
| H_f | Heat of formation | Kcal/mole |
| H_s | Total enthalpy | |
| i | Subscript denoting the i th species | |
| I | Emission intensity | watts/ cm ² ster cm ⁻¹ |
| $j_j^{i,u}$ | Upper lower state rotational quantum number | |
| $K_{\bar{\gamma}}, K_o$ | Coefficient of absorption at wavenumber $\bar{\gamma}$, or line center | |
| $(\bar{k}o\bar{l})$ | Equivalent centerline opacity along a line-of-sight | |
| K | Boltzmann constant (1.38×10^{-16}) | erg/ ^o K |

NOMENCLATURE (Continued)

| | | |
|---|---|---|
| $ \langle v'j' M_r v''j'' \rangle ^2$ | Dipole moment matrix element for the transaction ($v, 'j' \rightleftharpoons v, ''j''$) | |
| L | Nozzle length | |
| m | Molecular weight | gm/mole |
| \dot{m} | Mass flow rate | gm/sec |
| $ m $ | Rotational part of dipole moment matrix element | |
| M | Mach number | |
| n | Distance normal to wall | |
| \dot{n} | Molar flow rate | moles/sec |
| N_i | Number density for i^{th} species or state | molecules/cm ³ |
| $\int N(y)dy$ | Species number density integrated along a line-of-sight | molecules/cm ² |
| Q_r | Rotational part of the state partition function | |
| p | Pressure | |
| p_c | Combustion chamber pressure | psia |
| $p_{1,}$ | Laser cavity static pressure | torr |
| r | Subscript referring to a rotational parameter | |
| R | Gas constant (8.31×10^7) | erg/ ^o K mole |
| R | Laser molar flow ratio (definition specific to subscript) | |
| s | Distance along wall | |
| S_λ | System response at wavelength λ | volts/watt cm ⁻² ster ⁻¹ |
| t | Throat Width | |
| T | Temperature | ^o K |
| u | Velocity | (cm/sec) |

NOMENCLATURE (Continued)

| | | |
|-----------------------------|--|----------|
| V', U'' | Upper, lower vibrational quantum number | |
| V | Line voltage | volts |
| W | Laser power | kw |
| \dot{W} | Rate of heat transport or release | Kcal/sec |
| x | Distance from throat along nozzle axis | |
| x, y, z X, Y, Z | Spatial co-ordinates | cm |
| x_c | Mirror position | in. |
| y | Distance normal to nozzle axis | |
| α | Fractional F_2 dissociation | |
| α_v | Relative distribution of vibrational states $N_v / \sum N_v$ | |
| β | Pressure gradient coefficient | |
| β | Ratio of source temperatures in absorption/gain experiment; gas entrainment factor | |
| β | Combustion chamber diluent ratio | |
| γ | Ratio of specific heats | |
| $\Gamma(\bar{\nu} - \nu_0)$ | Line shape factor as a function of wavenumber | |
| δ | Boundary layer thickness | |
| δ^* | Boundary layer displacement thickness | |
| δ_t | Boundary layer thermal thickness | |
| Δ | Denotes the difference of two relatable quantities | |
| c | Constant in nozzle contour equation | |

NOMENCLATURE (Continued)

| | | |
|-----------------------------|---|------------------------|
| $\epsilon(\bar{\nu})$ | Coefficient of emission at wavenumber $\bar{\nu}$ | |
| η | Transformed normal coordinate; $\eta = u_e / \sqrt{2} \int_0^n \rho \, dn$ | |
| δ | Boundary layer momentum thickness | |
| θ_v | Vibrational temperature | |
| λ | Wavelength | cm |
| μ | Molecular weight | gm/mole |
| μ | Viscosity | |
| $\mu(\bar{\nu})$ | Energy density at wavenumber $\bar{\nu}$ | joule/cm ³ |
| $\bar{\nu}, \bar{\nu}_0$ | Wavenumber, subscript o denotes line center | cm ⁻¹ |
| $\Delta \nu_D$ | Doppler line width $\bar{\nu}_0 \sqrt{2RT \ln 2 / \mu c^2}$ | cm ⁻¹ |
| ξ | Transformed longitudinal coordinate; $\xi = \int_0^s \rho_w \mu_w u_e \, ds$ | |
| ρ | Mass density | |
| σ | Specific energy, ratio of laser power to flow rate | Kjoule/lbm or joule/gm |
| χ_i | Molar fraction of species i | |
| ψ | Line attenuation factor in absorption/gain experiment | |
| ψ | Combustion chamber diluent ratio | |
| ω | Angle of wall with respect to nozzle axis | |
| $\omega_e, \omega_e \chi_e$ | Molecular vibrational frequency terms | cm ⁻¹ |
| [HF] | Concentration of species | moles/cm ³ |
| $\langle \rangle$ | Mean value of parameter evaluated across flow section | |

NOMENCLATURE (Continued)

Subscripts:

| | |
|---|---|
| c | Plenum chamber parameter |
| e | External to boundary layer |
| L | At nozzle exit or cavity |
| o | Ground state, centerline |
| s | Stagnation condition |
| t | Translational, total, or throat parameter |
| w | At nozzle wall |

Superscript:

| | |
|---|------------------|
| * | At nozzle throat |
|---|------------------|

SECTION I

INTRODUCTION AND SUMMARY

(U) The task objectives of this program were:

(U) Task I: Develop and test the following diagnostic techniques:

- Infrared radiance mapping: Remote scanning of the entire lasing medium in a direction perpendicular to the lasing axis. This will be done with a narrow band infrared radiometer at a number of selected spectral lines to construct IR-intensity contours of the lasing region.
- Spectroscopic studies: Detailed spectral examination of selected laser cavity positions.
- Absorption (gain) measurements of the lasing medium at selected positions conducted with spectral emphasis of the 1-0 transition, both with and without cavity lasing.
- Computerized data reduction procedures to facilitate data analysis applied to the three diagnostic techniques mentioned above. The information available from the spectroscopic studies and infrared radiance mapping will be combined to produce a spectroscopic map of the laser cavity excitation.

(U) Task II: Design and fabricate new test article equipment. A new pre-cavity selection (combustor and mixing chamber) will be built which is calculated to reduce the heat losses and to improve flow uniformity over current designs. Also, a new nozzle bank will be designed and built which is deemed to be an improvement over the current nozzle designs.

(U) Task III: Provide testing at the TRW Capistrano Test Site and evaluate test data. A total of 8 test weeks will be provided. This test time will be used to test and perfect the diagnostic equipment and to evaluate regions of interest in the present HF chemical laser. Analysis and test result evaluations will be accomplished in support of this test effort.

(U) Prior to the start of this contract (September 1970) TRW had successfully tested an all-chemical, combustion-driven laser that was essentially a duplicate of the Aerospace Corporation arc driven chemical laser concept (Ref. 1-6). For this device, termed the CL-I, the electric arc source of gas heating used by Aerospace was replaced by a D_2 - F_2 combustor. In these initial experiments it was learned that combustion at mixture ratios of 15 or greater provided a highly satisfactory source of F-atom generation to support laser processes. The point of departure for the present contract was a newly designed, lower heat loss combustor termed CL-II. The combustor was configured to accept different cavity injectors, and during the course of the program, two nozzle banks, of dimensions $1/2 \times 7$ inches and 1×7 inches, were tested. The diagnostic techniques and performance testing reported herein were conducted with the CL-II combustor and the two nozzle banks.

(U) In carrying out all of the tasks listed above, significant advances in the understanding of the chemical laser medium were achieved. Data of exceptional quality were acquired during the course of the program leading to the following major accomplishments:

(U) In the area of diagnostics:

- First measurements of ground-state HF in the active chemical laser medium.
- Successful mapping of infrared intensities for the entire laser flow field.
- Demonstrated, with reasonable certainty, that recirculating gas entrainment in the laser cavity is one of the principal causes of decreased performance at higher than nominal cavity pressures. This conclusion was made possible only by complimenting chemiluminescence spectroscopy with ground-state HF absorption measurements. The conclusion is further augmented by infrared mapping of the flow field and flow field visualization techniques.
- The data strongly suggest that fuel-oxidizer jet mixing in chemical lasers is governed by turbulent mixing processes.

- (U) • The conclusions suggest steps for advanced laser designs, namely
1. Preclude ground state HF gas entrainment
 2. Enhance jet mixing by gas injection velocity control.

(U) In the area of performance testing:

- Demonstrated improved performance for all-chemical combustion-driven lasers with reduced combustor/mixer heat losses. Demonstrated height scaling. Performed flow parameter variation studies to demonstrate effects on laser performance.
- Demonstrated performance effects resulting from operation in the hot reaction regime.
- Designed and tested advanced combustion/mixer concepts (CL-II).
- Established a firm engineering basis for laser combustor/mixer design based on F_2/H_2 rocket engine experience.

(U) In subsequent portions of this section, the CL-II hardware is described in more detail and the basic diagnostic methods are summarized. Representative diagnostic data are then presented augmented by a summary discussion of the fluid mechanic considerations pertinent to the lasing cavity flow field.

(U) In the main body of the report the construction, operating procedures, data reduction techniques and expected errors of the infrared mapper, the chemiluminescence spectroscopy apparatus, and the absorption gain apparatus are presented. This is followed by a presentation and discussion of measurements conducted to assess flow field characteristics of the laser medium for the CL-II combustor with 1 x 7 inch cavity injector. The diagnostics section is augmented by an analysis of fluid mechanical observations of the active medium. Here, spatial aspects of the flow are discussed in compliment to the spectroscopic diagnostics, which average gas properties along a given line of sight. An analysis of boundary layer growth in the cavity injector nozzles is given to support arguments brought forth in addressing the nature of cavity mixing processes. Detailed results of testing the 1/2 x 7 and 1 x 7 inch cavity injectors, the CL-II combustor,

(U) and of general laser power performance are then presented. In the appendix, details of the CL-II combustor and injector test hardware, along with a description of laser test facilities are given.

1. CL-II DESIGN AND OPERATING CHARACTERISTICS

(U) Figures 1 through 6 summarize the salient features of the CL-II hardware designed to meet the requirements of the program. The CL-II hardware consists of the combustor injector, the combustor chamber, and the cavity injector nozzle assembly (Figure 1). The gas flow areas of all components are rectangular in shape with a 7-inch major dimension. The combustor injector is a raised post showerhead configuration schematically illustrated in Figure 2. Fuel (deuterium) is introduced through a raised central post and the fluorine is injected on either side of the fuel orifices. Figure 3 shows a photograph of the completed assembly. The combustor injector has ignited and operated smoothly with no malfunctions in over 24,000 seconds of lasing operation. Uniform mixtures of combustion gases and diluent gases were achieved by premixing diluent with fuel and oxidizer streams prior to injection into the combustion chamber. Two cavity injectors of the two-dimensional slit nozzle configuration were constructed. Both nozzle arrays were composed of 36 individual slit nozzles with a throat width of 0.01-inch and an area ratio of 15:1. One, of dimensions 1/2 by 7 inches, employed the Aerospace scheme of hydrogen

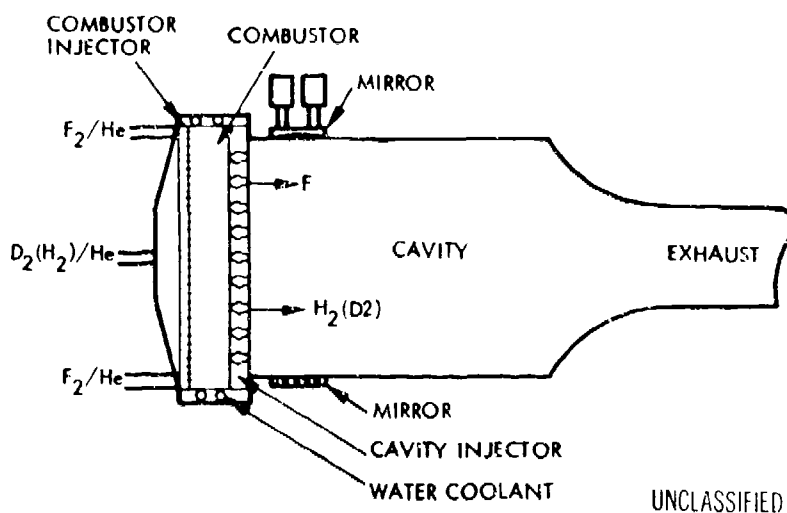


Figure 1. CL-II Combustor/Laser Schematic (U)

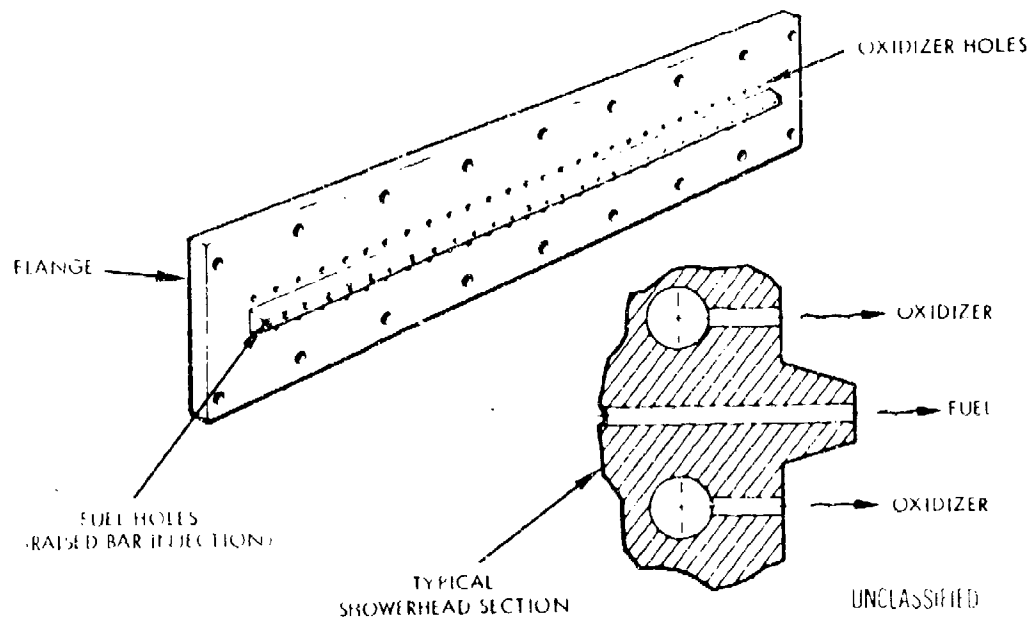


Figure 2. Combustor Injector Design Configuration (U)

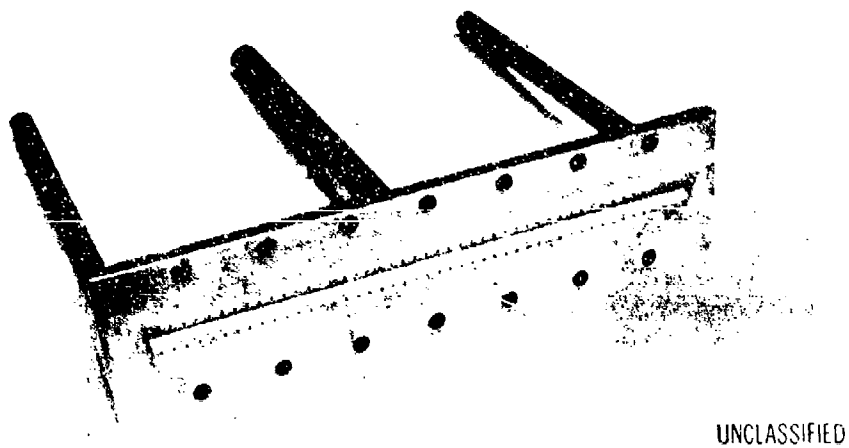


Figure 3. CL-II Combustor Injector (U)

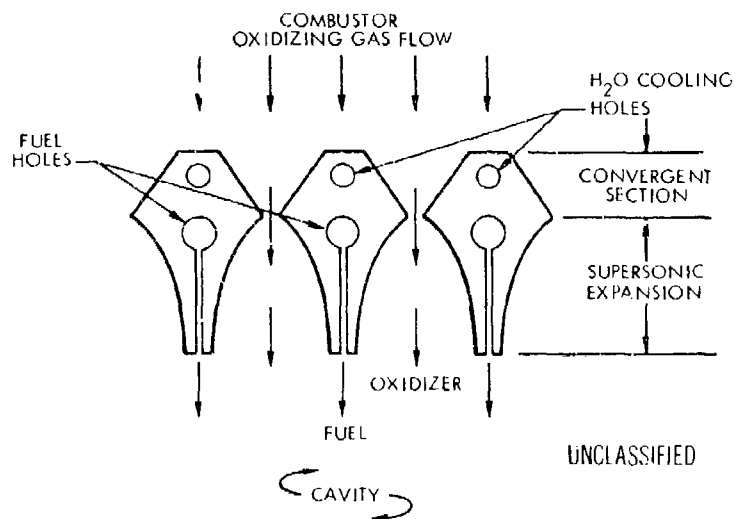
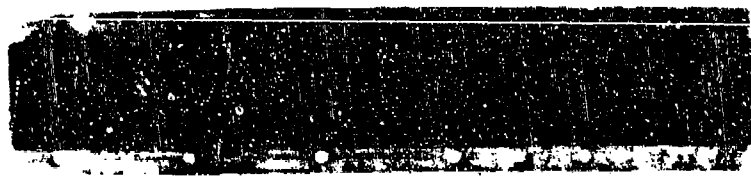
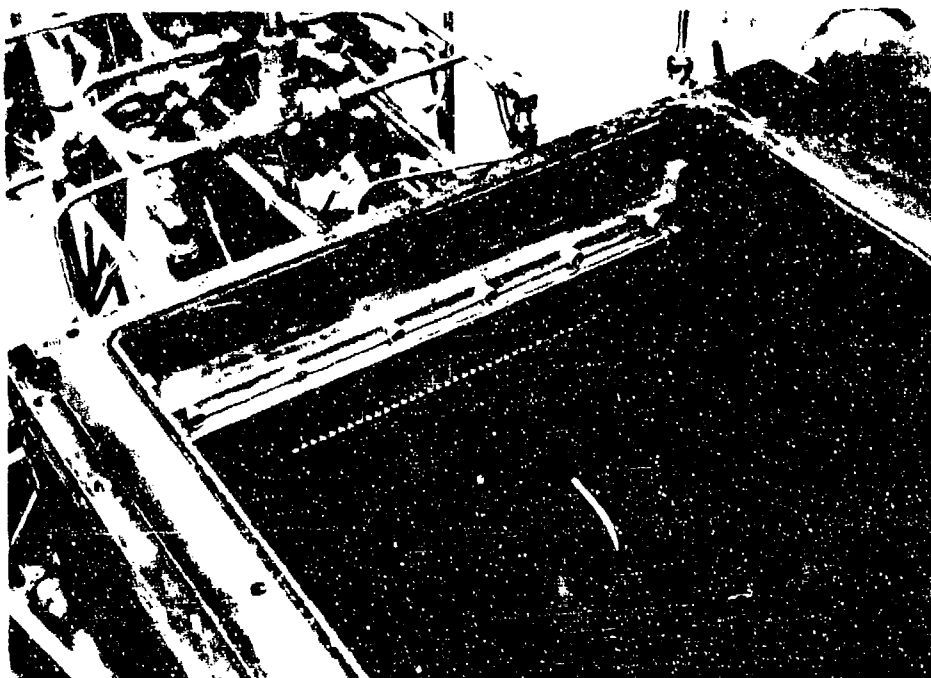


Figure 4. CL-II 1-by 7-Inch Nozzle Array (U)



UNCLASSIFIED

Figure 5. Face-on View of CL-II 1-by 7-Inch Multiple Slot Array Cavity Injector (U)



UNCLASSIFIED

Figure 6. Installation of 1- by 7-Inch Nozzle Array
in CL-II Cavity Box (U)

(U) injection by small, circular underexpanded jets. The second, shown in Figures 4 and 5, was designed for H_2 injection by means of vertical slits measuring the full height of the nozzle bank; dimensions for this injector are 1 x 7 inches. Figure 6 illustrates the installation of the 1 x 7 inch cavity injector in a 12 x 12 x 6-inch cavity box. The large cavity box has windows for photographic and spectroscopic observation of the flow field.

(U) Figures 7 and 8 present the specific power performance characteristics of the CL-II device while operating in the range of 1 to 3.5 kw of total power. Comparable data for the earlier CL-I device are also presented. The power data were acquired as closed-cavity measurements in which water-cooled mirrors acted as calorimeters. The combustor temperatures shown were determined by thermochemical equilibrium computations assuming complete reaction of the combustor reactants, and an enthalpy loss equal to the measured heat loss to the combustor cooling jackets.

CONFIDENTIAL

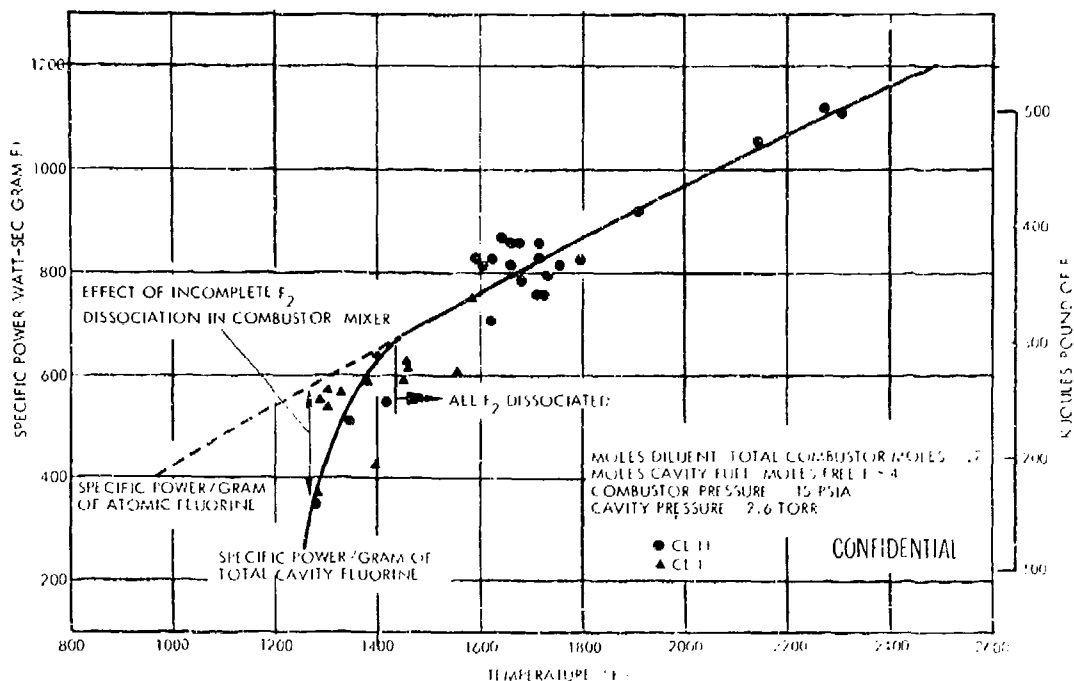


Figure 7. Effect of Cavity Fluorine Dissociation on Specific Power (U)

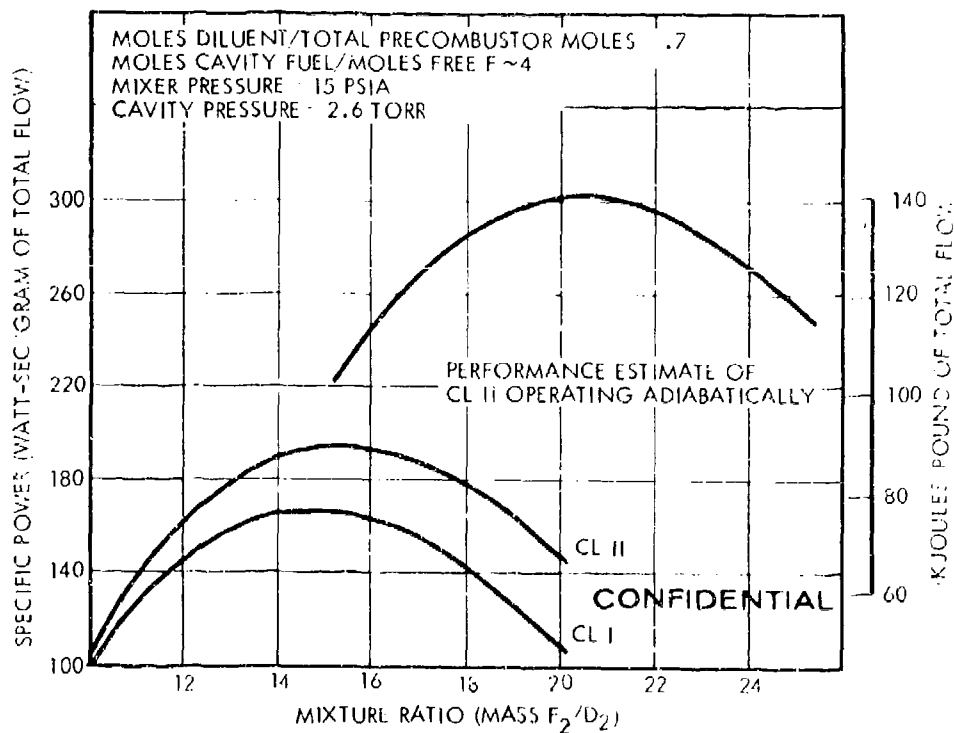


Figure 8. Summary Comparison Between CL-I and CL-II Combustor Configurations (U)

CONFIDENTIAL

(U) Figure 7 shows the observed effects of combustor temperature on laser performance. Below about 1500°K elemental F_2 remains after combustion and a severe break in the performance trend is seen to occur. Note that in this figure performance is given as power per unit mass flow rate of atomic fluorine. Specific power based on mass of F (or F_2) gives a quantitative measure of laser cavity performance divorced for the most part from combustor performance. The break below 1500°K is understood theoretically and discussed by Emanuel, et al (Ref. 7). The increase in performance with increasing temperature above 1500°K is, however, not completely understood at this time. Figure 7 emphasizes the now generally accepted view of superior laser performance in the cold reaction regime (i.e., by the reaction $\text{F} + \text{H}_2$) as laser action occurs in almost direct proportion to the cavity injected atomic fluorine; at lower temperatures where fluorine dissociation is incomplete, laser power decreases accordingly.

(C) Figure 8 presents a comparison between the earlier CL-I device and the CL-II configuration, emphasizing the effects of combustor heat losses. The CL-II design reduced combustor heat losses by 30 to 35 percent from CL-I and showed an increase in peak specific power from 165 to 195 watt-sec/gm of total flow (75 to 89 Kjoule/lb). Extrapolation of this effect to near adiabatic combustor design, as indicated in the figure, could provide about 300 watt-sec/gm of total flow (~140 Kjoule/lb). The total specific power peaks near a combustor mass mixture ratio (F_2/D_2) of approximately 16:1 in both devices. This mass mixture ratio corresponds to a combustor temperature of approximately 1600°K . Below this temperature the specific power diminishes because the dissociation of fluorine drops off (as shown in Figure 7); above this temperature the increase in combustor reactants required is not matched by a corresponding increase in atomic fluorine production. The increase in specific power for CL-II compared to CL-I is totally accounted for by a reduction in heat loss (and thus reduction in combustor reactant requirements) by improved design.

(U) In summary, the performance achieved with the CL-I and CL-II combustion driven lasers was comparable to that reported for the arc-driven devices by the Aerospace Corporation, both in overall efficiency and in trends with operating pressures and temperatures, which demonstrated

(U) that the products of combustion did not adversely affect lasing and appeared to act as diluents.

2. CAVITY DIAGNOSTICS

(C) A review of the closed-cavity power surveys of the 1 x 7 inch, two-dimensional slit nozzle array resulted in the selection of the following seven operating conditions for intensive diagnostic investigation (the corresponding power levels are noted for reference).

| | | |
|-----|--|--------|
| Ia | Baseline flow conditions | 2.9 kw |
| Ib | Cavity pressure increased by factor of 2 | 2.6 kw |
| Ic | Cavity pressure increased by factor of 4 | 2.1 kw |
| Id | Cavity pressure increased by factor of 6 | 0.9 kw |
| II | All flow rates and cavity pressures increased by 50 percent | 3.4 kw |
| III | Substitution of half of cavity hydrogen molar flow with helium | 3.1 kw |
| IV | Plenum temperature increased by 20 percent | 2.7 kw |

The selected baseline flow condition was a plenum pressure of 12.5 psia with a combustor temperature of 1900°K expanding to a cavity pressure of 1.3 torr. The corresponding total flow rate was 14.1 grams/sec.

(U) Cavity pressure variation at fixed combustor/plenum conditions (test conditions Ia through Id) was accomplished with a throttle valve located in the exhaust gas pumping system downstream of the lasing cavity. The calculated matched pressure ratio across the nozzle considering boundary layer development is approximately 180 (3.5 torr for 12.5 psia plenum pressure). Thus nozzle separation was likely to occur under test conditions Ic and Id, whereas the nozzle flow would be underexpanded under the other test conditions.

(U) The principal diagnostic measurement techniques employed were chemiluminescence spectroscopy (HF $\Delta v=1$ transitions 3 \rightarrow 2, 2 \rightarrow 1 and 1 \rightarrow 0), ground state resonance absorption spectroscopy, and infrared and visible intensity mapping of the flow field.

(U) Detailed wavelength scans of the cavity radiation were performed at four centerline locations of 0.51, 4.3, 7.1 and 17.8 cm downstream of the cavity injector exit plane. The viewing direction was chosen to be perpendicular both to the direction of the cavity flow and to the optical laser cavity axis. The purpose of the chemiluminescent spectral intensity distribution measurements was to determine the absolute excited state number densities for the chosen lines of sight. These data were then used to determine total HF vibrational state population and HF rotational temperatures.

(U) The chemiluminescent apparatus used in these experiments is shown schematically in Figure 9. The quartz windows were mounted in short tubes which were inserted into the laser cavity in order to reduce HF (1 \rightarrow 0) band absorption from the gas interposing between the window and the edge of the flow field. Optical axis alignment and precise focusing were achieved with an auxiliary laser and a small incandescent light source which could be lowered into the cavity and positioned at the precise location of the desired optical focus. Absolute sensitivity calibration of the

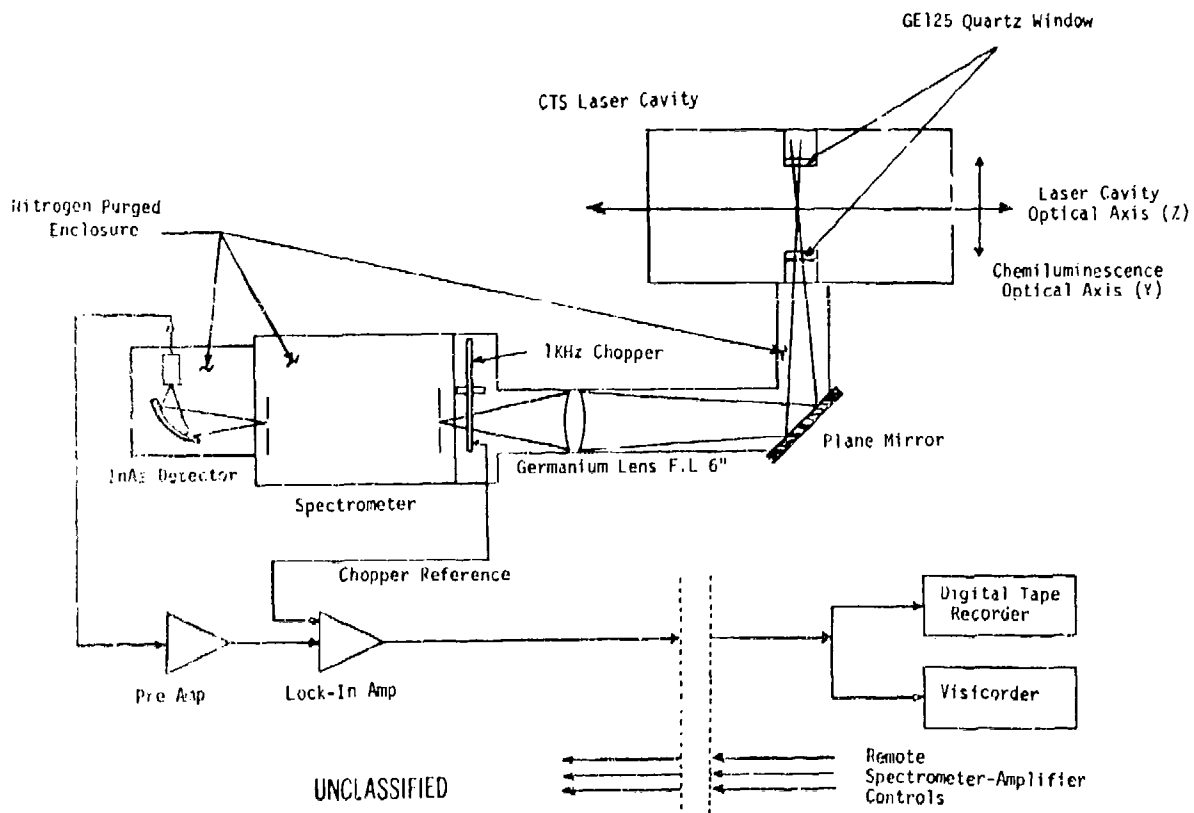


Figure 9. Schematic of Chemiluminescence Apparatus (U)

(U) chemiluminescent apparatus was achieved using a blackbody secondary standard at a temperature near 1000°K and controlled to within $\pm 3^{\circ}\text{K}$. Many calibration runs spread over several weeks of operation demonstrated calibration curve reproducibility to within better than $\pm 5\%$. A McPherson Model 218 spectrometer equipped with a 300 lines/mm grating and blaze angle optimized for 3μ was used in the apparatus. In order to achieve a very slender, nearly rectangular volume viewed by the spectrometer and yet utilize the full aperture of the spectrometer, the laser cavity center was imaged and demagnified by a factor of 4 onto the spectrometer slit. The slit height dimensions used were $3 \times 0.3 \text{ mm}$, resulting in an "effective slit image" of $12 \times 1.2 \text{ mm}$ in ZX plane of the laser cavity. Orientation of this slit image was such that chemiluminescent emission was averaged over a 12 mm span in the Z direction and a 1.2 mm length in the X direction. The averaging achieved in the Z direction is quite satisfactory since it covers the width of three individual slit nozzles. The spectrometer slit width of 0.3 mm determines also the spectrometer wavelength resolution as 0.03μ , which is equivalent to approximately 4 wavenumber resolution in the HF fundamental. This resolution is close to optimum for spectroscopy of the HF fundamental band since further reduction of slit width reduces spectrum intensity with no further increase in usable spectral resolution.

(U) A 10,000 sample/second infrared scanner was also constructed and used for the measurement of 2.7μ , HF band intensity distributions from the laser cavity. The IR scanner output was electronically processed and computer aided display techniques were employed to utilize these data for "flow field visualization" based upon infrared emission. Combining infrared scanner data with detailed, spectrally resolved chemiluminescent data, available from selected cavity positions, proved useful for determining HF excited state number density variations throughout the laser cavity. The infrared scanner design approach followed a fairly standard raster scan technique where the Z-direction scan, parallel to the laser optical axis, was accomplished by a ten-sided rotating mirror drum, while slowly scanning the optical assembly in a direction parallel to the cavity flow (X-direction) and about an axis through the radiometer lens (Figure 10). Aperture size and optical design parameters were chosen to accomplish spatial resolution as high as 1.5 mm near the scanner optical axis.

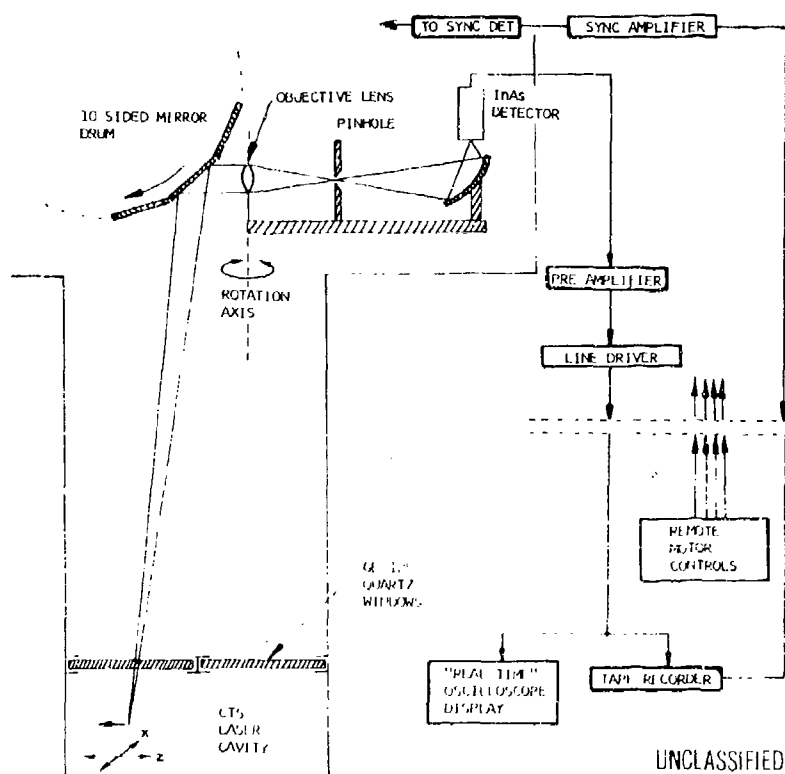


Figure 10. Schematic of IR Scanner Apparatus (U)

(U) Absolute radiative intensity calibration and 3 decades of dynamic range made it possible to use this apparatus for quantitative IIF band intensity measurements over a 12 x 12 inch area of the laser cavity downstream of the nozzle array. Characteristics of the electronics used in signal conditioning and recording the data limited the IR scanner to an effective bandwidth of 6 kHz, although the detector itself is capable of providing much faster system response.

(U) Chemiluminescent diagnostic measurements alone are not capable of yielding information on local HF vibrational ground state population when the radiating gas is optically thin. In the case of optical opacities between approximately 0.3 and 1, chemiluminescent data of the $1 \rightarrow 0$ transition can be evaluated to give information on HF, $v=0$ population. In both cases a direct measurement of HF-ground state by absorption of a probing signal has proven to be a more reliable technique. The HF-probing signal was obtained from a small HF-burner. The resonance line absorption measurements were performed using three HF-lines, namely P3, P5, P7

(U) of the $0 \rightarrow 1$ transition at the same four cavity locations which were chosen for the chemiluminescent spectral scans. In all cases, measurements with the P3 yielded net absorption, whereas the P5 and P7 lines yielded net absorption or net gain depending on experimental condition and window location.

(U) For the gain/absorption experiment, an apparatus was constructed which permits measurement of the amplification or attenuation of a small probing signal at the exact wavelength of selected vibration-rotation lines of the HF($1 \rightarrow 0$) band. In order to obtain the exact match of probing light wavelength with HF vibration-rotation lines the source of the probing radiation is derived from the emission of an H_2-F_2 flame. After isolating a selected spectral line, the total probing line attenuation and gain were measured and interpreted in terms of ground state population. A schematic of the apparatus is shown in Figure 11.

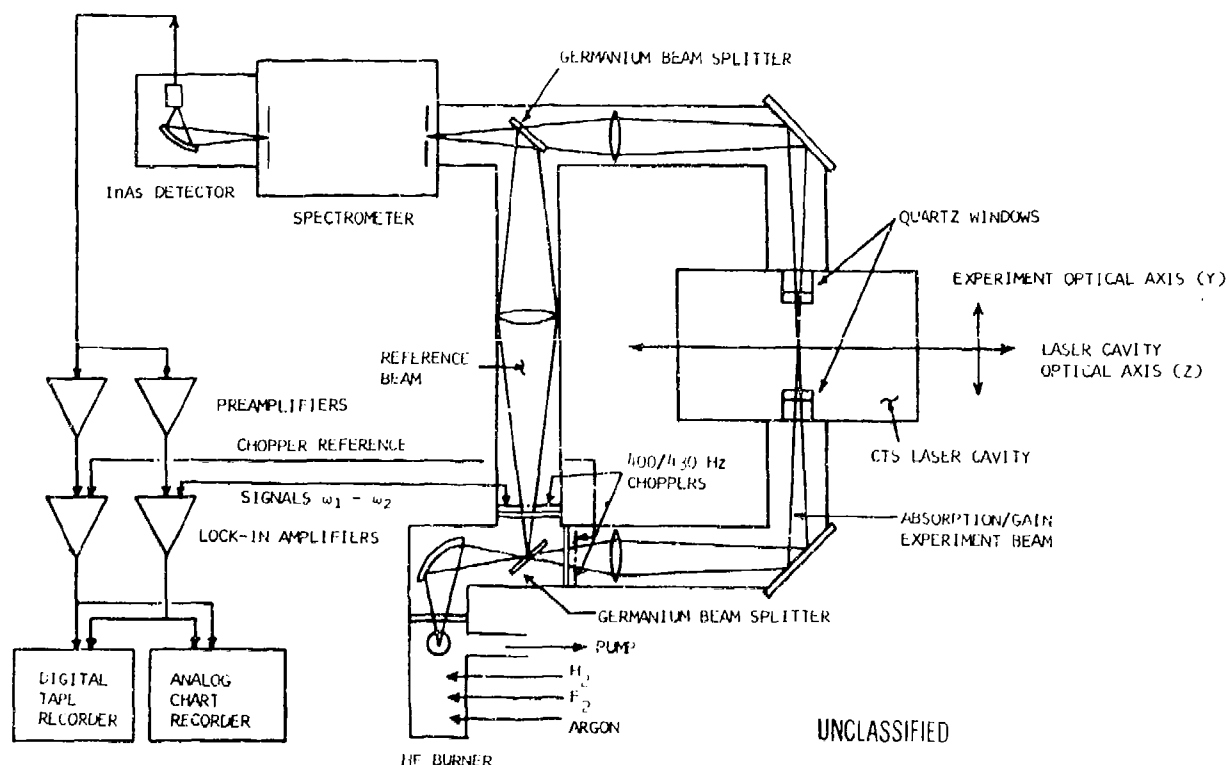


Figure 11. Schematic of Resonance Absorption/Gain Apparatus (U)

(U) The spectral line source for the HF resonance absorption was a low pressure H_2 - F_2 burner. Typical operating conditions for this burner are flow rates of 2.5×10^{-4} mole/sec H_2 , 3.5×10^{-4} mole/sec F_2 and total pressures in the range 2 to 5 torr. The exit window is protected from etching by a small flow of argon. Cryogenic (LN_2) pumping of HF and excess F_2 are used to reduce the HF partial pressure in the optical path inside the burner and to prevent any internal self-absorption of HF probing lines. In preliminary tests of the burner, it was verified by chemiluminescence measurements that this HF spectral line source is well described by assuming an optically thin radiating gas source, with Doppler line profiles corresponding to an effective Boltzman temperature of the order $1000^\circ K$. It is a necessary condition of the experiment to be able to define the source line shape in order to interpret the measured intensity attenuation data and derive the ground state HF concentrations in the laser cavity. A germanium beam splitter divides the total source output into reference and probing beams of approximately equal intensity which are modulated by chopper discs at different frequencies ω_1, ω_2 , respectively. The reference beam bypasses the laser cavity and is refocused at the entrance slit of the spectrometer; the probing beam is focused at the cavity centerline and again at the spectrometer entrance slit. Both reference and probing beams are merged at the second germanium beam splitter in front of the spectrometer. Each beam is partially plane polarized (~30 percent); however, the second beam splitter is arranged with a plane of incidence parallel to the first to avoid severe attenuation by crossed polarizers. The combined beams, after wavelength selection at the spectrometer, are detected by a single cooled indium arsenide detector. The reference and probing beam signals are then separated by two PAR 124 lock-in amplifiers in parallel circuits, one tuned to each of the chopper frequencies ω_1, ω_2 . The cavity chemiluminescent emission dc signal is rejected by the lock-in amplifiers except for contributions to the total noise of the measuring system. The entire optical system outside of the laser cavity (see Figure 11) is continuously purged with dry nitrogen to reduce absorption losses caused by atmospheric CO_2 and water vapor. In general, such losses can be reduced to less than 10 percent in the region near 2.7μ and are readily accounted for in the system calibration.

(U) The proper interpretation and significance of purely spectroscopic data became clear in many cases only by combining these data with other measurements of reactant and diluent mass flows, heat loss measurements and pressures, and visible light photography. The visible radiation from HF-flame is caused by high order transitions $\Delta v = 4, 5$ and 6 and is believed to be related to the reaction of atomic hydrogen with molecular fluorine. As the combustor operating conditions were selected to produce complete fluorine dissociation, the presence of molecular fluorine was attributed to recombination on the nozzle walls. Hence the visible "orange glow" frequently observed from the laser cavities is mostly related to gas volumes originating from the nozzle boundary layers. Therefore, visible light and IR flow field visualization are principally related to different chemical reactions and do not necessarily yield identical results. From the known reactant and diluent flow rates, heats of reactions and heat loss measurements equilibrium calculations were made to determine combustor plenum gas composition and stagnation enthalpy. Heat losses through the expansion nozzles were also measured and permitted a reasonably accurate determination of total laser cavity stagnation enthalpy.

(U) Determination of laser cavity HF - excited state number densities by chemiluminescent methods entails reduction of measured vibration - rotation spectral line intensities, $I(v'j' \rightarrow v''j'')$, as follows.

$$I(v'j' \rightarrow v''j'') = 10^{-7} \cdot \frac{16\pi^3}{3} c \cdot (\bar{\nu})^4 \cdot |\langle v'j' | M(r) | v''j'' \rangle|^2 \cdot |m| \\ \times \frac{1}{2j'+1} \int N_{v'j'}(y) d\vec{y}$$

Typical semilogarithmic plots of reduced HF vibration rotation state densities normalized to the statistical weight are shown in Figures 12 and 13. Matrix elements $|m|$ - factors are $j' + 1$ for P-branch and j'' for R-branch lines. Symbols $\{v'j'\}$ designate upper state vibrational and rotation quantum numbers whereas $\{v'', j''\}$ are for the lower state connected by the transition $v'j' \rightarrow v''j''$. Figures 12 and 13 show sample data with -O- points indicating measurements from P-branch lines and -Δ- from R-branch lines. The two lower curves in Figure 12 indicate the equivalent

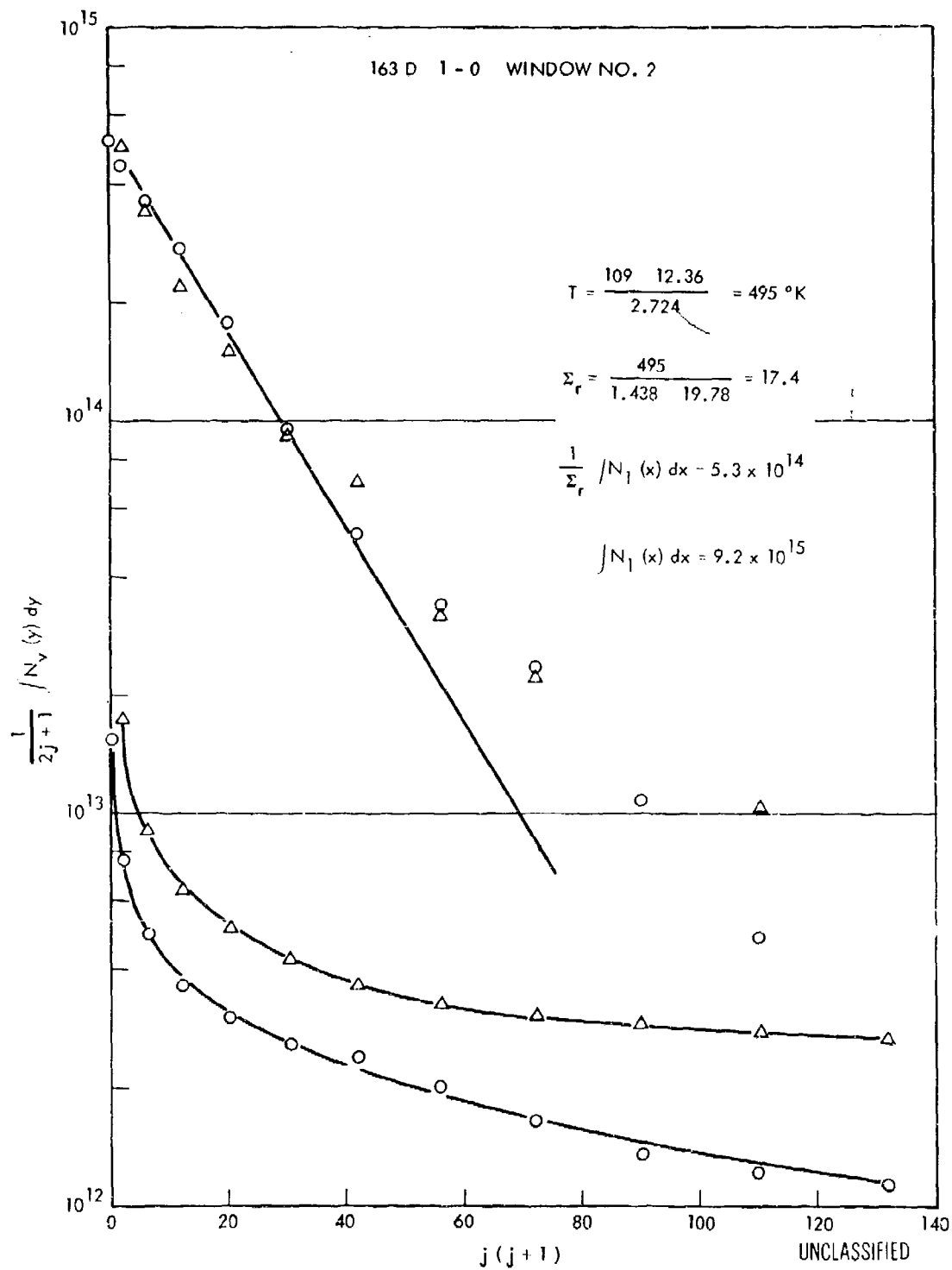


Figure 12. Typical "Boltzman" Plot of Chemiluminescent Data; Baseline Flow (1-0) (U)

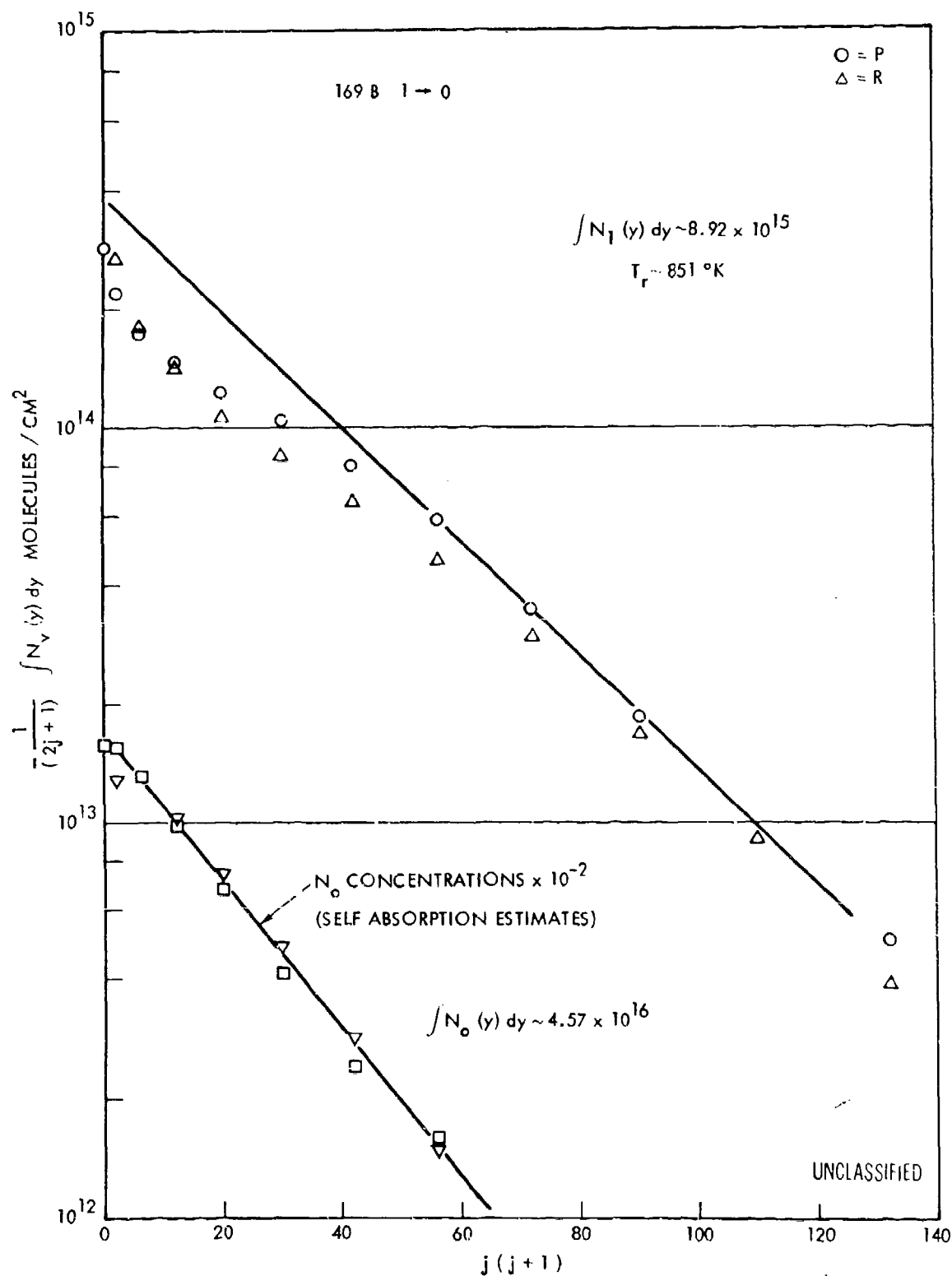


Figure 13. Typical "Boltzman" Plot of Chemiluminescent Data: Increased Cavity Pressure (1-0) (U)

(U) noise level of the respective data points. For all rotational levels up to $j'=6$ generally very excellent agreement of rotational temperatures determined by the slope technique between plots derived from $1 \rightarrow 0$, $2 \rightarrow 1$ and $3 \rightarrow 2$ lines is observed. Measurements of excited state densities from pairs of P- and R-branch lines also agree very well for optically thin conditions. It is therefore reasonable to equate thus measured rotational temperatures with local gas kinetic flow field temperatures averaged along the respective line of sight. At low cavity pressure, 1.3 torr, (Figure 12) significant discrepancy from a Boltzmann distribution of rotational sublevels j' -values in excess of 6 is observed. At cavity pressures of 5.5 torr (Figure 13) and higher very good Boltzmann distributions for rotational sublevels of at least up to $j'=10$ are indicated by the data.

(U) Figure 13 also shows a typical plot for a case where self-absorption is important. In this case the true Boltzmann distribution can be readily established from optically thin high j' -level lines. The measured apparent population deficiency of low j' -level lines, which is caused by self-absorption, was used to determine the lower state population. HF-vibrational ground states determined by this technique show excellent consistency comparing R-branch and P-branch lines (Figure 13) and agree very well with direct resonance line absorption/gain experiments.

(U) Observed populations of laser cavity HF in various modes of vibrational excitation without cavity mirror installed are presented in Figures 14 through 18 for test conditions I and II. The graphs include measured temperatures, excited vibrational and ground state populations summed over rotational sublevels and total excited state population as function of down-stream position.

(U) In the baseline flow case of Figure 14 the population levels of vibrational states 3 and 2 are seen rapidly rising to a maximum at about 3 cm downstream from the nozzle exit, followed by an approximately exponential decay with distance X . The vibrational level 1 continues to increase slowly to a downstream distance of 8 cm after the initial rapid rise to the level at 3 cm. The slow increase of N_1 downstream from approximately 4 cm is very likely caused by decay of N_2 and N_3 into N_1 . This is evident from noting the total HF population shown in Figure 14 by the curve designated as ΣN_v . The latter is seen to be constant within the

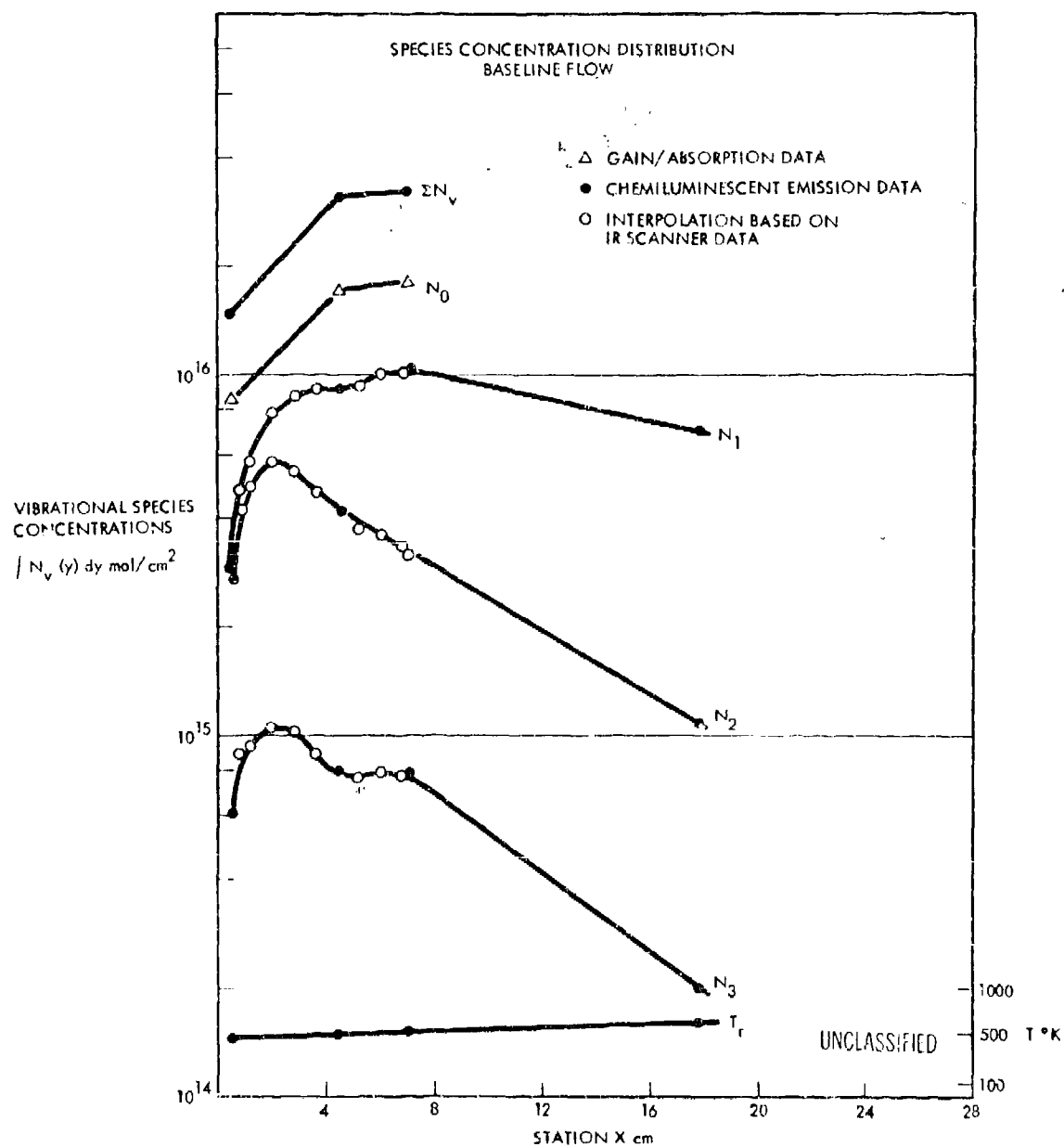


Figure 14. Vibrational State Distribution vs Laser Cavity Station X: Baseline Flow (U)

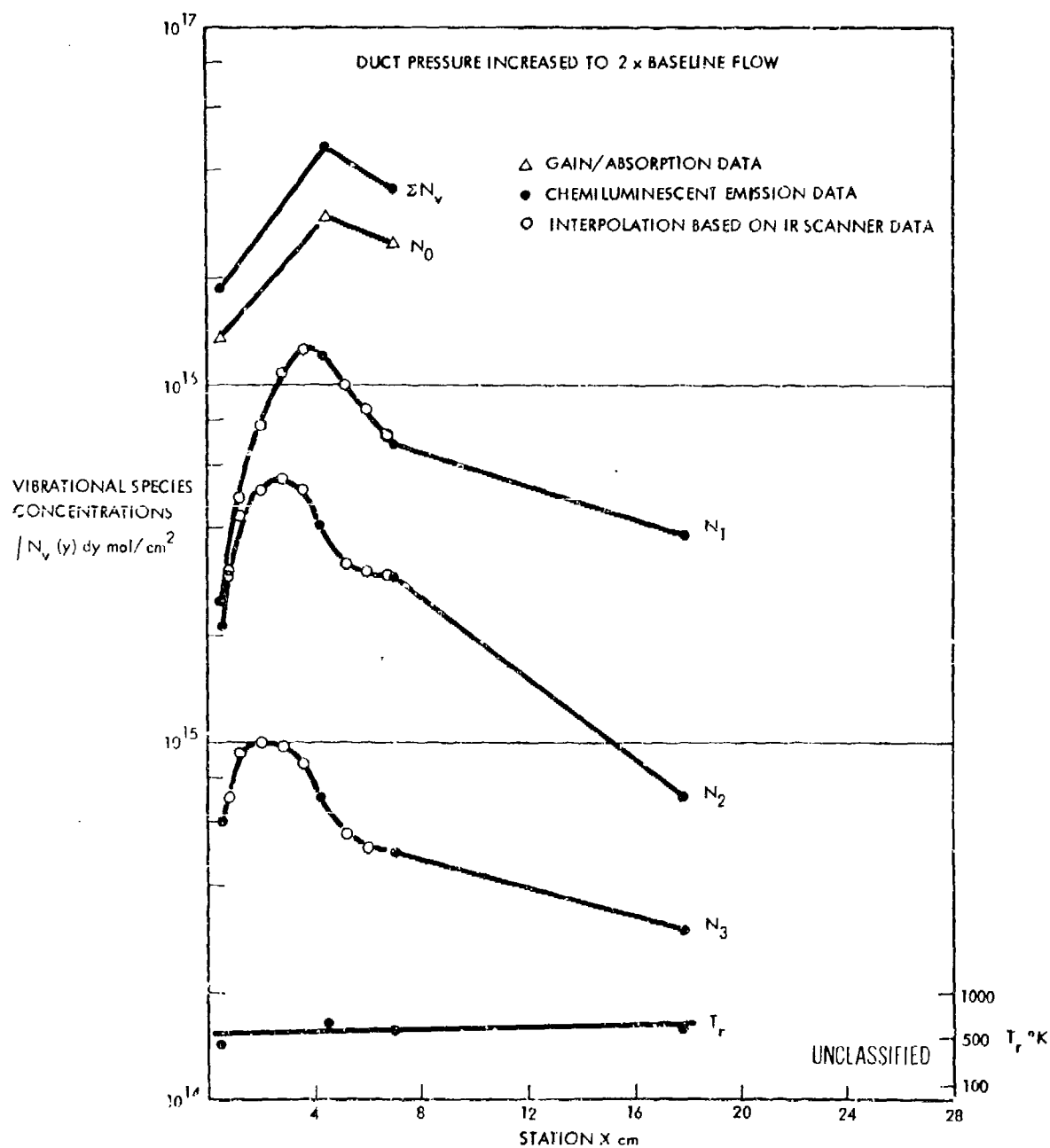


Figure 15. Vibrational State Distribution vs Laser Cavity Station X: Duct Pressure $\times 2$ (U)

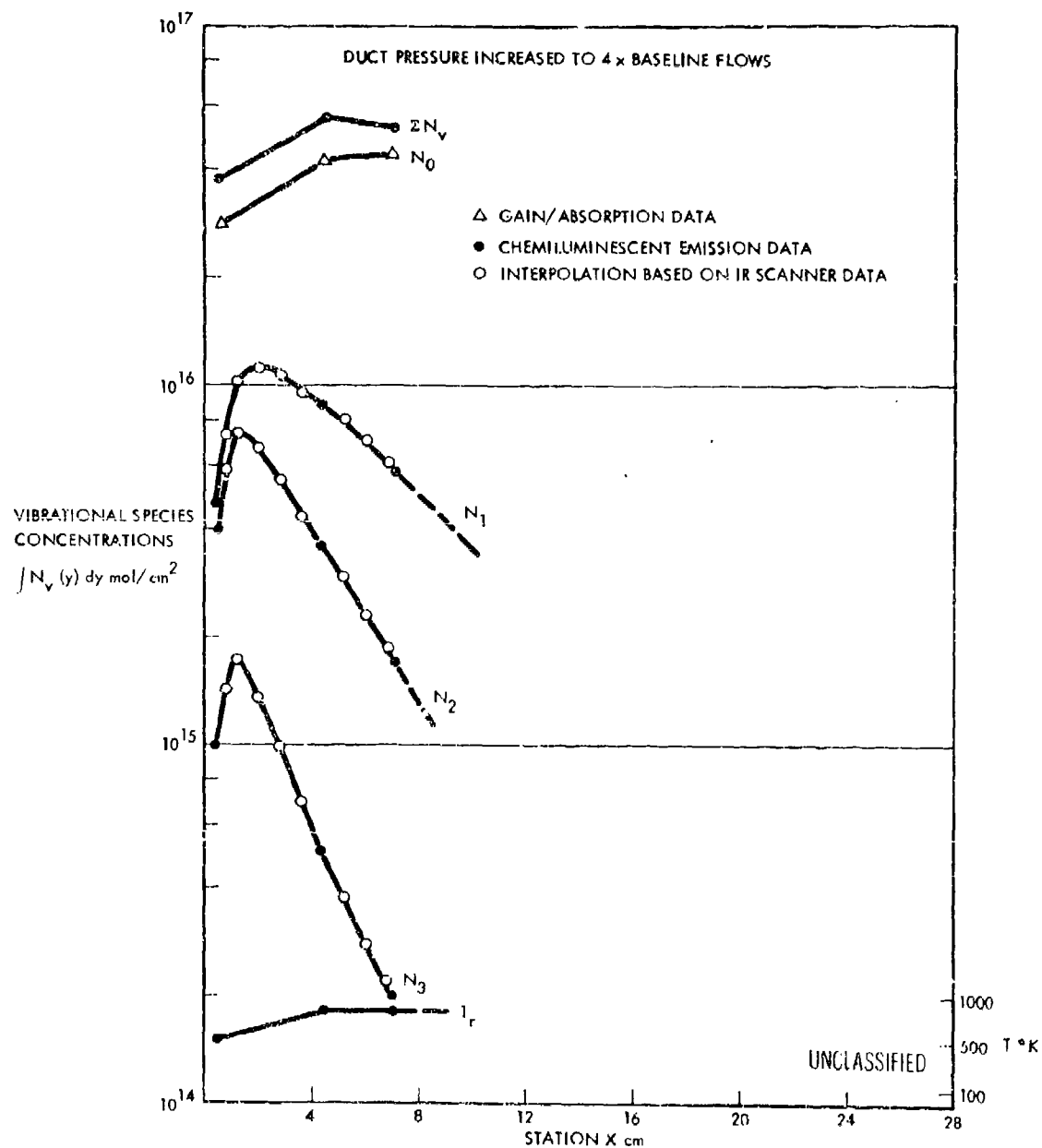


Figure 16. Vibrational State Distribution vs Laser Cavity Station X: Duct Pressure x 4 (U)

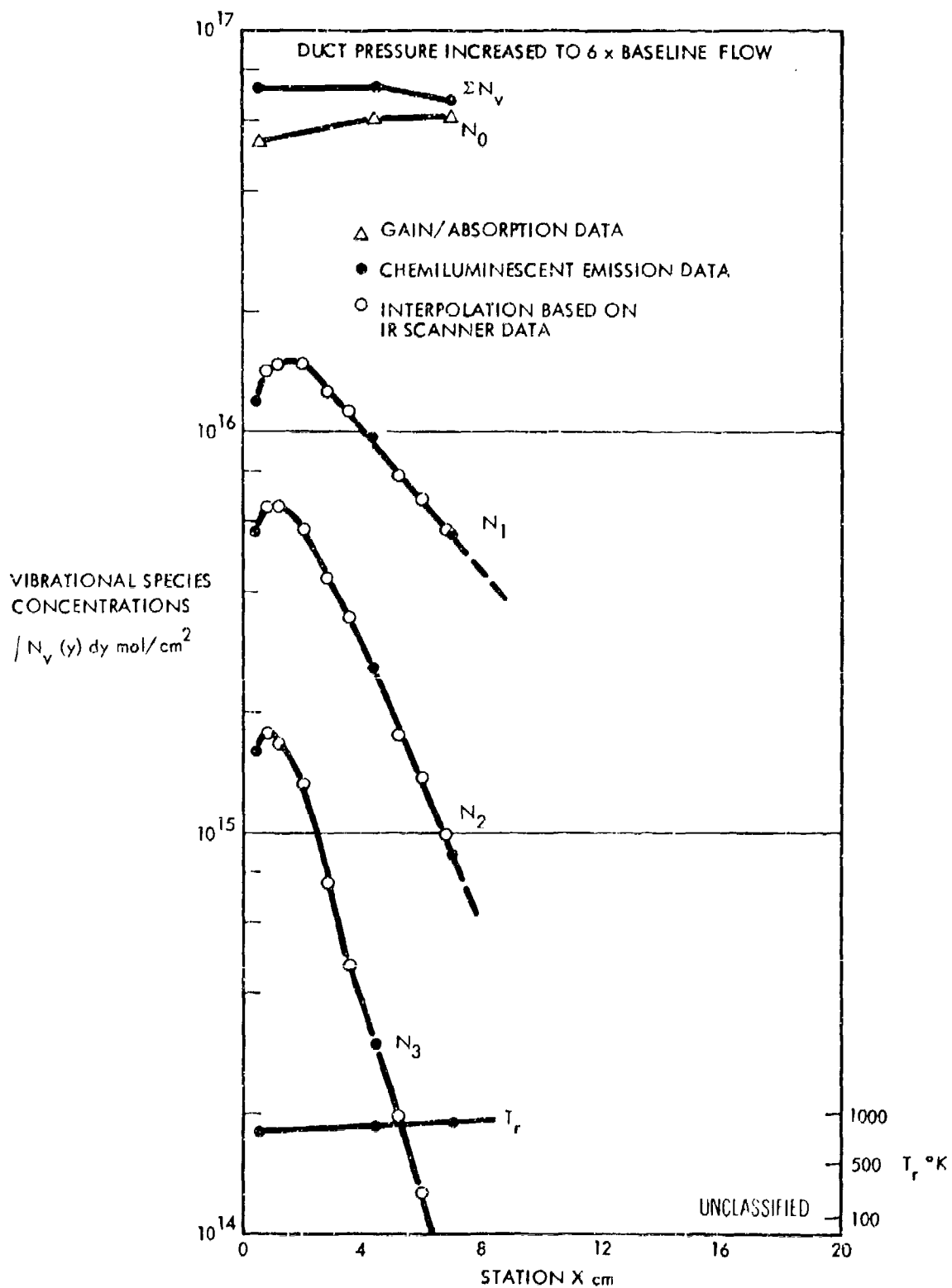


Figure 17. Vibrational State Distribution vs Laser Cavity Station X: Duct Pressure x 6 (U)

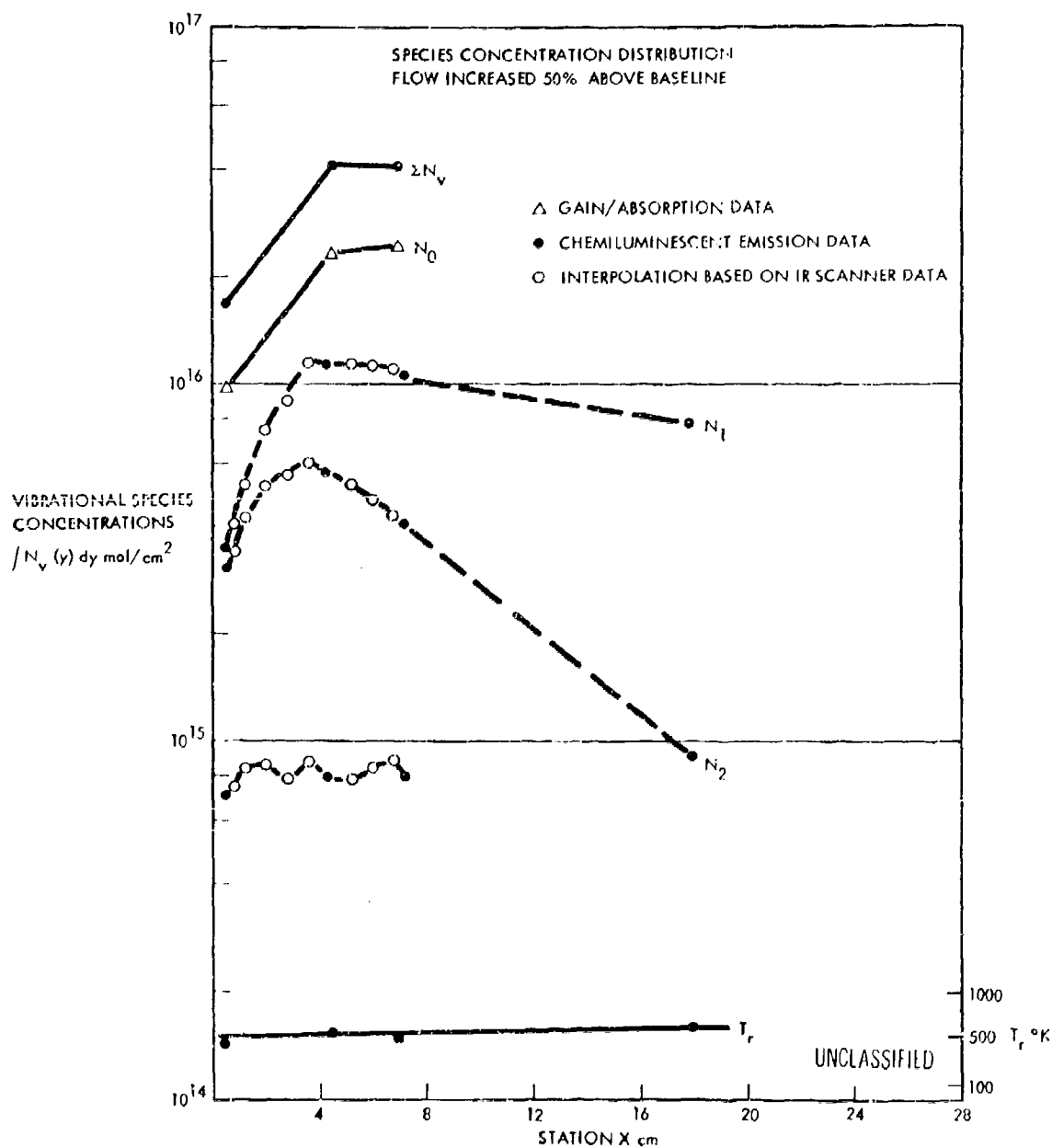


Figure 18. Vibrational State Distribution vs Laser Cavity Station X; Flow Increased 50% (U)

(U) measuring accuracy (20%) between window 2 ($X = 4.3$ cm) and window 3 ($X = 7.1$ cm). This latter fact implies that at the 4.3 cm station all the available fluorine has reacted to HF. Assuming this interpretation to be correct, the only mechanism by which N_1 can increase in population beyond 4.3 cm is by vibrational relaxation from N_2 and N_3 . The fact that the cavity reaction is virtually complete 4 cm downstream from the nozzle exit is of extreme importance for the laser. Clearly any laser power extracted further downstream, if any, for these conditions must be caused by residual pumping from relaxing N_2 and N_3 states. Of greater importance for the discussion of diagnostic experimental results is that once all the fluorine has reacted, the cavity gas composition, species molar flow rates, and total energy transport in the gas are known from measured reactant and diluent flow rates, heats of combustion and heat loss measurements.

(U) Figure 15 presents the vibrational state excitation profile for test condition Ib where the cavity pressure has been increased by approximately a factor of 2 from 1.3 torr to 2.7 torr, keeping all other experiment parameters unchanged. It is noted in Figure 15 that the levels N_1 , N_2 and N_3 are relatively unaffected by the cavity pressure change to a distance of approximately 3 cm. Between the 3 cm and the 7 cm position all excited vibrational levels experience a rapid decrease in population levels followed by a lesser rate of decrease. This is reflected in a shortening of the cavity lasing zone and probably result in a minor power loss. This observation is interpreted as the beginning effects of recirculating gas entrainment to be discussed later. Entrainment should result in a significant increase of N_0 population over the base flow case which is indeed observed. The apparent decrease of ground state and total HF population between windows 2 and 3 may be caused by a small increase in flow velocity.

(U) Increasing cavity pressure to 5.5 torr has the effect on HF cavity excitation as shown in Figure 16. Maximum population of N_1 , N_2 and N_3 now occurs very close to the nozzle at $X = 2$ cm followed by an extremely rapid decay downstream. Lasing zone length is now very short as compared to the baseline flow case. Significant entrainment is now occurring in the flow, effectively quenching HF excitation beyond the 2 cm position. As expected in the case of entrainment a drastic increase in HF ground state population is observed. Similar effects are observed for cavity pressure of 8.2 torr shown in Figure 17.

(U) In Test II all reactants and diluent mass flows were increased by a factor of 1.5 over the baseline flow case bringing the cavity pressure up to 1.9 torr from 1.3 torr. The resulting cavity excitation shown in Figure 18 is very similar to the baseline flow case. In this case entrainment would not be expected because of the low cavity pressure. From the measurements it appears that most of the increased flow rate of HF appears in the form of hydrogen-fluoride ground state. Therefore a significant laser power increase for this case in the 1-0 transition would not be expected. However, a proportionally larger increase in power from the 2-1 lines would be anticipated from the data. Measurements of laser output power for this flow condition are consistent with these observations.

(U) In test condition III, 50 percent of the molar hydrogen flow rate was replaced with helium to study the effect of hydrogen depletion. The chemiluminescent data did not indicate a significant effect although a slightly lower rate of HF deactivation by molecular hydrogen was expected. However, a modest increase in closed-cavity power was observed during conduct of a duplicate flow condition test with mirrors installed. Similarly the results of increased combustor temperature testing (condition IV) were not significant except that the chemiluminescent data predicted a decrease in laser power relative to the baseline flow case, which was indeed observed.

(U) The data of Figure 14, representing the "baseline flow" case (cavity pressure of 1.3 torr), indicate a state of "partial inversion" for all cavity locations, even those very close to the nozzles. This situation also prevails for all other test conditions (Figures 15 through 18). Also, substantial concentrations of ground state HF are observed at positions very close to the nozzle. These two facts are not consistent with known relative pumping rates into the various vibrational states or with acceptable collisional HF-deactivation rates. The observed data close to the nozzle require an HF-deactivation process which is orders of magnitudes faster than collisional quenching at the prevailing cavity pressures. Although not yet proven by experiment, the data suggest that the initial HF-deactivation process is radiative in nature caused by excessive initial gain in the medium. Parasitic modes sustained by partially reflecting walls are a well-recognized problem in high gain systems. This hypothesis finds further

(U) confirmation when comparing experimental data of Figure 11 with calculated HF state profiles of Figures 19 and 20 taken from Emanuel, et al (Ref. 7). Although these calculations are not for the exact test condition Ia they are sufficiently similar to warrant a qualitative comparison. In comparing the calculated HF state profiles with the measured results, the similarity of the trends presented in Figures 14 and 19 is very striking, although the latter figure represents a lasing case. In contrast, the calculated nonlasing case (Figure 20) shows both total inversion and very low vibrational ground state concentrations near the nozzle, in disagreement with the measured data. The apparent discrepancy between theory and experiment can be explained by the hypothesis of parasitic lasing near the nozzle exit.

(U) Returning to the discussion of the "baseline flow" case (Figure 14), it was noted that the total HF-population reaches a constant level at a downstream position of 4.3 cm. Since significant flow field velocity changes are not expected, the latter fact is interpreted as meaning that all the

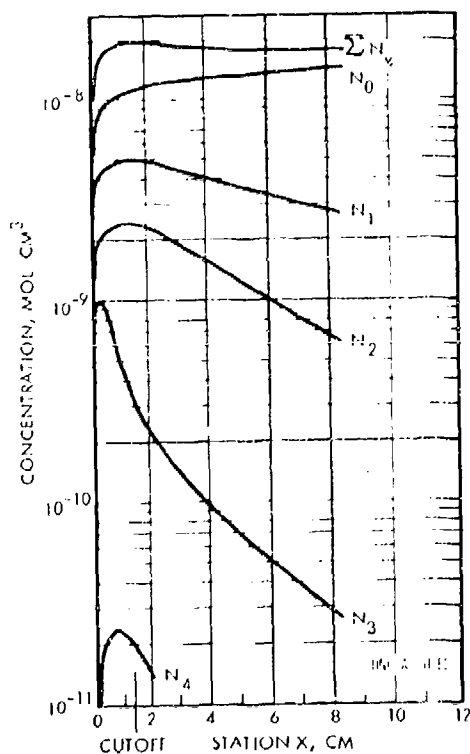


Figure 19. Calculated Excited Species Concentrations, Lasing Case (Ref. 7) (U)

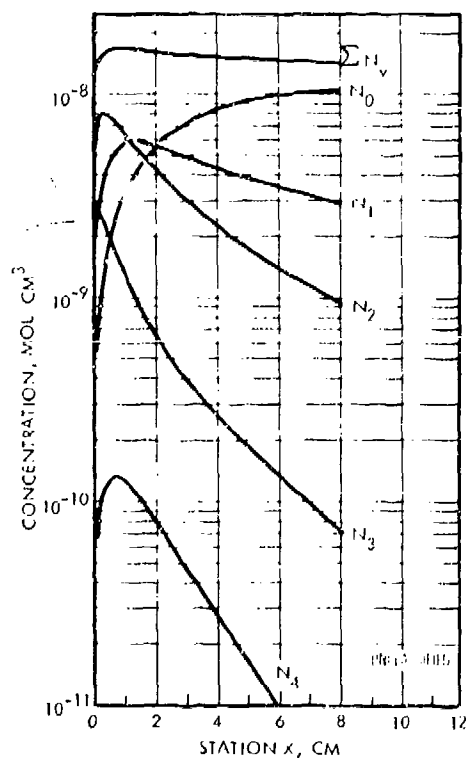


Figure 20. Calculated Excited Species Concentrations, Nonlasing Case (Ref. 7) (U)

(U) fluorine has reacted to form HF. In order for this to be possible, the laser fuel (H_2) and the atomic fluorine must have mixed. The required rapid mixing rates necessary to be consistent with the data are difficult to explain by laminar diffusion. Turbulent mixing, although not well understood theoretically in reacting flows, appears to be a more appropriate mixing model. The latter mixing hypothesis finds support from close inspection of flow field structure very close to the nozzles as observed with visible light photography.

(U) Figure 21 presents a scaled sketch of the edges of the orange glow region obtained from these photographs in relation to the nozzles. Postulated flow field features are also noted in the sketch. The freely expanding hydrogen jet attempts to overexpand to such an extent that the edge would reach the centerline of the fluorine nozzle at baseline flow conditions if the fluorine flow were not present. Thus, the interaction of the hydrogen and fluorine streams would be expected to generate a shock wave as shown schematically in the figure. The sharp bends in the orange region edges (that appear clearly in the color photograph originals) would be explained by these waves as the sketch indicates. The downstream contraction of the overexpanded hydrogen jet would generate expansion waves which together with the shock reflections could produce the curvature

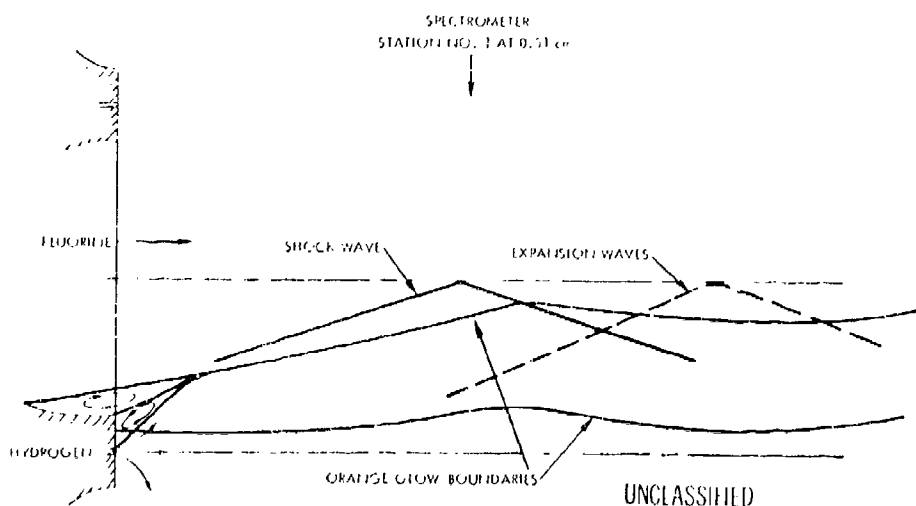


Figure 21. Top View of Cavity Flow Field (U)

(U) changes seen in the boundary edges. The large velocity difference between the underexpanded hydrogen jets and the highly viscous fluorine nozzle streams appears to promote the observed rapid mixing. The spreading angle of the luminous region into the fluorine stream was measured from the visible light photographs and was found to be essentially identical for all cavity pressure conditions tested. The rapid and, seemingly, pressure independent mixing can be explained by the turbulent mixing hypothesis, whereas it is difficult to rationalize these effects with a laminar diffusion model.

(U) The experimental observation of almost complete combustion of all laser cavity fluorine at locations of 4 cm downstream from the nozzle exit permits the determination of flow average velocities by applying a continuity relation

$$[\dot{\text{HF}}] = \frac{(\sum N_v) \cdot l \cdot \bar{v}}{6.025 \times 10^{23}} \text{ moles/sec}$$

where the molar flow rate of hydrogen fluoride, $[\dot{\text{HF}}]$, is known for the case of complete combustion from the input conditions, l is the nozzle bank width (17.8 cm) and \bar{v} is the average flow velocity. The observable total HF population integrated along the line of sight ($\sum N_v$ molecules/cm²) is read directly from Figure 14. The data yield an average flow velocity at 4 cm downstream for the baseline flow case of

$$\bar{v} = 3.0 \times 10^5 \text{ cm/sec} \pm 0.2 \times 10^5 \text{ cm/sec}$$

Assuming reasonably uniform velocity distribution over the entire flow cross section the kinetic energy of the flow can be calculated from the known total mass flow and the velocity by

$$\dot{W}_{\text{kin}} = \frac{\dot{m}_c}{8.37} \left(\frac{v}{10^5} \right)^2 \text{ Kcal/sec}$$

where \dot{m}_c is the total mass flow. For the baseline flow case (Figure 14) a total kinetic energy of 7.0 Kcal/sec is calculated. Similarly, the energy transport in random translational and rotational modes of the cavity gas is readily found from the measured temperature T , the cavity gas average

(U) degree of freedom \bar{f}_c and the total cavity gas molar flow rate, $\dot{\mu}_c$, using the relation

$$\dot{W}_{t-r} = \frac{2+\bar{f}_c}{2} \dot{\mu}_c \cdot R \cdot 10^{-3} \text{ (T-298) Kcal/sec}$$

where $R = 1.987 \text{ Kcal/mole } ^\circ\text{K}$. For the baseline flow case, \dot{W}_{t-r} is 2.4 Kcal/sec. The transport of vibrational HF-excitation energy can be calculated from

$$\dot{W}_v(\text{HF}) = [\text{HF}] \cdot \epsilon_1 \{y_1 + 2y_2 + 3y_3\} \text{ Kcal/sec}$$

where the excitation energy of HF is $\epsilon_1 = 11.3 \text{ Kcal/mole}$ and y_i is the relative concentration of the i -th HF vibrational state; i.e., $y_i = N_i / (\sum N_v)$. Transport of vibrational HF energy through the test cross section in the case shown in Figure 14 is $\dot{W}_v = 1.4 \text{ Kcal/sec}$. Ignoring possible vibrational excitation of H_2 and DF in the flow field, the total heat transport thus accounted for in the baseline flow case is

$$\dot{W} = \dot{W}_{t-r} + \dot{W}_v + \dot{W}_{\text{kin}} = 10.8 \text{ Kcal/sec}$$

The total available heat accounting for known input reactant flow rates and measured heat losses is 12.8 Kcal/sec assuming no recombination of atomic hydrogen. The agreement between measured total heat transport and available energy is good and well within the error bounds of the measurements. This good agreement lends considerable credibility and consistency to the energy partition in the flow field determined from the data. Combining all the data for the baseline flow condition it was concluded that approximately 70 percent of the chemical input energy was used to accelerate the gas, 20 percent went into random translational and rotational degrees of freedom and approximately 10 percent was found in vibrational excitation of HF molecules. Qualitatively very similar results were obtained for Test II (Figure 18) where all flow rates were increased by a factor 1.5. The effect of flow rate increase relative to Test Ia is seen in Figure 18 where the expected increase of N_o and $\sum N_v$ by a factor of 1.5 is observed. HF-excited state population, however, is not observed to rise as fast as the HF ground state population.

(U) The effect of cavity pressure increase on HF-excitation as evaluated in test conditions Ib, Ic and Id, was presented earlier as Figures 15 through 17. At fixed input flow rates these figures indicate a fast and dramatic increase in HF-ground state relative to HF-excited state, rapid excited state quenching and flow field temperature increase with increasing cavity pressure. These effects are best exemplified by test cases Ic (Figure 16) and Id (Figure 17). The observed fast collisional quenching of HF-excitation and the flow field temperature rise are consistent with the large increase in HF-ground state concentrations seen in Figures 16 and 17. Applying similar analysis as was used in the previous discussion of Test Ia and Test II data, it became apparent that the total measured HF-flow rates (ΣN_v), especially for test Ic (Figure 16) and Id (Figure 17), exceeded by far the available HF. This apparent discrepancy can be totally resolved by assuming entrainment of recirculating cavity gas. Entrainment by the higher cavity pressures is a reasonable assumption, considering that the matched nozzle exit pressure is about 3.5 torr whereas the cavity pressure in Test Ic was 5.5 torr and in Test Id was 8.2 torr. The entrainment hypothesis is strongly supported by the data of Figures 15, 16, and 17. Assuming an entrainment factor β and using measured HF concentrations and known input conditions, both the flow field average velocity and the entrainment factor can be estimated. Thus entrainment factors of 1.2 for Test Ib, 1.4 for Test Ic and 1.6 for Test Id, were determined from the data, confirming similar conclusions obtained initially from analyzing flow field photographs. Thus for the case of test Ic where the entrainment factor is approximately 1.4, 40 percent of the total gas flow through a cross section located 4 cm from the exit plane is caused by entrained cavity gas. Since the HF contained in the recirculating gases is expected to be mostly in the ground state, severe quenching of HF-cavity excitation and consequent power degradation are to be expected, and are in fact observed.

(U) In summary, chemiluminescent spectroscopy, infrared intensity scanner, and resonance absorption cavity diagnostic techniques were successfully employed in evaluating the flow field characteristics of a chemical laser cavity injector operated over a range of plenum pressures, mass flow rates and cavity pressures. Analysis of the data reveals a general rapid production of HF excited states which cannot be explained by a laminar

diffusion model for the mixing of the laser reactants, but is compatible with a turbulent mixing hypothesis. Additionally the data also indicated that significant entrainment of ground state HF by the expanding flow field was encountered as cavity pressure was increased. Therefore it was concluded that a major cause of decreased laser performance at high back pressures is entrainment of ground state HF with subsequent absorption in the optical path and increased deactivation of excited state populations.*

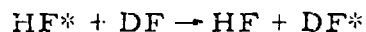
* Further evidence for the entrainment conclusion has been gained recently in experiments outside of this contract. Experiments with plume shrouds designed to prevent entrainment have shown substantial increases in laser power at high (~10 torr) back pressures.

SECTION II

LASER CAVITY DIAGNOSTIC MEASUREMENTS

1. INTRODUCTION

(U) The cavity diagnostic measurements conducted as part of this program were performed using the TRW CL-II configuration which has been discussed in detail in Appendix I of this report. The CL-II device uses a 1-inch by 7-inch slit nozzle bank in a configuration characteristic of the earlier "Mesa" design conceived by the Aerospace Corporation (Ref. 4). In the TRW, CL-II HF laser device, however, dissociation of F_2 is achieved by raising the temperature of the helium/fluorine gas mixture in the plenum chamber to the desired level by combusting a measured amount of deuterium with some of the injected fluorine in the precombustor. This method of gas heating adds molar concentrations of DF to the laser cavity gas mixture which amount to nearly twice the expected total HF concentrations. It is customary to ignore the possible effects of DF collisions and other dissimilarities on HF nonequilibrium excitation when comparing operational performance of the combustion heated slit nozzle configurations with the arc heated devices of the "Mesa" type. There are, however, no direct data presently available which totally justify such an assumption in all important details. For example, the effect of V-R transfer collisions between vibrationally excited HF molecules and ground state DF molecules following a scheme described by the relation



has not as yet been fully assessed.

(U) This point of direct comparison of the test results of arc driven and combustion driven HF lasers using the same slit nozzle configuration we believe requires further justification; this could most easily be achieved in future diagnostic studies by carefully studying the DF chemiluminescent spectrum, as well as that of HF. In some early tests we have in fact observed parts of the R branch of the DF, 1-0 transition; the intensities of these lines were hardly consistent with equilibrium excitation of the

(U) DF component at the prevailing cavity kinetic flow field temperatures of approximately 450°K.

(U) From a mechanical design point of view, the TRW CL-II configuration provided free access to side-on observation of the entire reactive cavity flow field region, starting at the nozzle bank exit plane and extending to downstream distances of 12 inches. In previous devices operated at TRW (CL-I), the slit nozzle exit plane, which is also the location of the hydrogen injection tubes, was covered by a "lip" obscuring the first 0.25 inch from direct side-on observation.

2. LASER CAVITY DIAGNOSTIC OBJECTIVES

(U) The laser cavity diagnostic measurements were directed at quantitative measurements of laser cavity excitation for the purpose of relating these data to laser apparatus design, operating parameters and performance characteristics. Of specific concern in this diagnostic measurements program was the definition of HF vibration-rotation state (nonequilibrium) population and excitation in the reactive flow field of the cavity, under varying operating conditions of a fixed injector/nozzle design. The purpose of this effort is to advance the physical understanding of the performance limiting effects in present HF/DF laser devices far enough to point the way towards improved engineering designs, or at least to better define unavoidable limitations of future devices in terms of achievable power output levels, beam properties and efficiencies.

(U) In accordance with the ultimate objectives of the Laser Technology Program we aimed the diagnostic measurements at three selected problem areas associated with present HF laser devices which utilize slit nozzle configurations. In close cooperation with the Air Force project engineer, we elected to acquire data primarily designed to help in clarifying the deleterious effects which result from the cavity pressure being increased beyond levels of approximately 5 torr. A second problem which we chose for investigation is the large excess flow rate of hydrogen required in the present operating devices. The third research objective was to study the cavity excitation levels as a function of a varying F/F_2 molar concentration ratio of fluorine injected into the cavity. We did, in fact, acquire data germane to the first two objectives; however, the test conditions

(U) actually selected for studying the effect of fluorine dissociation did not differ significantly in calculated F/F_2 ratios.

3. GENERAL CAVITY DIAGNOSTICS MEASUREMENTS TECHNICAL APPROACH

(U) Following the program outline of the TRW proposal No. 18273.000, 31 October 1970 (Ref. 8), specific cavity diagnostic measurements were developed and applied to the measurement of HF laser cavity nonequilibrium excitation. These measurements, originally outlined in our proposal and subsequently planned in greater detail, were performed during this program and included the following.

a. Measurement of HF Excited State Population at Selected Lines of Sight by Chemiluminescent Techniques

(U) The purpose of this experiment was to measure radiance of individual HF vibration-rotation lines, and to derive from these data upper state number densities integrated along the chosen line of sight through the reactive flow field. In order to average over the nonuniformities introduced into the flow field by the slit nozzle bank/injector design, the spectrometer slit height was chosen to cover a minimum of three individual slit nozzles in the direction perpendicular to both the flow direction and the nozzle slit throat. Spatial resolution in the direction of flow was made to be 1 mm.

b. Infrared and Visible Light Intensity Mapping of the Flow Field

(U) The specific diagnostic objective of the infrared intensity mapping experiment was to provide detailed information on the chemiluminescent intensity variations using spatial resolution (1 mm) small as compared to the width of the individual slit nozzles. These data were planned to be combined with the detailed chemiluminescent data obtained at selected cavity positions in order to construct a complete description of HF excitation throughout the cavity flow field.

(U) A second objective of the infrared mapper was to provide flow field visualization in the infrared. However, flow field visualization was also found to be possible by using visible light, "orange glow", photography. There is, however, an important difference between the two flow field visualization techniques. The infrared mapper localizes primarily

(U) flow field reaction zones where the "cold reaction" ($F + H_2$) is prevalent; this reaction is generally accepted as the one of dominant importance to the HF laser device. In contrast, it is now known that the "orange glow" (Ref. 9) photography depends on the ($H + F_2$) "hot reaction," i. e., on the presence of molecular fluorine in the flow field. Advanced HF/DF chemical laser engineering concepts aim at a complete dissociation of the injected fluorine and consequently the "orange glow" intensity really depends critically on catalytic fluorine recombination in the nozzle boundary layers.

c. Cavity Absorption/Gain Measurements for Determining HF Vibrational Ground State Population

(U) This experiment was aimed at complementing the information expected from the chemiluminescent and infrared mapping data with respect to the HF vibrational ground state population in the laser cavity. As one would expect from general laser principles, the ground state population is of critical importance to the operation and efficiency of the laser. Chemiluminescent emission, as applied to the measurement of HF excited state population, can be used in the case of the HF ($1 \rightarrow 0$) transitions for obtaining estimates on ground state ($v=0$) populations, provided that some of the observed emission lines exhibit self-absorption. For the case of very small self-absorption this method of HF ground state measurement clearly becomes impractical. Therefore, direct absorption techniques which determine absorption/gain coefficients for selected HF lines are needed. We chose to utilize a resonance absorption measurement in the HF fundamental, which is, according to our analysis, superior and more flexible than alternative techniques based upon the use of HF laser radiation.

(U) It was expected that a complete description of HF excitation, including a description of the ground state population, would be achieved for the selected laser operating parameters by combining the results from all three experiments. This diagnostic objective has been accomplished, although a few minor experimental problems still require further attention. At the time of writing our proposal, and at the beginning of this program, the chemiluminescent technique had been applied successfully to the diagnostics of HF laser cavities.

(U) Infrared pictures from HF laser cavities had been obtained by Aerospace Corporation using an IR-Vidicon technique. However, infrared intensity mapping with the wide dynamic range required for precision cavity excitation measurements had not been attempted before. Similarly, reliable HF ground state measurements using the HF resonance absorption technique required development. These development tasks were performed under this program but were aided to a considerable extent by separate but parallel efforts conducted under company sponsorship. Fortunately, the development of diagnostic techniques and equipment required only minor variations from our concepts as originally proposed. Subsequent use of the equipment in the diagnostic tests has demonstrated performance characteristics which were well within criteria set at the beginning of the program. In future tests we plan, however, to make minor changes to the infrared mapper and the absorption/gain equipment in order to achieve improved or more efficient operation.

4. CAVITY DIAGNOSTIC TECHNIQUES DESCRIPTION

(U) Development of diagnostic techniques for HF/DF laser research and development has been an important aspect of the Laser Technology Program. Therefore, a reasonably detailed description of these experimental techniques will be presented below, including a brief discussion of observables, technique limitations, and expected and experienced accuracies. Some experimental data will be presented for the purpose of discussing actual instrument performance, instrument problem areas and possible improvements.

a. Chemiluminescent Diagnostics Experiment

(U) Chemiluminescent diagnostic techniques have been applied successfully for several years in many areas of research, and including research directed at the development of chemical lasers (Refs. 10 and 11). The application of chemiluminescent diagnostic measurements for research on HF/DF chemical laser cavities appeared, therefore, logical and straightforward. TRW reported the first detailed chemiluminescent diagnostic data from a HF chemical laser cavity, and similar studies have since been reported by other laboratories. Our original results demonstrated the value of this technique for the measurement of HF laser cavity excitation and provided the first clear experimental verification

(U) that for most cavity positions, conditions characterized by "partial inversion" prevailed in the sense that $N_{v+1} \leq N_v$. It was, furthermore, convincingly demonstrated by the data that rotational sublevels of different vibrationally excited HF states were equilibrated to a common temperature; the most reasonable explanation of this observation is the assumption that the measured rotational temperature, which describes the Boltzmann distribution of rotational sublevels, is, in fact, equal to the local flow field gas kinetic temperature. This result was by no means surprising on the basis of expected rotational excitation relaxation rates. Under these conditions the local (small signal) cavity gain for all lines for a given $v' \rightarrow v''$ transition is entirely described by the total populations $N_{v'}$ and $N_{v''}$ of the upper and lower vibrational states, respectively, and by the rotational temperature (T_r). It is also well known that partial inversion gain can only exist for P-branch lines. The purpose of the chemiluminescent measurements is therefore to provide data on rotational (kinetic) cavity gas temperatures and on the total excited vibrational state number densities.

(U) There are some inherent principal limitations of chemiluminescent techniques. Perhaps the most severe one is the unavoidable spatial averaging effect over the entire volume from which the optical system collects light. Additional assumptions, or measurements of the relative excited state population distribution along the optical line of sight, are necessary in order to find local excited state number densities from the observable line intensity (watts/cm² sterad). Multiple line-of-sight techniques which could serve, in principle, to circumvent this problem do not appear practicable for HF laser cavity diagnostics because of the complicated and occasionally unpredictable symmetry of the radiating cavity gas. A second difficulty with chemiluminescent spectroscopy is the fact that it requires a relatively long time to acquire a complete spectral scan. One can, of course, expect to obtain interpretable chemiluminescent spectra only if the intensity variations during the scan time (~30 sec) are small as compared to the total signal. Fortunately, this potentially serious problem did not materialize in these experiments.

(U) As will be further discussed below, chemiluminescent data are interpretable only if the light is emitted from a slab of gas that is optically thin or nearly optically thin along the line of sight. For side-on observation (1-inch path) as used in these experiments this condition proved to be valid, although slight difficulties were encountered with the 1→0 and 2→1 bands in some experiments. For observations along the laser cavity axis (7-inch path), however, the expected large deviations from the optically thin case would render chemiluminescent data virtually uninterpretable and therefore our chemiluminescent data have been restricted to side-on observations only.

(U) Finally, problems of obtaining acceptable signal/noise ratios for reasonable spectral scan times have generally limited the measurements on observed spectra to the fundamental band ($\Delta v=1$) of HF, and in particular to the 4→3, 3→2, 2→1, and 1→0 bands. However, it is also logical to consider chemiluminescent diagnostic measurements using the HF harmonics $\Delta v=2, 3$, etc. Although the corresponding line matrix elements decrease, one expects this to be at least partially compensated by the availability of photo-emissive detectors of higher responsivity at the shorter wavelengths. In fact, detailed experimental work conducted at TRW has recently demonstrated the particular value of the harmonics

$$\Delta v = 3; \bar{\nu}_{0,0} = 11,373 \text{ cm}^{-1}; 0.878\mu$$

$$\Delta v = 4; \bar{\nu}_{0,0} = 14,833 \text{ cm}^{-1}, 0.675\mu$$

It appears that reliable matrix elements are now available for the $\Delta v=3$ transitions (Ref. 12), and future chemiluminescent spectroscopy using $\Delta v=3$ and possibly $\Delta v=4$ transitions is strongly recommended to obtain reliable data on high level excitation in HF laser cavities. Such research is required to answer questions relating to the apparent absence of the "hot" ($\text{H} + \text{F}_2$) reaction in experiments where, according to known plenum chamber conditions, large mole fractions of molecular fluorine exist. The present chemiluminescent apparatus can be adapted readily to this task, although no experiments directed at higher order harmonic emission from the high energy laser cavity have been attempted to date.

(1) Chemiluminescent Experiment Apparatus

(U) The chemiluminescent apparatus used in these experiments is shown schematically in Figure 22. Most of the details are readily explained by the schematic. Because of environmental safety constraints, all experimental components were controlled remotely by the operator. The quartz windows were mounted into short tubes which were inserted into the laser cavity in order to reduce HF ($1 \rightarrow 0$) band absorption from the gas interposing between the window and the edge of the reactive flow. We chose four window locations along the flow centerline (X-direction), at 0.51, 4.3, 7.1 and 17.8 cm, respectively, referring to the window centers. Optical axis alignment and precise focusing was achieved with an auxiliary laser and a small incandescent light source which could be lowered into the cavity and positioned at the precise location of the desired optical focus. Absolute sensitivity calibration of the chemiluminescent

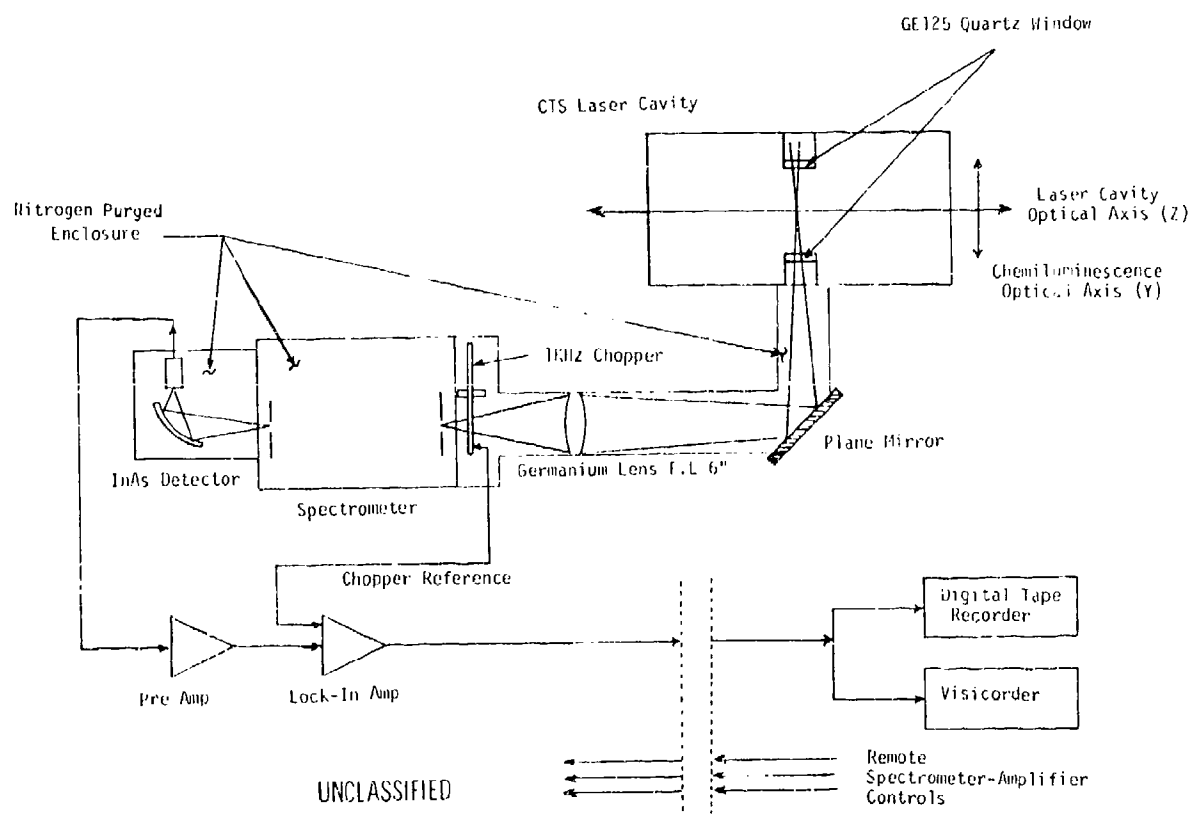


Figure 22. Chemiluminescence Experiment: Apparatus Schematic (U)

(U) apparatus was achieved using a blackbody secondary standard at a temperature near 1000°K and controlled to within $\pm 3^\circ\text{K}$. Many calibration runs spread over several weeks of operation demonstrated calibration curve reproducibility to within better than $\pm 5\%$. The absolute sensitivity of the chemiluminescent apparatus as a function of wavelength is shown in Figure 23. We used a McPherson Model 218 spectrometer equipped with a 300 lines/mm grating and blaze angle optimized for 3μ . In order to achieve a very slender, nearly rectangular volume viewed by the spectrometer and yet utilize the full aperture of the spectrometer (f/5.6) the laser

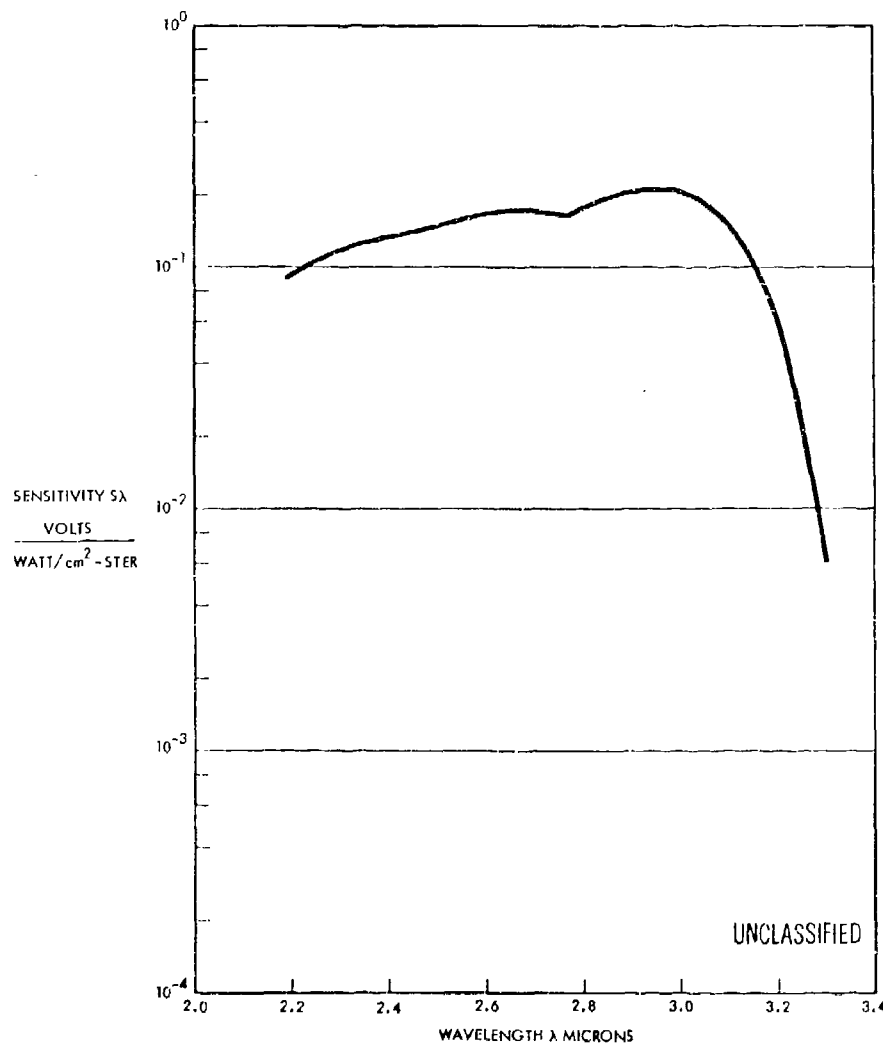


Figure 23. Chemiluminescence Experiment: Spectral Response (U)

(U) cavity center was imaged and demagnified by a factor of 4 onto the spectrometer slit. The slit height dimensions used were 3 x 0.3 mm, resulting in an "effective slit image" of 12 x 1.2 mm in ZX plane of the laser cavity. Orientation of this slit image was such that chemiluminescent emission was averaged over a 12 mm span in the Z direction and a 1.2 mm length in the X direction. The averaging achieved in the Z direction is quite satisfactory since it covers the width of three individual slit nozzles. The spectrometer slit width of 0.3 mm determines also the spectrometer wavelength resolution as 0.03μ , which is equivalent to approximately 4 wavenumber resolution in the HF fundamental. This resolution is close to optimum for spectroscopy of the HF fundamental band since further reduction of slit width reduces spectrum intensity with no further increase in usable spectral resolution. A photograph of the chemiluminescent apparatus is shown in Figure 24. A sample spectrum is shown in the discussion of experimental results, Section 6a.

(2) Chemiluminescent Experiment Data Interpretation

(U) For optically thin slabs of chemiluminescent gas, the observed intensity from an individual vibration-rotation line related to the transition ($v'j' \rightarrow v''j''$) is given in units watts/cm²·ster by

$$I(v'j' \rightarrow v''j'') = 10^{-7} \cdot \frac{16\pi^3}{3} c \cdot (\bar{\nu})^4 \cdot |\langle v'j' | M(r) | v''j'' \rangle|^2 \cdot |m| \quad (1)$$

$$\times \frac{1}{2j'+1} \int N_{v'j'}(y) d\vec{y}$$

where the factor $|m|$ is $(j'+1)$ for a P-branch line and (j') for an R-branch line, and the integral is extended over the line of sight. From Equation (1) it is evident that values of the normalized upper state population, i. e., upper state number density divided by its degeneracy factor, integrated along the chosen line of sight can be computed immediately from the observed intensity, provided that the relevant matrix elements are available.

(U) Experiments have yielded convincing evidence that the rotational sublevels of all vibrational states are in fact equilibrated and

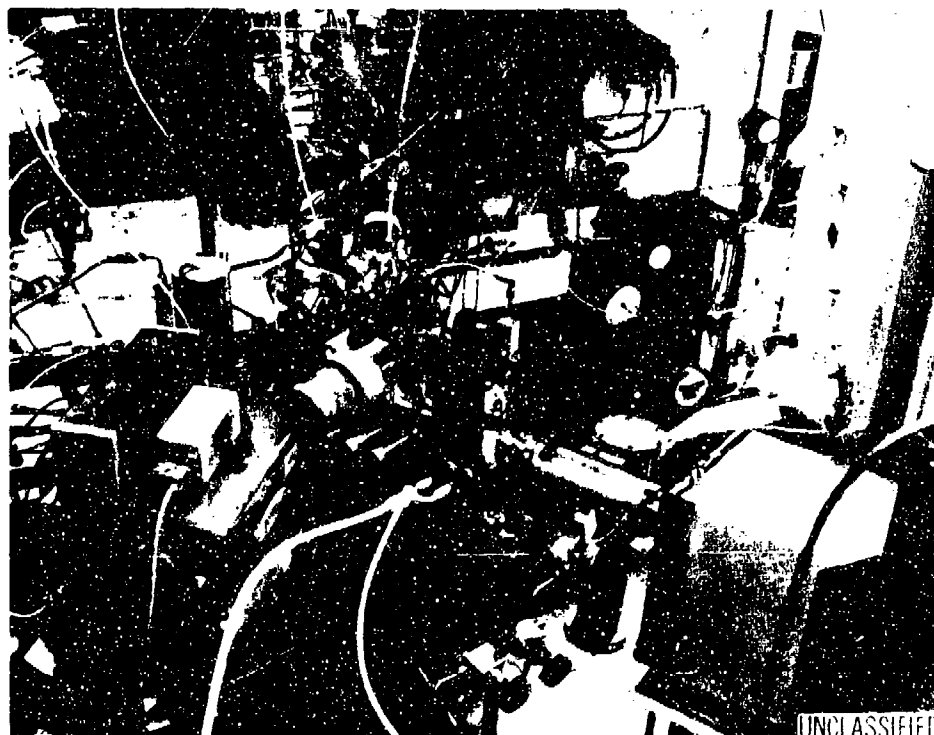


Figure 24. Chemiluminescence Experimental Apparatus -
Photograph of Test Setup (U)

(U) may be ascribed a Boltzmann temperature equal to the local flow field, gas kinetic temperature; in this case

$$\frac{1}{2j'+1} \int N_{v'j'}(y) dy = \frac{\int N_{v'}(y) dy}{\Sigma_{v'}(T)} e^{-\frac{1.438}{T} F_{v'}(j')} \quad (2)$$

where

$$\frac{1}{\Sigma_{v'}(T)} \approx \frac{1.438 \cdot B_{v'}}{T} ; F_{v'}(j') \approx B_{v'} j'(j'+1)$$

and $\int N_{v'}(y) dy$ is the total integrated population number density in the vibrational level v' obtained by summing over the population of all rotational sublevels. Gas kinetic temperatures and total vibrational state integrated number densities are, therefore, readily obtained from plots

(U) of the measured line intensities in the form $\log \left(\int N_{v',j'}(y) dy \right) / 2j'+1$ vs. $j'(j''+1)$, as is evident from Equation (3)

$$\log \frac{1}{2j'+1} \int N_{v',j'}(y) dy = \log \frac{\int N_{v'}(y) dy}{\Sigma_{v'}(T)} - (\log e) \cdot \frac{1.438 B_{v'}}{T} j'(j'+1) \quad (3)$$

Examples of such plots will be presented in the discussion of experimental results, Section 6a. Equations (1) and (2) are not entirely satisfactory for chemiluminescent intensity interpretations for all of the experiments discussed in this report because the assumption of an optically thin gas is not always correct; the more general case requires a complex radiative transport equation. Neglecting scattering, but accounting for spontaneous emission, absorption and induced emission, one finds:

$$d \{ I(\bar{\nu}, y) d\bar{\nu} \} = \epsilon(\bar{\nu}, y) d\bar{\nu} dy - k'(\bar{\nu}, y) \{ I(\bar{\nu}, y) d\bar{\nu} \} dy \quad \frac{\text{watt}}{\text{cm}^2 \text{ sterad}} \quad (4)$$

The coefficient of emission $\epsilon(\bar{\nu}, y)$ is

$$\epsilon(\bar{\nu}, y) d\bar{\nu} = 10^{-7} \frac{2 \cdot (2\pi)^3}{3} c (\bar{\nu})^4 | \langle v'j' | M(r) | v''j'' \rangle |^2 |m| \quad (5)$$

$$\times \frac{N_{v',j'}(y)}{2j'+1} \cdot \Gamma(\bar{\nu} - \bar{\nu}_0) d\bar{\nu} \quad \frac{\text{watt}}{\text{cm}^2 \text{ sterad}}$$

and the effective coefficient of absorption, accounting both for absorption and induced emission, is

$$k'(\bar{\nu}, y) d\bar{\nu} = \frac{(2\pi)^3}{3hc} \cdot \bar{\nu} \cdot | \langle v'j' | M(r) | v''j'' \rangle |^2 \cdot |m| \quad (6)$$

$$\times \left[\frac{N_{v'',j''}(y)}{2j''+1} - \frac{N_{v',j'}(y)}{2j'+1} \right] \cdot \Gamma(\bar{\nu} - \bar{\nu}_0) d\bar{\nu}$$

(U) The line shape factor $\Gamma(\bar{\nu} - \bar{\nu}_0)$ is normalized such that when integrating over the extent of a line

$$\int \Gamma(\bar{\nu} - \bar{\nu}_0) d\bar{\nu} = 1$$

In the special case of interest to HF laser cavities, total pressures do not exceed 10 torr and the HF vibration-rotation line shapes can be approximated by a Doppler profile; in that case

$$\Gamma(\bar{\nu} - \bar{\nu}_0) = \frac{1}{\sqrt{\pi} \Delta \bar{\nu}_D} e^{-\left(\frac{\bar{\nu} - \bar{\nu}_0}{\Delta \bar{\nu}_D}\right)^2} \quad (7)$$

where Doppler width, $\Delta \bar{\nu}_D$, is defined by

$$\frac{\Delta \bar{\nu}_D}{\bar{\nu}_0} = \frac{1}{c} \sqrt{\frac{2RT_{\text{kin}}}{\mu}} \quad (8)$$

(U) We will further assume that the energy density in the local radiation field, given by

$$u(\bar{\nu}, y) d\bar{\nu} = \frac{1}{c} \int_{\omega} d\omega \{I_{\omega}(\bar{\nu}, y) d\bar{\nu}\} \text{ joules/cm}^3$$

is sufficiently small to assure that the functions $k'(\bar{\nu}, y)$ and $\{I(\bar{\nu}, y) d\bar{\nu}\}$ in Equation (4) are uncoupled; this assumption is justified for all diagnostic tests because the above integral is extended only over solid angle ranges actually intercepted by the viewing spectrometer optics. It is practical to write Equation (4) in the form

$$d\{I(\bar{\nu}, y) d\bar{\nu}\} = \left(\frac{\epsilon(\bar{\nu}, y) d\bar{\nu}}{k'(\bar{\nu}, y) d\bar{\nu}} \right) - I(\bar{\nu}, y) \{k'(\bar{\nu}, y) d\bar{\nu}\} dy \quad (9)$$

(U) because the ratio of ϵ/k' is independent of specific molecular constants and can be derived from Equations (5) and (6) as

$$\frac{\epsilon(\bar{\nu}, y) d\bar{\nu}}{k'(\bar{\nu}, y) d\bar{\nu}} = 10^{-7} 2hc^2 (\bar{\nu})^3 \frac{1}{\left(\frac{N_{v''j''}(y)}{2j''+1} \right) \left(\frac{N_{v'j'}(y)}{2j'+1} \right) - 1} \quad (10)$$

$$\frac{\text{watt}}{\text{cm}^2 \text{ sterad } [\text{cm}^{-1}]}$$

This "generalized" Planck equation can readily be shown to reduce to the black body function when the ratio $\left(N_{v''j''}/(2j''+1) \right) \left(N_{v'j'}/(2j'+1) \right)$ is assumed to be in thermodynamic equilibrium. For uniform gas along the line-of-sight, i. e., when all functions in Equation (9) are independent of the coordinate y , then Equation (9) can be integrated to yield

$$I(\bar{\nu}) d\bar{\nu} = d\bar{\nu} \frac{\epsilon}{k'} \left(1 - e^{-k' \ell} \right) \quad (11)$$

where ℓ is the geometrical path length through the slab of gas. Equation (11) has the form of the well known "thermal radiation law" but is more general because it describes the radiation from nonthermal excitation as well. In the special case when $(N_{v''j''}/2j''+1) - (N_{v'j'}/2j'+1) = 0$ it follows that $k'=0$ and is independent of the number density for all ℓ

$$I(\bar{\nu}) d\bar{\nu} = \ell \cdot \epsilon(\bar{\nu}) d\bar{\nu} \text{ watt/cm}^2 \text{ sterad}$$

This special case is significant for diagnostics of laser cavities under conditions of near optical saturation. In the case of large gain along the line of sight, k' is negative and one can readily show that

$$I(\bar{\nu}) d\bar{\nu} = \frac{\epsilon}{|k'|} \left(e^{|k'| \ell} - 1 \right) \text{ watt/cm}^2 \text{ sterad} \quad (12)$$

(U) For large absorption, k' is positive and the intensity is given by

$$I(\bar{\nu})d\bar{\nu} = \frac{\epsilon}{k'} \left(1 - e^{-k'\ell} \right) \text{ watt/cm}^2 \text{ sterad} \quad (1)$$

Both Equations (12) and (13) reduce to the same equation which is valid for the optically thin case, namely

$$I(\bar{\nu})d\bar{\nu} = \ell \cdot \epsilon(\bar{\nu})d\bar{\nu} \text{ watt/cm}^2 \text{ sterad}$$

which, in turn, is identical to Equation (1).

(U) For the application of Equations (12) and (13) it is important to note that the spectral resolution of the chemiluminescent apparatus applied in these experiments was approximately 4 wavenumbers. This is much greater than the total Doppler halfwidths of the HF vibration-rotation lines, as can be verified from calculated line widths. The total line half width $\Delta\bar{\nu}_h$ is given in terms of the Doppler width $\Delta\bar{\nu}_D$ from

$$(\Delta\bar{\nu})_h = 2\sqrt{\ln 2} \cdot \Delta\bar{\nu}_D = 1.665 \cdot \Delta\bar{\nu}_D \text{ cm}^{-1}$$

At a typical cavity temperature of 450°K one calculates numerically, taking the P(4) line of the 1-0 transition as an example ($\bar{\nu}_0 = 3788 \text{ cm}^{-1}$), $\Delta\bar{\nu}_D = 0.773 \times 10^{-2} \text{ cm}^{-1}$ and $(\Delta\bar{\nu})_h = 1.29 \times 10^{-2} \text{ cm}^{-1}$. It is clear from the above stated choice of spectral resolution relative to actual line widths that the spectrometer is capable of measuring only the total line intensity and that the effects of self-absorption have to be accounted for by applying a "curve of growth" concept. For absorption (k' positive) Equation (13) yields for the observable total line intensity

$$\int I(\bar{\nu})d\bar{\nu} = \epsilon/k' \int d\bar{\nu} \left(1 - e^{-k'(\bar{\nu} - \bar{\nu}_0) \cdot \ell} \right) \frac{\text{watt}}{\text{cm}^2 \text{ sterad}} \quad (14)$$

(U) where according to Equations (6) and (7)

$$k'(\bar{\nu} - \bar{\nu}_0) = k'(\bar{\nu}_0) \cdot e^{-\left(\frac{\bar{\nu} - \bar{\nu}_0}{\Delta \bar{\nu}_D}\right)^2} \quad (15)$$

Combining Equations (14) and (15) and expanding the integral into a power series yields the following result for a Doppler broadened line profile:

$$\begin{aligned} \int d\bar{\nu} \left(1 - e^{-k'(\bar{\nu} - \bar{\nu}_0) \cdot \ell}\right) dx &= (k'_0 \cdot \ell) \sqrt{\pi} \Delta \bar{\nu}_D \cdot \\ &\times \left\{ 1 - \frac{k'_0 \cdot \ell}{2! \sqrt{2}} + \frac{(k'_0 \cdot \ell)^2}{3! \sqrt{3}} - \right. \\ &\left. + \dots \frac{(k'_0 \cdot \ell)^n (-1)^n}{(n+1)! \sqrt{n+1}} + \dots \right\} \end{aligned}$$

The total line intensity can now be determined and is

$$\int I(\bar{\nu}) d\bar{\nu} = \ell \cdot \int \epsilon(\bar{\nu}) d\bar{\nu} \cdot \left(\sum_0^{\infty} \frac{(-1)^n (k'_0 \cdot \ell)^n}{(n+1)! \sqrt{n+1}} \right) \frac{\text{watt}}{\text{cm}^2 \text{ sterad}} \quad (16)$$

Equation (16) is also applicable to the case of gain where $(k'_0 \cdot \ell)$ is negative. In the latter case the value of the sum is always greater than unity and the factor gives directly the total line intensity enhancement over the equivalent "optically thin" case. Values for the function defined in Equation (17)

$$\psi = \sum_0^{\infty} \frac{(-1)^n (k'_0 \cdot \ell)}{(n+1)! \sqrt{n+1}} \quad (17)$$

have been tabulated as function of $(\overline{k'_0 \cdot \ell})$ and have been presented graphically in Figure 25. The practical value of Equation (16) is that for

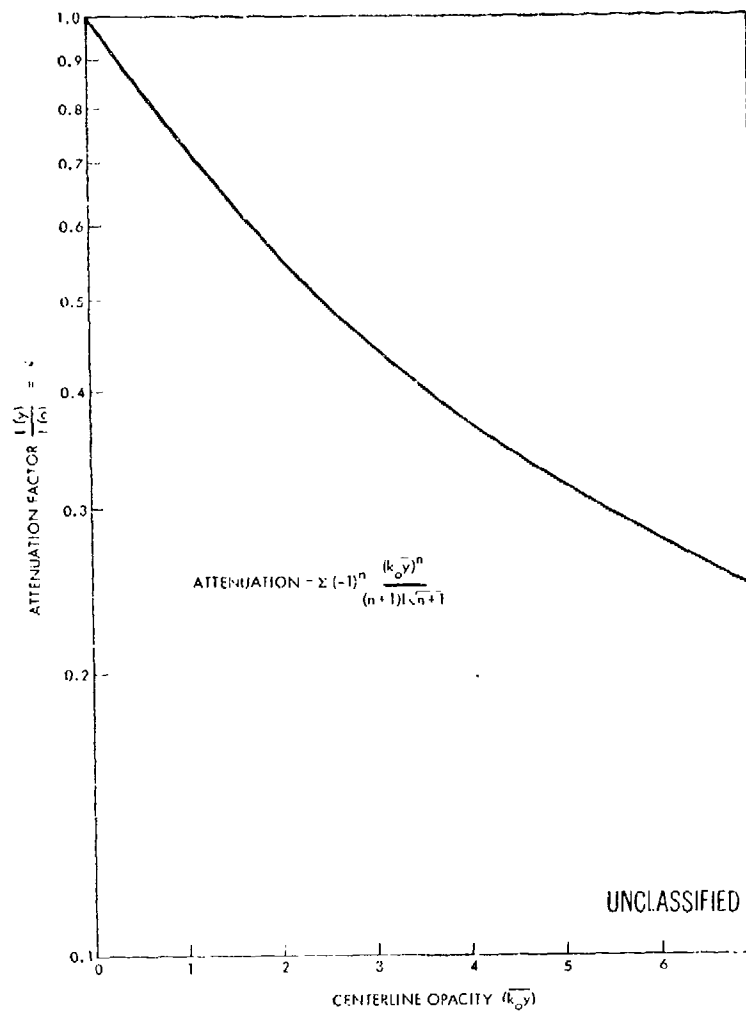


Figure 25. Line Attenuation Factor for Self Absorption vs Line Center Opacity (U)

(U) the diagnostic case of modest optical opacity ($0.3 < |k'_0 \ell| < 3$) the ratio " ψ " (Equation (17)) can be extracted from the data. Measured values of " ψ " can then be used in conjunction with Equation (17) or the graphical representation (Figure 25) to find for given lines values for $k'(\bar{v}_0) \cdot \ell$. These, in turn, can serve to determine numerical values for the difference between

(U) upper and lower state populations which is given by combining Equations (6), (7) and (8)

$$\int k(\bar{\nu}_0) dy = \overline{k_0 \cdot \ell} = \frac{(2\pi)^{5/2}}{3h} \sqrt{\frac{\mu}{RT}} \cdot |m| \cdot |\langle v'j' | M(r) | v''j'' \rangle|^2 \quad (18)$$

$$\times \left\{ \frac{1}{2j''+1} \int N_{v''j''}(y) dy - \frac{1}{2j'+1} \int N_{v'j'}(y) dy \right\}$$

(U) The remaining problem is how to determine in practice the attenuation/gain factors " ψ " (Equation (17)) from chemiluminescent data. This can be accomplished in the case of spectrally resolved vibration-rotation bands if it is possible to observe at least a few optically thin lines. This will always be possible when the strongest lines of the band are of modest opacity ($k_0 \cdot \ell < 3$), when the signal/noise ratio of the measurement (strongest lines) is 30 or better and when the rotational sublevels are thermalized. The chosen instrument sensitivities and experiment conditions were consistent with the above stated requirements for the data discussed in this report. Consequently measured intensities from the higher j' level, optically thin HF lines were used in appropriate cases to determine the normalized population in all rotational sublevels of a given vibrational state v' by using Equation (1) and plotting the data according to Equation (2). Then by using the observed intensities for the lines exhibiting noticeable absorption or gain and applying Equation (1), the "apparent" population levels were determined. The ratio of the thus determined apparent population to the true population established by extrapolating from the optically thin lines yields directly the " ψ " factor of Equation (17). A practical example of this procedure has been discussed in Section 6a.

(3) Chemiluminescent Data Error Analysis

(U) Rotational temperatures as determined from measured chemiluminescent HF vibration-rotation line intensities are reliable to within better than $\pm 7\%$. Absolute, vibrationally excited state densities are accurate to within $\pm 20\%$.

(U) Flow field temperatures and HF excited state number densities which are reported here have been computed from measured chemiluminescent line intensities and are subject, therefore, to uncertainties which can be determined from the relative errors in these intensity measurements.

(U) The measurement of rotational temperatures by the slope technique, as described in the previous section, depends upon measured line intensity ratios rather than upon the absolute line intensities. The intensity ratio (I_1/I_2) of two vibration-rotation lines of the same $\{v' \rightarrow v''\}$ transition can be derived by combining Equations (1) and (2) and is represented by:

$$\ln \frac{I_1}{I_2} = \ln \frac{\{(\tilde{\nu})^4 \cdot |m| \cdot |\langle v'j' | M(r) | v''j'' \rangle|^2\}_1}{\{(\tilde{\nu})^4 \cdot |m| \cdot |\langle v'j' | M(r) | v''j'' \rangle|^2\}_2} \quad (19)$$

$$- \frac{1.438 \cdot (X_1 - X_2)}{T}$$

where subscripts 1 and 2 refer to the two referenced lines and the excitation energies X_1 and X_2 are given respectively by

$$X_1 \approx B_{v'} \{j'(j'+1)\}_1 \text{ cm}^{-1}$$

and

$$X_2 \approx B_{v'} \{j'(j'+1)\}_2 \text{ cm}^{-1},$$

it can further be verified (most easily by computing numerical values) that for HF P-branch lines

$$\frac{\{(\tilde{\nu})^4 \cdot |m| \cdot |\langle v'j' | M(r) | v'', j'' \rangle|^2\}_1}{\{(\tilde{\nu})^4 \cdot |m| \cdot |\langle v'j' | M(r) | v'', j'' \rangle|^2\}_2} \approx \frac{|m|_1}{|m|_2} = \frac{\{j'+1\}_1}{\{j'+1\}_2}$$

(U) This relation holds to within better than 3% for lines up to $j'+11$.

Hence,

$$\ln\left(\frac{I_1}{I_2}\right) \approx \ln\left(\frac{\{j'+1\}_1}{\{j'+1\}_2}\right) - \frac{1.438 (X_1 - X_2)}{T} \quad (20)$$

Logarithmic differentiation of Equation (20) yields an equation relating the relative temperature uncertainty ($\Delta T/T$) to the relative intensity ratio uncertainty, $\Delta(I_1/I_2)/(I_1/I_2)$, as

$$\frac{\Delta(I_1/I_2)}{(I_1/I_2)} = - \frac{1.438 (X_1' - X_2')}{T} \cdot \frac{\Delta T}{T} \quad (21)$$

Approximately optimum measuring accuracy for temperature measurement can be achieved when the two lines are chosen such that $I_1 \approx I_2$ corresponds to $j'=0$. In that case $X_2'=0$ and Equation (20) reduces to

$$\ln \frac{I(j')}{I(j'=0)} \approx \ln(j'+1) - \frac{1.438 B_{v'} j'(j'+1)}{T} \quad (22)$$

Equal line intensities $I(j') \approx I(j'=0)$, requires that the left-hand side of Equation (22) be approximately zero so that

$$\ln(j'+1)_{\text{opt}} \approx \frac{1.438 B_{v'} j'(j'+1)}{T} \quad (23)$$

The relative temperature accuracy follows then as

$$\left| \frac{\Delta T}{T} \right| = \frac{1}{\ln(j'+1)_{\text{opt}}} \cdot \left| \frac{\Delta(I_1/I_2)}{(I_1/I_2)} \right| \quad (24)$$

For typical temperatures of $T=450^\circ\text{K}$ in the laser cavity and for the P-branch of the transition $\{v'=2 \rightarrow v''=1\}$ using for $B_{v'} = 19.033 \text{ cm}^{-1}$, one determines from Equation (23) that $(j'+1)_{\text{opt}} = 6$; i. e., $\ln(j'+1)_{\text{opt}} \approx 1.8$.

(U) Measuring accuracy of line intensity ratios depends upon the signal/noise ratio of the measurement and the relative calibration accuracy. Relative calibration accuracy is essentially determined by the calibration reproducibility for repeated calibration runs, and one can show that provided $I_1 \approx I_2$

$$\frac{\Delta(I_1/I_2)}{(I_1/I_2)} \approx 2 \cdot \left| \frac{1}{(S/N)} \right| + \left| \text{calibration} \right|_{\text{rep}} \quad (25)$$

Calibration reproducibility has been determined empirically to be better than $\pm 5\%$ and signal/noise is typically 30. It follows that the relative error in measuring line intensity ratios is expected to be

$$\left| \frac{\Delta(I_1/I_2)}{(I_1/I_2)} \right| \approx 0.12.$$

Using these data the relative error in the resulting temperature follows from Equation (24) as

$$\left| \frac{\Delta T}{T} \right| \approx 0.07$$

Measured IIF laser cavity temperatures are near 450°K and the temperature measuring uncertainties amount, therefore, to approximately $\pm 30^\circ\text{K}$. Measurement uncertainties on this level are quite consistent with the actual chemiluminescent data fluctuations. Empirically the systems peak-to-peak noise is found to be $8\ \mu\text{v}$; the resulting noise rms voltage is therefore $2.8\ \mu\text{v}$. A sample spectrum illustrating this analysis has been shown in Section 6a. Consistent with the preceding error analysis the P(1) and P(6) lines of the $\{1-0\}$ and the $\{2-1\}$ transitions are of approximately equal intensity. The signal voltages for P(1) and P(6) lines of the $\{2 \rightarrow 1\}$ band are $75\ \mu\text{v}$; the signal/noise ratio of the measurement is therefore 27. In the case of the $\{1-0\}$ transition the corresponding P(1) and P(6) lines exhibit signals of $115\ \mu\text{v}$ and the corresponding S/N is therefore 41. In order to reduce the errors in future measurements to those contributed solely by calibration, it would be necessary to improve the S/N of

(U) the measurements by approximately a factor of 3. This can most easily be accomplished by reducing electronic bandwidth by approximately a factor of 10, requiring a slow down in spectral scan speed from the present 30 seconds per scan. Improving detection sensitivity is not expected to be beneficial because experimental evidence indicates that the empirically determinal signal/noise ratios are characteristic of the laser cavity medium and spectrometer stray light and do not appear to be set by detector or amplifier noise. Reduction in calibration relative error is also possible but would require substantially improved and much more costly calibration setups.

(U) Relative error of "normalized excited state population" is equal to relative error of absolute line intensity measurements (Equation (1)); i. e. ,

$$\frac{\Delta \left\{ \frac{1}{2j'+1} \int N_{v'j'}(y) dy \right\}}{\left\{ \frac{1}{2j'+1} \int N_{v'j'}(y) dy \right\}} = \frac{\Delta \{ I(v'j' \rightarrow v''j'') \}}{\{ I(v'j' \rightarrow v''j'') \}} \quad (26)$$

(U) Absolute intensity relative error is essentially given by

$$\left| \frac{\Delta I}{I} \right| = \left| \frac{1}{S/N} \right| + \left| \text{calibration} \right|_{\text{rep.}} + \left| \text{calibration} \right|_B \quad (27)$$

The calibration error consists of two parts; calibration reproducibility for a fixed blackbody setting has been discussed above and was found empirically to be $\pm 5\%$. In absolute intensity measurements, however, absolute reliability of the standard can be the most serious problem. The blackbody used in these tests (Electro Optics Industries, Black Body Model WS154) permits us to provide absolute calibration of better than $\pm 5\%$. The total contribution from all errors caused by the calibration is therefore less than $\pm 10\%$. For signal measurements from lines exhibiting signal/noise of 30 we expect errors of approximately 3%. The total

(U) absolute intensity relative error is, therefore, conservatively estimated to be

$$\left| \frac{\Delta I}{I} \right| \leq 0.13$$

In contrast to the case for temperature measurements, the absolute intensity error is totally dominated by calibration procedures. Improvement in measurement accuracy must therefore come from an improvement in the infrared standards; this can be accomplished in a straightforward manner but involves considerably more complex experimental calibration procedures than have been used in these experiments.

(U) The total vibrational state number density is obtained from plots of Equation (3) by determining the straight line intersection with the ordinate hence the relative error is easily determined as

$$\left| \frac{\Delta \left\{ \int N_{v'}(y) dy \right\}}{\left\{ \int N_{v'}(y) dy \right\}} \right| = \left| \frac{\Delta I}{I} \right| + \left| \frac{\Delta T}{T} \right| \quad (28)$$

Adding up all the contributions one estimates for the total relative error

$$\frac{\Delta \left\{ \int N_{v'}(y) dy \right\}}{\left\{ \int N_{v'}(y) dy \right\}} \leq 0.20$$

b. Infrared Scanner Experiment

(U) A 10,000 sample/second infrared scanner has been built and applied to the measurement of 2.7μ , HF band intensity distributions from the laser cavity. The IR scanner output has been electronically processed and computer aided display techniques have been used to utilize these data for "flow field visualization" based upon infrared emission. Such displays have proven useful for localizing mixing and reaction zones in the cavity. Combining infrared scanner data with detailed, spectrally resolved chemiluminescent data, available from selected cavity positions, has proved useful for determining HF excited state number density variations throughout the laser cavity.

(U) In the preceding section a chemiluminescent diagnostic experiment has been described which aimed at measuring HF, line-by-line intensities from the laser cavity. Although this experiment is capable of providing highly reliable information on cavity excitation at the chosen locations, it is also relatively time consuming to perform. For a more cost-effective analysis of the entire cavity a technique is required which can rapidly determine the relative excitation levels throughout the cavity, relying upon the detailed information from the line-by-line scans for points of reference. The infrared scanner has been designed to fill this requirement.

(U) The infrared scanner design approach followed a fairly standard raster scan technique where the Z-direction scan, parallel to the laser optical axis, has been accomplished by a ten-sided rotating mirror drum, while slowly scanning the optical assembly in a direction parallel to the cavity flow (X-direction) and about an axis through the radiometer lens. Aperture size and optical design parameters were chosen to accomplish spatial resolution as high as 1.3 mm near the scanner optical axis. Absolute radiative intensity calibration and 3 decades of dynamic range made it possible to use this apparatus for quantitative HF band intensity measurements from a 12 x 12 inch section of the laser medium effusing from the nozzle array. Characteristics of the electronics used in signal conditioning and recording the data limited the IR scanner to an effective bandwidth of 6 kHz, although the detector itself is capable of providing much faster system response, up to 150 kHz bandwidth under optimum conditions.

(U) The output from the IR scanner was recorded on magnetic tape and the data subsequently processed by a computer using several programs which provide options of data output and display. The "perspective display" proved to be the most useful for "flow field visualization." This data presentation was generated by computer plotting successive sweeps in the flow direction with a slight offset in both the vertical and horizontal axes. This method provides displays of the flow field intensity distribution which are reminiscent of relief maps and lend themselves very well to visual recognition of the flow field structure. In a second display technique the computer generated a "contour map" of the flow field by connecting points of equal intensity. This latter display technique is most useful for quantitative evaluation of flow field intensities. In order to be valid, however, it requires very accurate synchronization of the data to a timing pulse generated by the scanner from the mirror rotation. Unfortunately, this requires a time resolution which is short compared to the system rise time of 100 μ sec, and this accuracy of timing proved to be beyond the capability of the present scanner and data processing system. It is being investigated whether the problem is entirely caused by the scanner itself, or whether the problem is also related to the computer processing. As a consequence of the timing problem experienced in the actual experiments, the flow field intensity contour maps did not prove successful although the computer program and the data processing routines were obviously adequate. We are confident that the problem has a straightforward solution once its source has been determined. The contour map approach, when perfected, will undoubtedly prove to be the most useful IR scanner data display technique in the future. For detailed analysis of individual IR data scans the latter can of course be obtained from the tape and plotted individually by the computer. This option has been widely used in the detailed analysis of the experimental data.

(U) Besides the computer aided data display techniques mentioned above, the IR scanner has been especially designed to permit real-time data presentation on an oscilloscope. Two real-time data display options are available: in the first display method the individual IR scans are displayed along the horizontal oscilloscope sweep with the intensity showing

(U) as vertical deflection. Each successive IR scan is, however, slightly offset in the vertical direction on the oscilloscope screen. The total event can be observed visually and recorded photographically providing pictures nearly identical to the "perspective displays" described above. A second real-time data display option can be obtained by modulating the oscilloscope beam brightness from the photodetector output signal while sweeping the horizontal and vertical oscilloscope traces to form a raster scan. This data display technique yields brightness modulated pictures when photographed and is essentially an IR vidicon display format of cavity flow field intensity distribution.

(1) Infrared Scanner Radiometer Description

(U) The infrared scanner apparatus was designed to provide rapid scan, high resolution infrared intensity mapping of the laser cavity flow field. Experiments to be discussed in this report deal exclusively with HF lasers, i. e., the wavelength band of interest covered the HF fundamental band near 2.7μ . This first experiment determined the specific choice of field lens material, and radiation detector shown in the scanner apparatus schematic of Figure 26. The present scanner, is however, designed to accommodate different detectors including photomultipliers for future use in other wavelength bands of interest to advanced HF/DF chemical laser diagnostic research. Figure 27 is a photograph of the apparatus.

(U) The scanner radiometer used a single arsenic trisulfide (As_2S_3) lens of slightly less than 1-inch diameter and 10-cm focal length. The lens images the center plane of the laser cavity (XZ plane) onto the plane A which contains the pinhole P. Two different pinhole sizes of 0.1 and 0.3 mm diameter can be placed in position by a remotely operated relay control. The distance separating the lens from the cavity XZ plane is 1 meter and the pinhole is located 0.1 meter away on the opposite side of the lens. The effective spatial resolution of the radiometer is determined by the pinhole, the field lens, and the depth of radiating gas viewed by the IR scanner optics. Near the exit plane of the slit nozzle array the depth of radiating gas along the viewing direction is approximately 25 mm.

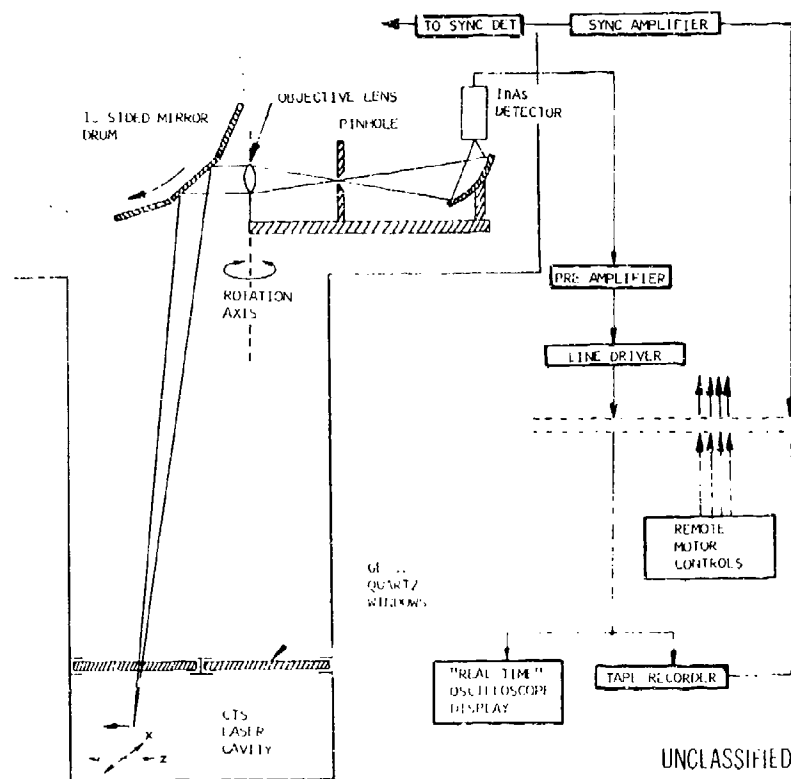


Figure 26. IR Scanner Experiment: Apparatus Schematic (U)

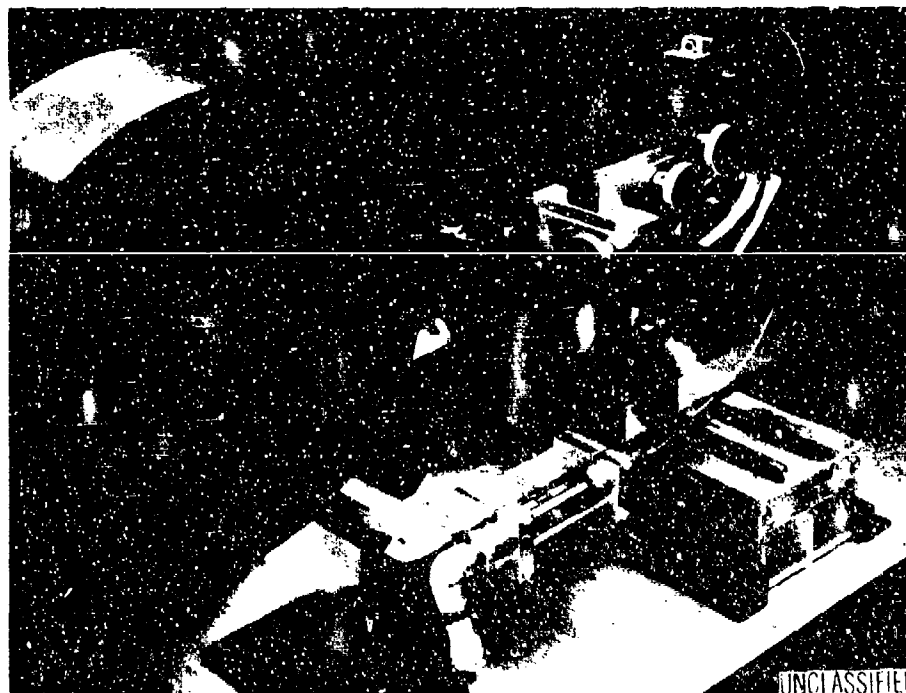


Figure 27. IR Scanner Apparatus - Photograph of Radiometer and Mirror Drum (U)

(U) Using the actual field lens diameter of 25 mm and distance of 1 meter, the beam divergence produces resolution degradation of

$$\Delta r = \frac{25 \cdot 12.5}{1000} \approx 0.3 \text{ mm}$$

on the principal optical axis. The most significant geometric factor limiting the spatial resolution at large displacement from the optical axis of the radiometer field of view results from the oblique optical path through the radiative plume. In order to define an "effective spatial resolution" we will implicitly assume that cavity volume emissivity depends only on coordinates X and Z and is independent of coordinate, Y; of course, this assumption can hold only in an approximate sense near the nozzle exit plane and at positions removed from the edges of the plume. The effective spatial resolution is, therefore, defined here by the cross-sectional dimension of a cylinder oriented along the Y direction containing all volume elements contributing to the radiometer signal at its instantaneous field of view. Let the instantaneous radiometer optical axis intercept the XY plane at a point $\{X_0; Z_0\}$, then the cross-sectional dimensions for the resolution cylinder (Figure 28) are respectively,

$$\Delta X = 25 \tan \frac{X_0}{1000} \text{ mm and } \Delta Z = 25 \tan \frac{Z_0}{1000} \text{ mm}$$

where all dimensions are in millimeters.

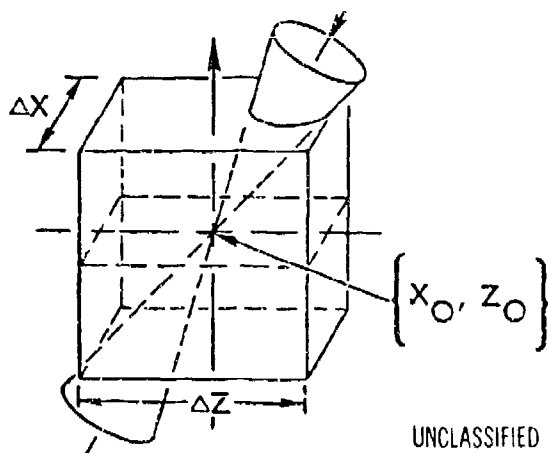


Figure 28. IR Scanner: Spatial Resolution Geometry. (U)

(U) From the design parameters one readily computes that the effective resolution in the Z direction is better than 1.8 mm within a strip $|Z_o| \leq 20$ mm; an identical relation holds for the resolution in the X direction. At the extreme edge of the radiation flow field, X_o or Z_o are each approximately 10 cm and the effective spatial resolution will be nearly 4 mm. These IR scanner parameters and choice of optical components indicated about represent an optimum tradeoff between scanner effective spatial resolution, instrument size, scan speed and sensitivity.

(U) Aside from the geometric design considerations affecting spatial resolution, the most critical design criterion is derived from the required instrument sensitivity and scan speed. Signal voltage is related to the incident intensity (watt/cm² sterad) of a given HF vibration-rotation line by the relation

$$V_\lambda = \frac{A_L \cdot A_P}{d^2} R_\lambda \cdot T_\lambda \cdot I_\lambda = S_\lambda \cdot I_\lambda \text{ (volts)} \quad (29)$$

The total HF vibration-rotation band generates, therefore, a signal voltage

$$V_s = \sum V_\lambda = \frac{A_L \cdot A_P}{d^2} \cdot \sum R_\lambda T_\lambda I_\lambda = \sum S_\lambda I_\lambda \text{ (volts)}$$

The latter equation can formally be written

$$V_s = S_{\lambda_o} \cdot \left(\frac{\bar{S}}{S_{\lambda_o}} \right) \cdot \sum I_\lambda \text{ (volts)} \quad (30)$$

where \bar{S} is the average sensitivity with respect to the HF band. The ratio \bar{S}/S_{λ_o} is therefore defined by

$$\left(\frac{\bar{S}}{S_{\lambda_o}} \right) = \frac{1}{S_{\lambda_o}} \frac{\sum S_\lambda I_\lambda}{\sum I_\lambda} \quad (31)$$

In the above equations all sums are extended over the lines of the HF vibration-rotation band and S_{λ_o} is the sensitivity at the particular wavelength λ_o chosen for IR scanner absolute sensitivity calibration. The value

(U) for relative sensitivity \bar{S}/S_{λ_0} can be evaluated for different laser cavity conditions using line-by-line data from the chemiluminescent experiment. This is possible because both experiments use identical detectors and the instrument transmission factors, T_{λ} , are virtually constant over the HF band in both instruments, although not necessarily of the same value. The chosen wavelength for IR scanner calibration was 2.4μ . Numerical evaluation of ratios $(\bar{S}/S_{2.4\mu})$ using chemiluminescent experiment data yielded the value

$$\left(\frac{\bar{S}}{S_{2.4\mu}}\right) = 1.20 \quad (32)$$

virtually independent of experiment condition, which is consistent with the near responsivity of the InAs detector over the wavelength range of interest. This establishes a simple relationship between IR scanner signal voltage and integrated HF band intensity. Combining Equations (30) and (32) yields the following quantitative expression for this relationship

$$V_s = 1.2 \cdot S_{2.4\mu} \cdot \Sigma I_{\lambda} \text{ (volts)}$$

Absolute calibration of the scanner has been accomplished with a black-body of 1730°K placed directly in the IR scanner object XZ plane. A narrow wavelength band around 2.4μ was isolated using an interference filter of 0.056 μ optical bandwidth and 55 percent peak transmission. Absolute calibration yielded

$$S_{2.4\mu} = 0.102 \frac{\text{volt}}{\text{watt/cm}^2 \text{ sterad}}$$

The IR scanner sensitivity for HF band intensity, as established by calibration, is therefore:

$$V_s = 0.122 \cdot (\Sigma I_{\lambda}) \text{ volts} \quad (33)$$

(U) According to Equation (29), the sensitivity S_λ relates to IR scanner design parameters and detector characteristics as

$$S_\lambda = \frac{A_P \cdot A_L}{d^2} \cdot (R_\lambda \cdot T_\lambda)$$

From the chosen radiometer design parameters one computes for

$$\frac{A_P \cdot A_L}{d^2} = \frac{6.25 \cdot 0.75 \cdot 10^{-4}}{10^2} = 4.9 \times 10^{-6} \text{ cm}^2 \text{ sterad}$$

Total optical transmission of the scanner is approximately 0.6 and from the system calibration at $\lambda = 2.4\mu$ we obtain a detector responsivity of 3.2×10^4 volts/watt. The IR scanner noise rms voltage was measured as

$$v_{n, \text{rms}} = 3.75 \mu\text{volt}$$

Using measured IR scanner sensitivity (Equation (33)) and the noise value, one determines that the scanner NEI (noise equivalent intensity) is

$$\text{NEI} = \frac{3.75 \times 10^{-6}}{0.122} = 3.1 \times 10^{-5} \frac{\text{watt}}{\text{cm}^2 \text{ sterad}}$$

Actual measured HF band intensities range from 1 to 30 milliwatt/cm² sterad; i. e., measured signal/noise ranges from 25 up to approximately 1000. Linearity of the output has been established to within better than ± 5 percent over the entire measurements range. Measured impulse rise time of the detection system has been determined as 100 μsec , yielding approximate electronic noise bandwidth of 5 kHz. In future experiments it may prove desirable to increase the system electronic bandwidth with consequent increase in the instrument NEI given above. At larger bandwidths the NEI is expected to increase in proportion to the square root of the bandwidth, provided the detector responsivity remains constant over the entire extended frequency band.

(2) Infrared Scanner Data Interpretation

(U) The IR scanner apparatus as used in these experiments was designed to measure total HF fundamental band intensities ($2I_\lambda$) as has

(U) been discussed in the preceding section. Total band intensity can be computed from fundamental relations as

$$\Sigma I_{\lambda} = \frac{16\pi^3}{3} c \sum_{v'j'} (\bar{\nu})^4 \left| \langle v'j' | M(r) | v''j'' \rangle \right|^2 \cdot \frac{|m|}{2j'+1} \int N_{v'j'}(y) dy$$

For HF transitions within a given $v' \rightarrow v''$ band

$$(\bar{\nu})^4 \left| \langle v'j' | M(r) | v''j'' \rangle \right|^2 \approx \text{constant}$$

as has been noted above. The summation over all lines in a given band is therefore particularly easy to accomplish and the resulting expression is

$$\Sigma I_{\lambda} = \frac{16\pi^3}{3} c \cdot 10^{-7} \Sigma \bar{\nu}^4 \left| \langle v' | M(r) | v'' \rangle \right|^2 \int N_{v'}(y) dy \text{ watt/cm}^2 \text{ sterad} \quad (34)$$

It is noteworthy that the total HF band intensity measured by the IR scanner is practically independent of the specific distribution of rotational sublevels within a given vibration state; i. e., the total band intensity does not depend on the flow field temperature but depends only on the total vibrational state population. It is for this reason that the IR scanner data provide such a powerful tool for flow field vibrational state excitation measurements. Combining Equations (33) and (34), the IR scanner voltage can be written as follows:

$$V_S(X, Z) = 0.122 \frac{16\pi^3}{3} c \cdot 10^{-7} \frac{\sum_{v'} (\bar{\nu})^4 \left| \langle v' | M(r) | v'' \rangle \right|^2 \int N_{v'}(y) dy}{\int N_{v'}(y) dy} \cdot \int N_{v'}(y) dy$$

This equation can be formally rewritten as

$$\int N_{v'}(y) dy = \frac{V_S(X, Z)}{\alpha_{v'}(X, Z)} \quad (35)$$

(U) where the functions $\alpha_{v_1}(X, Z)$ are determined empirically by combining data from the line-by-line chemiluminescent experiment with the scanner signal reading. In general the functions α_{v_1} depend both on coordinates X and Z and, of course, on the experimental conditions; however, because of the design of the laser nozzle bank, one expects α_{v_1} to be nearly independent of coordinate Z . At the positions where line-by-line chemiluminescent spectroscopic analysis has been performed, values for $\{\int N_{v_1}(y)dy\}_i$ are known and IR scanner signal readings are $V(X_i)$. Numerical values for $\alpha_{v_1}(X_i)$ can therefore be found at points X_i from the relation

$$\alpha_{v_1}(X_i) = \frac{V(X_i)}{\{\int N_{v_1}(y)dy\}_i} \quad (36)$$

For each experimental condition values of $\alpha_{v_1}(X_i)$ have been plotted and used for graphical interpolation to find $\alpha_{v_1}(X)$ at intermediate positions. In order to determine the proper $V(X_i)$ one has to average the high resolution IR scanner data over a spatial range consistent with the spectrometer slit image. In practice one observes only three excited vibrational HF states of significant population and the key formula for IR scanner data evaluation is therefore, Equation (35), with the three $\alpha_{v_1}(X)$ curves evaluated using Equation (36). We assume that the α functions do not depend on coordinate Z .

(U) Samples of IR scanner data, plots for the functions $\alpha_{v_1}(x)$, and finalized data displays will be shown and discussed in the experimental results section. In Figures 29 and 30 we show samples of two different real time data displays possible with the IR scanner. The figure captions give further details. In addition to the real time data displays superior performance can be obtained with computerized data reduction techniques as described in Sections 4.d(2) and 4.d(3).

c. Gain/Absorption Experiment

(U) The chemiluminescent experiment, involving line-by-line analysis, and the IR scanner experiment primarily yield information on excited HF states. The chemiluminescent experiment permits the computation of

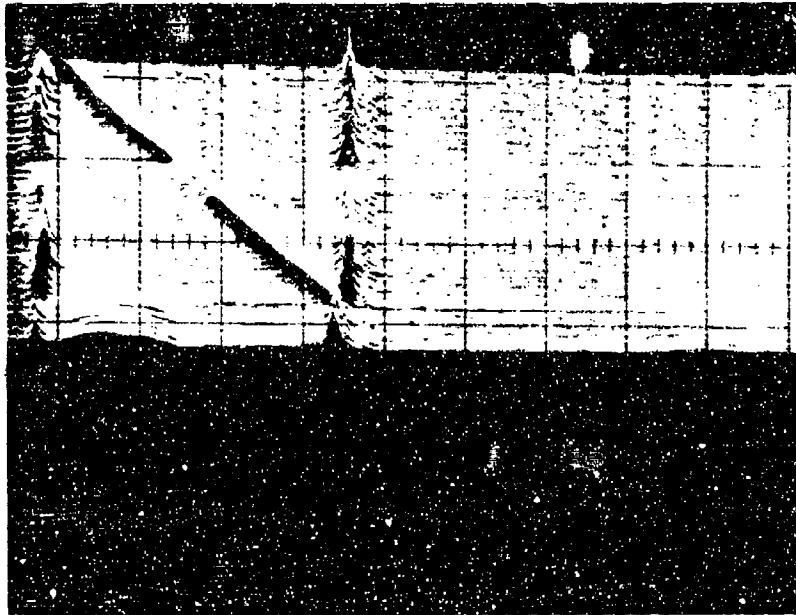


Figure 29. IR Scanner Real Time Oscilloscope Display: Amplitude
Modulation (U) UNCLASSIFIED

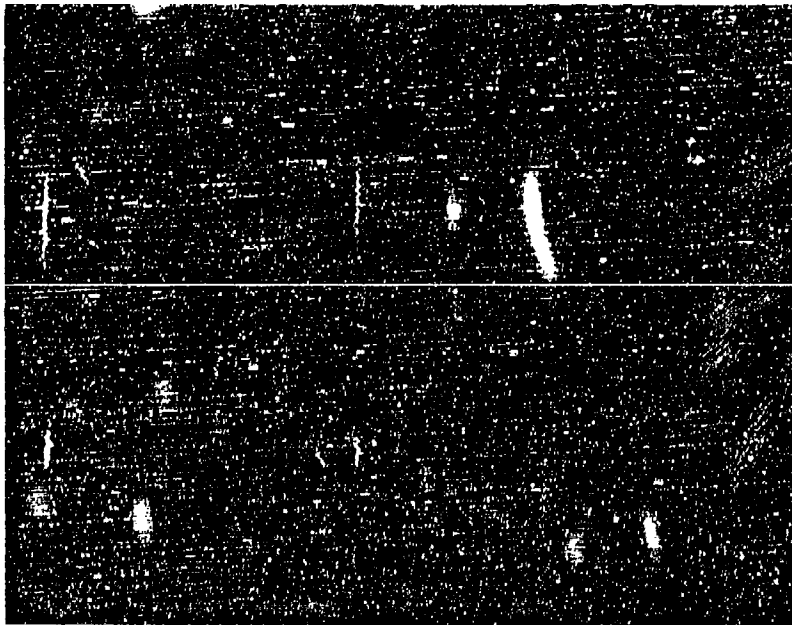


Figure 30. IR Scanner Real Time Oscilloscope Display: Intensity
Modulation (U) UNCLASSIFIED

(U) gain/absorption for $3 \rightarrow 2$ and $2 \rightarrow 1$ transitions. In order to gain a complete description of chemical laser cavity characteristics measurements of HF ground state population are needed. In a limited sense, information on ground state HF can be derived from line-by-line chemiluminescence data in all cases where some self-absorption of the $1 \rightarrow 0$ vibration-rotation lines is observed as has been fully discussed in Section 4. a. For many important diagnostic cases, however, cavity HF partial pressures are so low that absorption/gain effects are too small for self-absorption to occur and other techniques are required. Even in those cases where chemiluminescent data allow one to determine HF ground state number densities, important additional information can be obtained from a direct HF ground state measurement involving IR absorption. This latter point is illustrated in Figure 31 which shows a schematic of the line-of-sight geometry in the chemiluminescent and the absorption experiment.

(U) It is evident from Figure 31 that the chemiluminescent emission data can be affected by self-absorption in the "hot" plume and by absorption of "cold" HF contained in the gas interposed between the upper window and the plume. The probing radiation of the gain experiment traverses the hot plume and both of the cold regions above and below the plume.

(U) The experimental technique used in this program for absorption/gain studies is HF resonance absorption in the IR, where the HF probing intensities have been obtained from a burner especially designed to emit Doppler broadened lines of width that can be determined experimentally. The advantage of resonance absorption over other possible techniques is the fact that the interpretation of data requires no assumptions which cannot be verified experimentally. Therefore, the measurement results are expected to be very reliable.

(1) Gain/Absorption experiment Apparatus

(U) For the gain/absorption experiment we have built and applied an apparatus which permits measurement of the amplification or attenuation of a small probing signal at the exact wavelength of selected vibration-rotation lines of the HF($1 \rightarrow 0$) band. In order to obtain the exact match of

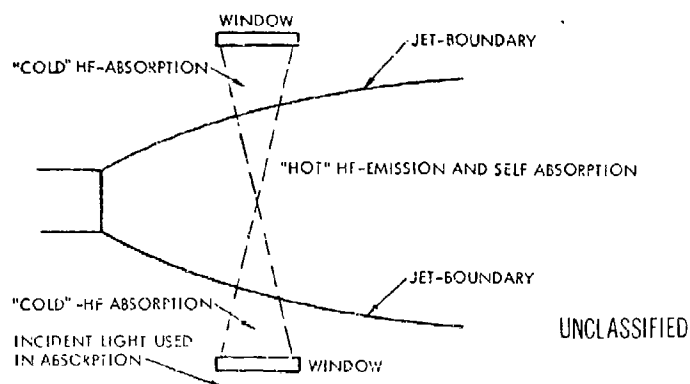


Figure 31. Line-of-Sight Geometry in Chemiluminescence and Gain/Absorption Experiment (U)

(U) probing light wavelength with HF vibration-rotation lines the source of the probing radiation is derived from the emission of an H_2-F_2 flame. After isolating a selected spectral line, the total probing line attenuation and gain have been measured and interpreted in terms of ground state population. A schematic of the apparatus is shown in Figure 32.

(U) The spectral line source for the HF resonance absorption was a low pressure H_2-F_2 burner. Typical operating conditions for this burner are flow rates of 2.5×10^{-4} mole/sec H_2 , 3.5×10^{-4} mole/sec F_2 and total pressures in the range 2 to 5 torr. The exit window is protected from etching by a small flow of argon. Cryogenic (LN_2) pumping of HF and excess F_2 are used to reduce the HF partial pressure in the optical path inside the burner and to prevent any internal self-absorption of HF probing lines. In preliminary tests of the burner it has been verified by chemiluminescence measurements that this HF spectral line source is well described by assuming an optically thin radiating gas source, with Doppler line profiles corresponding to an effective Boltzman temperature of the order $1000^\circ K$. As will be shown below, it is a necessary condition of the experiment to be able to define the source line shape in order to interpret the measured intensity attenuation data and derive the ground state HF concentrations in the laser cavity.

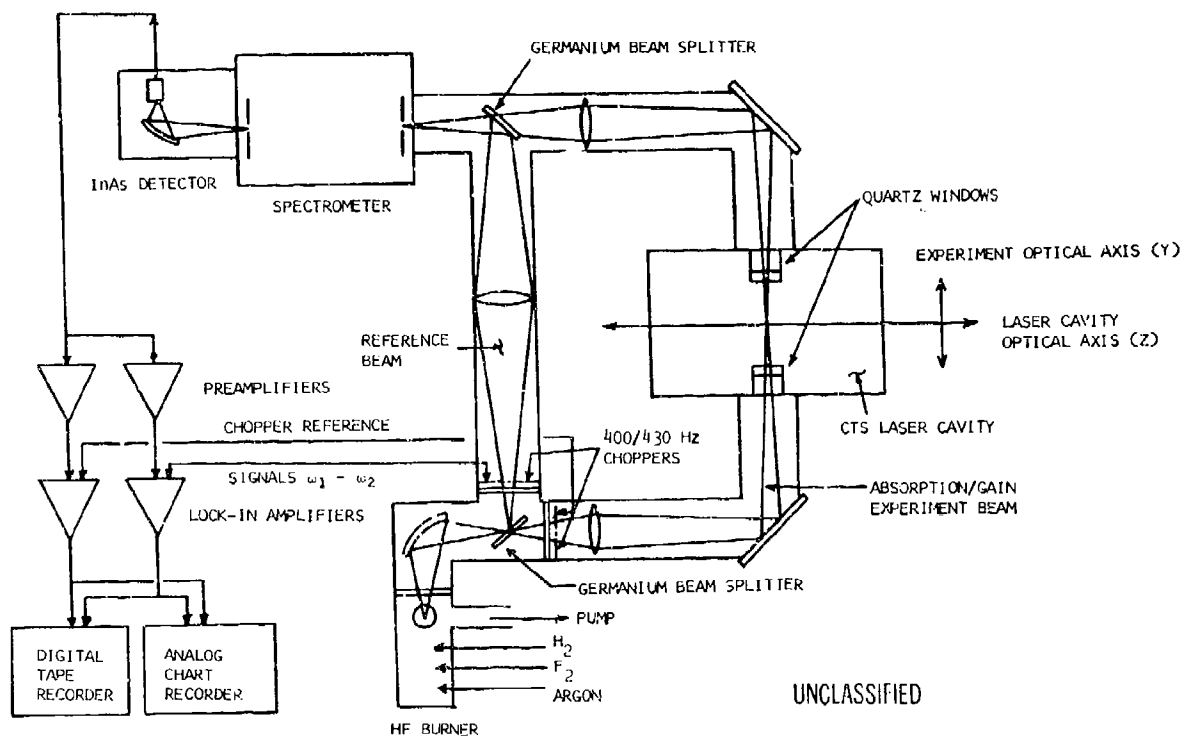


Figure 32. Resonance Absorption/Gain Experiment: Apparatus Schematic (U)

(U) A germanium beam splitter divides the total source output into reference and probing beams of approximately equal intensity which are modulated by chopper discs at different frequencies ω_1, ω_2 , respectively. The reference beam bypasses the laser cavity and is refocused at the entrance slit of the spectrometer; the probing beam is focused at the cavity centerline and again at the spectrometer entrance slit. Both reference and probing beams are merged at the second germanium beam splitter in front of the spectrometer. Each beam is partially plane polarized (~30 percent); however, the second beam splitter is arranged with a plane of incidence parallel to the first to avoid severe attenuation by crossed polarizers. The combined beams, after wavelength selection at the spectrometer, are detected by a single cooled indium arsenide

(U) detector. The reference and probing beam signals are then separated by two PAR 124 lock-in amplifiers in parallel circuits, one tuned to each of the chopper frequencies ω_1, ω_2 . The cavity chemiluminescent emission dc signal is rejected by the lock-in amplifiers except for contributions to the total noise of the measuring system.

(U) The entire optical system outside of the laser cavity is continuously purged with dry nitrogen to reduce absorption losses caused by atmospheric CO_2 and water vapor. In general, such losses can be reduced to less than 10 percent in the region near 2.7μ and are readily accounted for by a system calibration. At the laser cavity itself quartz (GE 125) windows were extended into the cavity from both top and bottom to reduce the volume of nonreactive flow gases which are included in the measurement region.

(2) Gain/Absorption Experiment Data Interpretation

(U) Consider experiment geometry as shown schematically in Figure 33.

(U) Let I_λ^s be the total rms probing line intensity chopped at frequency ω_1 originating from the burner of effective source temperature T_s . The Doppler width and line shape factor of the probing line are thus defined by $(\Delta\bar{\nu}_D)^s$ and Γ^s defined in accordance with Equations (7) and (8). The source line radiance distribution as a function of $(\bar{\nu} - \bar{\nu}_0)$ is then defined by

$$I_\lambda^s(\bar{\nu} - \bar{\nu}_0) = I_\lambda^s \cdot \Gamma(\bar{\nu} - \bar{\nu}_0) \frac{\text{watt}}{\text{cm}^2 \cdot \text{sterad} \cdot [\text{cm}^{-1}]} \quad (37)$$

The absorbing laser cavity medium is described at each point by an effective coefficient of absorption accounting both for absorption and stimulated emission effects. This function is

$$k'(\bar{\nu}, y) d\bar{\nu} = k'_0(y) \cdot e^{-\frac{\bar{\nu} - \bar{\nu}_0}{\Delta\bar{\nu}_D}} d\bar{\nu} \frac{[\text{cm}^{-1}]}{\text{cm}} \quad (38)$$

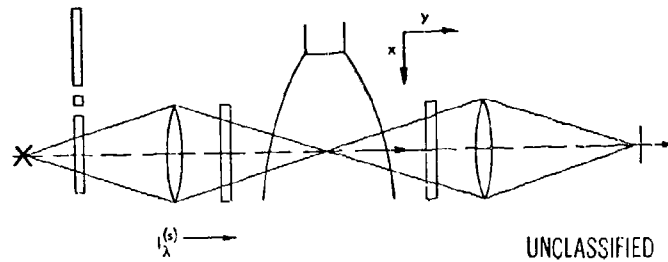


Figure 33. Absorption/Gain Experiment Geometry (U)

(U) where $k'_0(y)$ is the effective absorption coefficient at the line center wave number, $\bar{\nu}_0$. An expression for the latter has been given earlier by Equation (15). The objective of the absorption/gain experiment is to determine parameters $k_0 \cdot \ell$ and to derive population differences between upper and lower state in accordance with Equation (18).

(U) Neglecting scattering, the differential probing beam attenuation is

$$d \{ I_{\lambda}^s (\bar{\nu} - \bar{\nu}_0) d\bar{\nu} \} = -k'(\bar{\nu}, y) \{ I_{\lambda}^s (\bar{\nu} - \bar{\nu}_0) d\bar{\nu} \} dy \quad (39)$$

(U) The effective spectrometer slit width is $\sim 4 \text{ cm}^{-1}$ at 300 microns and with a 300 line/mm grating, as compared with the Doppler spectral line widths of the order 0.01 cm^{-1} . Hence, the total measured line intensities are given by integration of the spectral line intensities over the Doppler line width:

$$\int \{ I_{\lambda}^s (\bar{\nu} - \bar{\nu}_0, y) d\bar{\nu} \} = \int d\bar{\nu} I_{\lambda}^s (\bar{\nu} - \bar{\nu}_0) \cdot (-\int k'(\bar{\nu}, y) dy)$$

where $I_{\lambda}^s (\bar{\nu} - \bar{\nu}_0, y) d\bar{\nu}$ and $I_{\lambda}^s (\bar{\nu} - \bar{\nu}_0) d\bar{\nu}$ stand for probing beam intensity at coordinate y and the input intensity, respectively, and the subscript λ denotes a single spectral line at that wavelength. The resulting expression for the probing beam attenuation/gain can be conveniently expressed in a power series as

$$\frac{I_{\lambda}^s(y)}{I_{\lambda}^s} = \sum_{n=0}^{\infty} (-1)^n \frac{(\overline{k'_0 y})^n}{n!} \cdot \sqrt{\frac{\beta}{n+\beta}} \quad (40)$$

(U) where

$$\beta = \frac{T_L}{T_S}. \quad (41)$$

(U) Equation (40) has been solved numerically for values of $(\overline{k_o y})$ from 0 to 10 with values of the parameter β from 0 to 1 which include the ranges of interest for these cavity absorption gain measurements. A graphic representation of the functional relationship has been given in Figure 34. Hence, given the observed value of attenuation and knowledge of the cavity and source temperatures, a value for the equivalent center line absorption coefficient integrated over the line-of-sight can be deduced. Centerline integrated effective absorption coefficients in turn can be used to determine population differences between upper and lower state population using Equation (15). Lower state population can be determined from these differences when the upper state population is known from other data. The chemiluminescent experiment described in Section 4. a is of course the source of upper state population data. Great care has therefore been exercised to obtain pairs of chemiluminescent and absorption/gain experiments using optical geometry and laser operating conditions as identical as possible. Generally, this experimental objective has been fully achieved.

(U) It is worth noting that the maximum sensitivity of the attenuation measurement is obtained with

$$\beta = \frac{T_L}{T_S} \rightarrow \infty$$

equivalent to a source line width which is negligible compared with that of the cavity medium. Under these conditions, the absorption coefficient is effectively constant and equal to the centerline value k_o ; by inspection Equation (40) reduces to

$$\frac{I_{\lambda}^s(y)}{I_{\lambda}^s} \rightarrow (-1)^n \frac{(\overline{k_o y})^n}{n!} = e^{-\overline{k_o y}} \quad (42)$$

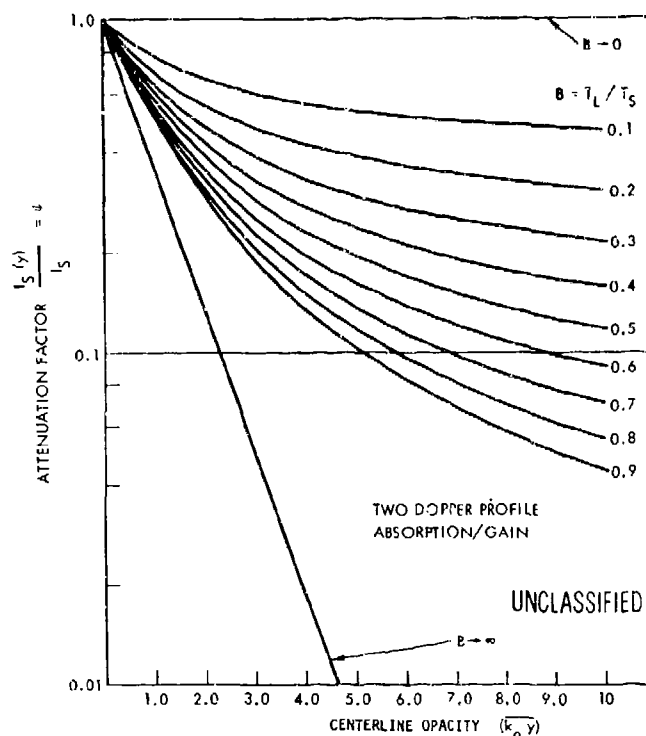


Figure 34. Doppler Profile Resonance Line absorption: Line Attenuation versus Line Center Opacity (U)

(U) Conversely, in the limit of very hot source temperatures relative to cavity temperatures probing beam attenuation becomes vanishingly small. From these limits it appears that source temperatures should be less than cavity temperatures for optimum sensitivity. However, this would result in available probing light intensity becoming too small and therefore a probing source temperature, a little hotter than cavity temperatures (1000°K vs. 450°K), is a near optimum compromise between measurements signal/noise and sensitivity.

d. Automated Data Reduction Techniques

(U) One of the most severe problems in the execution of the measurements program was the handling of the large data output from the experiments. This problem had been anticipated and several automated data reduction routines were initiated early in the program. One computer aided data reduction program has been prepared and used for line-by-line

(U) conversion of measured chemiluminescent emission spectra into data on excited vibration-rotation state population. Whereas in the chemiluminescent experiment automated data reduction was a matter of convenience and cost effectiveness, in the case of the IR scanner computer aided data reduction and display is a necessary step. For the IR scanner two different programs have been prepared serving different data display objectives. The "perspective plot" program is primarily for effective visual display of the flow field IR emission structure and distribution. A second routine which provides "intensity contour maps" is potentially of greater value for quantitative analysis, in spite of the fact that the latter program is still suffering from difficulties at this time. The chemiluminescent spectrum reduction program is discussed in Appendix II.

5. EXPERIMENT PARAMETERS SUMMARY

(U) Following the general laser cavity diagnostic objectives discussed in Section 2 several test series have been conducted. In a first test series laser cavity pressures were varied through cavity purging by factors of approximately 2, 4, and 6 over a nominal case, keeping plenum chamber pressure and flow rates constant. The purpose of this test series was to investigate the reason for laser output power degradation at the higher cavity pressures. A second test also aimed at the pressure effect; but cavity pressure was raised by increasing the flow through the nozzle bank. The effect of substituting a large mole fraction of the excess cavity hydrogen flow by helium has been investigated in the third test series, keeping all other operating parameters at the nominal conditions. This test was to demonstrate the effect of reducing the collisions of excited HF with H_2 molecules. The purpose of the fourth test series was to increase plenum chamber temperature beyond the nominal case. Higher plenum chamber temperatures affect the cavity flow field velocity, and the level of fluorine dissociation.

(U) Table 1 gives a summary of the four principal test series parameters. Each test consisted of a number of individual runs for the purpose of performing the planned diagnostic experiments involving chemiluminescent spectroscopic analysis, HF resonance absorption/gain measurements and infrared intensity mapping. The chemiluminescent and absorption tests

Table 1. Test Operating Parameters Summary for Tests Series I - IV (U)

| Test | Combustor/Plenum Input | | | | Cavity Injection | | Total Mass Flow | Plenum Cav. Press. | | | Plenum Heat Loss | noz. Heat Loss | Total Heat Loss | Purpose of Test |
|------|--------------------------|--------------------------|--------------------------|--------------------------|-----------------------|--------------------------|--------------------------|--------------------|---------------|-----------|-------------------------------|-------------------------------|-----------------------------|--|
| | $[F_2]_{in}$ mole/sec | $[O_2]_{in}$ mole/sec | $[H_2]_{in}$ mole/sec | $[H_e]_{in}$ mole/sec | \dot{m}_p gr/sec | $[H_2]_{in}$ mole/sec | $[H_e]_{in}$ mole/sec | P_o psia | P_x torr | P_o/P_x | $\Delta\dot{Q}_p$ kcal/sec | $\Delta\dot{Q}_n$ kcal/sec | $\Delta\dot{Q}$ kcal/sec | |
| Ia | .233 | .138 | .792 | 12.56 | | .792 | -- | 12.2 | 1.29 | 489 | 3.07 | 4.55 | 7.62 | Nominal operating condition. |
| Ib | | | | | | | | 2.73 | 231 | | | | | Increase cavity pressure by a factor of 2. |
| Ic | | | | | | | | 5.45 | 116 | | | | | Increase cavity pressure by a factor of 4. |
| Id | | | | | | | | 8.2 | 77.1 | | | | | Increase cavity pressure by a factor of 6. |
| II | .346 | .211 | 1.188 | 18.75 | | 1.201 | -- | 19.2 | 1.93 | 516 | 4.30 | 5.79 | 10.09 | Increase all flow rates by factor of 1.5 thereby increasing cavity pressure by a factor of 1.5. This maintains plenum to cavity press. ratio at nominal condition (approximately 500). |
| III | .233 | .139 | .793 | 12.58 | | .402 | .402 | 12.3 | 1.44 | 441 | 3.15 | 4.55 | 7.70 | Substitute 1/2 of cavity hydrogen molar flow by helium. |
| IV | .230 | .162 | .859 | 12.82 | | .600 | -- | 13.6 | 1.34 | 527 | 3.59 | 5.59 | 9.18 | Increase plenum chamber temperature from nominal 1900°K to nominal 2300°K by increasing combustor U_2 flow rate. |
| | | | | | | | | | | | | | UNCLASSIFIED | |

(U) were performed at up to four different window locations for any fixed operating condition. Hydrogen fluoride resonance absorption experiments were conducted in the HF, 0-1 band utilizing the P_3 and P_5 lines. The P_3 transition is a line which generally exhibited absorption, whereas the P_5 yielded gain in most experiments. Infrared scanner intensity displays of the cavity flow field were produced with high and low optical resolution. The low resolution mode provides higher signal/noise ratios at the expense of detail. In order to be able to compare the different diagnostic results for nominal identical test conditions it was, of course, most important to reproduce test operating parameters from run to run. This latter task was accomplished quite successfully, and only minor variations occurred. The extensive Table 2 is a test-by-test record of individual run operating parameters, listing also the TRW test log number and the specific diagnostic test which was performed on that run. From this table average test operating parameters have been determined and maximum deviations of operating parameters from achieved averages are recognized to be insignificant.

a. Plenum Gas Characteristics

(U) From the measured combustor/plenum chamber input flow rates, plenum pressure, P_0 , and measured heat losses, it is possible to define the important plenum chamber gas parameters. In order to perform the necessary calculations, we require molecular and chemical thermodynamic properties of all injected gases and reaction products. In Table 3 a summary of the most important thermodynamic properties, as well as molecular atomic constants as used in this report have been listed. In our formal data reduction procedures we employ standard thermodynamic digital computer codes. It is frequently necessary, however, to make rapid, yet reasonably accurate, calculations without resort to the digital codes. Our procedures for these rapid calculations are given below.

(1) Plenum Gas Composition

(U) Plenum gas composition can be readily determined from the known input flow rates of Table 1 assuming complete combustion of all injected D_2 with F_2 . The excess fluorine (F_2) will partially or totally dissociate, depending upon the plenum chamber gas temperature. With

Table 2. Detailed Test Operating Parameters* (U)

| Test | Test No. | Comustor/Plenum Input | | | | Cavity Injection | | P_o P_x P_o/P_x | | | $\Delta\dot{Q}_p$ | $\Delta\dot{Q}_n$ | $\Delta\dot{Q}$ | N_2 -purge | |
|--------------|-----------------------------------|-----------------------|--------------|--------------|-------------|------------------|--------------|-----------------------|------|-------|-------------------|-------------------|-----------------|--------------|----------|
| | | $[F_2]_{in}$ | $[O_2]_{in}$ | $[H_2]_{in}$ | \dot{m}_p | $[H_2]_{in}$ | $[H_2]_{in}$ | \dot{m}_c | psia | torr | | Kcal/sec | Kcal/sec | Kcal/sec | mole/sec |
| 1a | CH-1 | .2324 | .1410 | .8040 | 12.61 | -- | .8010 | 14.214 | 12.6 | 1.344 | 485 | 3.40 | 4.59 | 7.99 | -- |
| | CH-2 | .23 | .1385 | .7810 | .51 | -- | .7340 | 14.094 | 12.4 | 1.448 | 443 | 3.40 | .54 | .94 | -- |
| | CH-3 | .41 | .90 | .7995 | .55 | -- | .8015 | .254 | 12.5 | 1.293 | 500 | 3.28 | .44 | .71 | -- |
| | CH-4 | .41 | .95 | .7950 | .63 | -- | .8070 | .246 | 12.5 | 1.241 | 521 | 2.77 | .33 | .11 | -- |
| | IR-C | .08 | .85 | .7883 | .48 | -- | .7510 | 14.061 | 12.2 | 1.447 | 436 | 3.38 | -- | -- | -- |
| | IR-F | .00 | .1368 | .7795 | .41 | -- | .7885 | 13.782 | 12.0 | 1.447 | 427 | 3.15 | -- | -- | -- |
| | A-1-P ₃ P ₅ | .37 | .1403 | .8025 | .65 | -- | .7900 | 14.150 | 12.5 | 1.444 | 401 | 3.00 | 4.54 | 7.54 | -- |
| | A-2-P ₅ | .67 | .23 | .8078 | .80 | -- | .8165 | .434 | 12.5 | 1.056 | 595 | 2.75 | .56 | 7.31 | -- |
| | A-2-P ₃ | .61 | .28 | .8088 | .78 | -- | .8170 | .415 | 12.5 | 1.086 | 595 | 2.41 | .44 | 6.85 | -- |
| | A-2-P ₇ | .48 | .15 | .8090 | .72 | -- | .8035 | .331 | 12.0 | .293 | 480 | 2.55 | .46 | 7.01 | -- |
| 1b | A-3-P ₃ P ₅ | .46 | .00 | .8080 | .71 | -- | .8050 | 14.317 | 12.2 | .189 | 530 | 2.90 | .56 | 7.46 | -- |
| | AVERAGE 1a | .2336 | .1400 | .7987 | 12.63 | -- | .7983 | 14.23 | 12.4 | 1.293 | 494 | 3.00 | 4.50 | 7.50 | -- |
| | CH-1 | .2321 | .1398 | .8035 | 12.59 | -- | .8010 | 14.193 | 12.5 | 2.689 | 240 | 3.53 | 4.59 | 8.12 | .1429 |
| | CH-2 | .23 | .85 | .7780 | 12.50 | -- | .7985 | 14.092 | 12.3 | 2.792 | 228 | 3.48 | 4.54 | 8.02 | .1429 |
| | CH-3 | .42 | .85 | .7953 | 12.63 | -- | .8030 | 14.24 | 12.5 | 2.689 | 240 | 3.38 | 4.49 | 7.86 | .1429 |
| | CH-4 | .30 | .90 | .7890 | 12.57 | -- | .8090 | 14.183 | 12.4 | 2.741 | 240 | 3.35 | 4.59 | 7.94 | .1429 |
| | IR-C | -- | -- | -- | -- | -- | -- | -- | -- | -- | -- | -- | -- | -- | -- |
| | IR-F | .13 | .1370 | .7770 | 12.45 | -- | .7200 | 13.886 | 12.1 | 2.947 | 212 | -- | -- | -- | -- |
| | A-1-P ₃ P ₅ | .2343 | .1410 | .7950 | 12.65 | -- | .8050 | 14.259 | 12.5 | 2.586 | 250 | 3.27 | 4.66 | 7.93 | -- |
| | A-2-P ₃ P ₅ | .48 | .1423 | .8043 | 12.71 | -- | .8005 | 14.311 | 12.4 | 2.792 | 230 | 3.02 | 4.56 | 7.68 | -- |
| AVERAGE 1b | A-3-P ₃ P ₅ | .71 | .1415 | .8050 | 12.80 | -- | .8045 | 14.405 | 12.3 | 2.637 | 241 | 2.90 | 4.56 | 7.46 | -- |
| | AVERAGE 1b | .2336 | .1397 | .7934 | 12.61 | -- | .7927 | 14.20 | 12.4 | 2.734 | 234 | 3.28 | 4.58 | 7.86 | -- |
| UNCLASSIFIED | | | | | | | | | | | | | | | |

*Nomenclature: CH-1: chemiluminescent experiment at window 1; CH-2,3,4 the same but at window 2,3 and 4, respectively.

IR-f: infrared scanner experiment using fine (high) resolution scanner mode.

IR-c: infrared scanner experiment using coarse (low) resolution scanner mode.

A-1-P₃P₅: absorption gain experiment at window 1 using P₃ and P₅, 1-0 line.

Table 2. Detailed Test Operating Parameters* (U) (Continued)

| Test | Test no. | Combustor/plenum Input | | | Cavity Injection | | P_o P_x P_o/P_x | | $\Delta\dot{h}_p$ | $\Delta\dot{h}_n$ | $\Delta\dot{h}$ | n_2 -purge |
|--------------|-----------------------------------|------------------------|--------------------|--------------------|--------------------|-------------|-----------------------|-------|-------------------|-------------------|-----------------|--------------|
| | | $[\dot{F}_2]_{in}$ | $[\dot{v}_2]_{in}$ | $[\dot{H}_e]_{in}$ | $[\dot{H}_e]_{in}$ | \dot{m}_c | psia | torr | Kcal/sec | Kcal/sec | Kcal/sec | mole/sec |
| Ic | CH-1 | .2293 | .1348 | .7775 | .788 | 13.939 | 11.9 | 5.688 | 108 | 3.35 | -- | -- |
| | CH-2 | .2292 | .1348 | .7803 | .705 | 13.780 | 11.9 | 5.636 | 109 | 3.40 | -- | -- |
| | CH-3 | .2284 | .1345 | .7795 | .781 | 13.876 | 11.9 | 5.740 | 107 | 3.28 | -- | -- |
| | IR-C | .2287 | .1353 | .7838 | .802 | 13.971 | 12.0 | 5.585 | 111 | 3.45 | -- | -- |
| | IR-f | | | | | | | | | | | |
| | A-1-P ₃ P ₅ | .2338 | .1383 | .7925 | .7785 | 14.164 | 12.4 | 5.668 | 126.5 | 3.48 | 4.63 | 8.17 |
| | A-2-P ₃ P ₅ | .2354 | .1400 | .8043 | .80 | 14.323 | 12.2 | 5.171 | 122.0 | 2.67 | 4.41 | 7.08 |
| | A-3-P ₃ P ₅ | .2359 | .1393 | .803 | .808 | 14.349 | 12.3 | 5.274 | 120.6 | 2.95 | 4.56 | 7.51 |
| | AVERAGE | .2315 | .1367 | .7887 | .7804 | 14.06 | 12.1 | 5.452 | 114.6 | 3.03 | 4.55 | 7.58 |
| | Ic | | | | | | | | | | | |
| Id | CH-1 | .2281 | .1345 | .779 | .7855 | 13.892 | 11.9 | 8.325 | 73.9 | 3.33 | -- | -- |
| | CH-2 | .2301 | .1348 | .780 | .8085 | 14.023 | 12.0 | 8.17 | 75.9 | 3.35 | -- | -- |
| | CH-3 | .2290 | .1353 | .7783 | .785 | 13.926 | 11.9 | 8.325 | 73.9 | 3.40 | -- | -- |
| | IR-C | .2309 | .1353 | .782 | .808 | 14.058 | 12.0 | 8.222 | 75.5 | 3.43 | -- | -- |
| | IR-f | | | | | | | | | | | |
| | A-1-P ₃ P ₅ | .2333 | .1383 | .7913 | .7775 | 14.137 | 12.3 | 8.068 | 78.8 | 3.33 | 4.69 | 8.02 |
| | A-2-P ₃ P ₅ | .2348 | .1405 | .8028 | .8025 | 14.300 | 12.3 | 8.274 | 76.9 | 2.92 | 4.54 | 7.46 |
| | A-3-P ₃ P ₅ | .2349 | .1398 | .803 | .8095 | 14.315 | 12.3 | 8.016 | 79.4 | 2.60 | 4.41 | 7.01 |
| | AVERAGE | .2316 | .1369 | .788 | .7967 | 14.093 | 12.1 | 8.2 | 76.6 | 2.95 | 4.55 | 7.50 |
| | Id | | | | | | | | | | | |
| AVERAGE | | .2326 | .1383 | .7922 | .792 | 14.144 | 12.2 | | | 3.07 | 4.55 | 7.62 |
| UNCLASSIFIED | | | | | | | | | | | | |

Table 2. Detailed Test Operating Parameters* (U) (Continued)

| Test | Test No. | Comustor/Plenum Input | | Cavity/Injection | | P_x P_o/P_x $\Delta\dot{Q}_p$ | | $\Delta\dot{Q}_n$ | \dot{Q} | \dot{n}_2 -ourge |
|------|--------------------|-----------------------|--------------------|--------------------|-------------|-----------------------------------|-----------|-------------------|-----------|--------------------|
| | | $[\dot{F}_2]_{in}$ | $[\dot{H}_e]_{in}$ | $[\dot{H}_e]_{in}$ | \dot{m}_c | P_x torr | P_o/P_x | Kcal/sec | Kcal/sec | mole/sec |
| II | CH-1 | .3467 | .2093 | 1.195 | 18.79 | 19.4 | 1.965 | 510.5 | 5.17 | 11.09 |
| | CH-2 | .3443 | .2093 | 1.161 | 18.55 | 19.3 | 2.017 | 494.9 | 4.69 | 10.49 |
| | CH-3 | .3456 | .21 | 1.180 | 18.69 | 19.5 | 1.852 | 541.6 | 4.74 | 10.53 |
| | CH-4 | .3452 | .208 | 1.184 | 18.69 | 19.4 | 1.852 | 538.9 | 4.51 | 10.26 |
| | IR-C | .3388 | .2135 | 1.201 | 18.93 | 19.4 | 2.017 | 497.4 | 4.94 | -- |
| | IR-F | .3439 | .2068 | 1.172 | 18.59 | 18.9 | 2.172 | 450 | 4.74 | -- |
| | A-1-P ₅ | .3478 | .2115 | 1.212 | 18.91 | 19.0 | 1.965 | 500 | 4.21 | 10.03 |
| | A-1-P ₃ | .3469 | .2135 | 1.226 | 18.94 | 19.5 | 1.862 | 541.7 | 4.18 | 10.05 |
| | A-2-P ₃ | .3474 | .2118 | 1.174 | 18.75 | 18.9 | 1.81 | 540 | 3.60 | 9.37 |
| | A-2-P ₅ | .3499 | .2118 | 1.178 | 18.86 | 19.1 | 1.706 | 578.8 | 3.73 | 9.48 |
| | A-3-P ₃ | .3477 | .2118 | 1.190 | 18.82 | 19.1 | 1.913 | 516.2 | 3.38 | 9.02 |
| | A-3-P ₅ | .3498 | .2095 | 1.185 | 18.87 | 19.0 | 1.965 | 500 | 3.73 | 9.49 |
| | AVERAGE II | .3462 | .2106 | 1.188 | 18.75 | 19.2 | 1.926 | 515.7 | 4.30 | 10.09 |
| III | CH-1 | .2308 | .1385 | .8013 | 12.51 | 12.4 | 1.5 | 427.5 | 3.45 | 8.04 |
| | CH-2 | .2316 | .139 | .7806 | 12.48 | 12.3 | 1.551 | 410 | 3.43 | 8.02 |
| | CH-3 | .2331 | .1383 | .793 | 12.58 | 12.4 | 1.396 | 459.3 | 3.28 | 7.79 |
| | CH-4 | .235 | .1393 | .788 | 12.64 | 12.4 | 1.396 | 459.3 | 3.18 | 7.69 |
| | IR-F | .2309 | .1373 | .7766 | 12.43 | 12.0 | 1.551 | 400 | 3.23 | -- |
| | IR-C | .2302 | .1390 | .7843 | 12.44 | 12.2 | 1.5 | 420.7 | 3.15 | -- |
| | A-1-P ₃ | .2348 | .1403 | .8078 | 12.76 | 12.5 | 1.5 | 420.7 | 2.97 | 7.51 |
| | A-2-P ₃ | .2359 | .1403 | .8078 | 12.76 | 12.4 | 1.138 | 563.6 | 2.62 | 7.11 |
| | A-3-P ₃ | .235 | .1398 | .8053 | 12.71 | 12.1 | 1.448 | 432.1 | 3.00 | 7.64 |
| | AVERAGE III | .2330 | .1391 | .7933 | | 12.3 | 1.442 | 441 | 3.15 | 7.70 |

UNCLASSIFIED

Table 2. Detailed Test Operating Parameters (Continued)

| Test | Test No. | Combustor/Plenum Input | | | Cavity Injection | | | P_o P_x P_o/P_x | | | $\Delta\dot{Q}_p$ | $\Delta\dot{Q}_n$ | $\Delta\dot{Q}$ | N_2 -purge |
|---------|-----------------------------------|------------------------|---------------|---------------|------------------|---------------|---------------|-----------------------|-------|-------|-------------------|-------------------|-----------------|--------------|
| | | $[\dot{F}_2]$ | $[\dot{U}_2]$ | $[\dot{H}_e]$ | \dot{m}_F | $[\dot{H}_2]$ | $[\dot{H}_e]$ | torr | | | Kcal/sec | Kcal/sec | Kcal/sec | mole/sec |
| IV | CH-1 | .2278 | .159 | .8533 | 12.70 | .596 | -- | 13.6 | 1.189 | 591.3 | 4.01 | 5.59 | 9.60 | -- |
| | CH-2 | .2284 | .1608 | .862 | 12.77 | .606 | -- | 13.7 | 1.448 | 489.3 | 3.98 | 5.59 | 9.57 | .1429 |
| | CH-3 | .2309 | .1605 | .8568 | 12.84 | .6065 | -- | 13.7 | 1.293 | 548 | 3.78 | 5.54 | 9.32 | .1429 |
| | CH-4 | .2303 | .1605 | .866 | 12.86 | .6045 | -- | 13.8 | 1.293 | 552 | 3.75 | 5.54 | 9.29 | .1429 |
| | IR-f | .2285 | .1598 | .8503 | 12.72 | .5985 | -- | 13.5 | 1.448 | 482.1 | 3.52 | -- | -- | -- |
| | IR-c | .2289 | .1613 | .844 | 12.72 | .593 | -- | 13.5 | 1.448 | 482.1 | 3.78 | -- | -- | -- |
| | A-1-P ₃ P ₅ | .2298 | .163 | .865 | 12.84 | .592 | -- | 13.8 | 1.241 | 575 | 3.25 | 5.62 | 8.87 | -- |
| | A-2-P ₃ P ₅ | .2322 | .165 | .8693 | 12.96 | .601 | -- | 13.8 | 1.293 | 552 | 3.40 | 5.85 | 9.25 | -- |
| | A-3-P ₃ P ₅ | .2330 | .1538 | .864 | 12.97 | .604 | -- | 13.3 | 1.396 | 492.6 | 2.82 | 5.42 | 8.24 | -- |
| AVERAGE | IV | .2300 | .1615 | .859 | 12.82 | .600 | -- | 13.6 | 1.339 | 526.5 | 3.59 | 5.59 | 9.16 | -- |

UNCLASSIFIED

Table 3. Chemical Thermodynamic Properties and Molecular and Atomic Constants (U)

| Substance | | ΔH_f° 298°K Kcal/mole | θ_v °K | θ_r °K | λ_D °K | e_{g_0} | ω_e cm ⁻¹ | $\omega_e x_e$ cm ⁻¹ | B_e cm ⁻¹ | d_e cm ⁻¹ | $G(1)-G(0)$ cm ⁻¹ Kcal/mole | B_0 cm ⁻¹ | |
|-----------------------|----------------|--|------------------|------------------|-------------------|-----------|--------------------------------|------------------------------------|---------------------------|---------------------------|--|---------------------------|-------|
| Hydrogen | H | 1 | 52.10 | - | - | - | 2 | - | - | - | - | - | |
| | H ₂ | 2 | 0.00 | 5,964 | 85.34 | 52,450 | 1 | 4395.2 | 117.99 | 60.807 | 2.993 | 4159 11.89 | 59.31 |
| Deuterium | D | 2 | 53.25 | - | - | - | 2 | - | - | - | - | - | |
| | D ₂ | 4 | 0.00 | 4,302 | 29.90 | 53,600 | 1 | 3118.4 | 64.09 | 30.429 | 1.049 | 2990 8.547 | 29.90 |
| Fluorine | F | 19 | 18.7 | - | - | - | 6 | - | - | - | - | - | |
| | F ₂ | 38 | 0.00 | 1,283 | 1.24 | 19,030 | 1 | 892 | - | .862 | - | (899) (2.55) | - |
| Hydrogen Fluorine | HF | 20 | -64.8 | 5,620 | 29.57 | 68,350 | 1 | 4138.73 | 90.05 | 20.939 | .7985 | 3959 11.32 | 20.54 |
| Deuterium Fluorine | DF | 21 | -64.98 | 4,182 | 15.62 | 69,020 | 1 | 2998.25 | 45.71 | 11.007 | .293 | 2907 8.309 | 10.86 |
| Helium | He | 4 | - | - | - | - | 1 | - | - | - | - | - | - |

UNCLASSIFIED

(U) these assumptions one has the following obvious relations for plenum chamber molar flow rates (mole/sec):

$$[\dot{DF}]_p = 2[\dot{D}_2]_{in}; [\dot{He}]_p = [\dot{He}]_{in};$$

$$[\dot{F}]_p + 2[\dot{F}_2]_p = 2\left\{[F_2]_{in} - [D_2]_{in}\right\} \quad (43)$$

Plenum chamber molar flow rates through the exit nozzle band have been computed and listed in Table 4. As will be justified below, plenum chamber equilibrium temperatures are expected to rise to levels high enough to fully dissociate all excess fluorine, while not dissociating any DF. Therefore, in Table 4 all excess fluorine has been assumed to contribute to the atomic fluorine molar flow rate. Total molar (\dot{n}_p), and mass flow rates (\dot{m}_p) through the nozzle bank have been listed in columns 4 and 5,

Table 4. Plenum Chamber Equilibrium Molar Flow Rates and Salient Gas Parameters (U)

| Test | $[F]_p$ mole/sec | $[DF]_p$ mole/sec | $[He]_p$ mole/sec | \dot{u}_p mole/sec | \dot{m}_p gr/sec | \bar{u} gr/mole | $x_p(F)$ | $x_p(DF)$ | $x_p(He)$ |
|------|---------------------|----------------------|----------------------|-------------------------|-----------------------|----------------------|----------|-----------|-----------|
| I | .187 | .277 | .792 | 1.258 | 12.56 | 9.984 | .15 | .22 | .63 |
| II | .271 | .421 | 1.188 | 1.880 | 18.75 | 9.973 | .144 | .224 | .632 |
| III | .182 | .278 | .793 | 1.257 | 12.58 | 9.992 | .149 | .221 | .63 |
| IV | .137 | .323 | .859 | 1.319 | 12.82 | 9.719 | .104 | .245 | .651 |

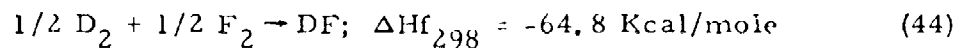
| Test | \dot{W}_o Kcal/sec | $\dot{W}_o - \Delta \dot{Q}_p$ Kcal/sec | $\Delta \dot{Q}_D$ Kcal/sec | \dot{W}_p Kcal/sec | $f_p^*(DF)$ | \bar{f}_p | γ_p | T_o °K | P_o psia | $n_o \times 10^{-19}$ part/cm ³ | $\rho_o \times 10^5$ gr/cm ³ | a_o km/sec |
|------|-------------------------|--|--------------------------------|-------------------------|-------------|-------------|------------|-------------|---------------|---|--|-----------------|
| I | 18.00 | 14.93 | 3.57 | 11.36 | 5.562 | 3.564 | 1.561 | 1930 | 12.2 | .3163 | 5.71 | 1.59 |
| II | 27.36 | 23.06 | 5.12 | 17.94 | 5.590 | 3.580 | 1.559 | 2020 | 19.2 | .474 | 8.58 | 1.62 |
| III | 18.06 | 14.91 | 3.55 | 11.36 | 5.562 | 3.564 | 1.561 | 1930 | 12.3 | .3183 | 5.75 | 1.58 |
| IV | 20.99 | 17.40 | 2.59 | 14.81 | 5.705 | 3.663 | 1.546 | 2290 | 13.6 | .2973 | 5.23 | 1.74 |

UNCLASSIFIED

(U) respectively. Plenum gas average molecular weight (μ) follows from dividing mass flow rate into molar flow rate; this has been given in column 6. The next three columns of Table 4 give the important molar concentrations in the equilibrium plenum chamber gas for atomic fluorine $X_p(F)$, helium, $X_p(He)$, and fluorine, $X_p(DF)$.

(2) Plenum Gas Heat Content

(U) Plenum gas heat content can be calculated from the measured reactant flow rates and the heat of combustion of the combustor reaction using



Reacting all the available deuterium releases heat at the rate \dot{W}_O as listed in column 10 of Table 4. Actually, because of heat losses to the plenum chamber walls, not all this heating power is available for raising the plenum chamber gas temperatures. Heat losses to the plenum chamber walls have been measured and have been recorded in Table 1 and the available heat $\dot{W}_O - \Delta \dot{W}_p$, has been listed for test series I through IV in Table 4. Complete dissociation of all the excess fluorine requires heat input at the rate of

$$\dot{W}_{Dis} = 2 \cdot [\dot{F}]_p \cdot 18.9 \text{ Kcal/sec} \quad (45)$$

where the heat of formation of F is given in Table 2. Having thus accounted for dissociation the remaining power which is listed in Table 4 as

$$\dot{W}_p = \dot{W}_O - \Delta \dot{W}_p - \Delta \dot{W}_{Dis} \text{ Kcal/sec} \quad (46)$$

and can be thought of as raising the temperature of the hypothetical gas mixture consisting of atomic fluorine, helium and deuterium fluoride from 298°K to plenum chamber stagnation temperature T_O .

(3) Plenum Gas Stagnation Temperature

(U) Plenum gas stagnation temperature is found from equating heat power \dot{W}_p to the heat carried away by the gas. Excepting dissociation energy, the molar heat content of the plenum chamber gas is

(U)

$$H_T - H_{298} = R\Delta T \left\{ \frac{1}{2} \sum_i S_i f_i + 1 \right\} \text{ Kcal/mole} \quad (47)$$

where the X_i are the molar concentrations of plenum gas constituents listed in Table 4. Multiplying Equation (47) by the total molar flow rates yields a solution for determining the temperature increment T over room temperature (298°K): i. e.,

$$\dot{W}_p = (H_T - H_{298}) \cdot \dot{\mu}_p = \Delta T \cdot R \cdot \dot{\mu}_p \left\{ \frac{1}{2} \sum_i X_i f_i + 1 \right\} \text{ (Kcal/sec)} \quad (48)$$

Here, the universal gas constant R is measured in units of (Kcal/mole $^\circ\text{K}$); i. e., its numerical value is $R = 1.987 \times 10^{-3}$. Species molar concentrations, X_i , and total plenum gas molar flow rate, $\dot{\mu}_p$, are from Table 4. In order to carry out the necessary calculations the species degrees of freedom have to be known; this is 3 for atomic species F and He. The appropriate effective degrees of freedom for a diatomic species are given by the well known relation

$$f^* = 5 + 2 \frac{\theta_v/T}{e^{\theta_v/T} - 1} \quad (49)$$

i. e., it is temperature dependent. Using Equations (48) and (49) plenum gas stagnation temperatures have been calculated and results have been recorded in Table 4. Since plenum pressure has been measured, plenum gas number densities and mass density can be computed utilizing the ideal gas law. The average plenum gas degree of freedom, \bar{f}_p , can then be used to determine the specific heat ratio by

$$\gamma_p = \frac{2 + \bar{f}_p}{\bar{f}_p}$$

This solution, in turn, permits one to determine the important sound velocity a_o of the plenum gas at stagnation temperature T_o from

$$a_o = 10^{-5} \sqrt{\gamma_p \frac{RT_o}{\mu_p}} \text{ km/sec}$$

(U) Here the universal gas constant R is usually measured in cgs units, as used throughout this report unless specifically stated otherwise, i. e., $R = 8.314 \times 10^7$ ergs/mole $^{\circ}\text{K}$.

(4) Plenum Gas Dissociation

(U) Plenum gas dissociation, especially that of the excess fluorine, is of critical importance for the functioning of the apparatus as a laser. In fact the very purpose of the plenum gas heating is to provide high molar flow rates of atomic fluorine into the downstream laser cavity. From the known plenum temperature, pressure and composition, the dissociation of all gas components can be computed with great reliability provided a state of complete thermodynamic equilibrium exists in the plenum gas.

(U) The complete set of equations describing the dissociation and the six possible plenum gas species number densities n_{H} , n_{F} , n_{F_2} , n_{DF} , n_{D_2} and n_{D} would consist of three equations defining the dissociation of F_2 , DF and D_2 , respectively, of two relations conserving the ratio of total fluorine and deuterium mass flow relative to the total mass flow and of the ideal gas law fixing the total plenum particle number density for given temperature and pressure. From Table 3 it is readily evident, however, that the dissociation energies of DF and D_2 on the one hand and F_2 on the other hand are quite different. This fact implies that the thermal dissociation of DF and F_2 are practically uncoupled and occur in very different temperature regimes. The dissociation of F_2 alone, which occurs at relatively low plenum temperatures, is described by the following simple set of equations:

$$\frac{n_{\text{F}} \cdot n_{\text{F}}}{n_{\text{F}_2}} = \frac{e_{g_{\text{F}}} \cdot e_{g_{\text{F}}}}{e_{g_{\text{F}_2}}} \cdot \left(\frac{\pi k T m_{\text{F}}}{h^2} \right)^{3/2}$$

$$\frac{2 \theta_{\text{r}}}{T} \left(1 - e^{-\theta_{\text{v}}/T} \right) e^{-\frac{X_{\text{D}}}{T}} = K_{\text{n}}(T_0) \quad (50)$$

$$(U) \quad \beta = \frac{[\dot{\text{He}}] + [\dot{\text{DF}}]}{[\dot{\text{F}}] + 2[\dot{\text{F}}_2]} = \frac{n_{\text{He}} + n_{\text{DF}}}{n_{\text{F}} + 2n_{\text{F}_2}} \quad (51)$$

$$n_o = N_o \frac{P_o}{760} \cdot \frac{273}{T_o} = n_{\text{He}} + n_{\text{DF}} + n_{\text{F}} + n_{\text{F}_2} \frac{\text{particles}}{\text{cm}^3} \quad (52)$$

The molecular and atomic constants in Equation (50) are found in Table 3 and refer to F or F₂. The atomic mass of the fluorine atom, is $m_{\text{F}} = 19 \times 1.66 \cdot 10^{-24}$ gr and (in Equation (52)) N_o is Loschmidt's number (2.67×10^{19} particles/cm³). Values for the total particle densities for the plenum have been recorded in Table 4. Equations (50) through (52) have a solution which can be expressed in closed form:

$$n_{\text{F}} = \frac{K_n}{2} \frac{\beta + 1}{2\beta + 1} \left\{ \sqrt{1 + \frac{4(2\beta + 1)n_o}{K_n(\beta + 1)^2}} - 1 \right\} \text{cm}^{-3} \quad (53)$$

For large degree of dissociation Equation (50) can be approximated by

$$n_{\text{F}} = \frac{n_o}{\beta + 1} \left\{ 1 - \frac{n_o(2\beta + 1)}{K_n(\beta + 1)^2} \right\} \text{cm}^{-3} \quad (54)$$

With Equations (51) and (52), the molecular fluorine number densities near the large degree of dissociation limit follows as

$$2n_{\text{F}_2} \approx \frac{2n_o^2}{K_n(\beta + 1)^2} \text{cm}^{-3} \quad (55)$$

Defining the degree of dissociation as is customary by

$$\alpha = \frac{n_{\text{F}}}{n_{\text{F}} + 2n_{\text{F}_2}}$$

one readily verifies the approximate relation

$$1 - \alpha = \frac{2n_{\text{F}_2}}{n_{\text{F}} + 2n_{\text{F}_2}} \approx \frac{2n_o(\beta + 1)}{K_n(\beta + 1)^2 + n_o} \approx \frac{2n_o}{K_n(\beta + 1)} \quad (56)$$

(U) which is valid for large degrees of dissociation. With the help of Equation (56) one can determine the factor $(1-\alpha)$ for the sample case of Test I where one expects to find the lowest degree of molecular fluorine dissociation realized in our test series. Specifically, Equation (50) yields for $T_o = 1930^\circ\text{K}$:

$$K_n(T_o) = 5.47 \times 10^{20} \text{ cm}^{-3}$$

The factor β can be readily computed from the known input conditions, i. e.,

$$\beta = \frac{0.792 + 0.277}{0.189} = 5.66$$

and n_o is listed in Table 4 as $0.316 \times 10^{19} \text{ cm}^{-3}$. It follows that $(1-\alpha)$ for this case is

$$1-\alpha = 1.73 \times 10^{-3}$$

This calculation justifies the original assumption of total excess fluorine dissociation used in determining plenum gas composition. A second assumption implicit in computing plenum gas composition is that deuterium fluoride is not dissociated at the plenum gas temperatures used in these experiments. The dissociation of DF is governed by an equation similar to Equation (50) with appropriate changes which account for the fact that DF is a heteronuclear molecule and with appropriate molecular constants.

$$\frac{n_D \cdot n_F}{n_{DF}} = \frac{e^{g_D} \cdot e^{g_F}}{e^{g_{DF}}} \left(\frac{2\pi kT}{h^2} \frac{m_F \cdot m_D}{m_F + m_D} \right)^{3/2}$$

$$\frac{\theta_r}{T} \left(1 - e^{-\theta_v/T} \right) e^{-\frac{X_D}{T}} = K_n(T_o) \quad (57)$$

In the limit of small DF dissociation the atomic fluorine concentration is constant and determined by the already fully dissociated excess fluorine. Hence,

$$\alpha = \frac{n_D}{n_{DF} + n_D} \approx \frac{n_D}{n_{DF}} \approx \frac{K_n}{n_F} \quad (58)$$

(U) For the test series IV, involving the highest temperatures encountered in our experiments, one computes for DF at $T_0 = 2290^\circ\text{K}$

$$K_n = 2.80 \times 10^{11} \text{ cm}^{-3}$$

The degree of dissociation for DF computes from Equation (58) and Table 4 ($n_F = 3.09 \times 10^{17} \text{ cm}^{-3}$) as

$$\alpha = \frac{2.8 \times 10^{11}}{3.09 \times 10^{17}} \approx 0.906 \times 10^{-6}$$

These calculations totally verify our original assumption that for thermodynamic equilibrium the dissociation of DF is totally negligible and that excess fluorine is totally dissociated for the range of test conditions and plenum temperatures used in these experiments.

(U) The equilibrium dissociation of fluorine is expected to depend strongly upon plenum temperature once the temperature is low enough to permit molecular and atomic fluorine to coexist. Therefore, any appreciable error in computed plenum temperatures could principally have large effects on fluorine dissociation. We must, therefore, consider the question of what temperature uncertainties we can permit to exist while retaining the premise of total fluorine dissociation. In the limit of large fluorine dissociation Equation (56) can be used to determine the relative change of $(1-\alpha)$ with plenum temperature at fixed pressure. The resulting expression can be used to determine the plenum temperature below which appreciable equilibrium molecular fluorine is to be expected. This temperature limit is chosen here as that temperature where $(1-\alpha)$ assumes a value of approximately 0.1. Combining Equation (56) with the ideal gas law for the relative change of $(1-\alpha)$ with temperature yields the following expression:

$$\frac{(1-\alpha)T_1}{(1-\alpha)T_2} = \frac{T_2 K_n(T_2)}{T_1 K_n(T_1)} = \left(\frac{T_2}{T_1}\right)^{3/2} \frac{1 - e^{-\theta_v/T_2}}{1 - e^{-\theta_v/T_1}} e^{-\theta_D \left(\frac{1}{T_2} - \frac{1}{T_1}\right)}$$

Using this expression and the preceding calculations at $T_2 = 1930^\circ\text{K}$, one determines that for $T_1 = 1400^\circ\text{K}$ the dissociation factor of fluorine is $1-\alpha = 0.095$. Large mole fractions of F_2 are, therefore, to be expected

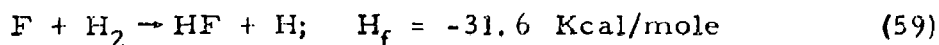
(U) at plenum temperatures below 1400°K . Similarly, (1-c) assumes the value of 1.1×10^{-2} at $T_0 = 1640^{\circ}\text{K}$. In conclusion, dissociation of molecular fluorine is virtually complete above 1650°K . Between 1650° and 1400 the molar concentration ratio of F_2/F increases from less than 1% to approximately 5%. A reduction by 20% of plenum heating power from approximately 11.4 Kcal/sec (Table 4) to 9.5 Kcal/sec would reduce the plenum temperature to 1650°K where molecular fluorine would become noticeable. Since the total measured plenum chamber heat loss for the Test I series was only 3 Kcal/sec, a reduction of the total heat available for gas heating by 2 Kcal/sec through incomplete heat loss measurements appears highly unlikely. Incomplete combustion of the deuterium would be the only other plausible cause for heating power deficiency. This latter alternative is considered equally unlikely. Considering the high plenum chamber pressures, the large fluorine excess and the long residence time (several milliseconds) incomplete combustion of deuterium is not likely. Therefore the assumption that all the excess fluorine in the plenum was indeed dissociated appears to be well justified.

(U) Finite rate chemistry calculations (Ref. 13) show that recombination of molecular fluorine during the expansion of the plenum gas through the nozzle is too slow to cause an appreciable effect. From these considerations it appears that molecular fluorine, believed to exist in the laser cavity, was most likely generated in the nozzle boundary layers. The "orange glow" was observed to be evidence of the presence of molecular fluorine in the laser cavity and related to the "hot" reaction, $\text{H} + \text{F}_2$.

b. Laser Cavity Gas Characteristics

(U) The purpose of the preceding discussion on plenum gas characteristics was to define the input gas into the laser cavity where the diagnostic measurements have been performed. Depending critically on the state of mixing, atomic fluorine reacts in the laser cavity with molecular hydrogen and this reaction provides the chemical pumping of HF^* vibrational states necessary for lasing. The progress of the cavity reactions can be thought of as proceeding through three hypothetical steps which can be defined as follows: In the first step the plenum gas is mixed with molecular hydrogen but the gas has not yet had time to react. At the end of the second step all atomic fluorine has reacted with cavity molecular hydrogen producing atomic hydrogen in the process. Of course

(U) this step releases additional heat into the cavity flow field. A further substantial heat release into the flow field is effected by the third and final step in which the atomic hydrogen is assumed to be recombined to molecular hydrogen. In reality, the state of progress (in the average sense) at each downstream cavity flow field cross section will be a mixture of all three steps in varying degrees of completeness. However, at the exit plane of the nozzle bank the gas composition averaged over the entire exit plane will closely approach that of the first step. The cavity reactions will then rapidly move the average gas characteristics towards completing Step 2. The third and final step, involving the recombination of atomic hydrogen, is not believed to take place at all in the laser cavity flow time because of the low cavity pressures and the slow rate of the two-body recombination. Table 5 summarizes the salient cavity gas characteristics which can be readily derived from known flow rates, heat of combustion, and heat loss measurements. The first nine columns of Table 5 give the molar flow rates of all components before the cavity reaction commences (step 1), after all atomic fluorine has been reacted (step 2), and after all atomic hydrogen has been recombined (step 3). From the molar flow rates cavity molar species concentration $X_c(i)$ can be computed and these have also been listed in Table 5. Average cavity gas degrees of freedom, assuming no contributions from vibrational degrees of freedoms, and average specific heat ratios have been computed from the molar concentrations. Since cavity gas temperatures are generally substantially below 1000°K , the specific heat ratios of Table 5 are expected to be quite accurate. The total heat released per second in the cavity at the end of step 2 from the reaction



is listed in Table 5 as $\Delta\dot{Q}_c$. The total heat power carried by the cavity flow field has been given as \dot{w}_c for conditions relevant to Step 1, 2, and 3. In accounting for the total heat carried into the cavity by the plenum gas one has, of course, to consider the substantial heat losses occurring in the nozzle bank; measured values of the nozzle heat losses have been included in Table 1. One expects of course that a significant fraction of the power $\Delta\dot{Q}_c$ added to the cavity flow field from the chemical pumping reaction will end up in nonequilibrium excitation of HF vibrational levels

Table 5. Laser Cavity Molar Flow Rates and Gas Parameters (U)

| Test Step | $[F]_c$ mole/sec | $[H]_c$ mole/sec | $[HF]_c$ mole/sec | $[H_2]_c$ mole/sec | $[DF]_c$ mole/sec | $[He]_c$ mole/sec | \dot{t}_c mole/sec | \dot{m}_c gr/sec | \bar{c} gr/mole |
|-----------|---------------------|---------------------|----------------------|-----------------------|----------------------|----------------------|-------------------------|-----------------------|----------------------|
| I | 1 | .189 | 0 | .792 | .277 | .792 | 2.05 | 14.14 | 6.898 |
| | 2 | 0 | .189 | .603 | .277 | .792 | 2.05 | 14.14 | 6.878 |
| | 3 | 0 | .189 | .698 | .277 | .792 | 1.956 | 14.14 | 7.229 |
| II | 1 | .271 | 0 | 1.201 | .421 | 1.188 | 3.081 | 21.15 | 6.865 |
| | 2 | 0 | .271 | .73 | .421 | 1.188 | 3.081 | 21.15 | 6.865 |
| | 3 | 0 | .271 | 1.066 | .421 | 1.188 | 2.946 | 21.15 | 7.179 |
| III | 1 | .188 | 0 | .402 | .278 | 1.195 | 2.063 | 14.99 | 7.266 |
| | 2 | 0 | .188 | .214 | .278 | 1.195 | 2.063 | 14.99 | 7.266 |
| | 3 | 0 | .188 | .308 | .278 | 1.195 | 1.969 | 14.99 | 7.613 |
| IV | 1 | .137 | 0 | .6 | .323 | .859 | 1.919 | 14.02 | 7.306 |
| | 2 | 0 | .137 | .463 | .323 | .859 | 1.919 | 14.02 | 7.306 |
| | 3 | 0 | .137 | .532 | .323 | .859 | 1.851 | 14.02 | 7.574 |

| | $X_c(F)$ | $X_c(H)$ | $X_c(HF)$ | $X_c(H_2)$ | $X_c(DF)$ | $X_c(He)$ | \bar{f}_c | γ_c | \dot{Q}_c kcal/sec | \dot{W}_c kcal/sec | T_o °K |
|-----|----------|----------|-----------|------------|-----------|-----------|-------------|------------|-------------------------|-------------------------|-------------|
| I | 1 | .092 | 0 | .386 | .135 | .387 | 4.042 | 1.495 | 5.97 | 6.81 | 852 |
| | 2 | 0 | .097 | .294 | .135 | .387 | 4.042 | 1.495 | 5.97 | 12.78 | 1340 |
| | 3 | 0 | .097 | .357 | .141 | .405 | 4.19 | 1.477 | 9.85 | 22.63 | 2180 |
| II | 1 | .088 | 0 | .37 | .137 | .385 | 4.054 | 1.493 | 8.56 | 12.15 | 954 |
| | 2 | 0 | .088 | .302 | .137 | .385 | 4.054 | 1.493 | 8.56 | 20.71 | 1420 |
| | 3 | 0 | .092 | .362 | .143 | .403 | 4.194 | 1.477 | 14.12 | 34.83 | 2220 |
| III | 1 | .091 | 0 | .195 | .135 | .579 | 3.66 | 1.546 | 5.94 | 6.81 | 885 |
| | 2 | 0 | .091 | .104 | .135 | .579 | 3.66 | 1.546 | 5.94 | 12.75 | 1400 |
| | 3 | 0 | .095 | .157 | .141 | .607 | 3.786 | 1.528 | 9.79 | 22.55 | 2290 |
| IV | 1 | .071 | 0 | .313 | .168 | .448 | 3.762 | 1.505 | 4.33 | 9.22 | 1110 |
| | 2 | 0 | .071 | .242 | .168 | .448 | 3.762 | 1.505 | 4.33 | 13.54 | 1470 |
| | 3 | 0 | .074 | .287 | .175 | .464 | 4.072 | 1.491 | 7.14 | 20.69 | 2150 |

UNCLASSIFIED

(U) and, hence, will not add to the heat in translation-rotational degrees of freedom of the flow field. Perhaps the most significant fact about step 3 is the very large heat released into the flow field when atomic hydrogen is recombined, as is evident from the values of \dot{w}_c and $\Delta\dot{Q}_c$ for step 3 listed in Table 5. Flow field stagnation temperatures have been computed under the assumption of frozen vibrational degrees of freedom using average cavity gas translation-rotational degrees of freedom, f_c from Table 5. Stagnation temperatures for complete thermodynamic equilibrium, where vibrational degrees of freedoms have to be accounted for, are only insignificantly lower than those listed in the table. In test I, for example, instead of 1340°K for Step 2 the complete equilibrium stagnation temperature would be 1320°K, and for Step 3 instead of 2180°K one would compute 2110°K. Computed effective stagnation temperatures have been listed in Table 5.

c. Energy Transport in the Laser Cavity Flow Field

(U) Energy transport in the laser cavity flow field is of significance in understanding the laser apparatus. Some of the laser cavity diagnostic data reported later will be used to provide partial answers to the energy transport question. In this section we shall state the necessary relations for later use.

(1) Energy Transport in Random Translational and Rotational Modes

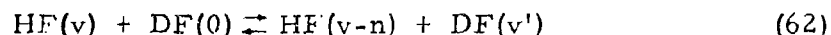
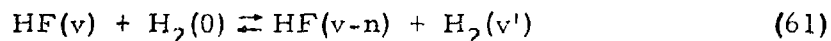
(U) Part of the power carried in the flow field serves to raise the cavity gas temperature by exciting the random translational and rotational degrees of freedom. For equilibrium between local flow field gas kinetic temperatures and molecular rotational temperatures the heat transport \dot{w}_{t-r} can readily be computed from

$$\dot{w}_{t-r} = \frac{2+\bar{f}_c}{2} \dot{\mu}_c \cdot R \cdot 10^{-3} (T-298) \text{ Kcal/sec} \quad (60)$$

where $R = 1.987 \text{ Kcal/mole } ^\circ\text{K}$ and \bar{f}_c and $\dot{\mu}_c$ are from Table 5. Assuming a temperature rise by 200°K from 300°K to 500°K, and using approximate values for test I from Table 5 of $\bar{f}_c = 4$ and $\dot{\mu}_c = 2 \text{ mole/sec}$, one would expect heat transport on the order of 2.4 Kcal/sec by the flow field in excitation of translational and rotational degrees of freedom.

(2) Energy Transport in Nonequilibrium Vibrational Modes

(U) The very principle of HF chemical laser action requires substantial deviation of vibrational excitation of HF from a state of thermodynamic equilibrium. For the other molecular species, DF and H₂, the question of vibrational equilibrium is far from clear. The chemiluminescent measurements discussed in this report have been conducted principally to define the state of nonequilibrium excitation of the HF molecules in the cavity. No such measurements exist to date on the nonequilibrium excitation of DF or H₂. On the other hand, there can be little doubt that energy transfer collisions between excited HF molecules and H₂ or DF do occur following the schemes



The energy transfer, particularly, to H₂ is facilitated because H₂ and HF vibrational states are near resonance. The heat transport in the vibrational excitation of HF, at least, can be tied readily to measured observables: Heat transport in HF vibrational modes is

$$\dot{w}_v(\text{HF}) = \epsilon_1[\dot{\text{HF}}]_1 + \epsilon_2[\dot{\text{HF}}]_2 + \epsilon_3[\dot{\text{HF}}]_3 + \dots \text{ Kcal/sec} \quad (63)$$

where the ϵ_i are vibrational state energies for the i^{th} level counted from the molecular ground state. Defining the mole fractions

$$y_i(\text{HF}) = \frac{[\dot{\text{HF}}]_i}{[\dot{\text{HF}}]} ; [\dot{\text{HF}}] = \sum_{i=0} [\dot{\text{HF}}]_i \text{ mole/sec} \quad (64)$$

Equation (63) can be written as

$$\dot{w}_v(\text{HF}) = [\dot{\text{HF}}] \{ \epsilon_1 y_1 + \epsilon_2 y_2 + \epsilon_3 y_3 + \dots \} \text{ Kcal/sec} \quad (65)$$

For approximate calculations we can use the harmonic oscillator approximation to describe the vibrational state energies as $\epsilon_n = n \epsilon_1$. Equation (65) simplifies further to

$$\dot{w}_v(\text{HF}) = [\dot{\text{HF}}] \cdot \epsilon_1 \{ y_1 + 2y_2 + 3y_3 + \dots \} \text{ Kcal/sec} \quad (66)$$

(U) Expressions identical in form to Equations (63), (64) and (65) hold for molecular species H_2 and DF . The respective energies of the first vibrational states can be calculated readily from the molecular constants of Table 3 by using the relation

$$\epsilon_1 \approx \omega_e - 2 \omega_e x_e \text{ cm}^{-1}$$

Numerically, one computes for the molecules of interest the following values:

$$HF: \epsilon_1 = 3959 \text{ cm}^{-1} \rightarrow 11.3 \text{ Kcal/mole}$$

$$DF: \epsilon_1 = 2907 \text{ cm}^{-1} \rightarrow 8.31 \text{ Kcal/mole}$$

$$H_2: \epsilon_1 = 4159 \text{ cm}^{-1} \rightarrow 11.9 \text{ Kcal/mole}$$

The total heat transport in nonequilibrium vibrational excitation is the sum of the three molecular components.

(3) Kinetic Energy Transport in Directed Motion

(U) Kinetic energy transport in directed motion is expected to account for a significant fraction of the total energy transport listed in Table 5. It is

$$\dot{w}_{\text{kin}} = \frac{\dot{m}_c}{2} u^2 \text{ ergs/sec} = \frac{\dot{m}_c}{2 \cdot 4.187} \left(\frac{u}{10^5} \right)^2 \text{ Kcal/sec} \quad (67)$$

where \dot{m}_c is the total cavity mass flow in gr/sec and u is the flow field velocity in cm/sec. For a typical case of test I, total mass flow \dot{m}_c is approximately 14 gm/sec. If the gas were to move with average velocity of 2 km/sec, the heat transport in kinetic energy of motion would be 6.7 Kcal/sec.

(4) Total Heat Loss from Incoherent Infrared Radiation

(U) The total heat loss from incoherent infrared radiation is totally negligible as compared to other terms in the heat balance equations. This fact is most easily recognized when considering that the mean radiative lifetime of HF vibrational states is approximately 5 millisecc. Since the flow time of the gas through the cavity is only

(U) about 50 μ sec, the mean power loss through incoherent radiation can be at most 0.01 of the mean heat transport in HF vibrational excitation. This latter statement does not necessarily imply that radiative terms are insignificant in the heat balance equation. For example even in the case where there are no laser cavity mirrors, significant power loss may result from uncontrolled lasing (super radiance) because of excessive gain in the cavity medium.

(U) Combining all the sources of heat transport, an overall energy transport equation may be written as follows:

$$\begin{aligned} \frac{\dot{w} - \dot{w}_{t-r}}{c} = & \frac{\dot{\mu} u^2}{2} + x_c(\text{HF}) \left(\sum_{\text{HF}} \epsilon_i y_i \right) + x_c(\text{DF}) \left(\sum_{\text{DF}} \epsilon_i y_i \right) \\ & + x_c(\text{H}_2) \left(\sum_{\text{H}_2} \epsilon_i y_i \right) + \frac{\dot{w}_r}{\dot{\mu} c} \text{ Kcal/mole} \end{aligned} \quad (68)$$

The term on the left-hand side of Equation (68) is well-known from measurements of reactant and diluent molar flow rates, heat losses, and cavity gas kinetic temperatures. On the right hand side of the equation the value of the sum $\sum \epsilon_i y_i$ for the HF molecule can be determined from chemiluminescent data. Also the molar concentration of deuterium fluoride $x_c(\text{DF})$ in the laser cavity is well-known from reactant molar flow rate measurements. Ignoring recombination of atomic hydrogen to molecular hydrogen, there is, furthermore, a conservation relation connecting the molar concentrations of HF and H_2 such that, in the cavity, the sum of relative concentrations of HF and H_2 are constant, i. e.,

$$x_c(\text{HF}) + x_c(\text{H}_2) = \text{const} \quad (69)$$

Although measurements conducted in the present program leave some of the terms in Equation (68) undetermined, there is no reason why, in a future program, they could not be evaluated by experimental measurements. We believe this should be an important objective in future measurements programs because the exact nature of the energy balance

(U) permits significant insight into overall high energy chemical laser cavity kinetics and processes.

6. CAVITY DIAGNOSTIC EXPERIMENT RESULTS

(U) In the following sections on laser cavity diagnostic results, reduced data summaries are presented for only the investigated laser conditions rather than attempting to present all original data. This is necessary in order to communicate the wealth of experimental information in a reasonably condensed format. For some selected cases we shall also present direct experimental data for the purpose of illustrating applied data reduction procedures and for discussing data problems. Most discussions in this section will be confined to presenting experimental data reduction results rather than attempting any detailed interpretation. In this sense this section will be limited to factual information which relies only on straightforward and proven experimental data reduction procedures as have been discussed in detail in Section 4. Diagnostic results interpretations and discussions involving less reliable assumptions on laser apparatus and cavity characteristics are presented in Section 7.

a. Chemiluminescent Experimental Results

(U) Measurement of laser cavity HF-excited state number densities by chemiluminescent methods is one of the most straightforward and informative diagnostic measurements that can be made. The experimental apparatus, the principles, limitations and inherent error sources of the chemiluminescent experiment have been fully discussed in Section 4, a. The technique is to reduce measured vibration-rotation spectral line intensities to excited state number densities integrated along the chosen optical line of sight, applying Equation (1). In this section the experimental results of the chemiluminescent experiment are discussed.

(U) In the case of Boltzman distribution for rotational sublevels of a given excited vibrational level, the most practical way of presenting the reduced data is by making graphs, according to Equation (3), of normalized vibration-rotation state densities versus rotational state energy, i. e., versus $j'(j'+1)$. This can be readily done if the obtained spectra are sufficiently spectrally resolved to permit line-by-line analysis. Figure 35 shows a sample spectrum demonstrating that

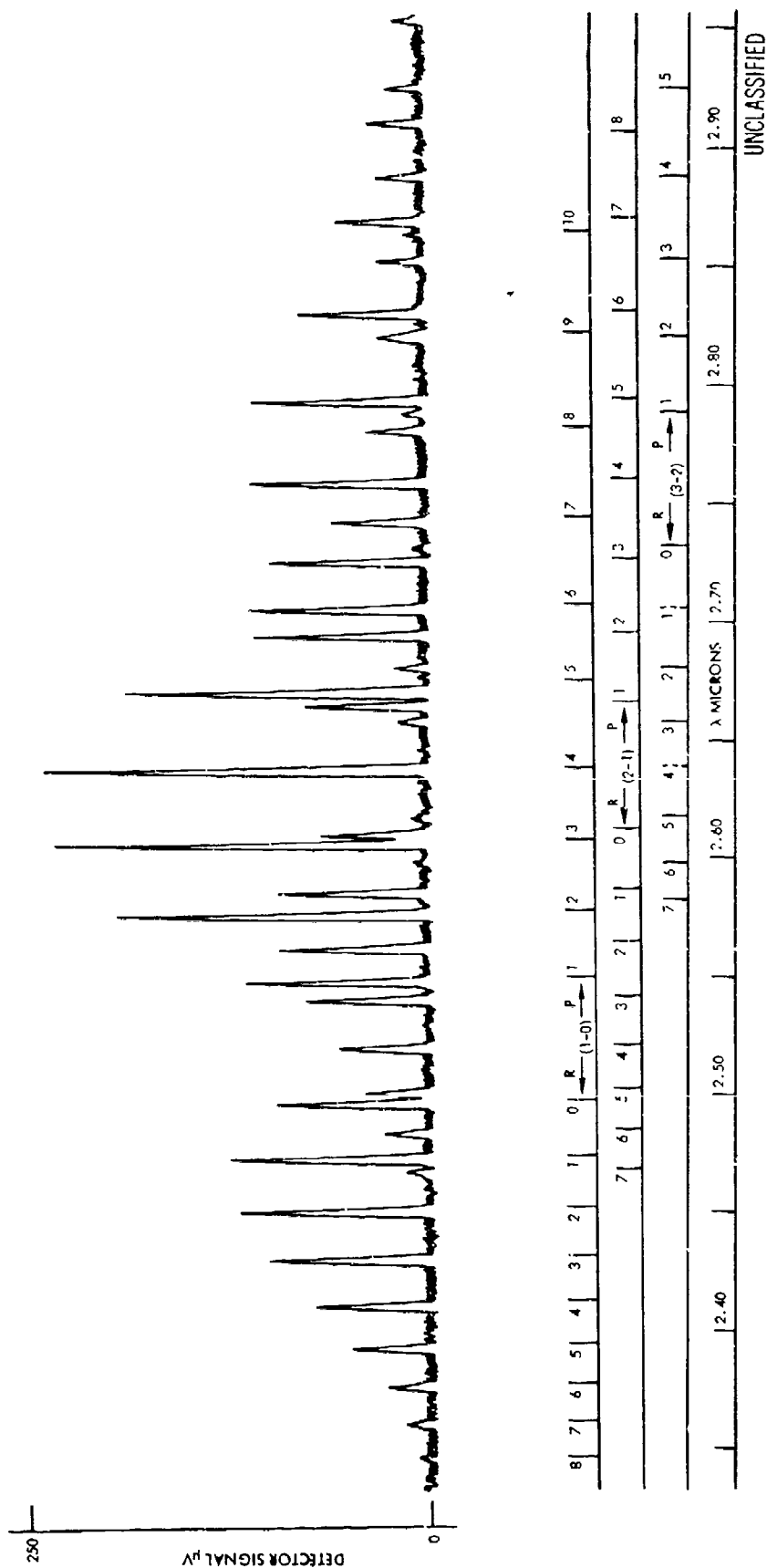


Figure 35. Typical Chemiluminescence Spectrum (U)

(U) sufficient spectral resolution was in fact obtained. The data reduction itself has been mechanized as described in Section 4. a.

(U) As a sample case, we will show and discuss in some detail the data for test series Ia using window 2 located 4.3 cm from the nozzle exit bank. This test represents the nominal laser operating conditions (see Tables 1 and 2) and, from a data point of view, shows the characteristic features of a test where the spectrum is from an "optically thin" volume. Figures 36, 37 and 38 show plots of data for the 1-0, 2-1 and 3-2 bands, separately. For most levels $\{v', j'\}$ two separate and independent measurements have been obtained from a pair of P-branch and R-branch lines. In the graphs the state densities from P-branch lines have been shown by -0- and those derived from R-branch lines have been designated by -Δ-. For each line the measured instrument noise level has been converted to equivalent "state density noise"; the equivalent state density noise levels have been included in the graphs as two curves connecting all P-branch (-0-) and all R-branch (-Δ-) equivalent noise levels. The signal/noise ratio of the measurement can therefore be directly read from the graphs. Inspecting Figures 36 through 38, one recognizes that for rotational sublevels of $j'=0$ up to $j'=6$ (i. e., up to P_7 and R_6 in the P-branch and R-branch, respectively) the normalized integrated state densities obey an exponential distribution law which can be described by a "rotational" temperature. This temperature can be directly read from the slopes of the semilogarithmic plots of Figures 36 through 38. Measured rotational temperatures have been noted on the graphs. Comparing rotational temperatures measured separately from the 1-0, 2-1 and 3-2 band for vibrational levels 1, 2 and 3, respectively, indicate that these temperatures are independent of vibrational state, in this case 494°K. The same independence of rotational temperatures of vibrational level is found in all data. By far the simplest explanation of this fact is that the rotational temperatures, at least up to $j'=6$, are in equilibrium with the flow field kinetic temperatures. This fact is not surprising considering the high relaxation rates, especially for low quantum number rotational sublevels. Therefore the first experimental conclusion can be stated as follows:

$$T_{\text{rot}} = T_{\text{kin}} \text{ for } j' \leq 6$$

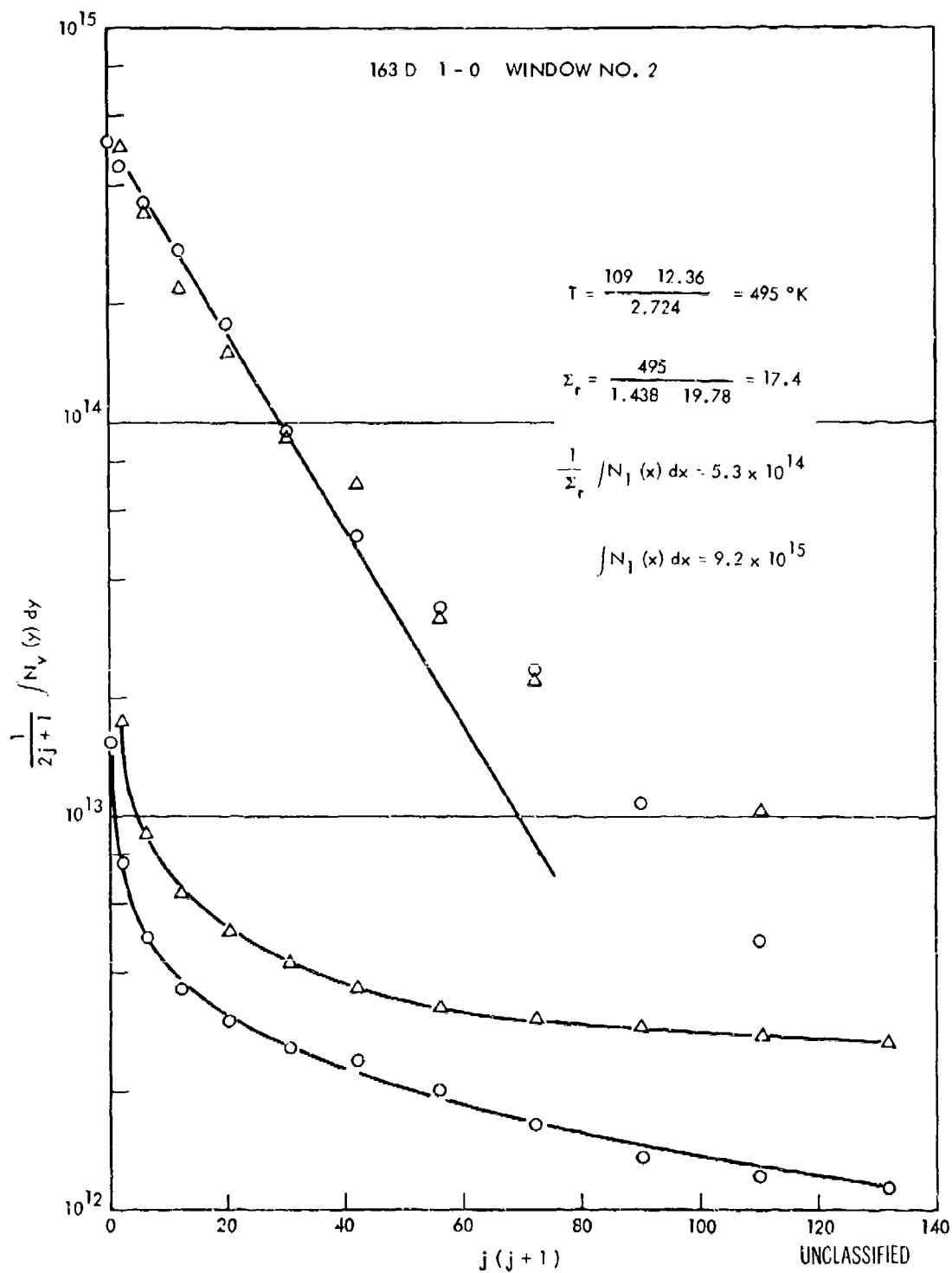


Figure 36. Typical "Boltzman" Plot of Chemiluminescent Data:
Baseline Flow (1-0) (U)

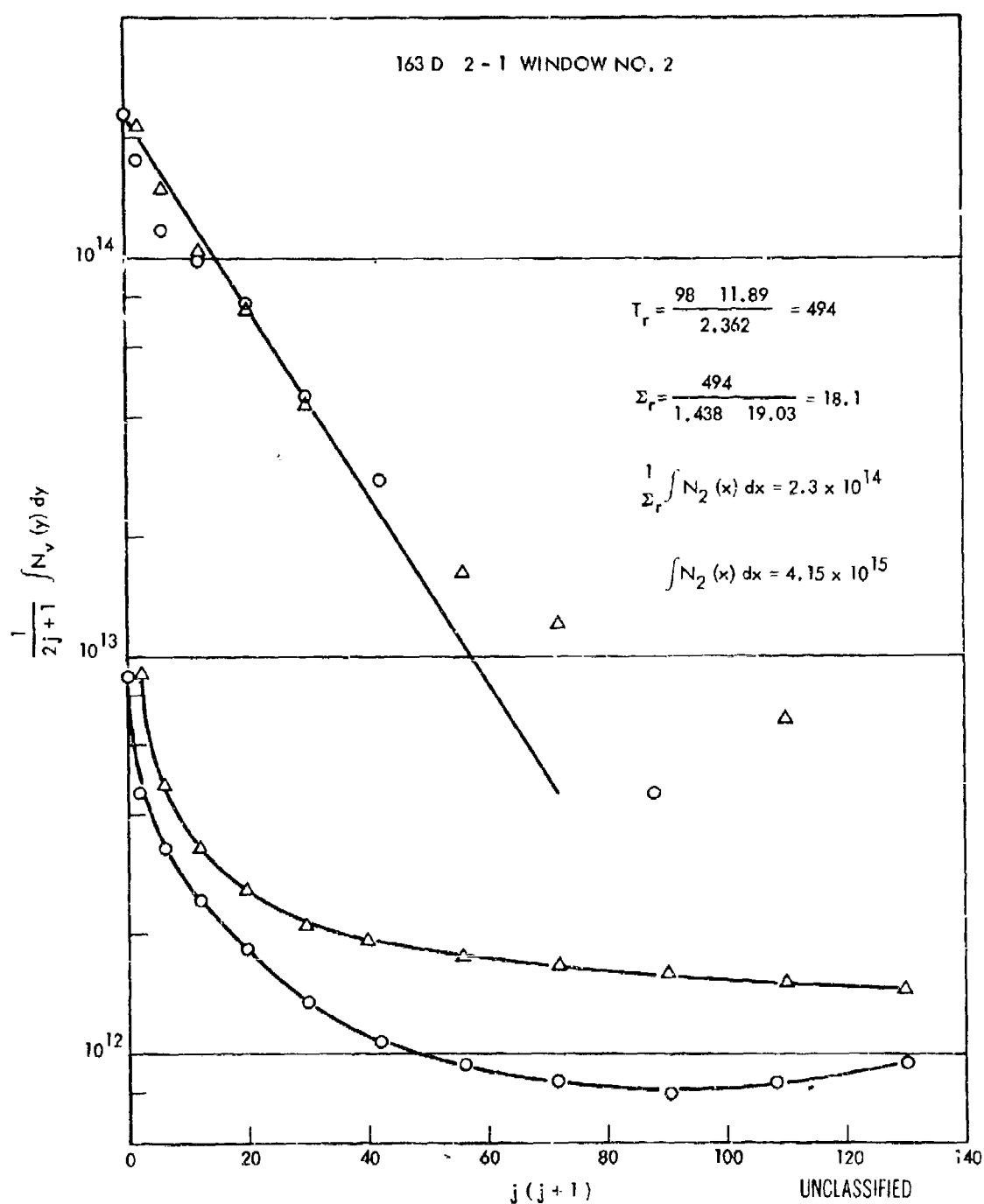


Figure 37. Typical "Boltzman" Plot of Chemiluminescent Data:
Baseline Flow (2-1) (U)

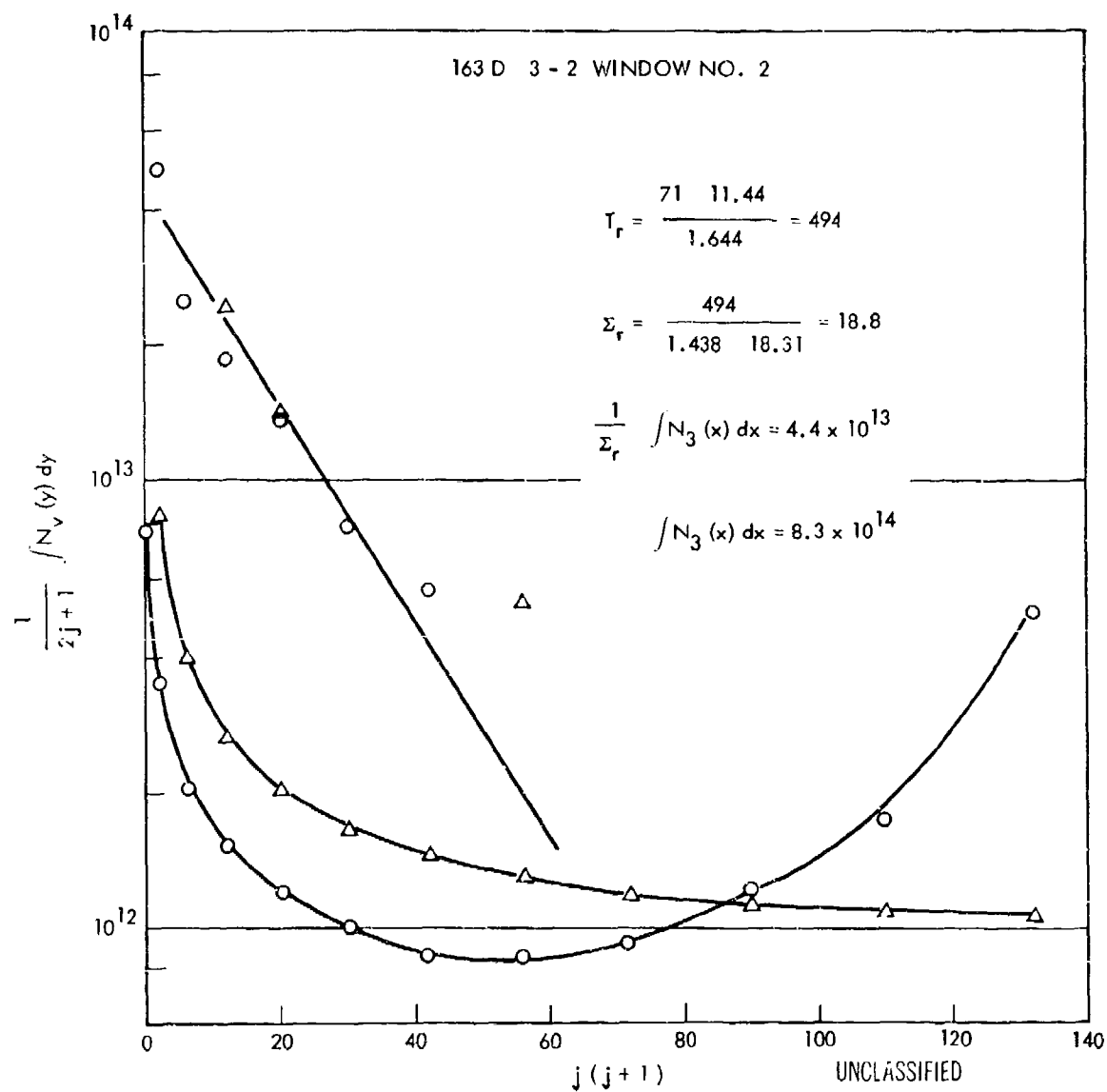


Figure 38. Typical "Boltzman" Plot of Chemiluminescent Data; Baseline Flow (3-2) (U)

(U) We wish to emphasize that our data do not necessarily confirm a Boltzman distribution of rotational sublevels for rotational quantum numbers in excess of $j'=6$. Actually, our data in most cases indicate excessive populations of higher j' levels relative to the Boltzman distributions of the lower j' states. This effect could have several causes: Measured line intensities for the higher j' states are generally low and consequently, the signal/noise is small as compared to the more intense lines associated with $j' \leq 6$ levels. The mechanized data reduction technique tends to read the intensities too high for the low intensity lines by always reading maximum possible line signal voltages. This explanation alone does not always give a satisfactory explanation of the observed effect, however. In some cases, like the one shown in Figure 35 for the 2-1 band, excess intensities appear to be much larger than could be rationalized on the basis of actual signal/noise ratios. It appears, therefore, that there are deviations from Boltzman distributions for larger j' levels, particularly for the lower cavity pressures. Such deviations could be apparent and could be the result of "hot spots" in the field of view of the spectrometer optics. One cannot ignore the possibility, however, that this observed discrepancy is real and is related to the large rotational quantum energy for high rotational sublevels. From principles of molecular motion it is well known that the quantum energy which has to be transferred into kinetic energy when a rotational level relaxes from sublevel j' to $j'-1$ is $2B_v j' \text{ cm}^{-1}$; since $B_v = 19.03 \text{ cm}^{-1}$ for $v'=2$, it follows that $2B_v j' = 266.4 \text{ cm}^{-1}$ for $j'=7$. This corresponds to an energy of kT equivalent to 384°K , whereas the cavity flow field temperature is only 494°K . In other words the rotational quantum energy is comparable to kT and may significantly affect the relaxation rate of the higher j' levels. The latter hypothesis is somewhat supported by a set of chemiluminescent data shown in Figures 39 through 41 representing data from test series 1c where the cavity pressure has been increased from 1.29 to 5.45 torr. In the latter case the deviation of high j' levels is clearly less severe and is satisfactory at least up to levels of $j'=11$. Fortunately, highly excited j' levels are not found to be very important in high energy laser operation and they do not significantly affect the total vibrational state distribution or the flow field total heat content. It is therefore justified, at least at the present state of requirements and sophistication, to ignore high j' levels in our further discussions.

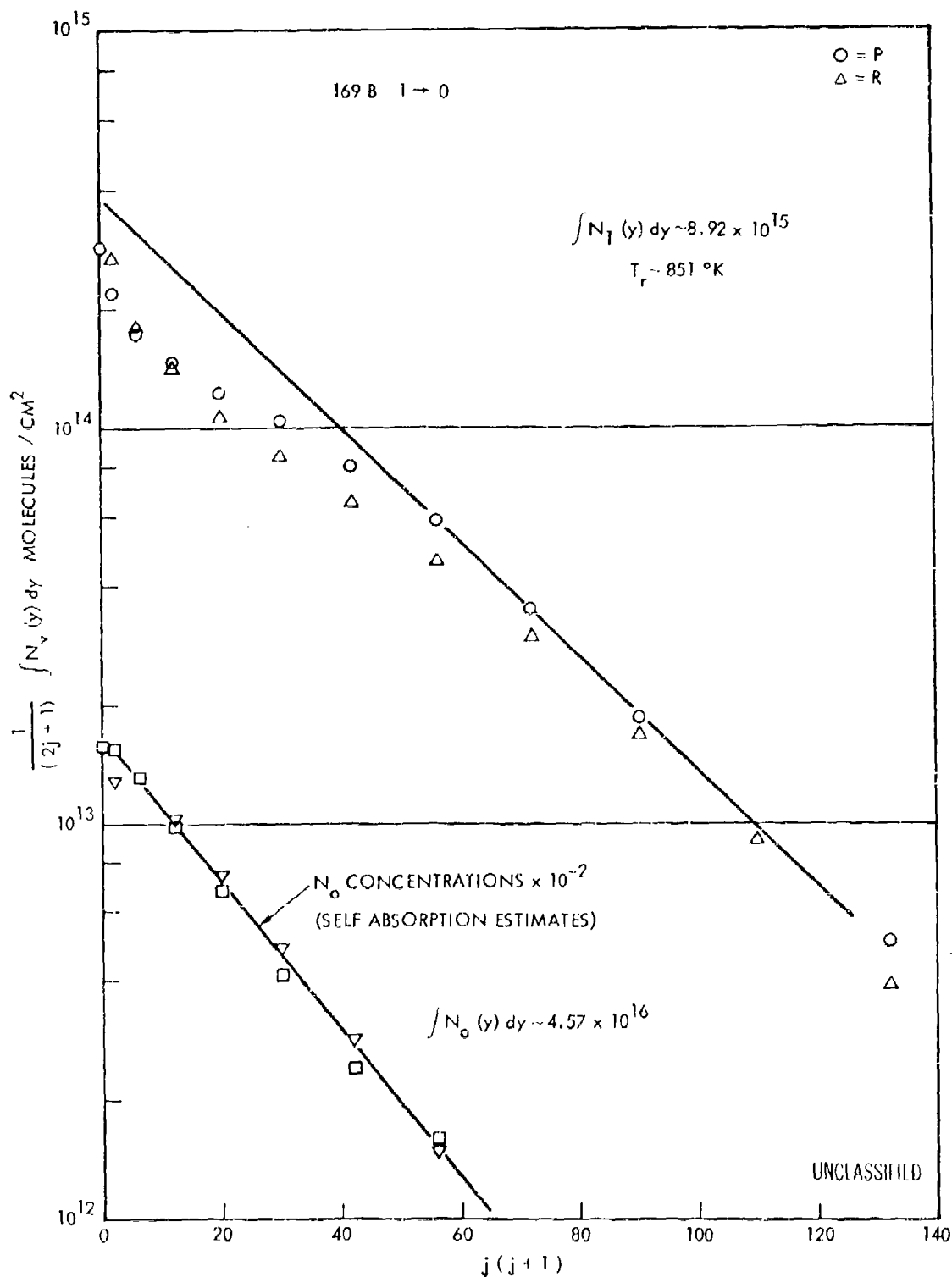


Figure 39. Typical "Boltzman" Plot of Chemiluminescent Data: Increased Cavity Pressure (1-0) (U)

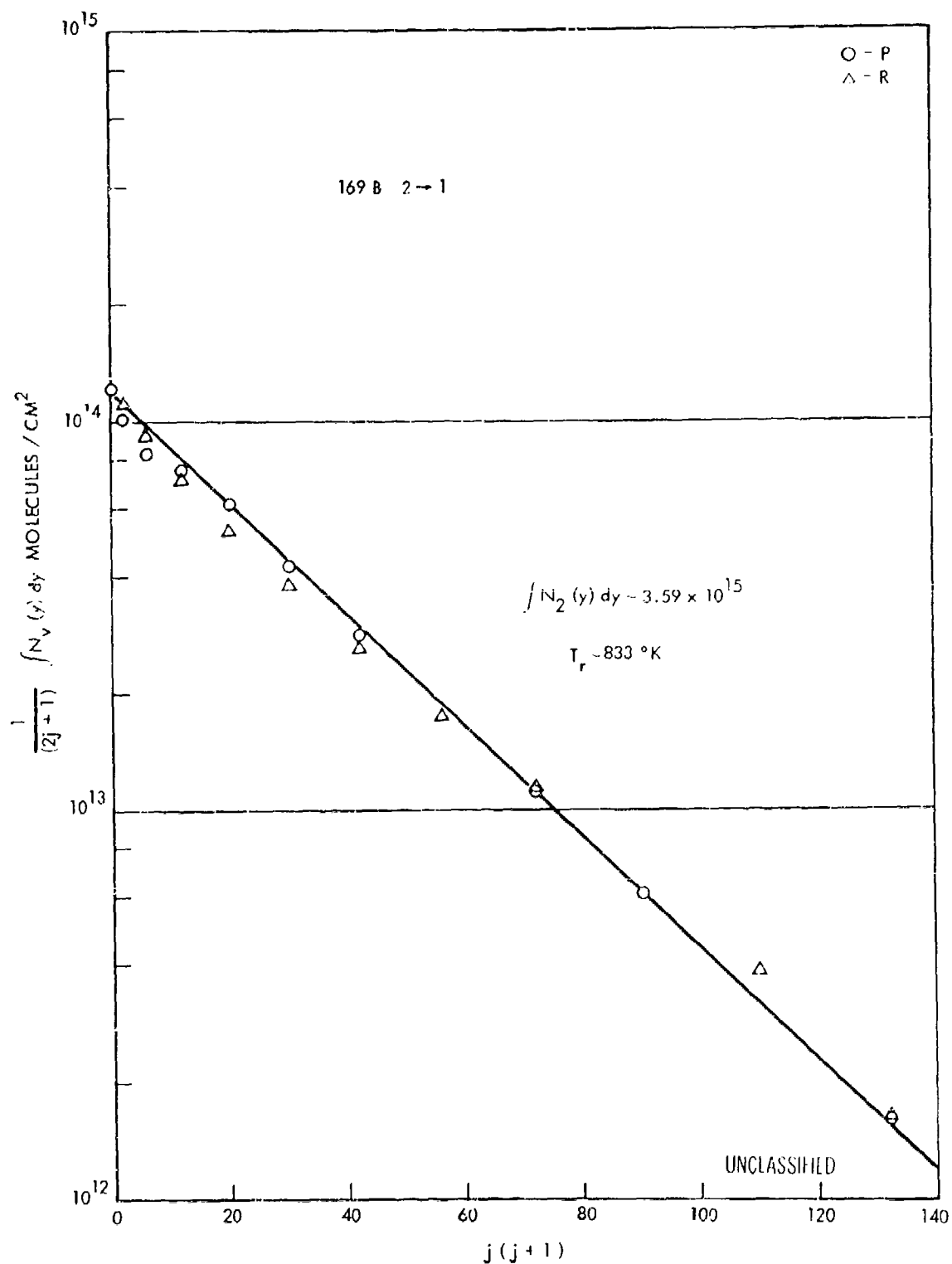


Figure 40. Typical "Boltzman" Plot of Chemiluminescent Data: Increased Cavity Pressure (2-1) (U)

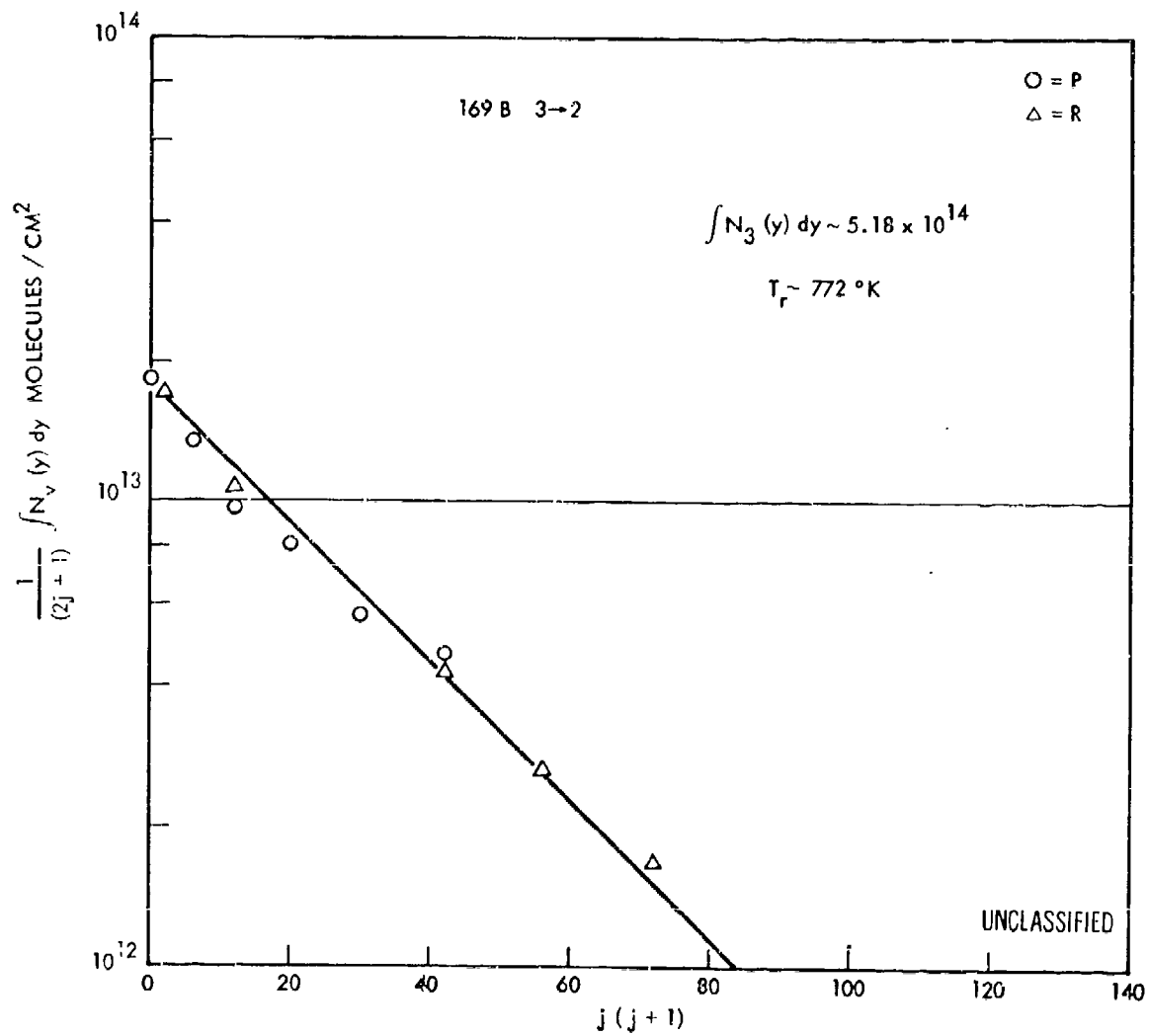


Figure 41. Typical "Boltzman" Plot of Chemiluminescent Data: Increased Cavity Pressure (3-2) (U)

(U) In some of the chemiluminescent data self-absorption effects had to be considered following the data reduction procedures described in Section 4. a(2). Equations (16), (17) and (18), especially, form the basis for reducing these data rather than the simpler Equation (1) which is used for the optically thin case. The representative case of test Ic observed at window 2 located 4.3 cm from the nozzle bank exit will thus be discussed in some detail. Figures 39, 40 and 41 show plots of the apparent vibration-rotation state densities derived from measured line intensities and using Equation (1). Because the observed line intensities are attenuated by self-absorption, an apparent sagging at intermediate j levels is observed. This effect is particularly noticeable in Figure 39, showing the apparent state densities for $v'=1$; a noticeable but less severe effect is also observed for the R-branch lines of the 2-1 transitions plotted in Figure 40. The discrepancies between apparent state densities derived from R-branch lines and P-branch lines, are consistent with expectations for self-absorption. The true Boltzman distribution of rotational sublevels is established by high j -level transitions where self-absorption is negligible. The exponential state density distribution shown in Figure 39 by the upper straight line has been thus established. For intermediate j levels the apparent state density deficiency can now be used to obtain information on the lower level population; for the case of Figure 39 the lower state levels are associated with the vibrational ground state $v''=0$. With each lower state $\{v'', j''\}$ there is a pair of R- and P-branch lines associated, giving two independent measurements for each lower level. The lower straight line in Figure 39 shows the resulting populations for the various j levels of the vibrational ground state. Excellent agreement between the data points reduced from P- and R-branch lines is observed. Furthermore, a very good exponential distribution of vibrational ground state j levels is evident from the graph, although the corresponding temperature is approximately 100°K lower than the average established by the chemiluminescent levels $v=1, 2$ and 3 . This apparently lower temperature of the ground state is presently not understood; it is possible that it is merely a matter of accuracy in establishing the original slope of the upper level distribution.

(U) The importance of HF-ground state population measurements by the self-absorption technique lies primarily in the fact that these latter

(U) data can be compared with ground state population measurements by resonance absorption, described in the next section. Combining both sets of data, information of HF-ground state population outside the jet is obtainable. Unfortunately, reliable self-absorption data on HF-ground state number densities could only be obtained in a few tests. In most tests self-absorption effects were marginal and within the experiment noise. In some tests at the highest cavity pressures self-absorption was so severe that difficulties were encountered with establishing the fine upper level Boltzman distribution because of self-absorption even in the high j-level lines. The cases where HF-ground state population was determined by the self-absorption technique have been listed in Table 6 and measurement results have been recorded. Excellent, reliable data were obtained in the case of test series Ic where the cavity pressure was raised to a value of 5.45 torr from 1.29 torr for the nominal operating condition. In all other cases either no data at all could be obtained or the accuracy of the data was seriously impaired by unfavorable conditions as discussed above.

(U) The primary objective of the chemiluminescent experiment was to establish HF-excited state densities in order to obtain data on laser cavity nonequilibrium excitation. All data obtained thus far have demonstrated that the important j levels are equilibrated to the same temperature, presumably the flow field kinetic gas temperature. With this latter fact firmly established it suffices to measure total vibrational state number density and temperature.

(U) According to Equation (3), total vibrational state number densities can be determined from graphs as shown in Figures 36 through 41 by determining the intersection of the straight line, representing the Boltzman distribution of the rotational sublevels, with the ordinate. Plots of measured vibrational state distributions as function of downstream cavity position X have been plotted for all test conditions in Figures 42 through 48. The same test data have been summarized in convenient form in Table 7. Table 7 and Figures 42 through 48 contain additional data on the HF-ground state population to be discussed in the following section. In Figures 42 through 45 the vibrational state population data plotted have been augmented by information from the IR-scanner experiment, also

Table 6. HF Ground State Densities from Self Absorption (U)

| Test | Cavity Pressure | $\int N_o (y) dy$ Molecules/cm ² | | | Remarks |
|------|--------------------------------|---|-----------------------|-----------------------|--|
| Ib | nominal pressure 1.229 torr | window 1 | window 2 | window 3 | Measurement marginal because of low self- absorption |
| | 2x nominal = 2.73 torr | | 4.7×10^{16} | | |
| Ic | 4x nominal = 5.45 torr | 2.96×10^{16} | 4.57×10^{16} | 5.03×10^{16} | Excellent data |
| | 6x nominal = 8.2 torr | 10.7×10^{16} | 9.3×10^{16} | 9.2×10^{16} | |
| Id | | | | | Low accuracy because of too high self-absorption |

UNCLASSIFIED

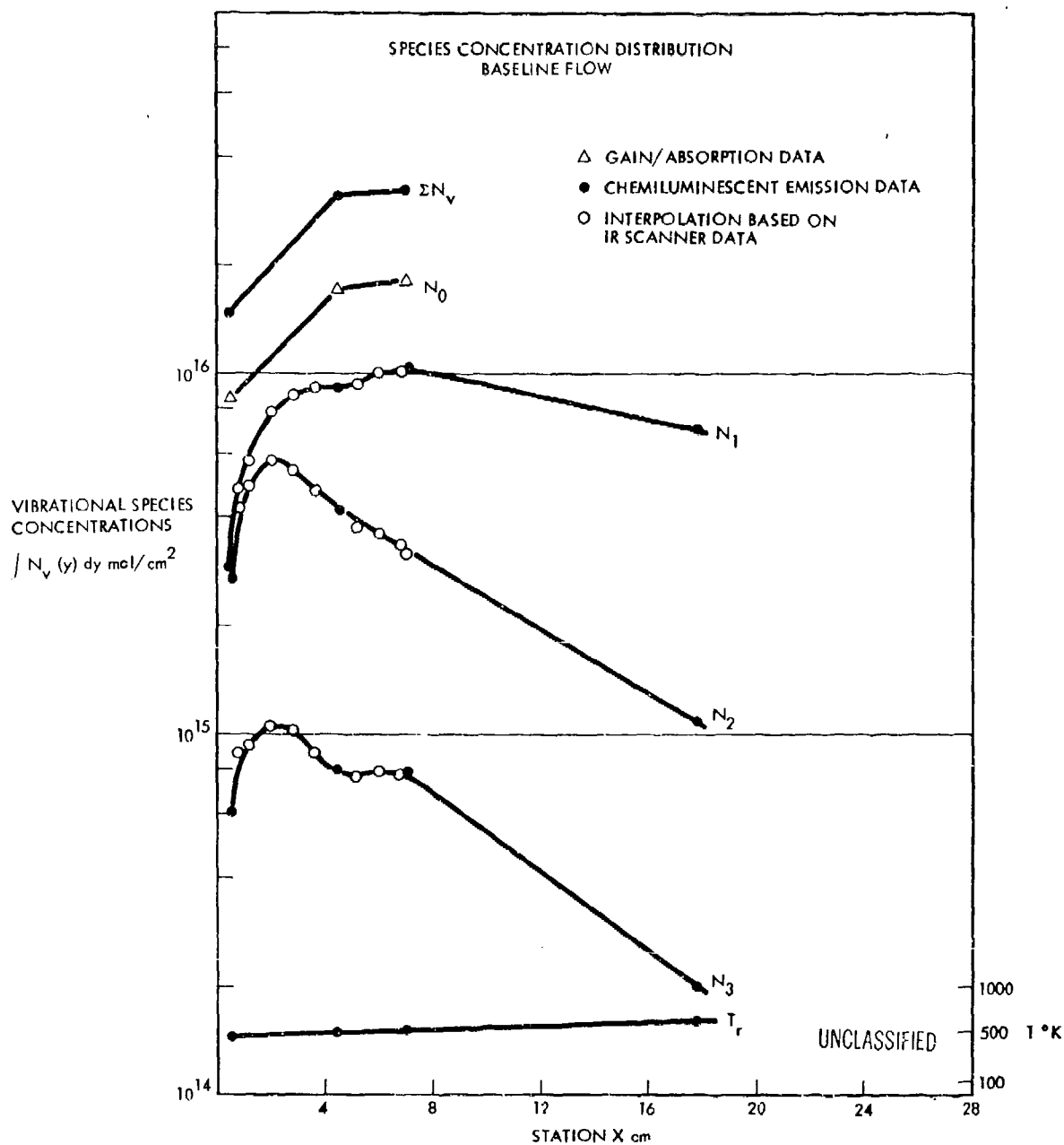


Figure 42. Vibrational State Distribution vs Laser Cavity Station X: Baseline Flow (U)

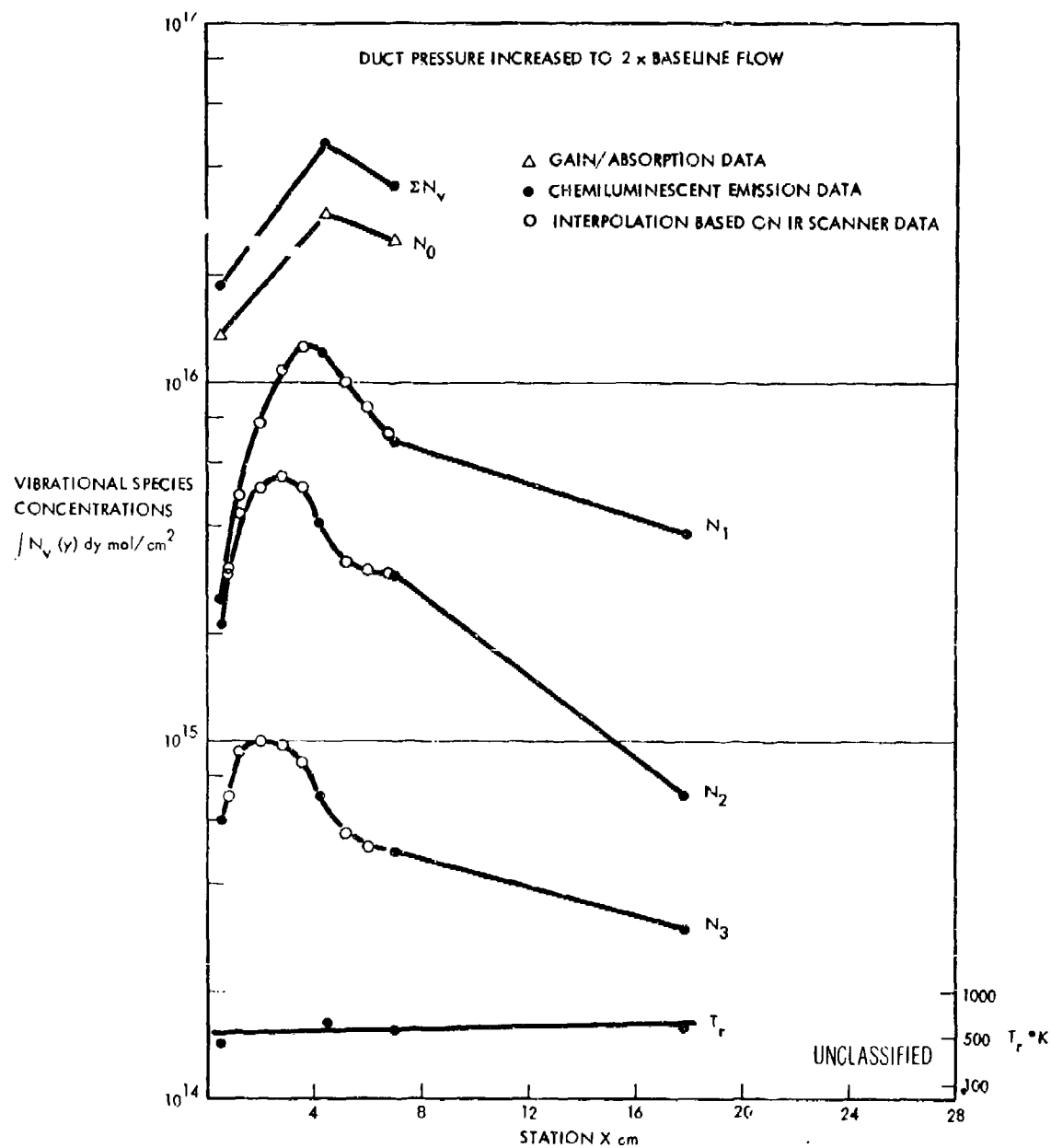


Figure 43. Vibrational State Distribution vs Laser Cavity
 Station X: Duct Pressure $\times 2$ (U)

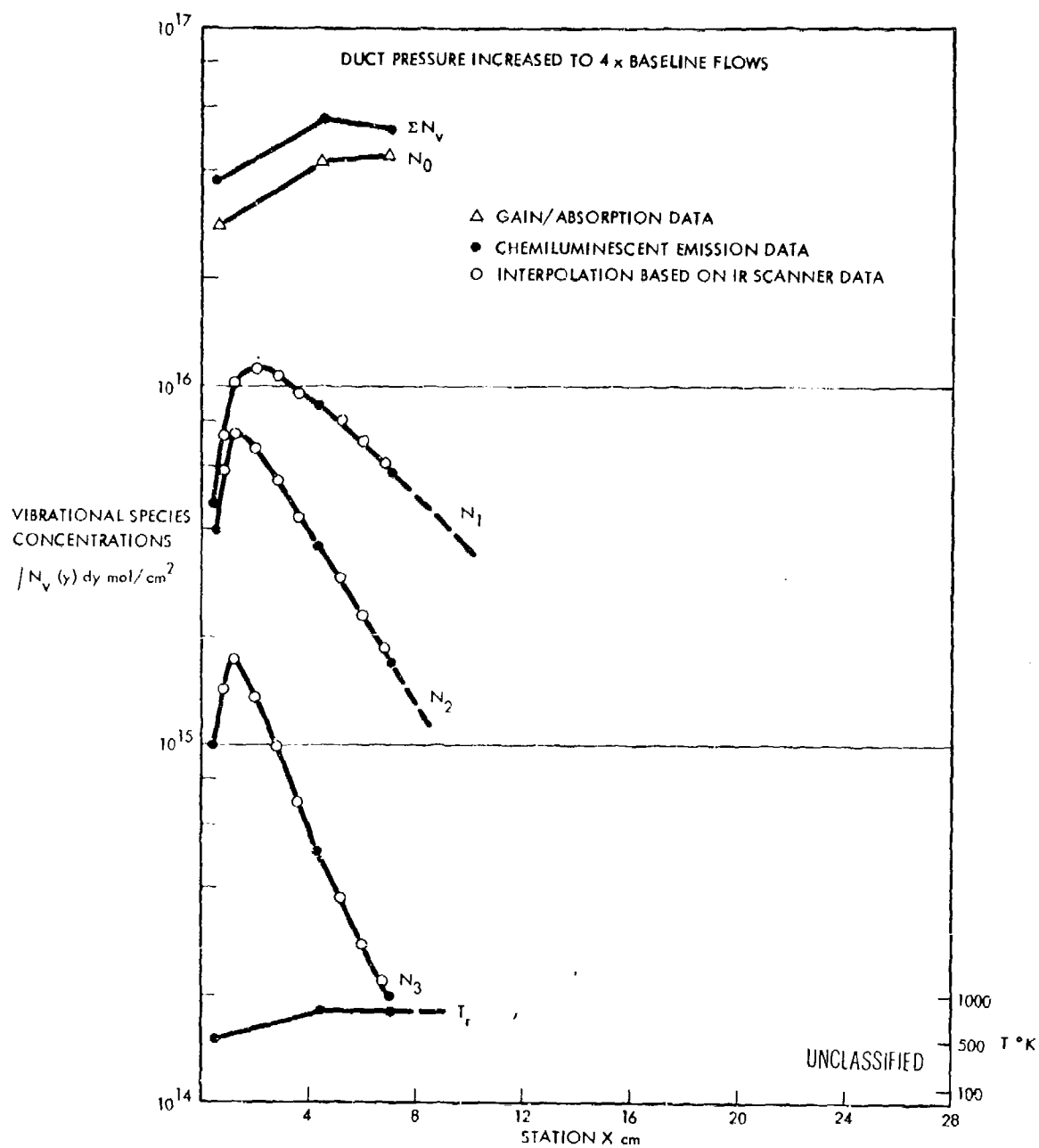


Figure 44. Vibrational State Distribution vs Laser Cavity
 Station X: Duct Pressure x 4 (U)

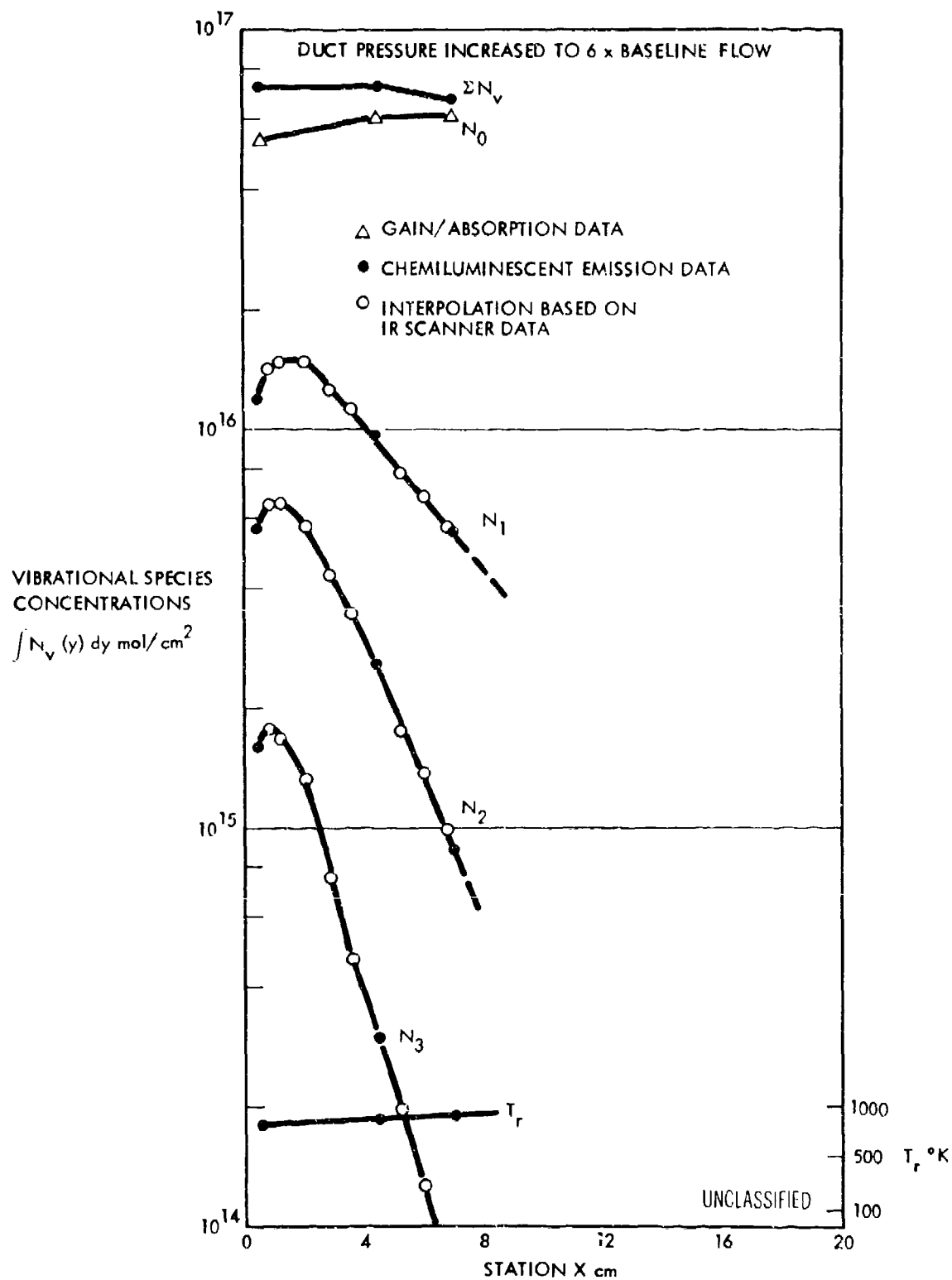


Figure 45. Vibrational State Distribution vs Laser Cavity Station X: Duct Pressure $\times 6$ (U)

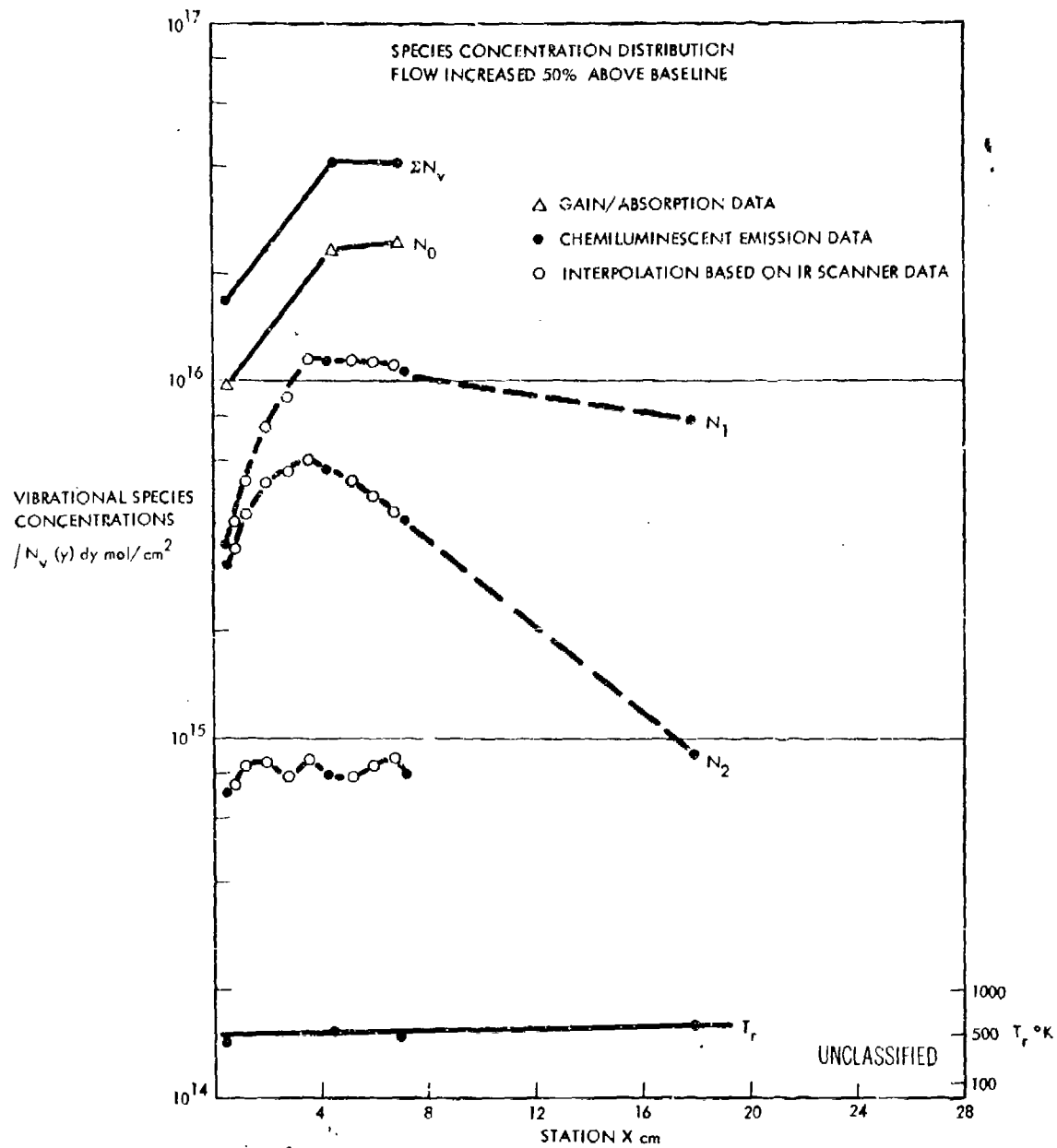


Figure 46. Vibrational State Distribution vs Laser Cavity Station X: Flow Increased 50% (U)

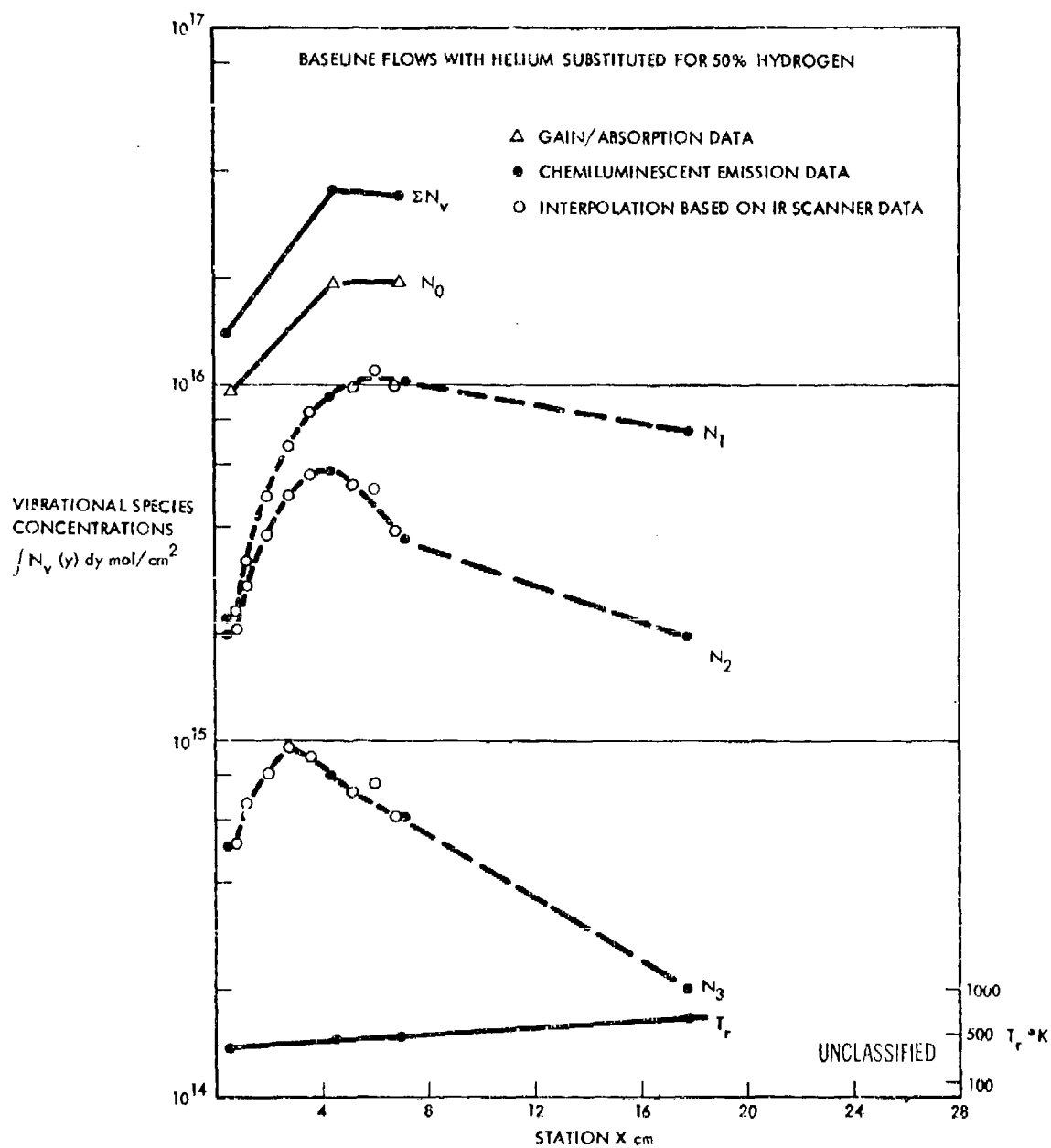


Figure 47. Vibrational State Distribution vs Laser Cavity Station X: Helium Substitution (U)

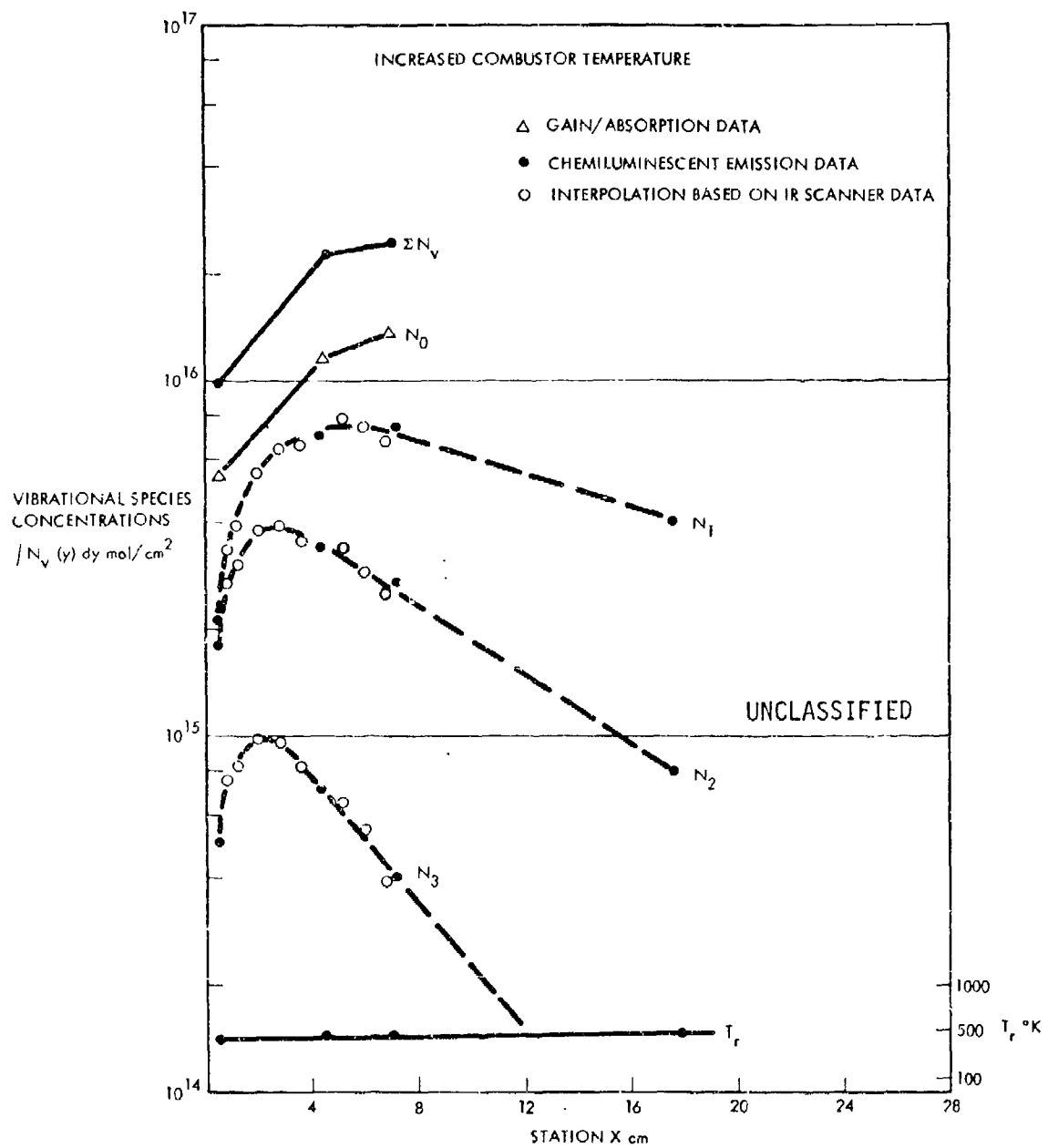


Figure 48. Vibrational State Distribution vs Laser Cavity Station X: Increased Combustor Temperature (U)

(U) discussed later. Flow field temperatures determined by equating the latter to measure rotational temperatures have been reported in the figures and in Table 7.

(U) In many respects the measured ratios of HF vibrational state population relative to the total HF-population are more instructive than the absolute excited state densities. These ratios, which follow directly from the measurements, have been included in Table 7 and in Figure 49.

b. Resonance Absorption/Gain Experiment Results

(U) The principal purpose of the resonance absorption/gain experiment has been to determine HF-vibrational ground state densities not generally accessible by chemiluminescent data. The experimental apparatus, the measurements approach, and the reduction technique of the observables to values of line-of-sight integrated HF-ground state number densities have been fully discussed in Section 4.c. The basic equations used to reduce resonance absorption/gain apparatus observables are Equations (40), (41) and (15). Measurements were conducted using P-branch lines P_3 , P_5 and P_7 of the 1-0 transition. At least two independent measurements using two lines were conducted for each case and in some cases three lines were used. The consistency of the data has generally been found to be excellent. In some cases further comparison has been possible with HF-ground state measurements using the self-absorption technique discussed in Sections 4.c and 6.a.

(U) A typical data recording format obtained from the gain experiment is illustrated in Figures 50 and 51. The upper trace shows the probing beam signal as a function of time, and the lower trace is the corresponding reference beam signal. For each experiment run the HF burner was operated continuously while the laser cavity flow system was activated and each target test flow condition was established. The various flow conditions established for each experiment are noted in the lower trace and the signal levels V_o , V_a and V_b used in the data reduction are indicated on the upper trace.

(U) V_o corresponds to the unattenuated probe beam signal observed before and after the cavity flow condition is activated. V_a and V_b indicate a range of signal levels observed during the cavity flow

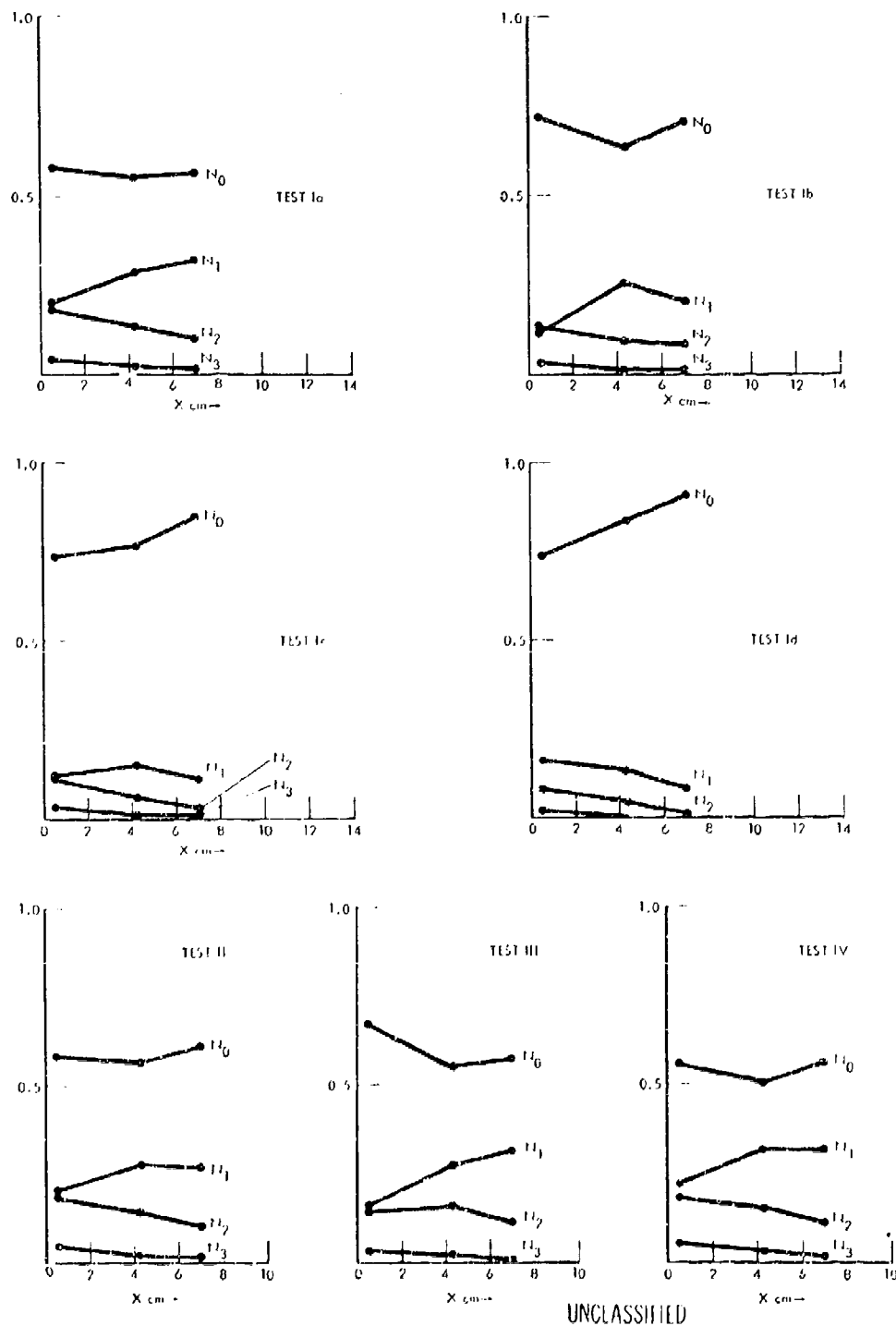


Figure 49. Vibrational State Distribution Ratios $\frac{\int N_v(y)dy}{\sum_v \int N_v(y)dy}$ (U)

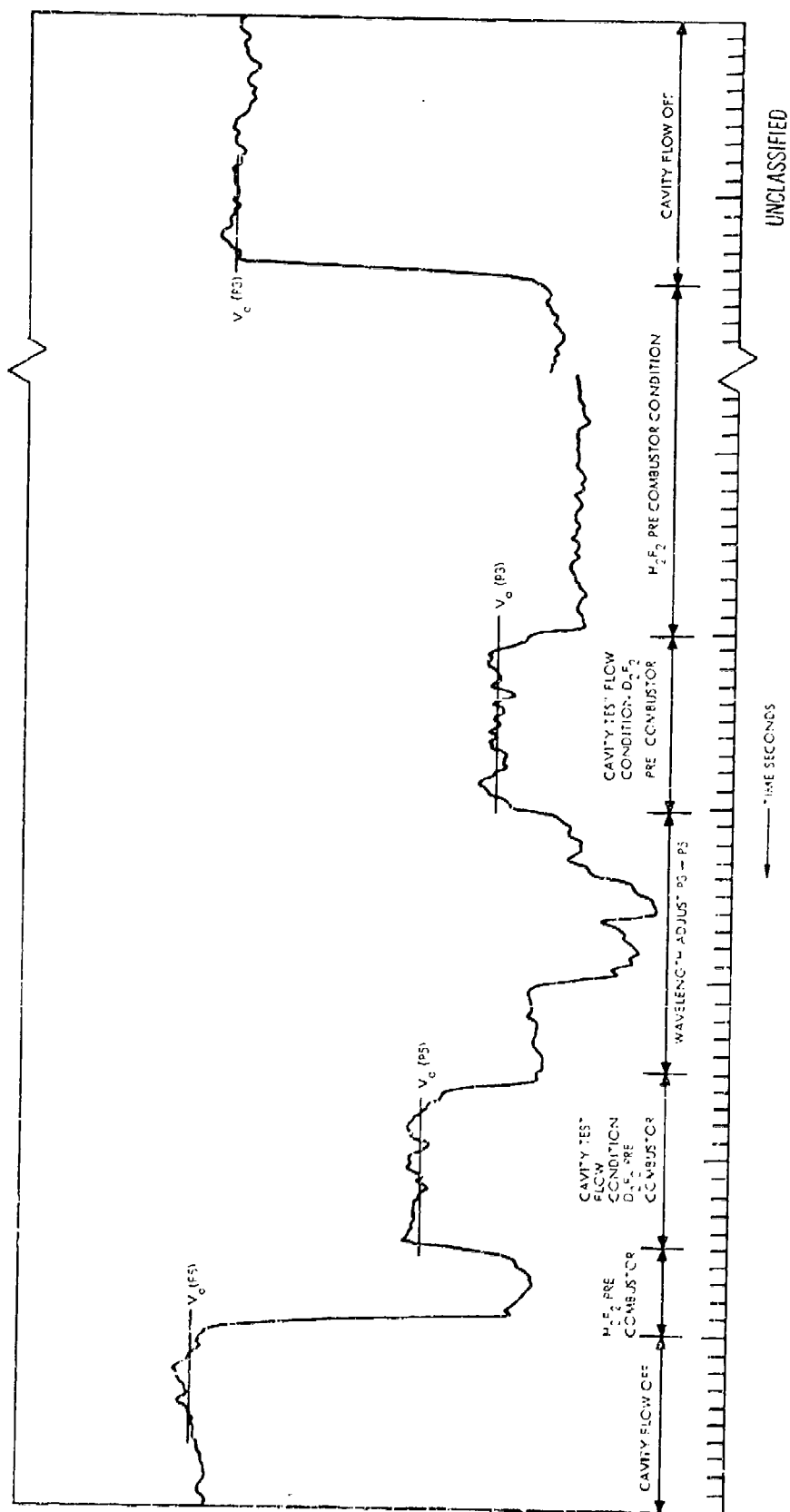


Figure 50. Typical Absorption/Gain Experimental Data: Attenuation for (1-0) P3, P5 Spectral Lines (U)

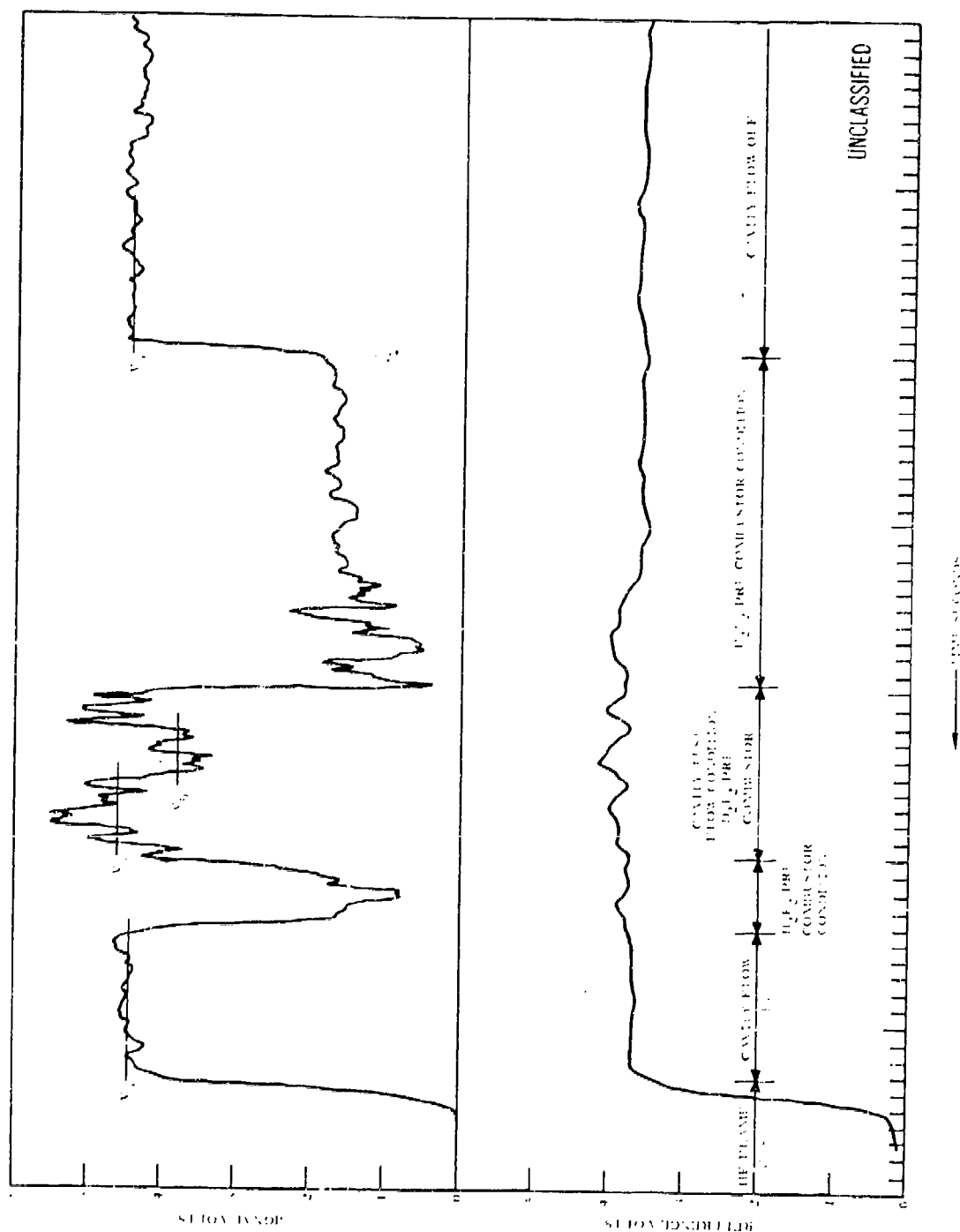


Figure 51. Typical Absorption/Gain Experimental Data: Attenuation Gain Factors (U)

(U) experiment with HF lasing conditions. The variations in these signal levels will be discussed further below, but in general it is observed that a net gain or absorption is indicated by the ratios V_a/V_o , V_b/V_o . The reference beam signal, and hence the source intensity, is found to be sensibly constant during the experiment so no correction has been applied in the preliminary data reduction.

(U) As has been discussed in Section 4. c, the attenuation factor $\psi = V_a/V_o$ leads directly to values of the centerline coefficient $(\overline{k_o y})$ and ground state species concentrations $\int N_o(y)dy$. Table 8 gives the results for each of the experimental conditions measured. The data for the P_3 and P_5 lines were computed independently so that the agreement obtained in the computed ground state populations from these two independent measurements is an indication of the good experimental precision obtained.

(U) In practically all of the experimental runs the probe beam signals show considerable variations during cavity flow conditions. Where these variations are significant (as in Figure 51) two values V_a and V_b have been used in the data reduction and the corresponding ground state concentrations are given in the Table 8. In general 10 to 20% variations are obtained in the final results.

(U) The observed variations in both the probe and reference beam signals appear to be caused by true fluctuations in the cavity concentrations and not simply noise in the HF burner system. This has been illustrated in Figure 52, which shows the experimental data for a similar cavity flow condition but with operation as a DF laser. In the absence of hydrogen injection into the cavity we observe essentially constant values in both the probe and reference beam signals. The absorption which is observed results from the HF generated at the precombustor in this experiment.

(U) The observed cavity attenuation variations are likely to be explained by variations in the concentration differences between lower and upper states and hence in the observed attenuation. Observed reference signal variations are likely to have been caused by variations in the upper ($v=1$) level concentrations alone with consequent modulation of the laser cavity HF emission intensities. Reference beam variations were found not to severely degrade the measurement accuracy. The

Table 8. HF Ground State Densities from Gain/Absorption Experiment (U)

| Test designation | Test No. | Measured Attenuation $\epsilon = \frac{I}{I_0}$ | Centerline opacity $(K_c \gamma)$ | Differential State Densities $-\int \frac{N_{ij}(\gamma) d\gamma}{2j' + 1} \times 10^{-14} \frac{\text{mol}}{\text{cm}^2}$ | Upper State Densities* $\int \frac{N_{ij}(\gamma) d\gamma}{2j' + 1} \times 10^{-14} \frac{\text{mol}}{\text{cm}^2}$ | Ground State Densities $\int \frac{N_{ij}(\gamma) d\gamma}{2j' + 1} \times 10^{-14} \frac{\text{mol}}{\text{cm}^2}$ | Total Ground State Densities* $\int H_0(\gamma) d\gamma \times 10^{-16} \frac{\text{mol}}{\text{cm}^2}$ |
|------------------|--------------------|--|---|--|---|---|---|
| 1a | A-1-P ₃ | 0.738 | 0.59 | 1.50 | 1.22 | 2.72 | 0.91 |
| | A-1-P ₅ | 0.912 | 0.16 | 0.22 | 0.51 | 0.73 | 0.81 |
| | A-2-P ₃ | 0.734-0.807 | 0.57-0.38 | 1.52 - 1.03 | 3.75 | 5.27 - 4.78 | 1.81 - 1.64 |
| | A-2-P ₅ | 0.940-1.036 | 0.10-(-0.09) | 0.15 - (-0.13) | 1.68 | 1.83 - 1.55 | 1.84 - 1.55 |
| | A-2-P ₇ | 1.137 | (-0.150) | (-0.14) | 0.48 | 0.34 | 1.62 |
| | A-3-P ₃ | 0.871 | 0.24 | 0.64 | 4.15 | 4.79 | 1.66 |
| 1b | A-3-P ₅ | 0.943 | 0.10 | 0.14 | 1.86 | 2.00 | 1.96 |
| | 205F-2 | 0.519 | 1.45 | 3.60 | 0.90 | 4.50 | 1.49 |
| | 205F-1 | 0.763 | 0.52 | 0.69 | 0.36 | 1.50 | 1.21 |
| | 207H-1 | 0.435 | 1.50 | 4.52 | 3.30 | 7.82 | 2.93 |
| | 207H-2 | 0.743 | 0.43 | 0.80 | 2.23 | 3.03 | 2.64 |
| | 208F-1 | 0.417 | 1.75 | 4.96 | 2.60 | 7.56 | 2.69 |
| 1c | A-3-P ₅ | 0.646 | 0.80 | 1.23 | 1.26 | 2.49 | 2.31 |
| | 205G-1 | 0.370 | 2.20 | 6.00 | 1.85 | 7.85 | 2.72 |
| | 205G-2 | 0.500 | 1.40 | 2.07 | 0.83 | 2.90 | 2.83 |
| | 207I-2 | 0.318 | 1.95 | 6.66 | 3.13 | 9.79 | 4.15 |
| | 207I-1 | 0.33 | 1.85 | 3.43 | 1.95 | 5.38 | 4.41 |
| | 208G-2 | 0.240 | 2.65 | 9.03 | 2.14 | 11.17 | 4.72 |
| | A-3-P ₅ | 0.311 | 2.05 | 3.79 | 1.30 | 5.09 | 4.17 |
| | 208G-1 | | | | | | UNCLASSIFIED |

Table 8. HF Ground State Densities from Gain/Absorption Experiment (U) (Continued)

| Test designation | Test No. | Measured Attenuation $\alpha = \frac{1}{L_0}$ | Centerline opacity $(k_0 y)$ | Differential State Densities $\int \frac{N_2(v)}{2\sqrt{\pi}} dv \times 10^{-10} \frac{\text{mol}}{\text{cm}^2} \times 10^{-10} \frac{\text{mol}}{\text{cm}^2} \times 10^{-10} \frac{\text{mol}}{\text{cm}^2}$ | Upper State Densities* $\int \frac{N_2(v)}{2\sqrt{\pi}} dv \times 10^{-10} \frac{\text{mol}}{\text{cm}^2} \times 10^{-10} \frac{\text{mol}}{\text{cm}^2} \times 10^{-10} \frac{\text{mol}}{\text{cm}^2}$ | Ground State Densities $\int \frac{N_1(v)}{2\sqrt{\pi}} dv \times 10^{-10} \frac{\text{mol}}{\text{cm}^2} \times 10^{-10} \frac{\text{mol}}{\text{cm}^2} \times 10^{-10} \frac{\text{mol}}{\text{cm}^2}$ | Total Ground State Densities* $\int_0^\infty N_1(v) dv \times 10^{-10} \frac{\text{mol}}{\text{cm}^2}$ |
|--|----------|--|------------------------------------|--|--|--|--|
| Ia A-1-P ₃ A-1-P ₃ A-2-P ₃ A-2-P ₃ A-3-P ₃ A-3-P ₃ | 206H-1 | 0.270 | 2.27 | 7.83 | 3.30 | 11.10 | 4.71 |
| | 206H-2 | 0.303 | 7.73 | 5.11 | 2.09 | 7.10 | 5.95 |
| | 207J-1 | 0.151 | 3.80 | 13.22 | 2.63 | 15.85 | 6.66 |
| | 207G-2 | 0.247 | 2.00 | 4.72 | 1.61 | 6.33 | 5.21 |
| | 208H-1 | 0.101 | 3.60 | 13.23 | 1.41 | 14.63 | 6.76 |
| | 208H-2 | 0.143 | 2.90 | 5.79 | 0.93 | 6.72 | 5.49 |
| Ii A-1-P ₃ A-1-P ₃ A-2-F ₃ A-2-P ₃ A-3-P ₃ A-3-P ₃ | 206b | 0.730 | 0.59 | 1.49 | 1.03 | 3.02 | 1.01 |
| | 206A | 0.507 | 0.17 | 0.23 | 0.01 | 0.84 | 0.94 |
| | 2070 | 0.643 | 0.81 | 2.28 | 4.26 | 6.53 | 2.32 |
| | 207C | 0.854-1.034 | 0.27-(-0.055) | 0.21 - (-0.081) | 2.13 | 2.50 + 2.05 | 2.37 + 1.91 |
| | 208A | 0.642 | 0.85 | 2.23 | 4.46 | 6.60 | 2.27 |
| | 208B | 0.772 | 0.47 | 0.67 | 1.90 | 2.62 | 2.68 |
| Iii A-1-P ₃ A-1-P ₃ A-2-P ₃ A-2-F ₃ A-3-P ₃ A-3-P ₃ | 2060-2 | 0.712 | 0.73 | 1.66 | 1.06 | 2.72 | 0.88 |
| | 2060-1 | 0.873 | 0.27 | 0.33 | 0.36 | 0.69 | 0.99 |
| | 207E-1 | 0.727 | 0.02 | 1.00 | 4.10 | 5.70 | 1.32 |
| | 207F-2 | 0.936-1.034 | 0.11-(-0.05) | 0.10 - (-0.07) | 1.68 | 1.83 + 1.61 | 1.94 + 1.71 |
| | 2080-1 | 0.827 | 0.34 | 0.87 | 4.45 | 5.32 | 1.80 |
| | 2080-2 | 0.967 | 0.05 | 0.07 | 1.90 | 1.97 | 2.07 |
| UNCLASSIFIED | | | | | | | |

Table 8. HF Ground State Densities from Gain/Absorption Experiment (U) (Continued)

| Test designation | Test no. | Measured Attenuation $\epsilon = \frac{I}{I_0}$ | Centerline opacity $(K_0 \bar{y})$ | Differential State Densities $\int \frac{I_{ij}(y)}{2j'+1} dy \times 10^{-14} \frac{\text{mol}}{\text{cm}^2}$ | Upper State Densities* $\int \frac{I_{ij}(y)}{2j'+1} dy \times 10^{-14} \frac{\text{mol}}{\text{cm}^2}$ | Ground State Densities $\int \frac{I_{oj}(y)}{2j'+1} dy \times 10^{-14} \frac{\text{mol}}{\text{cm}^2}$ | Total Ground State Densities* $\int I_0(y) dy \times 10^{-16} \frac{\text{mol}}{\text{cm}^2}$ |
|-----------------------|----------|--|---------------------------------------|--|--|--|--|
| IV A-1-P _J | 205E-1 | 0.881 | 0.23 | 0.56 | 0.95 | 1.51 | 0.50 |
| A-1-P _J | 205E-2 | 0.947 | 0.09 | 0.12 | 0.37 | 0.49 | 0.58 |
| A-2-P _J | 207G-2 | 0.875 | 0.24 | 0.61 | 2.94 | 3.55 | 1.13 |
| A-2-P _J | 207G-1 | 1.093 | (-0.17) | (-0.23) | 1.27 | 1.04 | 1.13 |
| A-3-P _J | 208E-2 | 0.862 | 0.27 | 0.63 | 3.35 | 4.04 | 1.35 |
| A-3-P _J | 208E-1 | 1.033 | (-0.05) | (-0.07) | 1.34 | 1.27 | 1.39 |
| | | | | | | | UNCLASSIFIED |

*upper state densities and effective Boltzman temperatures obtained from chemiluminescence data.

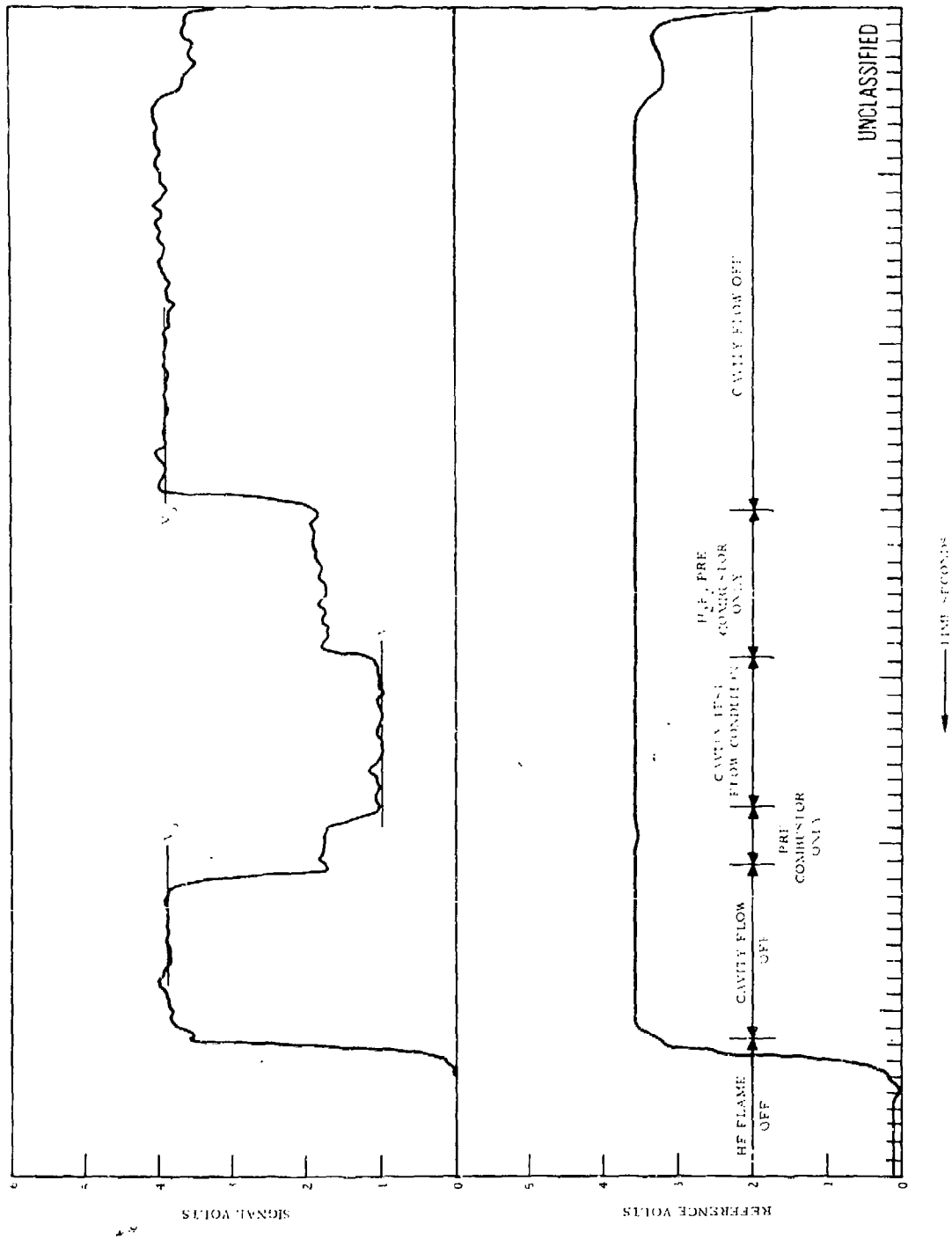


Figure 52. Absorption/Gain Experimental Data for DF Laser Condition (U)

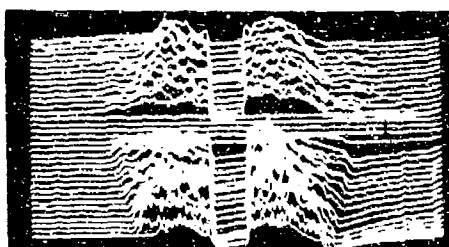
(U) probe beam and reference beam channels will see that frequency component of the cavity signal fluctuations which correspond to the respective experimental modulation frequencies in these two channels. The experimental data leads to the conclusion that the local species concentrations exhibit 10 to 20% variation or more under the conditions of the gain experiment. We believe this to be a most important experimental fact which will be discussed later.

c. Infrared Scanner Experimental Results

(U) The prime purpose of the Infrared Scanner Experiment has been to provide high spatial resolution chemiluminescent diagnostic coverage of the entire laser cavity flow field. These data were intended to be interpreted in conjunction with the detailed chemiluminescent investigations described in Sections 4. a and 6. a. The actual experimental results have fully satisfied these expectations and have in addition provided data which go considerably beyond the original objectives. In spite of the automatic data processing techniques used to process IR-scanner output, much of the data still awaits detailed analysis because of the large amount of information and because automated data reduction techniques were aimed solely at the original objectives. A further problem is that the automated data display programs still suffer from a sweep start signal uncertainty of several resolution elements. This latter problem prevented us from producing intelligible intensity contour maps. The perspective displays are much less sensitive to this problem and, therefore, yielded most useful infrared flow field intensity displays.

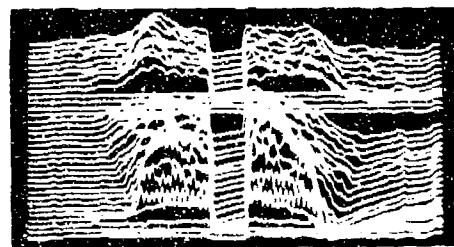
(U) The infrared scanner apparatus and data reduction procedures have been discussed in Section 4. b and the computerized data display programs have been described in Section 4. d.

(U) Sample oscillographs of real time amplitude modulated IR-scanner outputs are shown in Figures 53 and 54. These data are suited for on-spot analysis of overall laser cavity excitation and flow field structure. Only data obtained with the IR-scanner operating in the high resolution mode are shown. Data from the low resolution mode are of lesser quality because of the lower resolution and have been disregarded, therefore, in the experimental results analysis. The low resolution mode was initially used only because the cavity signal



$$\begin{array}{ll} p_c \sim 13.5 \text{ psia} & \frac{p_c}{p_L} \sim 500 \\ p_L \sim 1.4 \text{ torr} & \end{array}$$

Increased Combustion
Temperature



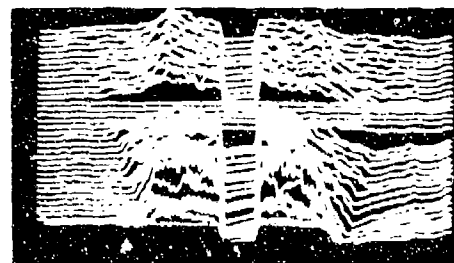
$$\begin{array}{ll} p_c \sim 12 \text{ psia} & \frac{p_c}{p_L} \sim 430 \\ p_L \sim 1.45 \text{ torr} & \end{array}$$

Helium Substitution for
50% H₂



$$\begin{array}{ll} p_c \sim 12 \text{ psia} & \frac{p_c}{p_L} \sim 440 \\ p_L \sim 1.4 \text{ torr} & \end{array}$$

Nominal Baseline Flow

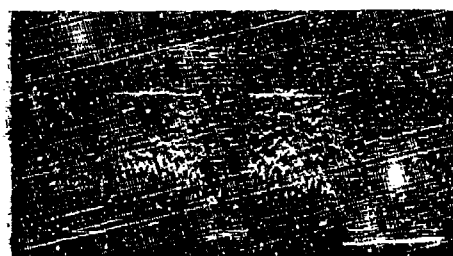
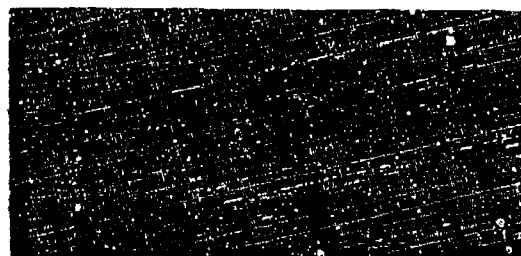
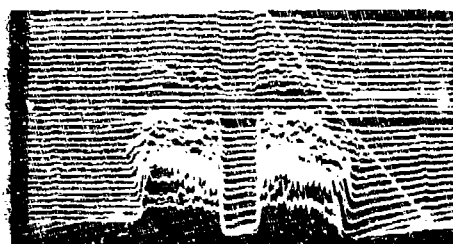
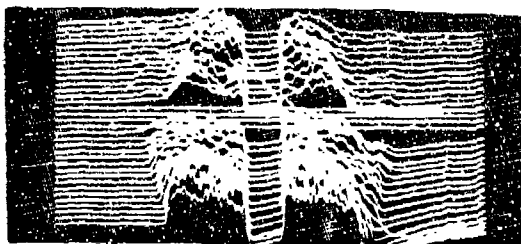


$$\begin{array}{ll} p_c \sim 19.3 \text{ psia} & \frac{p_c}{p_L} \sim 500 \\ p_L \sim 2.0 \text{ torr} & \end{array}$$

50% Increase Above Nominal

UNCLASSIFIED

Figure 53. IR Scanner: Oscilloscope Real Time Data Display:
Test Flow Conditions I - IV (U)

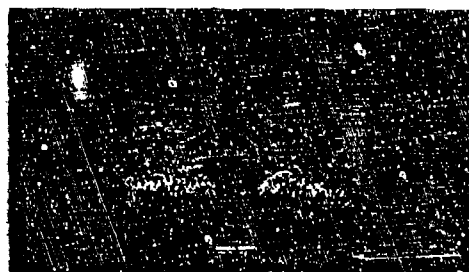
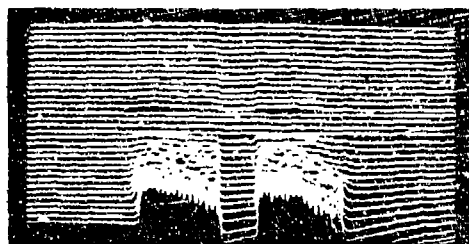


$p_c \sim 12 \text{ psia}$
 $p_L \sim 2.84 \text{ torr}$ $\frac{p_c}{p_L} \sim 218$

Cavity Pressure Increased 2X
 Nominal

$p_c \sim 12 \text{ psia}$
 $p_L \sim 5.5 \text{ torr}$ $\frac{p_c}{p_L} \sim 113$

Cavity Pressure Increased 4X
 Nominal



$p_c \sim 12 \text{ psia}$
 $p_L \sim 8.2 \text{ torr}$ $\frac{p_c}{p_L} \sim 75$

Cavity Pressure Increased 6X Nominal

UNCLASSIFIED

Figure 54. IR Scanner: Oscilloscope Real Time Data Display:
 Test Flow Conditions I - IV (U)

(U) strengths and noise were not well established. Experimental results clearly indicated very satisfactory signal/noise for the high resolution mode. The same data that have been shown in real time in Figures 53 and 54 were stored on tape and plotted by a computer and are displayed in Figures 55 through 61. The perspective plots have been generated by plotting each successive trace, offset in both the horizontal and vertical direction. For the chosen sequence of plotting the viewer appears to be looking in the direction of cavity flow. The observed scene is the cavity viewed through four large quartz windows supported by a metal frame. The cross-shaped feature observed in all displays is part of the window supporting frame. Complementary displays, not shown here, have been made where the plots are displayed as if the viewer is looking upstream. The latter display method is favored for viewing details of the downstream flow field. The front view of the flow field as shown is particularly suited for viewing the structure near the exit nozzles.

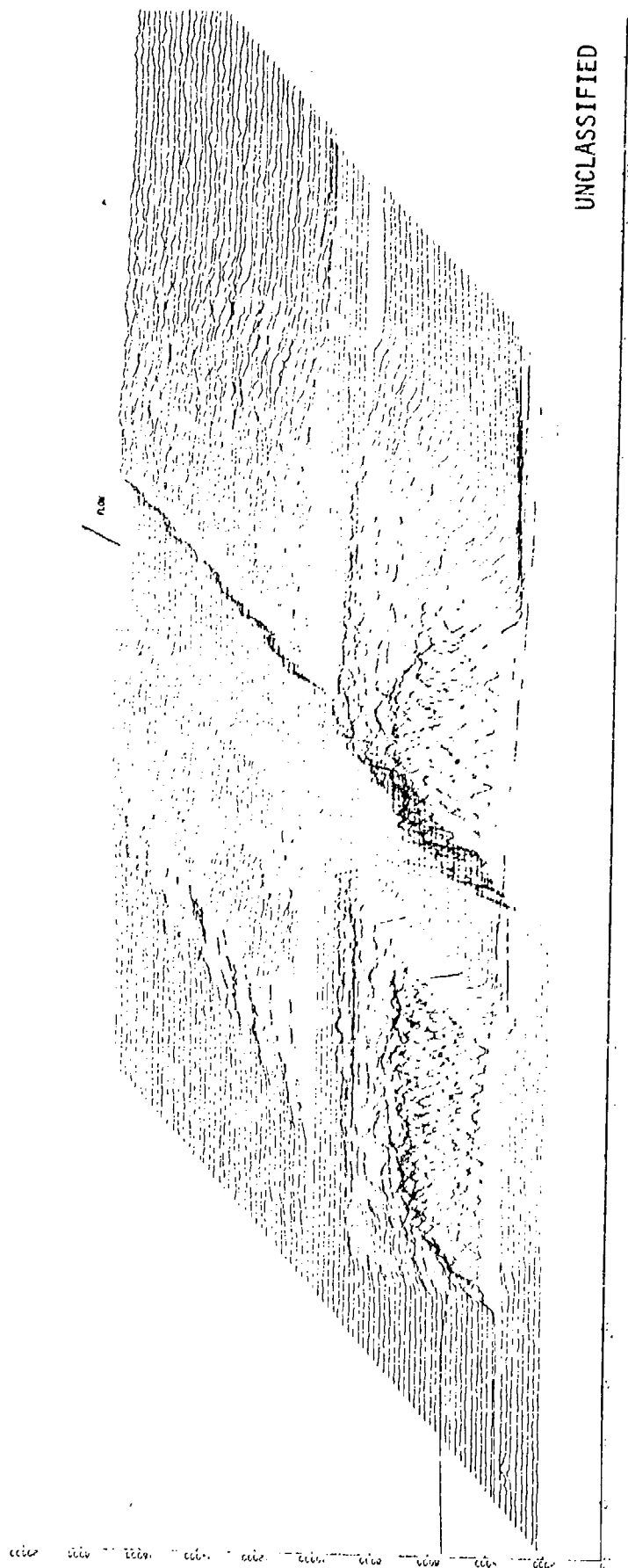
(U) By inspecting the IR-scanner data displays, some facts about the structure of the IR-cavity radiation field are quite evident. For the nominal case, test Ia, one recognizes an oscillatory variation of infrared intensity. These oscillations are almost certainly associated with the individual exit nozzle flows. Inspecting the peaks in more detail, one recognizes small secondary minima for sweeps close to the nozzles; these are almost certainly associated with the hydrogen injection slits. The larger minima are therefore collocated with the nozzle centers where the gas consists primarily of plenum chamber gas. The observed depths of the minima are very likely resolution limited and in reality are probably even more pronounced than in the scanner data displays. Each successive sweep is separated by 0.37 cm. Peak radiation amplitudes are observed to occur in test Ia at approximately the twelfth sweep from the nozzle or 4.5 cm downstream. At about the same downstream location the oscillatory structure is seen to disappear and is then followed by a somewhat noisy, but otherwise constant average amplitude across the flow field. We interpret this phenomenon as a break-up of distinct jets exit from the individual nozzles. Infrared intensity levels are observed to decay slowly in the downstream direction and are observed to persist

(U) beyond the location of the downstream set of observation ports.

Expansion of the infrared radiation and the associated flow field in width is clearly visible. One notices furthermore that in test Ia cavity excitation is not quite uniform over a flow area cross section. The changes of flow field infrared intensity profiles with changing cavity pressures are quite evident from inspecting the succession of Figures 55 through 58. With increasing cavity pressures the flow field infrared intensities appear to be localized closer and closer to the exit nozzle bank with subsequent very rapid decay of downstream infrared emission. In the highest cavity pressure at 8.2 torr no measurable HF infrared emission is observed through the downstream set of quartz windows. Test conditions II, III and IV have been shown in Figures 59, 60 and 61. Of these the infrared map of Test II, where all mass flows were increased by factors of 1.5 over nominal, is remarkable both for its intensity and the clarity of the display of the fine structure of the jets.

(U) The infrared scanner data were applied to interpolate chemiluminescent data for intermediate window positions following data reduction procedures as discussed in Section 4. b. As a first step, relative vibrational species population have been interpolated between window positions where detailed spectroscopic data are available. IR-scanner data are then used to determine intermediate excited state population densities. A sample plot of functions $\alpha_{v_i}(x)$ as defined in Equation (36) has been shown in Figure 62. IR-scanner data have been included in Figures 42 through 48 showing detailed excited state distributions as a function of downstream cavity position. These latter data, discussed in Section 6. a, are of course averaged over the spectrometer slit height. Using the IR-scanner output for more detailed information on the population density, variations in a direction perpendicular to the flow direction were obtained. Examples of such data have been plotted in Figures 63 and 64. In the latter plots HF-excited state variations from the average have been indicated at each location X by the excursions of the vertical bars.

Test Ia: Cavity Pressure Nominal
 $P_0 = 12.2$ psia
 $P_X = 1.29$ torr



UNCLASSIFIED

Figure 55. Infrared Chemiluminescent Intensity Display of Laser Cavity: Test Ia (U)

Test Ib: Cavity Pressure 2X Nominal
 $P_0 = 12.1 \text{ psia}$
 $P_X = 2.94 \text{ torr}$

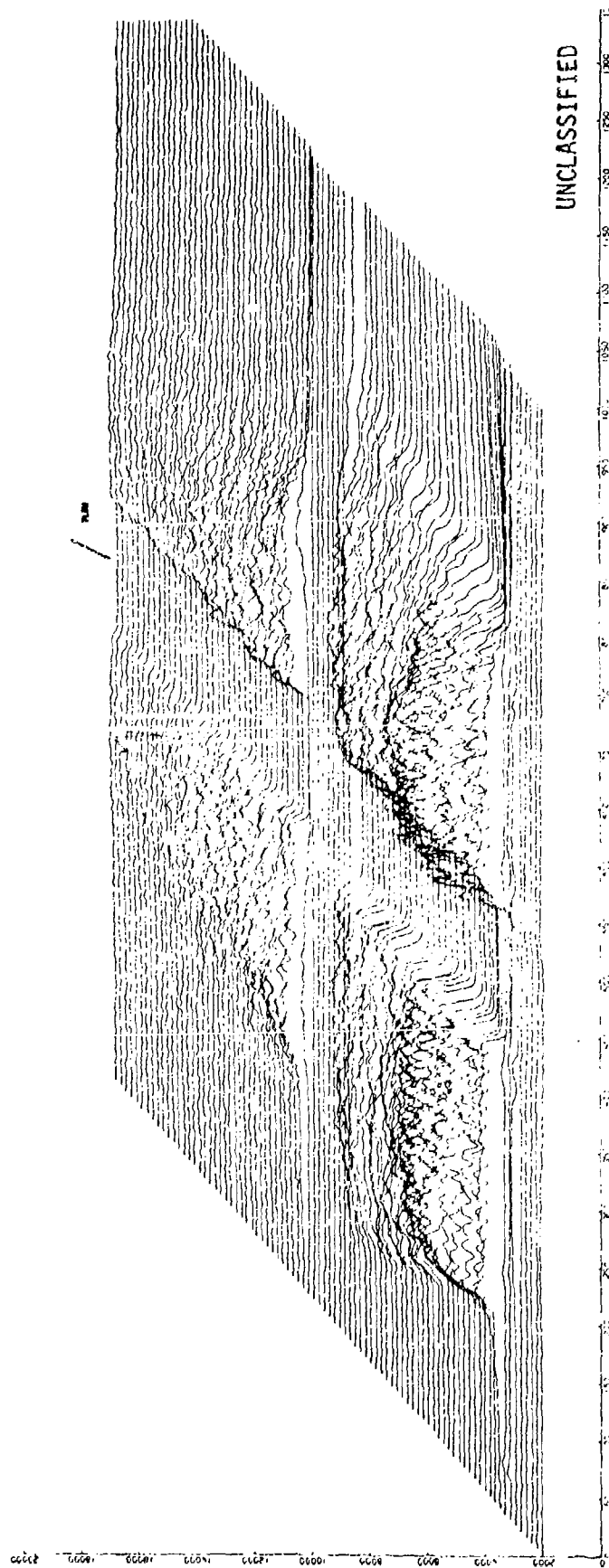


Figure 56. Infrared Chemiluminescent Intensity Display of Laser Cavity: Test Ib (U)

Test Ic: Cavity Pressure 4X Nominal
 $p_0 = 11.9$ psia
 $p_v = 5.67$ torr

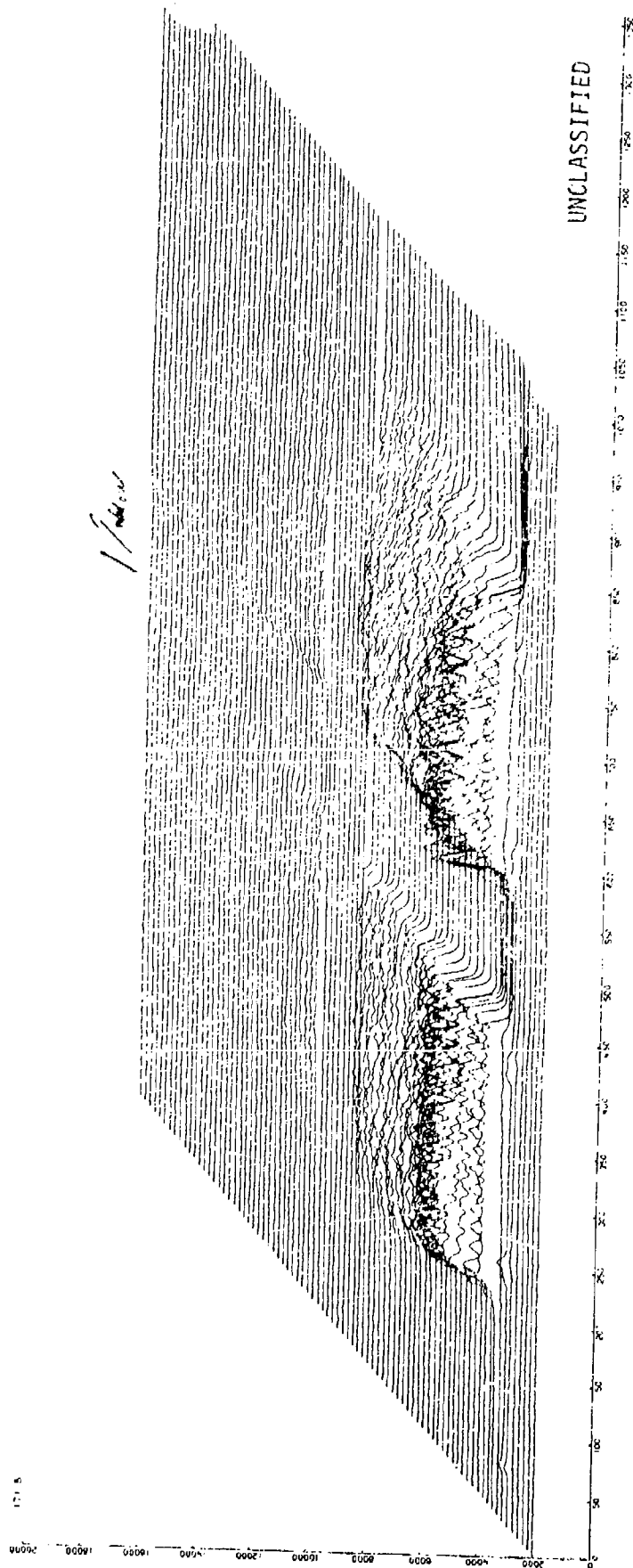


Figure 57. Infrared Chemiluminescent Intensity Display of Laser Cavity: Test Ic (U)

Test Id: Cavity Pressure 6X Nominal
 $P_0 = 12.0$ psia
 $P_X = 2.8$ torr

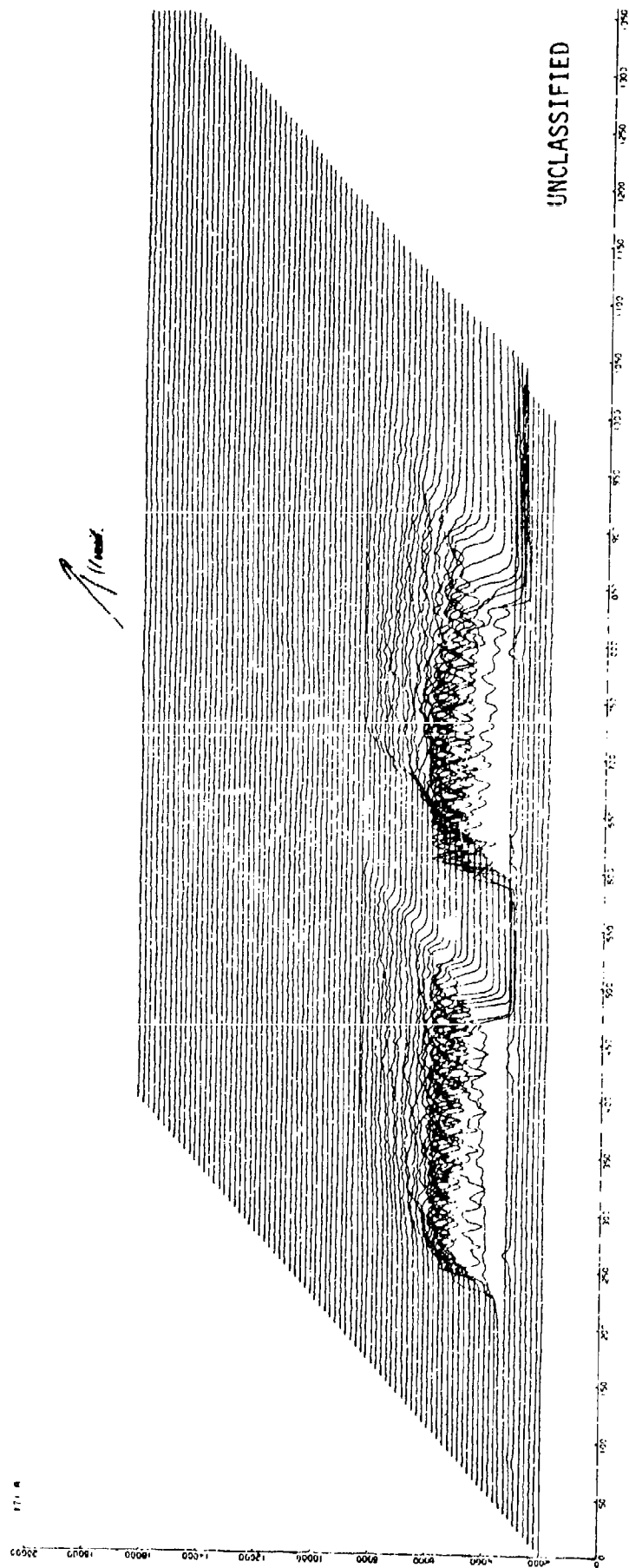


Figure 58. Infrared Chemiluminescent Intensity Display of Laser Cavity: Test Id (U)

Test II: 50% Increased Flow Rate
 $p_0 = 19.2$ psia
 $p_N = 1.93$ torr

1.0

0.8

0.6

0.4

0.2

0.0

0.0

0.0

0.0

0.0

0.0

0.0

0.0

0.0

0.0

0.0

0.0

0.0

1.0



UNCLASSIFIED

Figure 59. Infrared Chemiluminescent Intensity Display of Laser Cavity: Test II

Test III: Helium Substitution
 $p_o = 12.3 \text{ psia}$
 $p_x = 1.44 \text{ torr}$

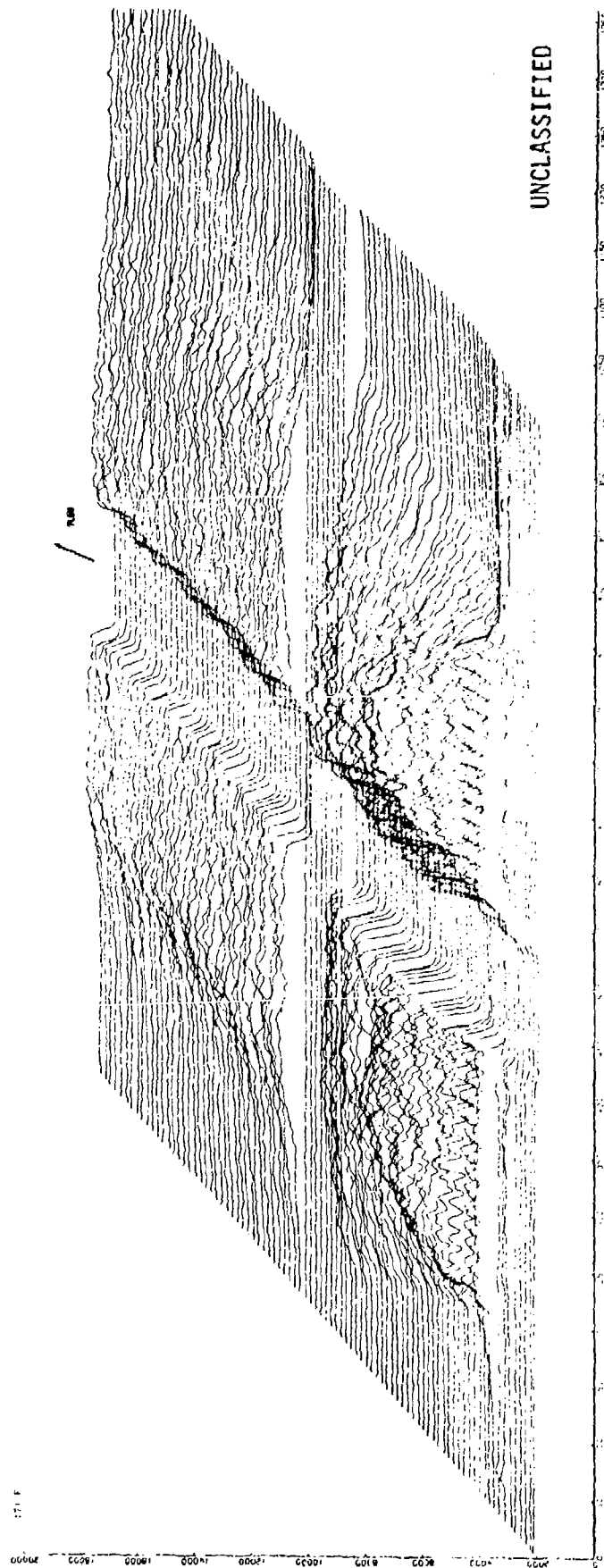


Figure 60. Infrared Chemiluminescent Intensity Display of Laser Cavity: Test III (U)

Test IV: Increased Combustor Temperature

$P_0 = 13.6$ psia

$P_X = 1.34$ torr

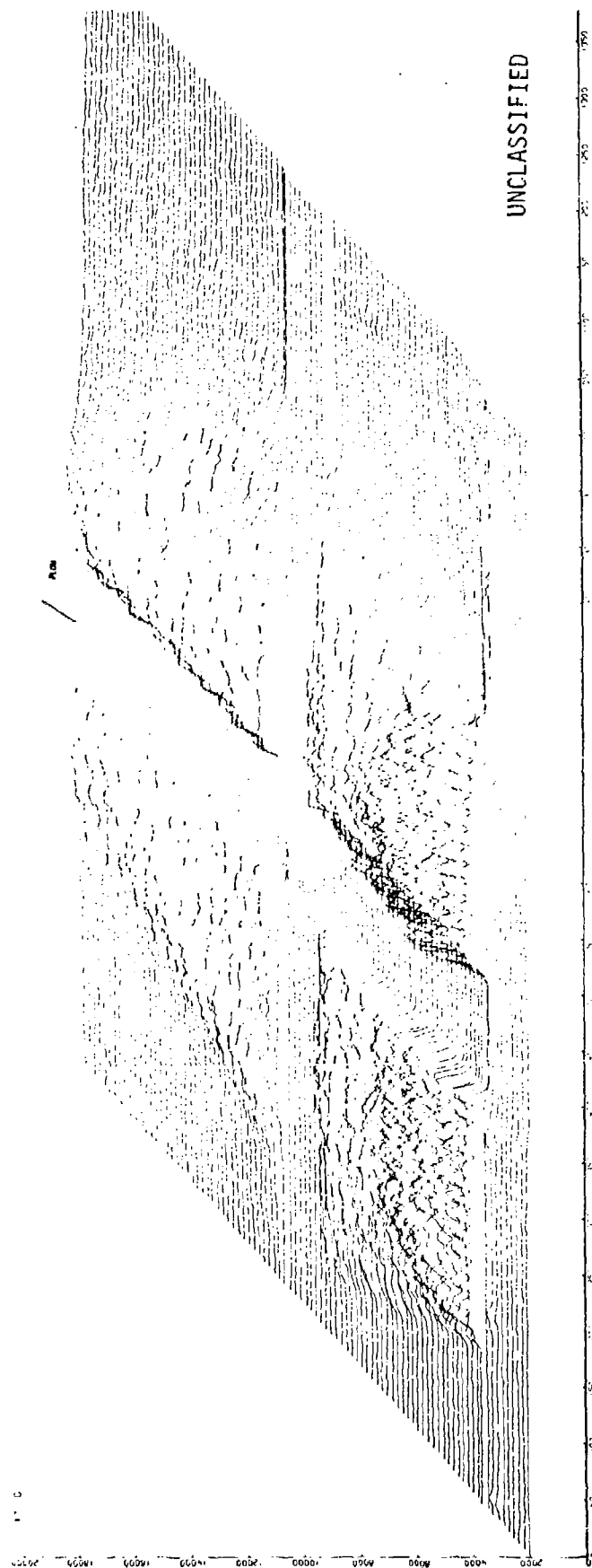
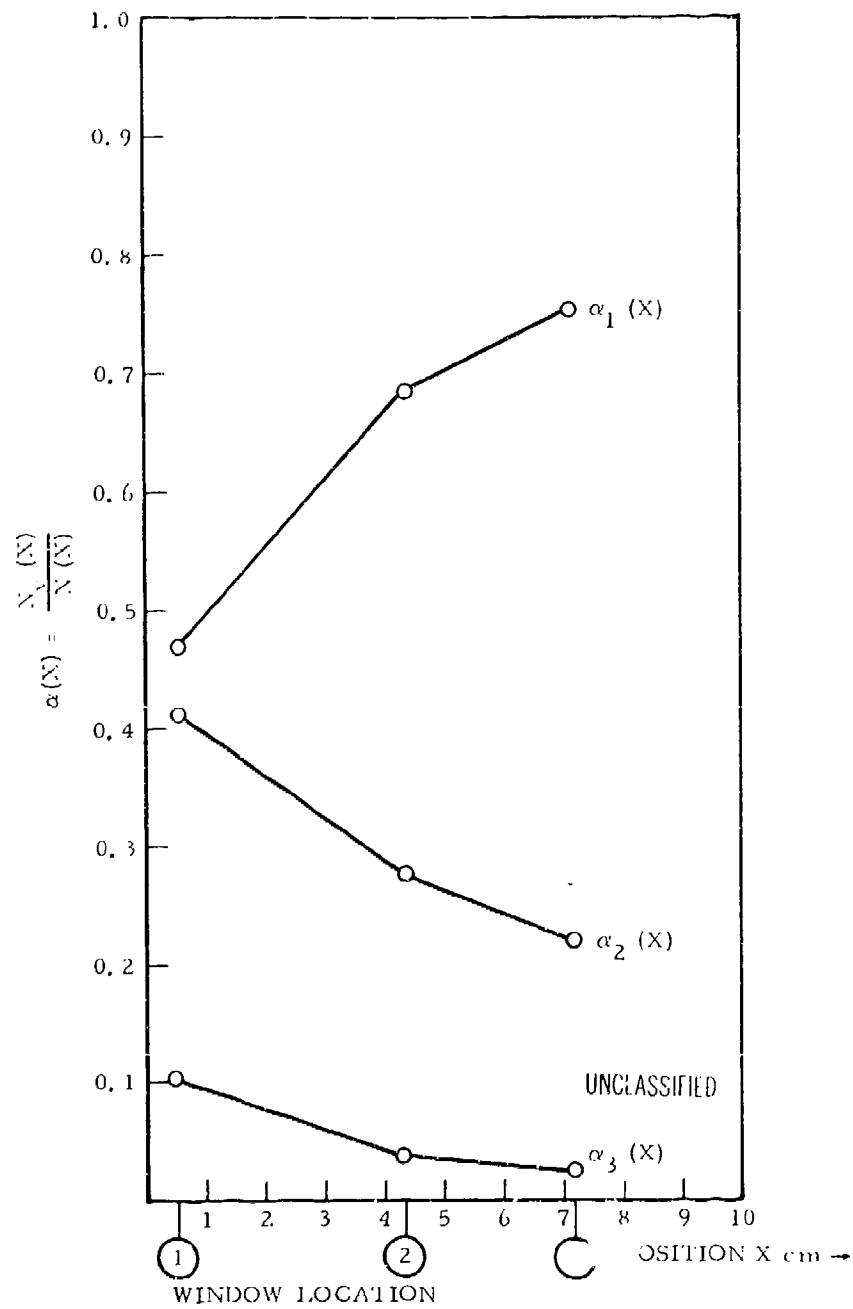


Figure 61. Infrared Chemiluminescent Intensity Display of Laser Cavity: Test IV (U)

TEST CONDITION NO. 6 - INCREASED DUCT PRESSURE (X4)

Figure 62. Relative Vibrational Species Population $\alpha_v(X)$ (U)

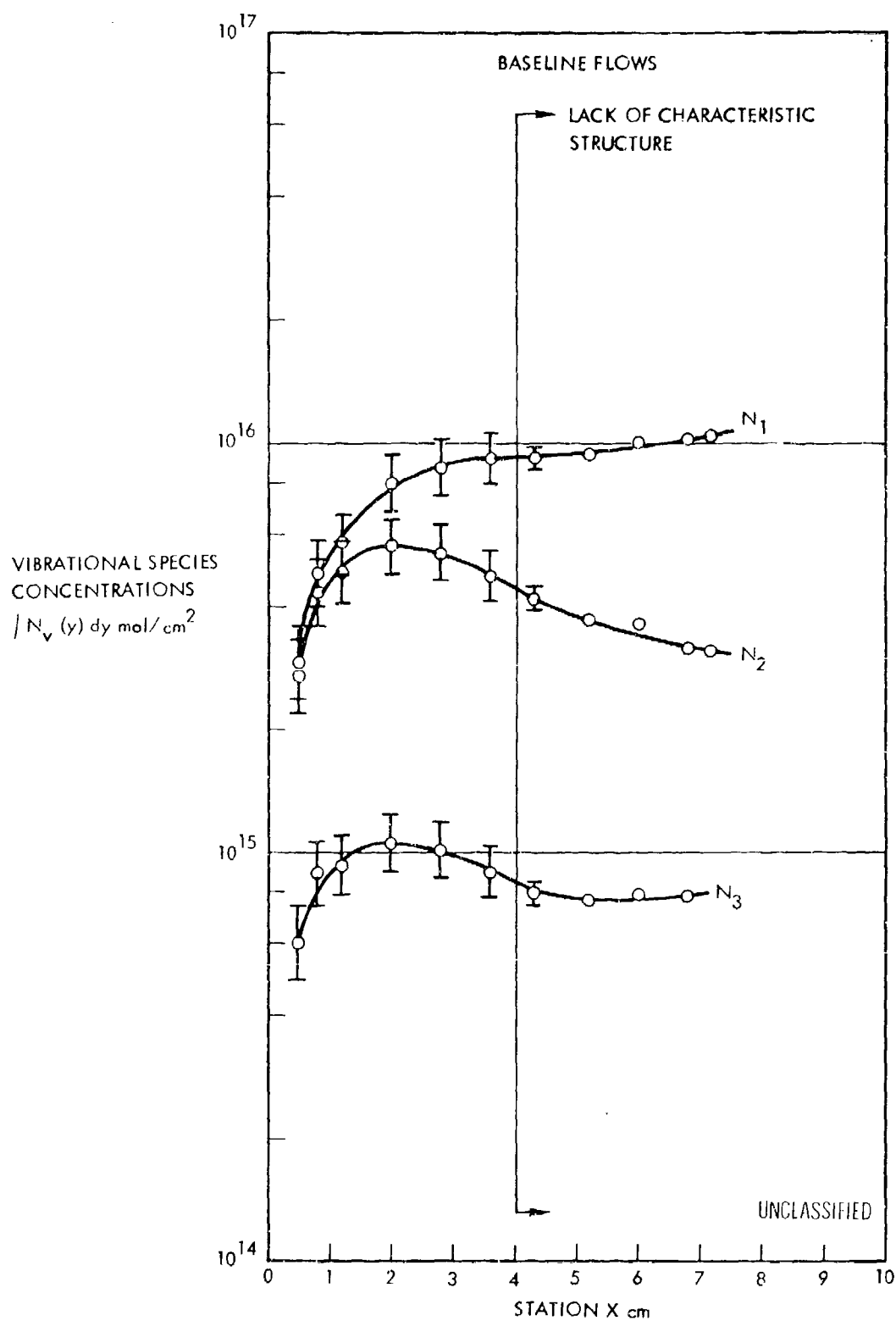


Figure 63. Vibrational Species Population and Variations:
 Baseline Flows (U)

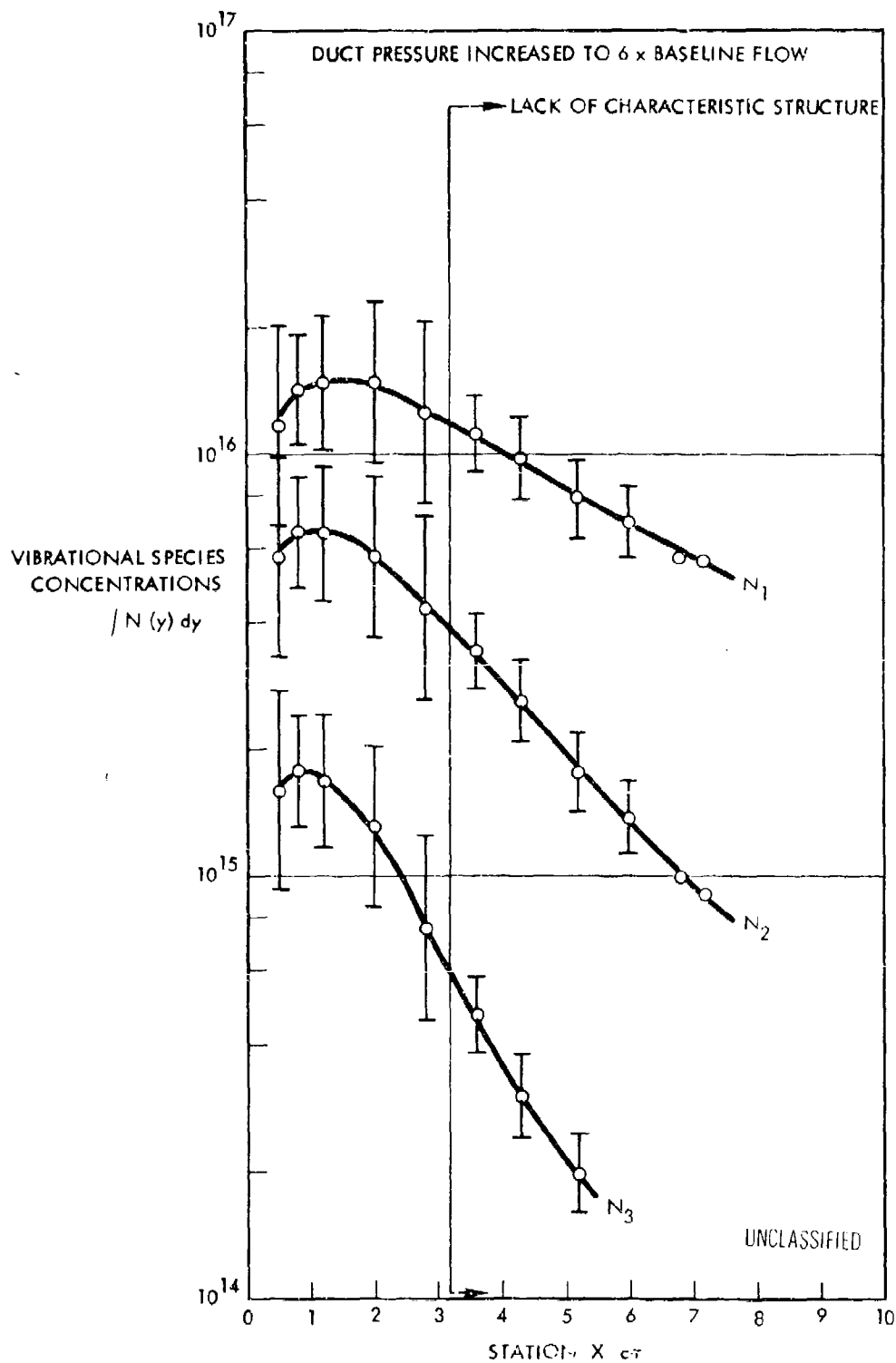


Figure 64. Vibrational Species Population and Variations:
Duct Pressure Increased x 6 (U)

7. CAVITY DIAGNOSTIC EXPERIMENTAL RESULTS DISCUSSION

(U) Spectroscopic diagnostic results which have been discussed in the preceding section have generated new information of great significance to the understanding and advanced engineering designs of HF chemical lasers. The proper interpretation and significance of purely spectroscopic data have become clear in many cases only by combining these data with other measurements of reactants and diluents mass flows, heat loss measurements and pressures. Since laser cavity processes are strongly governed by fluid dynamic effects, a fluid dynamically based model for interpreting all data is most natural. In the following technical discussion we have attempted to interpret all available data using highly simplified fluid mechanic models. Partly because of incomplete experimental information and partly because of fundamental theoretical difficulties on the subject of supersonic reactive flows and turbulent mixing processes our present data interpretations are necessarily incomplete and perhaps unsatisfying at this time. Future progress and further data analyses are likely to produce further advances in our understanding of the cavity environment. In the following sections we intend to review all the data, not from an individual experiment point of view but rather by addressing specific questions for which we will attempt to provide answers from the spectroscopic diagnostic data. In sequence of the following discussion we have data of relevance to the questions given below.

a. Laser Cavity Excitation and Flow Field Temperatures

(U) Chemiluminescent, resonance absorption and IR-scanner experimental results have provided a wealth of detailed data on HF excitation in laser cavities and flow field temperatures. Of particular interest are also the data obtained during this program on HF vibrational ground state population; without the data on HF-ground states the interpretation of the remaining spectroscopic data would have been far less complete.

(U) Hydrogen-fluoride rotational state excitation and flow field temperatures have been discussed in sufficient detail in the experimental results, Section 6a. Rotational sublevel distributions have generally been

(U) found to be well represented by Boltzman functions with the possible exception of high j levels at the lower cavity pressures (1-2 torr). Rotational temperatures for a given case have further been found to be independent of vibrational quantum numbers; these facts have been interpreted as direct experimental evidence that rotational temperatures are equilibrated with local kinetic flow field temperatures. The measurement of rotational sublevel relative distribution is therefore equivalent to a local flow field temperature measurement. Measured flow field temperatures have been included in Table 9. The significance of the flow field temperatures to the laser cavity dynamics will be further discussed below.

(U) Hydrogen-fluoride nonequilibrium excitation in the cavity has been shown in Figures 42 through 48. Comparing the measured vibrational population levels for each of the test conditions, one finds in all cases and for all conditions

$$N_{v+1} < N_v$$

In conjunction with measured rotational temperatures one readily confirms that partial inversion exists between vibrational levels 2 and 1 and 1-0 in most cases. This experimental result requires some comments. From the data of Pimentel (Ref. 14), Polanyi (Ref. 15) and Jonathan (Ref. 16) there can be little doubt that the chemical pumping reaction, $F + H_2$, which is the only pumping reaction of relevance in these experiments, will populate primarily HF vibrational levels 2, 3 and 1. Yet we observe even at the station closest to the nozzle exits (0.51 cm) partial inversion. With flow velocities near 2×10^5 cm, deactivation times would have to be shorter than 2.5 μ sec at a pressure of no more than 3 torr in the case of the baseline flow condition (Test 1a). No known collisional vibrational relaxation rates, expected to be active in the laser cavity, are consistent with such fast deactivation. We must therefore search for other deactivation processes. Radiative deactivation by stimulated emission, although not yet conclusively demonstrated in our device by experiment, appears to be consistent with all known facts. In fact, theoretical predictives comparing saturated and unsaturated gain distributions under conditions similar to ours make it highly likely that we are observing in our experiments a medium saturated by a crude cavity

Table 9. Cavity Heat Transport and Velocities (U)

| Test | Window | Window Location | T _r °K | \dot{W}_{t-r} Kcal/sec | \dot{W}_V (HF) Kcal/sec | Velocity Km/sec | \dot{W}_{kin} Kcal/sec | \dot{W}_{total} Kcal/sec | Energy Defect mJ Kcal/sec | Velocity Km/sec | Velocity of Sound Km/sec | Entrain- ment Factor ξ | Velocity W. Entr. Km/sec |
|------|--------|-----------------|----------------------|-----------------------------|------------------------------|--------------------|-----------------------------|-------------------------------|------------------------------------|--------------------|--------------------------------|----------------------------------|--------------------------------|
| Ia | 1 | 51 | 445 | 1.8 | | | | | | | .90 | | |
| | 2 | 4.3 | 475 | 2.4 | 1.4 | 2.0 | 7.0 | 10.8 | 9.0 | 2.3 | .94 | | |
| | 3 | 7.1 | 510 | 2.6 | 1.2 | 2.0 | 6.6 | 10.4 | 8.7 | 2.3 | .96 | | |
| | 4 | 17.8 | 610 | 3.8 | | | | | | | 1.05 | | |
| Ib | 1 | | 426 | 1.6 | | | | | | | .88 | | |
| | 2 | | 630 | 4.1 | 1.0 | 1.4 | | | 7.7 | 2.1 | 1.07 | 1.3 | 1.8 |
| | 3 | | 556 | 3.2 | .8 | 1.9 | | | 8.8 | 2.3 | 1.00 | 1.2 | 2.1 |
| | 4 | | 580 | 3.5 | | | | | | | 1.02 | | |
| Ic | 1 | | 515 | 2.7 | | | | | | | .96 | | |
| | 2 | | 808 | 6.3 | 0.7 | 1.2 | | | 5.8 | 1.9 | 1.21 | 1.4 | 1.6 |
| | 3 | | 804 | 6.2 | 0.4 | 1.2 | | | 6.1 | 1.9 | 1.20 | 1.3 | 1.6 |
| | 4 | | | | | | | | | | | | |
| Id | 1 | | 824 | 6.5 | | | | | | | 1.22 | | |
| | 2 | | 838 | 6.7 | 0.5 | 0.9 | | | 5.8 | 1.8 | 1.23 | 1.6 | 1.4 |
| | 3 | | 936 | 7.9 | 0.2 | 0.9 | | | | | 1.30 | | |
| | 4 | | | | | | | | | | | | |
| II | 1 | | 440 | 2.6 | | | | | | | .89 | | |
| | 2 | | 550 | 4.8 | 1.7 | 2.2 | 12.3 | 18.9 | 14.1 | 2.4 | 1.00 | | |
| | 3 | | 484 | 3.5 | 1.6 | 2.3 | 12.9 | 18.0 | 15.6 | 2.5 | .94 | | |
| | 4 | | 590 | 5.4 | | | | | | | 1.03 | | |
| III | 1 | | 360 | 0.7 | | | | | | | .80 | | |
| | 2 | | 464 | 1.9 | 1.4 | 1.8 | 5.8 | 9.1 | 9.4 | 2.3 | .91 | | |
| | 3 | | 470 | 2.0 | 1.8 | 1.9 | 6.2 | 9.4 | 9.6 | 2.3 | .91 | | |
| | 4 | | 660 | 4.2 | | | | | | | 1.08 | | |
| IV | 1 | | 415 | 1.8 | | | | | | | .84 | | |
| | 2 | | 452 | 1.8 | 1.1 | 2.0 | 6.9 | 9.7 | 10.7 | 2.5 | .88 | | |
| | 3 | | 451 | 1.7 | 0.9 | 1.9 | 6.1 | 8.8 | 10.9 | 2.6 | .88 | | |
| | 4 | | 472 | 2.0 | | | | | | | .90 | | UNCLASSIFIED |

(U) formed by the adjacent surfaces of the nozzle bank and pressure vessel. An interesting unsolved question is the power loss associated with radiative relaxations. We are interested in the answer to this latter question not only from a scientific viewpoint but even more so from a practical engineering aspect. Suppose that, because of practical limitations in laser optical cavity design, it were not possible to prevent radiative relaxation; one would expect very serious problems in future HF lasers very much larger than present devices.

(U) In the baseline flow case (Test 1a; $P_c = 1.3$ torr) of Figure 42 the population levels of vibrational states 3 and 2 are seen rapidly rising to a maximum at about 3 cm downstream from the nozzle exit, followed by an approximately exponential decay with coordinate X . The vibrational level 1 continues to increase slowly to a downstream distance of 8 cm after the initial rapid rise to the level at 3 cm. The slow increase of N_1 downstream from approximately 4 cm is very likely caused by decay of N_2 and N_3 into N_1 . This is evident from noting the total HF population shown in Figure 42 by the curve designated as ΣN_v . The latter is seen to be constant within the measuring accuracy (20%) between window 2 ($X = 4.3$ cm) and window 3 ($X = 7.1$ cm). We interpret this latter fact as implying that at the 4.3 cm station all the available fluorine has reacted to HF. Assuming this interpretation to be correct, the only mechanism by which N_1 can increase in population beyond 4.3 cm is by vibrational relaxation from N_2 and N_3 . The fact that the cavity reaction is virtually complete 4 cm downstream from the nozzle exit is of extreme importance for the laser. Clearly any laser power extracted further downstream, if any, for these conditions must be caused by residual pumping from relaxing N_2 and N_3 states. Of greater importance for the following discussion on diagnostic experimental results is, however, the fact that once all the fluorine has reacted, the cavity gas composition, species molar flow rates, and total energy transport in the gas are known from measured reactants and diluents flow rates, heats of combustion and heat loss measurements. Relevant data have been listed for all experiment conditions in Table 5 as step 2. We shall use this important fact later in our discussion on energy transport, velocities and gas entrainment in the laser cavity flow field.

(U) Continuing the discussion on vibrational state excitation we now progress to the baseline flow condition of test Ib where the cavity pressure has been increased by approximately a factor of 2 from 1.3 torr to 2.7 torr, keeping all other experiment parameters unchanged. We note in Figure 43 that the levels N_1 , N_2 and N_3 are relatively unaffected by the cavity pressure change to a distance of approximately 3 cm. Between the 3 cm and the 7 cm position all excited vibrational levels experience a rapid decrease in population levels followed by a lesser rate of decrease. This will be reflected in a shortening of the cavity lasing zone and probably result in a minor power loss. We interpret this observation as the beginning effects of recirculating gas entrainment to be discussed later. Taking gas entrainment for granted for the moment, one would interpret the observed decrease in HF excited state population as increased V-R and V-T transfer. Entrainment should result in a significant increase of N_0 population over the base flow case which is indeed observed. The apparent decrease of ground state and total HF population between windows 2 and 3 may be caused by an increase in flow velocity as will be discussed further later.

(U) Increasing cavity pressure to 5.5 torr has the effect on HF cavity excitation as shown in Figure 44. Maximum population of N_1 , N_2 and N_3 now occurs very close to the nozzle at $X = 2$ cm followed by an extremely rapid decay downstream. Lasing zone length will now be very short as compared to the baseline flow case. Significant entrainment is now occurring in the flow, effectively quenching HF excitation beyond the 2 cm position. As one would expect in the case of entrainment one observes a drastic increase in HF ground state population. Similar effects are observed for cavity pressure of 8.2 torr shown in Figure 45.

(U) In Test II all reactants and diluent mass flows were increased by a factor of 1.5 over the baseline flow case bringing the cavity pressure up to 1.9 torr from 1.3 torr. The resulting cavity excitation shown in Figure 46 is very similar to the baseline flow case. In this case one does not expect any entrainment because of the low cavity pressure. From the measurements it appears that most of the increased flow rate of HF appears in the form of hydrogen-fluoride ground state. Therefore we do not expect significant laser power increase for this case in the

(U) 1-0 transition. However, from our data we would expect proportionally larger increase in power from the 2-1 lines. Measurements on laser output power for this flow condition are consistent with these experimental data. The physical reason for the relatively large increase in HF ground state relative to excited state is not fully understood and requires further studies.

(U) In accordance with our overall test objectives in Test III we substituted 50% of the molar hydrogen cavity flow rate by helium in order to study the effect of hydrogen depletion. The experimental results have been shown in Figure 47. The chemiluminescent data do not indicate a significant effect although one would have expected a slightly lower rate of HF deactivation by molecular hydrogen. Similarly the test of increased combustor temperature (Test IV) shown in Figure 48 indicates little of significance except that the data predict a decrease in laser power as compared to the baseline flow case. The latter test was originally planned to investigate the effect of increased fluorine dissociation; it was a failure from this point of view because fluorine dissociation was actually complete for all cases.

b. HF Ground State Population

(U) Many of the key conclusions from the spectroscopic data have only been made possible through the measurement of HF ground state population. A separate discussion of the HF ground state population measurement is therefore in order. The data on vibrational ground state have been derived from two principally different experiments, namely the resonance line absorption/gain experiment and in some cases the self-absorption technique in the chemiluminescent experiment. In the case of resonance line absorption, measurements were made in at least two lines (P_3 and P_5) or with a third line (P_7) of the 1-0 transition. Experimental results have been discussed in more detail in Section 6.b and have been summarized in Table 7. It will suffice here to point out specifically that all different measurements on HF ground state yielded consistent results generally within better than $\pm 20\%$. The only exception to the latter is the self-absorption data for the high cavity pressure Test Id (8.2 torr cavity pressure) which yielded apparent HF ground state population about 50% higher than the resonance absorption technique which is more reliable in this case. The uncertainty of the self-absorption in this singular case

(U) could be traced to problems related to excessive self-absorption. The fact that self-absorption data agreed so well with resonance absorption/gain measurements is proof of the fact that the bulk of the observed hydrogen-fluoride in the line of sight between the two window faces was contained in the expanding jet. Our attempt to enforce this condition by lowering the windows into the cavity volume, approaching the jet boundary as close as appeared safe, was therefore totally successful.

(U) Data on HF ground state enable us to make conclusive statements on total HF in the line of sight and Table 7 quotes measured values. Information on total HF permits one to compute the important relative excitation of HF in the cavity; i.e., the mole fractions defined in Equation (64)

$$y_v(\text{HF}) = \frac{[\dot{\text{HF}}]_v}{[\dot{\text{HF}}]} = \frac{\int N_1(y)dy}{\sum_v \int N_v(y)dy}$$

(U) Figure 50 shows the measured relative HF vibrational state distribution; numerical values have been quoted in Table 7. Inspecting the data on relative HF excitation, one recognizes that quite consistently, approximately 60% of all the HF in the cavity flow field is in the vibrational ground state for all cases where there was no significant entrainment (Tests Ia, II, III and IV). For the higher cavity pressure, 75 to 85% of the measured HF is in the ground state. This high percentage is, we believe, further evidence of recirculating gas entrainment since the HF component of the entrained gas is exclusively in the ground state.

c. Energy Transport in the Cavity Flow Field

(U) Spectroscopic data in conjunction with known reactants and diluent molar flow rates and heat loss measurements can be used to make certain statements on the overall energy transport in the laser cavity flow field. The importance of this is that the total energy transport in the flow is rather well known and therefore can be used to check overall consistency of the data and to put limits on certain energy terms.

(U) Specifically, we will be able to set upper and lower limits of flow field average kinetic energy of motion, i.e., determine an average flow field velocity.

(U) We shall start the discussion with the experiments where, because of the low cavity pressures, one does not expect any significant gas entrainment to occur. These conditions are represented by the base-line flow case (Test Ia, $P_c = 1.3$ torr), the case where all mass flow rates were increased by a factor of 1.5 (Test II; $P_c = 1.9$ torr), and Test III and Test IV involving cavity hydrogen substitution and increased combustor temperature.

(U) Inspecting the measured total HF concentrations for the relevant cases, one observes practically constant total HF between windows 2 and 3. This fact was interpreted as implying that all the cavity fluorine had reacted to HF as discussed in Section 7a. In this case, as noted before, the cavity gas composition and total heat content are known from the test input conditions and are listed in Table 5, Step 2 (all fluorine reacted but no atomic hydrogen recombination). With these data we can apply a simple conservation equation balancing the total hydrogen fluorine molar flow rates. One finds

$$[\dot{H}F] = \frac{\left\{ \sum_v \dot{N}_v(y) dy \right\} \cdot \ell \cdot \bar{v}}{6.025 \times 10^{23}} \quad \text{moles/sec} \quad (69)$$

In Equation (69) the total molar flow rate for completed cavity reaction can be found in Table 5. Measured values of total HF in the line of sight is from Table 7. The effective width of the flow field, ℓ , is 7 inches (17.8 cm) and does not change appreciably with downstream position X ; the value of the Avogadro number is 6.025×10^{23} molecules/mole. Equation (69) becomes, therefore, an equation determining average flow field velocity \bar{v} at the position of the respective windows 2 and 3. Computed values for velocities from applying Equation (69) have been listed in Table 9. One finds that computed average velocities are very consistently 2.0 km/sec at windows 2 and 3 ($X_2 = 4.3$ cm and $X_3 = 7.1$ cm) for tests Ia, III and IV. For the higher total flow rate, test II, computed

(U) velocities appear to be 10% higher at levels of 2.2 km/sec. Of course, the significance of the latter small 10% discrepancy has to be looked upon with caution since we claim only 20% accuracy for the spectroscopic HF-population measurement.

(U) Having obtained a value for the flow field velocities, we can proceed with discussing the energy transport in the flow field following the general discussion in Section 5. Energy transport in cavity gas rotational and translational degrees of freedom can be directly computed from the measured flow field temperatures, data in Table 5, and using Equation (60). Numerical values have been listed in Table 9 as \dot{w}_{t-r} for all experiments. Specifically for the baseline flow case, we find a value of 2.4 kcal/sec at window 2. Similarly by using Equation (66) and data of Table 7, we can readily determine the heat transport in vibrational HF-excitation, provided the cavity reaction has been completed which is true for windows 2 and 3. In the baseline flow case we find 1.4 kcal/sec in vibrational excitation. Values for this latter term $\dot{w}_v(\text{HF})$ has been listed in Table 9 for all tests. Since the total cavity mass flow rate is well known (Table 5), the flow field average velocity can be used to determine the total flow field kinetic energy transport from Equation (67). The appropriate data have been listed in Table 9 as \dot{w}_{kin} ; for the baseline flow case we determine that $\dot{w}_{kin} = 7$ kcal/sec. Adding up all the power terms, \dot{w}_{t-r} , $\dot{w}_v(\text{HF})$ and \dot{w}_{kin} gives the total energy, \dot{w}_{total} , accounted for in the measurements. Values for \dot{w}_{total} have been given in Table 9. The total power thus accounted for, yields a value of 10.8 kcal/sec for the baseline flow case. The next column in Table 9 lists the energy deficiency $\Delta\dot{w}$ not accounted for by subtracting total heat transport \dot{w}_{total} of Table 9 from total available power, \dot{w}_c , listed in Table 5.

(U) For the baseline flow case this energy deficiency is only 2 kcal/sec out of a total available of 12.8 kcal/sec. This small energy deficiency is insignificant on the basis of involved measurements accuracy. This is readily recognized when realizing that total energy balance in the case of the baseline flow is achieved by increasing flow velocity from 2.0 to 2.3 km/sec. Since at present we cannot claim better average velocity error than 20%, kinetic energy uncertainty would be approximately 40%; the conclusion of this section is therefore that our

experimental data are very consistent with overall energy conservation in the flow field. Conversely, we have gained firm knowledge of the relative size of various heat transport mechanisms in the cavity flow field. For all investigated cases where there is no entrainment we find the following approximate relations:

| | |
|--|-----|
| Heat transport in kinetic energy of motion: | 70% |
| Heat transport in translation-rotational degrees of freedom: | 20% |
| Heat transport in vibrational excitation: | 10% |

(U) We shall next consider the energy balance for the test cases Ib, Ic and Id where we do expect significant entrainment. The purpose of the discussion in this section is both to provide further evidence for entrainment and to arrive at least at an estimate of the relative magnitude of gas entrainment.

(U) A typical case where severe gas entrainment is believed to be significant is test Ic where the cavity pressure was held at 5.5 torr. Applying Equation (69) to this case yields an apparent velocity of 1.2 km/sec. We believe this apparent low velocity to be caused by an erroneous application of Equation (69). Assume that the actual total molar HF-flow rate is $[\dot{H}\dot{F}]$ is higher by a factor of β over the one computed from the input condition caused by recirculating gas entrainment. Then the correct conservation equation is

$$\beta \cdot [\dot{H}\dot{F}] = \frac{\left\{ \sum_v N_v(y) dy \right\} \cdot \ell \cdot \bar{v}}{6.025 \times 10^{23}} \text{ moles/sec} \quad (70)$$

With the entrained HF there will be other gas entrained as well reflecting the composition of the cavity gas. The total entrained gas has to be accelerated to an average velocity giving the correct kinetic energy of motion. From the measurements the total power available for kinetic energy of motion is available from the known inputs and measurements of temperature and vibrational excitation. In the case of Test Ic the

(U) available energy is $\Delta\dot{w} = 5.8$ kcal/sec. This yields a second relation connecting β and v through

$$\frac{\beta \dot{m}}{2 \cdot 4.187} \frac{v^2}{10^5} = \Delta\dot{w} \text{ kcal/sec} \quad (71)$$

Combining Equations (69) with (71) yields two equations for determining both the entrainment factor and the velocity. For the case of Test Ic we find $\beta=1.4$ and $V=1.6$ km/sec at window 2. This estimate means that approximately 40% of the total gas flowing through the cross section at window 2 is entrained gas. In order to balance available energy, flow field velocity must be lower than in the case of no entrainment. The proper average flow field velocity balancing energy is in this case 1.6 km/sec which compares with 2.3 km/sec when there is no entrainment. The sound velocity at this station is 1.2 km/sec. Equivalent data for other entrainment cases have been included in Table 9. For the very high cavity pressure experiment the data yield an estimated entrainment factor of 1.6; i.e., 60% of the total gas flow is entrained.

(U) In conclusion of these discussions we are now prepared to answer one of the basic questions motivating this particular research. On the basis of the spectroscopic diagnostic data the observed laser power drop at increased cavity pressures is very likely caused by severe entrainment of recirculating cavity gas producing both heating and increased HF-vibrational state deactivation. It should be possible, therefore, to eliminate this problem by preventing entrainment through proper placement of baffles.

SECTION III

FLUID MECHANICAL ANALYSIS

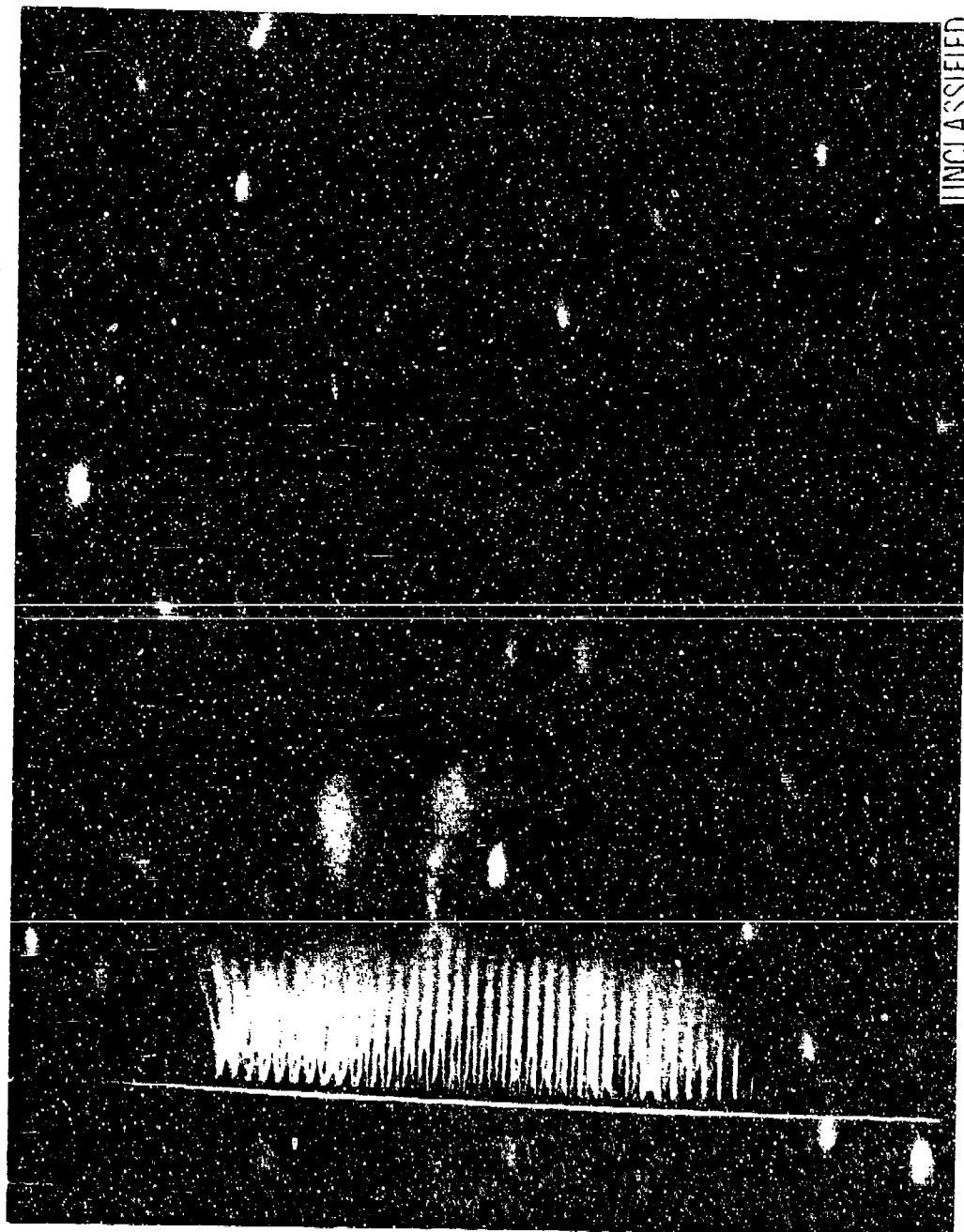
1. CAVITY FLOW FIELD STRUCTURE

(U) In this section, the results of the chemiluminescence and infrared measurements, and nozzle boundary layer analyses are combined with an interpretation of cavity color photographs (discussed below) to form a more detailed picture of the flow field structure in the cavity. Specifically, the chemiluminescence and infrared measurements represent spatial averages for a given direction of observation. Additional information can be gained by combining this source of data with flow visualization techniques along with fluid mechanical analysis. The salient features derived for the flow field are:

- When the boundary layer displacement effects are accounted for, the nozzle design pressure ratio is about 180. Thus, at a plenum pressure, p_c , of 12 psia, the nozzles are correctly expanded when the cavity pressure is about 0.068 psia or 3.4 torr.
- The reactions $H_2 + F \rightarrow HF^* + H$ and $H + F_2 \rightarrow HF^* + F$ are completed about 5 cm from the nozzle exit plane when the nozzles are correctly expanded.
- The mixing between the hydrogen and the fluorine-helium streams is turbulent.
- Two major causes of the loss in power when p_c is raised at fixed p_p is the contraction of the reacting jet and the increased importance of cavity gas entrainment into the jet.

The evidence and reasoning that leads to the above views are presented in the following paragraphs.

(U) Consider first the photographs of the flow field. Figure 65 is a black and white reproduction of a color photograph, taken from above, of the CL-II flow field in the laser cavity. The operating conditions were $p_c = 11.8$ psia, $p_L = 1.9$ torr. The dark triangular regions originate at the fluorine nozzle exit plane, and the thin dark streaks came from the hydrogen slits. In the original color photographs, the light areas between these two regions is orange and marks, at least approximately, the region



UNCLASSIFIED

Figure 65. Cavity Flow Field, Top View, Run 182A
 $P_c = 11.8$ psia; $P_L = 0.038$ psia (1.0 torr) (U)

(U) of reaction between the two streams. The orange glow is known to arise from $\Delta v = 4$ and 5 overtones of HF resulting from the reaction $H + F_2$.

(U) In Figure 66, the edges of the orange region are sketched to scale on a drawing of the nozzles, together with some of the postulated flow field features.

(U) A method of characteristics solution of a two-dimensional expansion from a sonic jet (Ref. 17) shows that a freely expanding hydrogen jet overexpands to such an extent that the edge would reach the centerline of the fluorine nozzle at a pressure ratio of about 250, approximately the condition in the photograph. Thus, it seems plausible that the interaction of the hydrogen and fluorine streams would generate a shock wave as shown schematically in the figure. The sharp bends in the orange region edges (that appear clearly in the color originals) would be explained by these waves as the sketch indicates. The downstream contraction of the overexpanded hydrogen jet would generate expansion waves which together with the shock reflections could produce oscillation seen in the boundary edges.

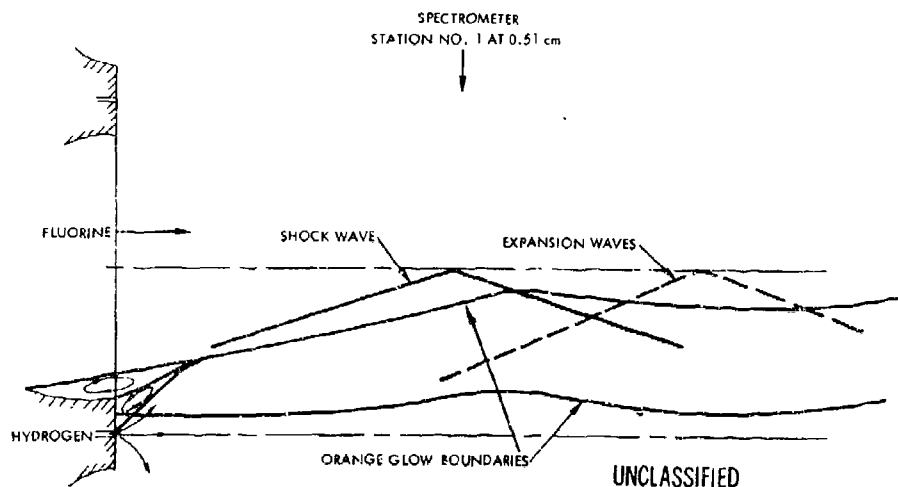


Figure 66. Cavity Flow Field, Top View (U)

(U) Before discussing the chemical reactions between the hydrogen and fluorine stream, it will be helpful to determine the cavity pressure at which the nozzles are correctly expanded. (This condition produces the most easily interpreted conditions.)

(U) First, the nozzle boundary layer calculations in Section III.2 predict that the correct pressure ratio is about 180. This corresponds to a cavity pressure of 3.4 torr, a value lying between those of Figure 43 and Figure 44 of the chemiluminescent results. Observe that the rotational temperature falls between stations 2 and 3 when $p_L = 2.5$ torr and that the temperature at station 1 is about 100°K higher at $p_L = 5$ torr than when $p_L = 2.5$ torr. These results can be explained by the wave system sketched in Figure 67 taken from a side view photograph, Figure 68, of the jet.

(U) When $p_L = 2.5$ torr, the lines visible in the photograph are interpreted as expansion waves, and the spectrometer at station 3 sees a flow in which a large fraction of the gas has passed through two expansion waves, in contrast to station 2 which is influenced mostly by one wave. Thus, the temperature should fall between stations 2 and 3. Even the magnitude of

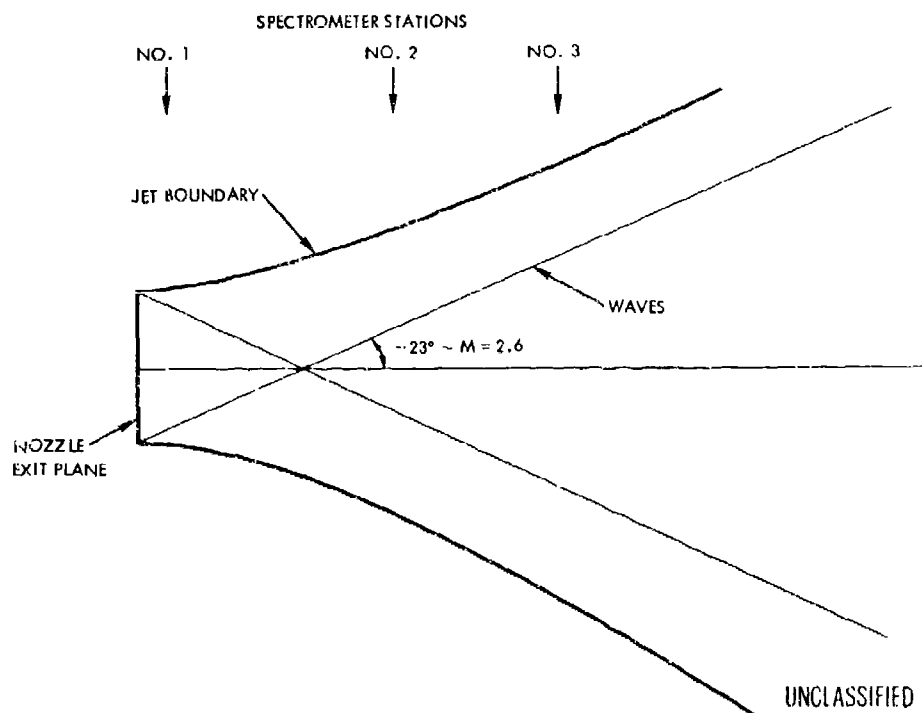


Figure 67. Cavity Flow Field, Side View (U)

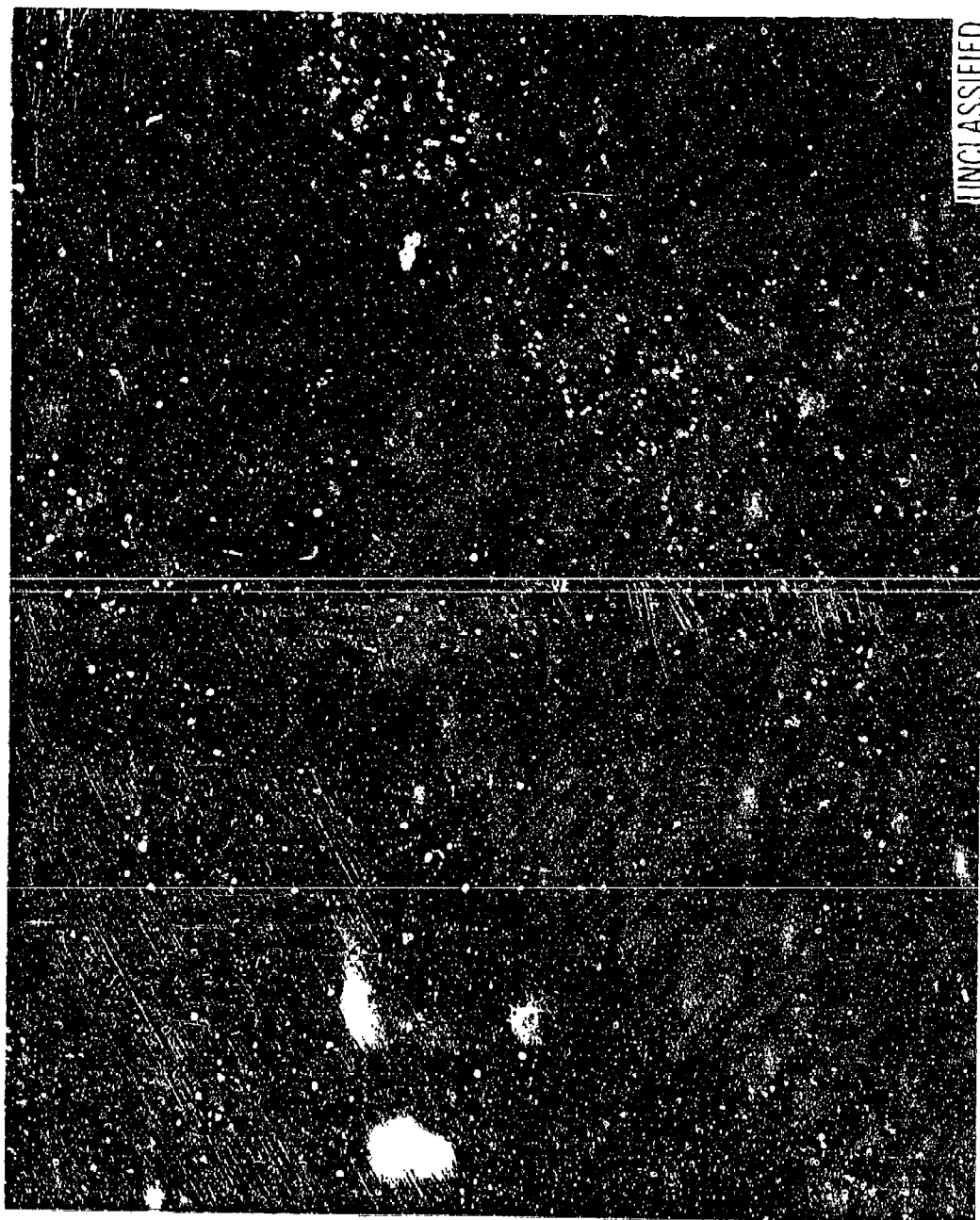


Figure 68. Cavity Flow Field, Side View, Run 192D
 $p_c = 11.9$ psia, $p_L = 0.091$ psia (4.5 torr) (U)

(U) the drop can be predicted approximately. From the boundary layer calculation of the exit pressure, the pressure drop across each wave should be $3.4 - 2.5 = 0.9$ torr. Then, neglecting the small vibrational energy change between stations 2 and 3

$$T_3 = T_2 \left(\frac{p_3}{p_2} \right)^{\frac{\gamma-1}{\gamma}} = 630 \left(\frac{2.5 - 0.9}{2.5} \right)^{.333} = 545^\circ\text{K}$$

The measured value is 556°K .

(U) If the above interpretation is correct, the nozzles are overexpanded when $p_L = 5$ torr, and the waves in the side view are shocks. It is likely that these shock waves will separate the very thick nozzle boundary layers, that hydrogen will flow back into the nozzles, and that the chemical reaction will begin with the nozzle. This would explain the higher temperature at station 1 for $p_L = 5$ torr.

(U) One conclusion, then, is that the boundary layer calculation which predicts a nozzle exit pressure of 3.4 torr is at least approximately correct. The other is that the chemiluminescent results in Figures 43 and 44 bracket the matched condition.

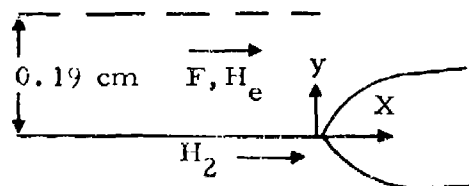
(U) It should also be mentioned that the boundary layer calculation predicts an average exit Mach number of 3.3, while the wave angles in Figure 67 correspond to $M = 2.6$. The large difference in these values is in accord with the chemiluminescence results of Figures 42 through 48 showing that much chemical reaction and thus significant heat release occurs within the 2 or 3 cm. (The length of the reaction region is discussed in detail below.)

(U) Let us return now to a discussion of the chemical reaction between the hydrogen and fluorine streams. We have established that the conditions for $p_L = 3$ torr are likely to be the most understandable. Thus, confining our attention to Figures 43 and 44, we estimate that the $\text{H}_2 + \text{F} \rightarrow \text{HF}^* + \text{H}$ and $\text{H} + \text{F}_2 \rightarrow \text{HF}^* + \text{F}$ reactions are complete ~ 5 cm from the nozzle exit plane. Since the reaction requires ~ 1 cm to reach completion from a fully mixed state, we may estimate that mixing is complete ~ 4 cm from the nozzle exit plane. An important question is whether the mixing is laminar or turbulent.

(U) First, it may be pointed out that the mixing rate in the CL II is not greatly different from that of the Aerospace 7 x 1/2 inch configuration. (The power versus X_c plots are similar.) In that configuration, the hydrogen enters through four 0.010-inch diameter sonic jets at a Reynolds number ~ 2500 . Demetriades (Ref. 18) confirms a crude theoretical estimate (Ref. 19) that the transition Reynolds number of jet is approximately 1000, corresponding, therefore, to a length less than a diameter in the Aerospace configuration. It should be stated that the experiment was conducted on a jet from a properly expanded nozzle instead of an underexpanded jet so that a direct comparison may not be justified. On the other hand, in the laser the hydrogen expands into the flow from the fluorine nozzle, a condition that seems most likely to produce large disturbance and transition.

(U) The conclusion that the mixing is turbulent is further strengthened by an estimate of the rate of laminar mixing, as follows.

(U) As was stated above, the Mach number in the mixing region is estimated to be 2.5. Combining this with the measured rotational (and therefore approximate translational) temperature of 500°K, we find that the velocity U is $2.5 \cdot 10^5$ cm/sec, a value approximately equal to both the computed nozzle exit velocity and hydrogen stream isentropic velocity. Consider then the laminar diffusion between two streams moving at $2.3 \cdot 10^5$ cm/sec brought together as shown in the sketch. Neglecting reaction



the solution for the concentration of H_2 in the upper half plane is

$$[H_2]/[H_2\infty] = \frac{1}{2} \left(1 - \int_0^{\zeta} e^{-s^2} ds \right)$$

(U) where $\xi = y/2\sqrt{DX/U}$, $H_{2\infty}$ is the H_2 concentration in the freestream, and D is the diffusion coefficient. The line on which $[H_2] / [H_{2\infty}] \sim 0.1$, the "edge" of the diffusion layer, is given by $\xi \sim 1$, i. e., by $X = y^2 U / 4D$.

(U) The binary diffusion coefficient for $H_2 - N_2$ mixtures at 300°K and 5 torr is 260 cm²/sec (Ref. 20). In the present case, the average molecular weight of the fluorine stream is approximately 10. Thus, since $D \sim [(M_1 + M_2)/(M_1 M_2)]^{1/2}$, the $H_2 - N_2$ value is a fair approximation.

(U) A more difficult question concerns the average temperature that should be used to evaluate D , which varies approximately as $T^{3/2}$. Initially, the hydrogen is very cold; the value after isentropic expansion is approximately 60°K. On the fluorine side, the lower portion of the boundary layer reaches ~700°K (see Section III.2, Figure 74), but a large fraction of the fluorine mass flow is below 400°K. The chemiluminescent value at the first station at 2.5 torr is 426°K and 630°K at station 2; however, these temperatures apply to the reacted gas only. Choosing what seems to be reasonable limiting values of 300°K and 500°K, we find that the edge of the hydrogen diffusion layer reaches the center of the fluorine nozzle 19 and 9 cm, respectively, from the nozzle exit plane. In view of the fact that this calculation ignores the consumption by reaction of part of the hydrogen as it diffuses into the fluorine, it is clear that these lengths should be increased by some, not negligible, factor. Thus, these results, combined with the estimate given above that the mixing is complete 4 cm from the exit, strengthens the hypothesis that the mixing is turbulent.

(U) The turbulent mixing layer between two-dimensional streams spreads at a rate that depends primarily upon the velocity difference between the streams. (See, for instance, Ref. 21.) Brown and Roshko, in a recent set of experiments (to be published), have shown that the density difference plays a secondary role. In the present slit nozzle configuration, there is initially a large velocity difference between the hydrogen jet and the boundary layer gas from the fluorine nozzles. Thus, the edges

(U) of the mixing zone may initially be given approximately by the expression

$$\frac{y}{X} = \frac{1}{\sigma} \sim \frac{1}{11}$$

where σ is the spreading angle parameter. Setting $y = 0.19$ cm, the fluorine nozzle half-width, we find that the hydrogen reaches the fluorine nozzle centerline about 2 cm from the nozzle exit plane. Molecular inter-diffusion must still precede the chemical reaction, of course, but this will now be rapid because of the greatly reduced diffusion distances.

(U) The spreading angle decreases as the velocity difference between the two streams decrease. Thus, in the present case in which the inviscid core velocity from the fluorine nozzle is approximately equal to the hydrogen jet velocity, the mixing further downstream will be much slower. This may explain the existence of nonuniformities as far as 6 or 7 cm downstream (Figure 65). (Nonuniformities can persist after complete combustion because there is excess hydrogen.)

(U) The final subject to be discussed in this section is the loss in laser power when the cavity pressure is increased, with the plenum condition held fixed. The decrease in power with pressure for the 7 x 1 inch slit nozzle configuration is discussed in Section IV. In the experiments, all conditions were held constant except the laser cavity pressure which was varied by changing the pumping rate from the cavity. The power was measured in the closed cavity mode and the mirrors were rotated to change X_c , the axial position of the perpendicular to both mirrors measured from the nozzle exit plane.

(U) The first point to note is that the power is higher at even the smallest X_c at the lower pressures. (For example see Figure 80.) This fact seems to weaken the often-stated explanation that increasing the laser cavity pressure makes the lasing zone too short and intense. The difficulty in interpreting curved mirror results, however, leaves this possibility open. If

(U) the power decrease does not come from optical losses, could the effect come from some gas dynamic affect on the chemical kinetics?

(U) The side views of the flow fields in the photographs suggest explanation of this power loss. These views show that at the lowest cavity pressure (Figure 69), the jet plume covers a large fraction of the lasing zone. As the pressure is raised, the plume narrows until, at the highest pressure, the plume boundaries lie within this zone. The mixing between the cavity and jet gases that occurs on the boundary layer is almost certainly turbulent and hence rapid. If this is the case and if the cavity gas consists in any large fraction of combustion products, then there are two mechanisms that reduce power. First, the combustion products consist in part of ground state HF molecules, which, as was discussed above, are powerful deactivators of the excited HF. As they are entrained by and mixed with the jet, the deactivation rate could be significantly increased. Secondly, the secondary flow of ground-state HF into the lasing zone is clearly detrimental even if it does not mix with the jet since here it acts as an absorption loss.

(U) The jet entrainment could also explain the regions of intense radiation at the jet boundaries for the highest pressure (Figure 70). It is along these boundaries that atomic hydrogen in the cavity gas would react with the F_2 in the nozzle boundary layers. This hot reaction produces the HF(v) necessary for the overtone radiation.

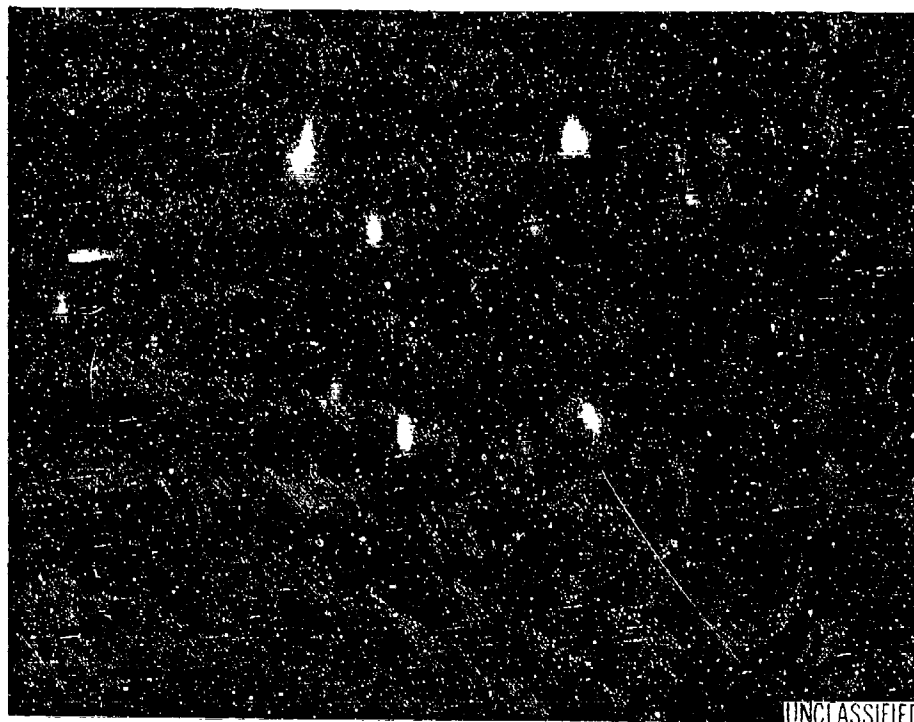


Figure 69. Cavity Flow Field, Side View, Run 182A
 $p_c = 11.8$ psia, $p_L = 0.038$ psia (1.9 torr) (U)



Figure 70. Cavity Flow Field, Side View, Run 182J
 $p_c = 12.0$ psia, $p_L = 9$ torr (U)

2. NOZZLE BOUNDARY LAYER ANALYSIS

a. Introduction

(U) The flow characteristics in supersonic nozzles can be greatly affected by the presence of relatively thick boundary layers when the dimensions of the nozzle are small or the gas density is low. Several effects may be important that would otherwise be negligible if the boundary layers were thin. For example, the effective expansion ratio, and therefore the exit Mach number, may be considerably reduced because of the displacement effect of the boundary layers as illustrated in Figure 71, and the total pressure may experience a significant drop because of viscous dissipation. Hence, to assist in the interpretation of the test results a viscous analysis was formulated to predict the nozzle boundary layer thickness and the integral flow properties at the exit of a two-dimensional nozzle. Described in the following are the boundary layer theory and the results of a series of computations.

(U) Since the Reynolds numbers for the nozzles and flow conditions under consideration are very low and the boundary layers are developing

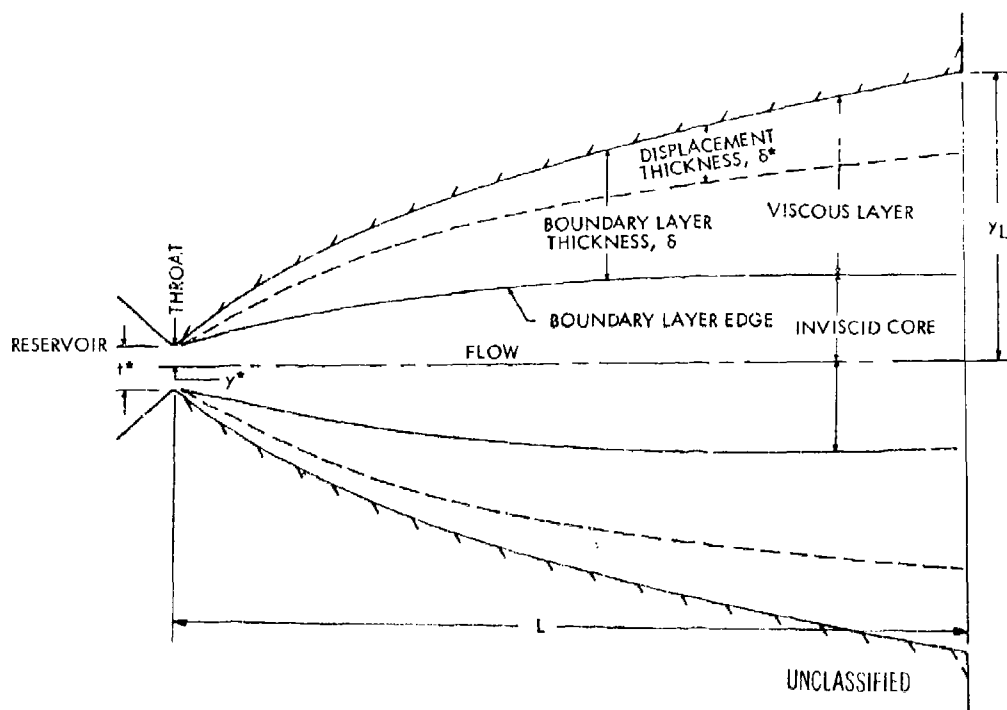


Figure 71. Nozzle Flow with Boundary Layers (U)

(U) in a strongly expanding flow (which has the effect of stabilizing the boundary layer), the boundary layer is assumed to be laminar. Analysis of the boundary layer development is for a two-dimensional nozzle and based on an approximate method which assumes local similarity. An interaction scheme was applied wherein the effective expansion area was set equal to the geometric flow area minus the boundary layer displacement cross-sectional area. Iterations were required to insure that the boundary layer displacement calculated from edge conditions for an assumed displaced inviscid flow was consistent with the resulting effective flow area (assuming one-dimensional flow). It is assumed that the boundary layer growth originates at the nozzle throat. Calculations have shown the boundary layer thickness to be very small in the region upstream of the throat and therefore has little effect on the boundary layer thickness at the nozzle exit.

(U) Since the purpose of the present analysis is to determine the effect of the boundary layer displacement to lowest order, a simplified analysis was applied which included the important effects of the strong favorable pressure gradient on the boundary layer development. The local similarity method is particularly well suited for this situation since it utilizes the results of a transformation theory which permits an important part of the pressure gradient and Reynolds number effects to be removed from the differential boundary layer equations. In particular, the boundary layer thickness, δ , and displacement thickness, δ^* , are written as

$$\delta = \frac{\sqrt{2\xi}}{\rho_e u_e} \int_0^{\eta_1} \frac{\rho_e}{\rho} d\eta$$

$$(\eta_1 \text{ chosen where } \frac{u}{u_e} = 0.995)$$

and

$$\delta^* = \frac{\sqrt{2\xi}}{\rho_e u_e} \int_0^{\infty} \left(\frac{\rho_e}{\rho} - \frac{u}{u_e} \right) d\eta$$

(U) where

$$\xi = \int_0^s \rho_w \mu_w u_e ds$$

The nomenclature is:

s = distance along nozzle wall

n = distance normal to wall

η = transformed coordinate normal to nozzle wall;

$$\eta = \frac{u_e}{\sqrt{2\xi}} \int_0^n \rho dn,$$

u = velocity

μ = viscosity

ρ = density

subscript e = edge conditions

subscript w = wall conditions

The term $\sqrt{2\xi}/\rho_e u_e$ can be rewritten in the form

$$\frac{\sqrt{2\xi}}{\rho_e u_e} = \sqrt{2} s \underbrace{\left(\frac{\mu_e}{\rho_e u_e s} \right)^{1/2}}_{\text{local Reynolds number}} \underbrace{\left[\frac{\int_0^s \rho_w \mu_w u_e ds}{\rho_e \mu_e u_e s} \right]^{1/2}}_{\text{shape factor}}$$

There are two effects of pressure gradient appearing in the above expression which are taken into account without solving the boundary layer equations. The first is the ordinary effect of local Reynolds numbers, which diminishes during the expansion. The second and more

(U) important result comes from the shape factor, which under the assumptions of a perfect gas and constant wall temperature, becomes

$$\text{shape factor} = \frac{\rho_w \mu_w}{\rho_e \mu_e} \left[\frac{\int_0^s p u_e ds}{p u_e s} \right]^{1/2}$$

This quantity increases significantly during the expansion because of the sharp reduction in pressure.

(U) Since the outer inviscid flow is isentropic, these two effects may be combined in a form containing initial (stagnation) conditions (subscript "s") and the local edge Mach number, M_e :

$$\frac{\sqrt{2\xi}}{\rho_e u_e} = \sqrt{2} \left(\frac{\mu_w}{\mu_s} \right)^{1/2} \left(\frac{H_{se}}{H_w} \right)^{1/2} \left(\frac{\mu_s}{\rho_s a_s} \right)^{1/2} \frac{(1 + \frac{\gamma-1}{2} M_e^2)^{\frac{\gamma+1}{2(\gamma-1)}}}{M_e} \left[\int_0^s M_e \left(1 + \frac{\gamma-1}{2} M_e^2 \right)^{-\frac{3\gamma-1}{2(\gamma-1)}} ds \right]^{1/2}$$

The quantity a_s is the speed of sound in the reservoir, and H_w/H_{se} is the total enthalpy ratio across the boundary layer.

(U) The final effect of pressure gradient appears in the terms

$$\int_0^{\eta_1} \frac{\rho_e}{\rho} d\eta$$

and

$$\int_0^\infty \left(\frac{\rho_e}{\rho} - \frac{u}{u_e} \right) d$$

and requires the solution of the boundary layer equations. However, rather than solve the full boundary layer equations, the assumption of

(U) local similarity is made, and only solutions to the similar boundary layer equations are used. These equations (assuming $\mu \sim T$ and unity Prandtl number) are characterized by two parameters; a pressure gradient parameter, β , and a cooling ratio H_w/H_{se} . These parameters may be evaluated locally from known external flow and wall conditions as the integrals can be determined from the corresponding solutions to the similarity equations. The latter have been previously obtained by Cohen and Reshotko, reference 22, and are employed here. The mathematical formulation of the analysis and the computational procedure are given below.

b. Computational Procedure

(U) The contour of the nozzle wall is analytically described by the empirical function:

$$\frac{y}{y^*} = \frac{1 - \frac{y_L}{y^*} \epsilon^m}{1 - \epsilon^m} - \frac{1 - \frac{y_L}{y^*}}{1 - \epsilon^m} \left[(1 - \epsilon) \frac{x}{L} + \epsilon \right]^m \quad (72)$$

in which

- y = nozzle half-width at distance x
- y^* = nozzle throat half-width
- y_L = nozzle exit half-width
- x = longitudinal coordinate distance; $x = s \cos \omega$
- L = nozzle length
- ϵ, m = constants

Representative nozzle contours for several values of ϵ and m are given in Figure 72.

(U) The flow boundary is defined by

$$\frac{y'}{y^*} = \frac{1 - \frac{y_L - \delta^*}{y^*} \epsilon^m}{1 - \epsilon^m} - \frac{1 - \frac{y_L - \delta^*}{y^*}}{1 - \epsilon^m} \left[(1 - \epsilon) \frac{x}{L} + \epsilon \right]^m \quad (73)$$

For the first iteration the boundary layer displacement thickness, δ^* , is assumed to be zero and the flow boundary is identical with the nozzle wall.

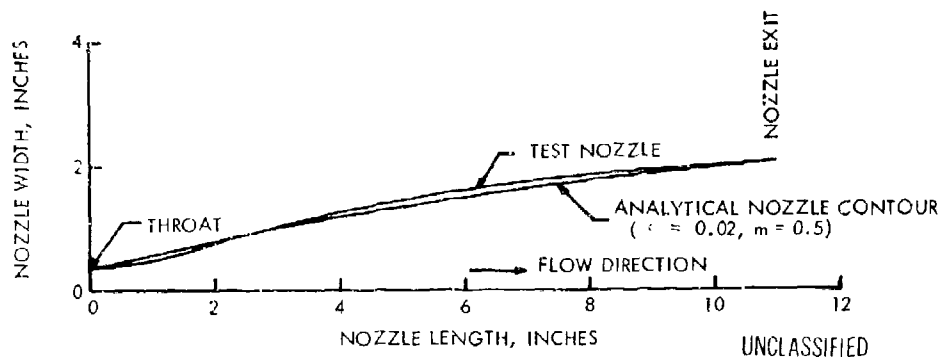


Figure 72. Contour of Wind Tunnel Test Nozzle and Its Analytic Approximation (U)

(U) First, the flow boundary is computed as a function of x/L from Equation (73). Then the distribution of the inviscid Mach number M_e along the nozzle is determined from the implicit relation

$$\frac{y}{y^*} = \left(\frac{2}{\gamma+1} \right)^{\frac{\gamma+1}{2(\gamma-1)}} \frac{1}{M_e} \left(1 + \frac{\gamma-1}{2} M_e^2 \right)^{\frac{\gamma+1}{2(\gamma-1)}} \quad (74)$$

in which γ is the gas specific heat ratio. (Subscript e denotes properties at the edge of the boundary layer.) For the corresponding distribution of M_e along the nozzle, the boundary layer properties are computed from the following functions:

$$I = \int_0^L \frac{M_e \left(1 + \frac{\gamma-1}{2} M_e^2 \right)^{-\frac{3\gamma-1}{2(\gamma-1)}}}{\cos \omega} dx \quad (74)$$

$$\omega = \tan^{-1} \left[\frac{y^*}{L} \left(\frac{d(y/y^*)}{d(x/L)} \right) \right] \quad (76)$$

$$\frac{d(y/y^*)}{d(x/L)} = -1 (1 - \epsilon) \frac{1 - \frac{y_L^*}{y^*}}{1 - \epsilon^m} \left[(1 - \epsilon) \frac{x}{L} + \epsilon \right]^{m-1} \quad (77)$$

(U) in which ω is the local angle of the nozzle wall with respect to the nozzle axis. Then the pressure gradient parameter $\bar{\beta}_L$ is computed from:

$$\bar{\beta}_L = \left(\frac{d \ln M_e^2}{dx} \right)_L \cos \omega_L \frac{1}{M_{eL} \left(1 + \frac{\gamma-1}{2} M_{eL}^2 \right)^{-\frac{3\gamma-1}{2(\gamma-1)}}} \quad (78)$$

$$\left(\frac{d \ln M_e^2}{dx} \right)_L = \frac{\tan \omega_L}{\gamma_L} \left[\frac{\gamma+1}{4} \frac{M_{eL}^2}{1 + \frac{\gamma-1}{2} M_{eL}^2} - 1 \right]^{-1} \quad (79)$$

Subscript L denotes value at the nozzle exit. The boundary layer parameters are then obtained from the tabulated functions in references 22 and 23 as a function* of $\bar{\beta}_L$ and S_w . The boundary layer parameters are S_w , Δ_{tr}^* and θ_{tr}^* , and $S_w = (H_w/H_{se}) - 1$. H_w and H_{se} are the gas enthalpies at the wall and freestream total temperatures, respectively.

(U) The boundary layer displacement thickness, δ^* , is computed from

$$\delta^* = \Delta \bar{\Delta}^* \quad (80)$$

$$\Delta = \left(\frac{2 \mu_w}{\rho_c a_o} \frac{H_{se}}{H_w} \right)^{1/2} \frac{\left(1 + \frac{\gamma-1}{2} M_{eL}^2 \right)^{\frac{\gamma+1}{2(\gamma-1)}}}{M_{eL}} \quad (81)$$

$$\bar{\Delta}^* = \frac{H_{se}}{H_e} \Delta_{tr}^* + \left(\frac{H_{se}}{H_e} - 1 \right) \theta_{tr}^* \quad (82)$$

$$\frac{H_{se}}{H_e} = 1 + \frac{\gamma-1}{2} M_{eL}^2 \quad (83)$$

* Asymptotic values of the parameters for very large values of $\bar{\beta}_L$ were obtained from reference 24.

(U) where

μ_w = viscosity at wall temperature

ρ_s = density at initial total pressure and total temperature

a_s = acoustic velocity at initial total temperature

H_{se} = freestream total enthalpy

H_e = freestream static enthalpy

(U) The computed value of δ^* is then put in Equation (73) and the boundary layer properties calculated again. Iterations are made until the resulting computed value of δ^* agrees with the value entered into Equation (73). The convergence criterion is set as

$$\frac{|\delta_n^* - \delta_{n-1}^*|}{\delta_{n-1}^*} \leq 10^{-3} \quad (84)$$

where n denotes the n th iteration. When convergence of δ^* is obtained, the following parameters are computed.

(1) Boundary Layer Thickness, δ :

$$\delta = \Delta \bar{\Delta} \quad (85)$$

$$\bar{\Delta} = \frac{H_{se}}{H_e} \Delta_{tr}^* + \left(\frac{H_{se}}{H_e} - 1 \right) \theta_{tr}^* + f(\eta^*) \quad (86)$$

(U) The term $f(\eta^*)$ is a function of $\bar{\beta}_L^*$ where η^* is the transformed stream function, reference 22, for a velocity ratio $u/u_\infty = 0.995$.

(2) Boundary Layer Momentum Thickness, θ :

$$\theta = \Delta \theta_{tr}^* \quad (87)$$

(3) Boundary Layer Thermal Thickness, δ_t :

$$\delta_t = - \Delta S_w \quad (88)$$

- (U) (4) Ratio of Initial to Mean Exit Total Pressures, $p_s / \langle p_{sL} \rangle$:

$$\frac{p_s}{\langle p_{sL} \rangle} = \frac{p_s}{p_L \left(1 + \frac{\gamma-1}{2} \langle M_L^2 \rangle \right)^{\frac{\gamma}{\gamma-1}}} \quad (89)$$

$$M_L^2 = \frac{\dot{m} a_s M_{eL}}{2 \gamma p_s y_L} \left(1 + \frac{\gamma-1}{2} M_{eL}^2 \right)^{\frac{\gamma+1}{2(\gamma-1)}} - M_{eL}^2 \frac{\epsilon}{y_L} \quad (90)$$

$$p_L = p_s \left(\frac{1}{1 + \frac{\gamma-1}{2} M_{eL}^2} \right)^{\frac{\gamma}{\gamma-1}} \quad (91)$$

$$\dot{m} = 2 a_s \rho_s y^* \left(\frac{2}{\gamma+1} \right)^{\frac{1+\gamma}{2(\gamma-1)}} \quad (92)$$

(U) In the above, $\langle M_L^2 \rangle$ is the square of the mean exit Mach number, p_L is the static pressure at the nozzle exit and \dot{m} is mass flow rate per unit depth of nozzle.

- (5) Ratio of Average Exit to Initial Total Enthalpies, $\langle H_{sL} \rangle / H_s$:

$$\frac{\langle H_{sL} \rangle}{H_s} = \frac{2 \rho_{eL} u_{eL}^2}{\dot{m}} + 1 \quad (93)$$

in which ρ_{eL} is the freestream density at the nozzle exit defined by

$$\rho_{eL} = \rho_s \left(\frac{1}{1 + \frac{\gamma-1}{2} M_{eL}^2} \right)^{\frac{1}{\gamma-1}} \quad (94)$$

and u_{eL} is the freestream exit velocity given by

$$u_{eL} = a_s M_{eL} \left[\left(\frac{2}{\gamma+1} \right) \left(\frac{\gamma+1}{2 + (\gamma-1) M_{eL}^2} \right) \right]^{1/2} \quad (95)$$

(U) (6) Exit Static Temperature, T_{e_L} :

(U) The freestream static temperature at the nozzle exit is computed from the relation

$$T_{e_L} = \frac{m (u_{e_L})^2}{\gamma R M_{e_L}^2} \quad (96)$$

in which m is the molecular weight and R is the universal gas constant.

(U) The physical significance of the mean properties at the nozzle exit can be interpreted as follows. If the flow at the nozzle exit were completely mixed, both adiabatically and without wall friction, at the exit pressure, the flux of momentum and energy would be conserved, and the following relations could be written between the resulting mixed uniform flow and the nozzle exit flow.

$$\rho_m U_m^2 Y_L = \int_0^\delta \rho U^2 dY + \int_\delta^{Y_L} \rho_e U_e^2 dY \quad (97)$$

$$\rho_m U_m H_m Y_L = \int_0^\delta \rho U H dY + \int_\delta^{Y_L} \rho_e U_e H_{se} dY \quad (98)$$

where the subscripts m and e refer to the mixed flow and to the inviscid core flow at the nozzle exit, respectively, and δ is the boundary layer thickness. The momentum and thermal thicknesses are defined as follows and may be substituted into the above relations:

$$\theta = \int_0^\delta \frac{\rho U}{\rho_e U_e} \left(1 - \frac{U}{U_e} \right) dY \quad (99)$$

$$\delta_t = \int_0^\delta \frac{\rho U}{\rho_e U_e} \left(\frac{H_s}{H_{se}} - 1 \right) dY \quad (100)$$

(U) from which

$$\rho_m U_m^2 = -\rho_e U_e^2 \frac{\theta}{Y_L} + \frac{U_e \dot{m}}{2Y_L} \quad (101)$$

and

$$\rho_m U_m H_m Y_L = \rho_e U_e H_{se} \delta_t + \frac{H_{se} \dot{m}}{2} \quad (102)$$

where \dot{m} is the total mass flow.

(U) These two relations provide the basis for determining the total pressure and total temperature of the mixed flow. The total pressure is

$$P_{sm} = P_L \left(1 + \frac{\gamma-1}{2} M_m^2 \right)^{\frac{\gamma}{\gamma-1}} \quad (103)$$

where

$$M_m^2 = \frac{\rho_m U_m^2}{\gamma P_L} \quad (104)$$

Using the isentropic core flow relations and Equation (101), it can be shown that

$$M_m^2 = \frac{\dot{m}_s}{2\gamma P_s Y_L} M_{eL} \left(1 + \frac{\gamma-1}{2} M_{eL}^2 \right)^{\frac{\gamma+1}{2(\gamma-1)}} - M_{eL}^2 \frac{\theta}{Y_L} \quad (105)$$

which is identical to Equation (90), whence, $M_m = \langle M_L \rangle$. Thus, also,

$$P_{sm} = \langle P_{sL} \rangle = P_L \left(1 + \frac{\gamma-1}{2} \langle M_L^2 \rangle \right)^{\frac{\gamma}{\gamma-1}} \quad (106)$$

(U) A simpler form is possible if it is recognized that

$$\dot{m} = 2\rho_e U_e (Y_L - \delta^*)$$

where

$$\delta^* = \int_0^\delta \left(1 - \frac{\rho U}{\rho_e U_e} \right) dY$$

(U) and then from Equation (105)

$$M_m^2 = \langle M_L^2 \rangle = \left(1 - \frac{\delta^* + \theta}{Y_L} \right) M_{eL}^2 \quad (107)$$

(U) Hence, it is seen that the mean properties $\langle M_L \rangle$ and $\langle p_{sL} \rangle$ are the properties that would exist in the flow, if the flow at the nozzle exit was subsequently ideally mixed.

(U) The total temperature follows directly from Equation (102) and the continuity equation which states that $\dot{m} = 2 \rho_m U_m Y_L$; thus,

$$\frac{H_m}{H_{se}} = \frac{\langle H_{sL} \rangle}{H_s} = \frac{2 \rho_e U_e \delta_t}{\dot{m}} + 1 \quad (108)$$

The consistent static enthalpy of the mixed flow is given by the relation

$$H_m = H_{sm} \left(1 + \frac{Y-1}{2} M_m^2 \right)^{-1} \quad (109)$$

c. Comparison with Low Reynolds Number Wind Tunnel Data

(U) Measurements were made by Talbot (Ref. 25) on a variable area ratio, two-dimensional supersonic nozzle which was designed for a low Reynolds number windtunnel. Measurements were made of the exit Mach number for nozzle area ratios over the range of 3 to 247 and for various initial total pressures. The gas was air with an initial total temperature of 525° R. Measurements of the Mach number profile across the exit plane showed the boundary layers were a large fraction of the total flow and that for the largest area ratio the boundary layers completely filled the nozzle at the exit.

(U) Using the nozzle dimensions and the test conditions, computations were made of the nozzle flow properties. The experimental nozzle contour and the analytic approximation of that contour are shown in Figure 72. The results are compared with the experiments in Table 10. The predicted exit Mach numbers $M_{eL})_{Theo.}$ are found to agree with the experimental data to within 2 to 4% for all cases. For the case in which the area ratio $A_L/A^* = 247$, and the measured boundary layers were found to fill the nozzle, the computation did not converge and no solution

Table 10. Comparison of Measured* and Theoretical Nozzle Exit Mach Numbers for Low Reynolds Number Wind Tunnel (U)

| Throat Half-Width y^* (cm) | Exit Half-Width y_L (cm) | Area Ratio* A_L/A^* | Reservoir Pressure P_s (psia) | Measured Exit Mach No. $M_{eL})_{Meas}$ | Calculated Exit Mach No $M_{eL})_{Theo}$ |
|---------------------------------------|-------------------------------------|-----------------------------|--|---|--|
| 2.145 | 6.525 | 3.04 | 0.0318 | 2.45 | 2.41 |
| 0.842 | 5.222 | 6.2 | 0.081 | 3.20 | 3.07 |
| 0.202 | 4.58 | 22.7 | 0.332 | 4.20 | 4.28 |
| 0.0902 | 4.47 | 49.6 | 0.752 | 5.00 | 5.11 |
| 0.0378 | 4.42 | 117.0 | 2.26 | 6.19 | 6.15 |
| 0.178 | 4.40 | 247.0 | 3.125 | 6.40 | No Convergence |

UNCLASSIFIED

*Reference 25

(U) could be obtained. This is consistent with the assumption in the formulation that the boundary layers do not merge and interact.

(U) Although the comparison between theory and experiment was made for only one gas and one set of stagnation conditions, the excellent agreement gives confidence that the predictions of nozzle performance will be of reasonable accuracy.

d. Laser Nozzle Flow Calculations*

(U) A series of boundary layer calculations were made for the CL-I and CL-II nozzles. (These nozzles have the same contour and widths and differ only in height; thus, the calculations are applicable to both.)

Computations were made for a series of plenum pressures for a gas with the following properties: $\gamma = 1.5$, molecular weight = 9.7, $T_p = 1800^\circ \text{K}$. The nozzle throat width was 0.010 inch and the area ratio was 15.

(U) The results at the exit are shown in Figure 73. We note first that for a plenum pressure, p_c , of 12 psia (the nominal case) the boundary layer nearly fills the exit area. The static pressure at the exit is 0.068 psia, compared to the inviscid pressure of 0.036 psia at this area ratio. The temperature and velocity profiles for $p_c = 12$ psia are shown in Figure 74. The average exit Mach number for these conditions is 3.32.

(U) The mass flow within the boundary layer can be calculated as follows,

$$\dot{m}_{bl} = \int_0^{\delta} \rho u \, dy$$

then, since

$$\delta^* = \int_0^{\delta} \left(1 - \frac{\rho u}{\rho_e u_e} \right) dy$$

$$\dot{m}_{bl} = \rho_e u_e (\delta - \delta^*)$$

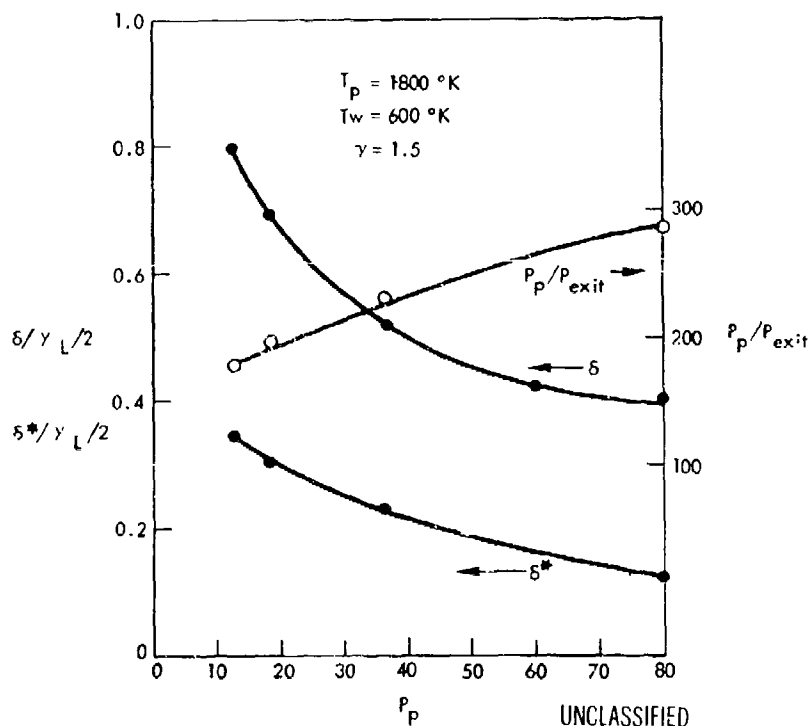


Figure 73. Boundary Layer Thickness and Exit Pressure vs Plenum Pressure (U)

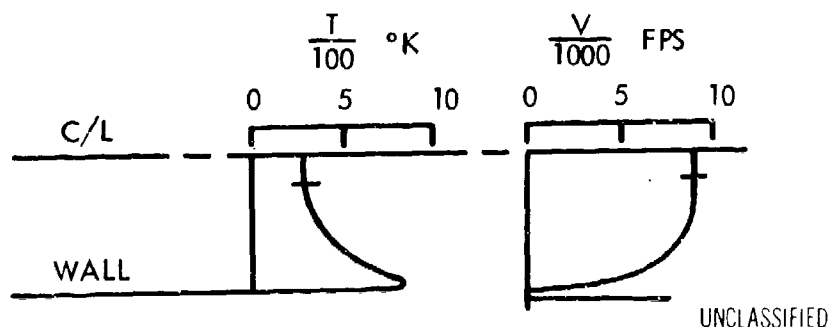
CL-II

Figure 74. CL-II Boundary Layer Profiles at Nozzle Exit (U)

(U) Hence, the fraction of the mass flow that is contained in the boundary layer is

$$\frac{\dot{m}_{bl}}{\dot{m}} = \frac{\delta - \delta^*}{y - \delta^*}$$

For Case C at $p_c = 12$ psia, this fraction is 0.69. This value depends, of course, on the arbitrary choice of δ , which is taken here as the y value for which $u/u_e = 0.995$.

(U) The decreasing effects of viscosity with increased plenum pressure and, therefore, increasing Reynolds number are as expected.

e. Catalytic Recombination of F_2

(U) It is now well known that the observed orange glow arises from overtone transitions of HF^* and hence occurs only after the reaction $F_2 + H \rightarrow HF^* (v) + F$. Thus for plenum conditions that produce only atomic fluorine, recombination must occur for the glow to be observed.

(U) An analysis indicated that significant fluorine recombination will occur only very close to the wall primarily because of the increased residence times of flow. The outer inviscid flow and remainder of the

(U) boundary layer are chemically frozen. In order to assess the amount of F recombination, a calculation was made assuming full recombination of F at the wall, i. e., that no recombination occurred in the gas but the wall was assumed to be catalytic. Similarity between the mass fraction of F and the velocity was also assumed such that

$$\omega_F = \omega_{F,e} \left(\frac{u}{u_e} \right)$$

and hence,

$$\omega_{F_2} = \omega_{F,e} \left(1 - \frac{u}{u_e} \right)$$

where ω_F and ω_{F_2} are the local mass fractions of F and F_2 in the boundary layer. This similarity relation is not strictly correct because the pressure gradient tends to destroy the similarity; nevertheless, it is accurate enough for comparative purposes. The mass flow of F_2 in the boundary layer is

$$\dot{m}_{F_2} = \int_0^\delta \rho u \omega_{F_2} dy$$

In terms of the transformation discussed earlier, and the above relation for ω_{F_2} , this becomes

$$\dot{m}_{F_2} = \sqrt{2\xi} \omega_{F,e} \int_0^\infty \left(1 - \frac{u}{u_e} \right) \frac{u}{u_e} d$$

where the latter integral is evaluated assuming local similarity. An evaluation was made for the CL-II flow conditions, and it was found that the F recombination amounted to 10 percent of the mass flow of F entering the nozzle array based upon the assumed recombination conditions.

SECTION IV

LASER PERFORMANCE

(U) In accomplishing the objectives of the HF Laser Technology Program, tests were conducted during 12 test week periods which entailed 28 different test days, excluding test setup and modification activities. Over 24,000 seconds of HF lasing time were accumulated during 270 separate tests. Approximately 200 tests were conducted with the 1 x 7 inch slit nozzle and 70 tests with the 1/2 x 7 inch slit nozzle. Over 800 separate test data points were recorded. Some of the key milestone dates during this test program are shown in Table 11.

Table 11. Test Program Milestones (U)

| | |
|-------------------|---|
| 5 April 1971 | First test with CL-II combustor |
| 27 April 1971 | First test with the plane-parallel externally mounted resonator |
| 25 May 1971 | First test with 1 x 7 inch slit nozzle closed cavity |
| 8 June 1971 | First test of the diagnostic test series (chemiluminescence spectroscopy) |
| 22 June 1971 | Initiated IR scanner diagnostic tests |
| 19 July 1971 | First test with the Aerospace Corporation confocal unstable resonator for beam quality measurements |
| 15 September 1971 | First successful HF, ground-state absorption measurements |
| 17 September 1971 | Last test series of the test program (closed cavity power) |

UNCLASSIFIED

(U) The diagnostic test run numbers conducted with the CL-II laser and the 1 x 7 inch slit nozzle are summarized in Table 12 and the target test conditions of the diagnostic test matrix are summarized in Table 13. The discussion of the results of the diagnostic test series was presented earlier in Sections II and III. The subsequent paragraphs of this section present the closed cavity power performance data obtained and the results of the beam quality measurements. The procedures employed in reducing the test data are described in Appendix I.

Table 12. Diagnostics Test Run Summary CL-II Combustor and 1 x 7 Nozzle (U)

| Test Conditions | Chemiluminescence Tests | | | | IR Scan | | Signal Gain | | | Orange Glow Photography | | Closed Cavity Power Profile |
|--|-------------------------|------|------|------|---------|----------------------|-----------------|----------------------|--------------|-------------------------|--------------|-----------------------------|
| | Window Position | | | | Coarse | Fine | Window Position | | | Top | Side | |
| | 1 | 2 | 3 | 4 | | | 1 | 2 | 3 | | | |
| Ia Nominal Flows (Baseline Case) | 162E | 163D | 164C | 165B | 168D | 171D | 205C | 207D | 208C | 161C | 161C | 160B1 210 |
| Ib Nominal Flows, Cavity Pressure Increased to 2 Times Nominal | 163F | 163E | 164D | 165C | 168E | 171E | 205F | 207H | 208F | 161B | 161B 205F | 160A |
| Ic Nominal Flows, Cavity Pressure Increased to 4 Times Nominal | 171B | 169B | 170A | - | 168H | 169B 170A | 205G | 207I 206C | 208G | 161E | 161E 205G | 160C1 |
| Id Nominal Flows, Cavity Pressure Increased to 6 Times Nominal | 171A | 169A | 170B | - | 168I | 169A 170B 171A | 205H | 207J 206A 206B | 208H | 161F | 161F 205H | 160C2 |
| II 150% of Nominal Flows | 162C | 163C | 164B | 165A | 168C | 171C | 205A 205B | 207B 207C | 208A 208B | 167A 214 | 205B 205D | 167A1 214 |
| III Nominal Combustor Flows with 50% of Cavity Hydrogen Replaced with Equivalent Helium Molar Flow | 162G | 163F | 164E | 165D | 172A | 171F | 205D | 207F | 208D | 211 | 205D | 211 |
| IV Nominal Total Flows with Increased Combustor Temperature | 162H | 163H | 164F | 165E | 168G | 171G | 205E | 207G | 208E | 212 | 205E | 212 |

UNCLASSIFIED

UNCLASSIFIED

(U) The operating parameters presented in Table 13 were selected from a review of closed cavity power surveys of the 1 x 7 inch, two-dimensional, multiple slit nozzle as representative conditions for intensive diagnostic mapping. The discussion of the individual tests and their results are presented in the following subsection. The results of these tests are presented graphically, as power profiles, and in tabular form, as summarized by the data reduction computer program output. Briefly, the selected baseline condition was an approximate 1900°K combustor temperature (corresponds to a mass mixture ratio of 15.7:1 for $F_2:D_2$) with a molar diluent ratio of approximately 0.7 (ratio of moles of helium to total combustor molar flow) at a plenum pressure of 12.5 psia. The corresponding cavity fuel flow condition was 4.4 moles of molecular hydrogen per mole of atomic fluorine (or 8.8 moles H_2 per mole F_2).

Table 13 is a foldout located on page 275.

1. CLOSED CAVITY POWER PERFORMANCE DATA AND CORRELATIONS

(C) This section of the HF Laser Technology program final report presents the performance measurements obtained with the TRW CL-II device during the period of April through September 1971 and utilizing the 1/2 x 7 inch and 1 x 7 inch two-dimensional slit nozzle configurations described in Appendix I. The data are presented in terms of basic power versus X_c plots, tabulations of all thermodynamic and fluid mechanic parameters of interest, and by regression analysis curves for significant parameters. The term X_c is defined as the measured distance from the exit of the cavity injector nozzles to the centerline axis of a symmetric mirror system. Results of the CL-I configuration 1/2 x 7 inch nozzle tests are included in the regression analysis although these data were taken prior to contract initiation since they are directly applicable and increase the reliability of the analysis.

(C) A methodical test and data analysis program was followed for both the CL-I and CL-II devices. Techniques of variable-isolation and regression analysis were used in the handling of all data obtained on the 1/2 x 7 inch nozzle. No attempt was made to perform regression analysis on the data from the 1 x 7 inch configuration; however, the trends appear to closely follow the 1/2 x 7 inch results. (See Section b, Figure 81.) The effects of combustor fuel-to-oxidizer mixture ratio, heat losses, combustor pressure and temperature, cavity pressure, diluent, and fuel proportions were studied and isolated. The basic analyses are for the F_2 , H_2 , D_2 , helium reactant systems. Selected operating points were also tested with N_2 diluent.

a. CL-II 1/2 x 7 Inch Two-Dimensional Slit Nozzle Results

(C) Testing of the CL-II 1/2 x 7 inch slit nozzle was initiated on April 5, 1971. The CL-II combustor was designed to reduce significantly the energy losses experienced with the CL-I combustor/mixer hardware configuration. The objectives of the initial tests, 097 through 099, were to check out and characterize the CL-II combustor for comparison with the CL-I combustor/mixer and to determine optimum operating conditions for subsequent diagnostic testing.

(C) Mirrors available for the initial test series were a set of original TRW mirrors of improper design from a calorimetry standpoint. Subsequent testing with Aerospace Corporation and improved-design TRW mirrors revealed that a constant correction factor for results obtained with these mirrors was required and could be justified for data analysis. This factor has been included in the data presented herein.

(1) Tests 097A through D

(C) These tests were conducted to determine the effect of nozzle inlet temperature on specific power per mole of F, holding all other parameters constant. For these tests the helium mole percent was maintained at 63.3% and the H_2 cavity flow to F flow at a molar ratio of 4:3:1.

(C) Target flow conditions (g/sec) for lasing were:

| <u>Test No.</u> | <u>97A</u> | <u>97B</u> | <u>97C</u> | <u>97D</u> |
|-----------------|------------|------------|------------|------------|
| $\dot{m}D_{2p}$ | 0.35 | 0.35 | 0.35 | 0.35 |
| $\dot{m}F_{2p}$ | 5.5 | 4.5 | 6.5 | 7.5 |
| $\dot{m}H_{cp}$ | 2.0 | 1.63 | 2.36 | 2.72 |
| $\dot{m}H_{2C}$ | 1.0 | 0.59 | 1.44 | 1.93 |

(C) Resultant data are presented in Figure 75 and Table 14.

(2) Tests 098 through 098E

(C) These tests were conducted to determine the effects of helium flow variations while maintaining T_p constant. To accomplish this, the free F flow was held constant and the reactants D_2 and F_2 , supplying the heat of reaction, varied in proportion to He flow.

(C) Target flow conditions (g/sec) for lasing were:

| <u>Test No.</u> | <u>98A</u> | <u>98B</u> | <u>98C</u> | <u>98D</u> | <u>98E</u> |
|-----------------|------------|------------|------------|------------|------------|
| $\dot{m}D_{2p}$ | 0.35 | 0.31 | 0.29 | 0.37 | 0.40 |
| $\dot{m}F_{2p}$ | 5.5 | 5.2 | 5.0 | 5.8 | 5.9 |
| $\dot{m}H_{cp}$ | 2.0 | 1.5 | 1.0 | 2.4 | 2.9 |
| $\dot{m}H_{2C}$ | 1.0 | 1.0 | 1.0 | 1.0 | 1.0 |

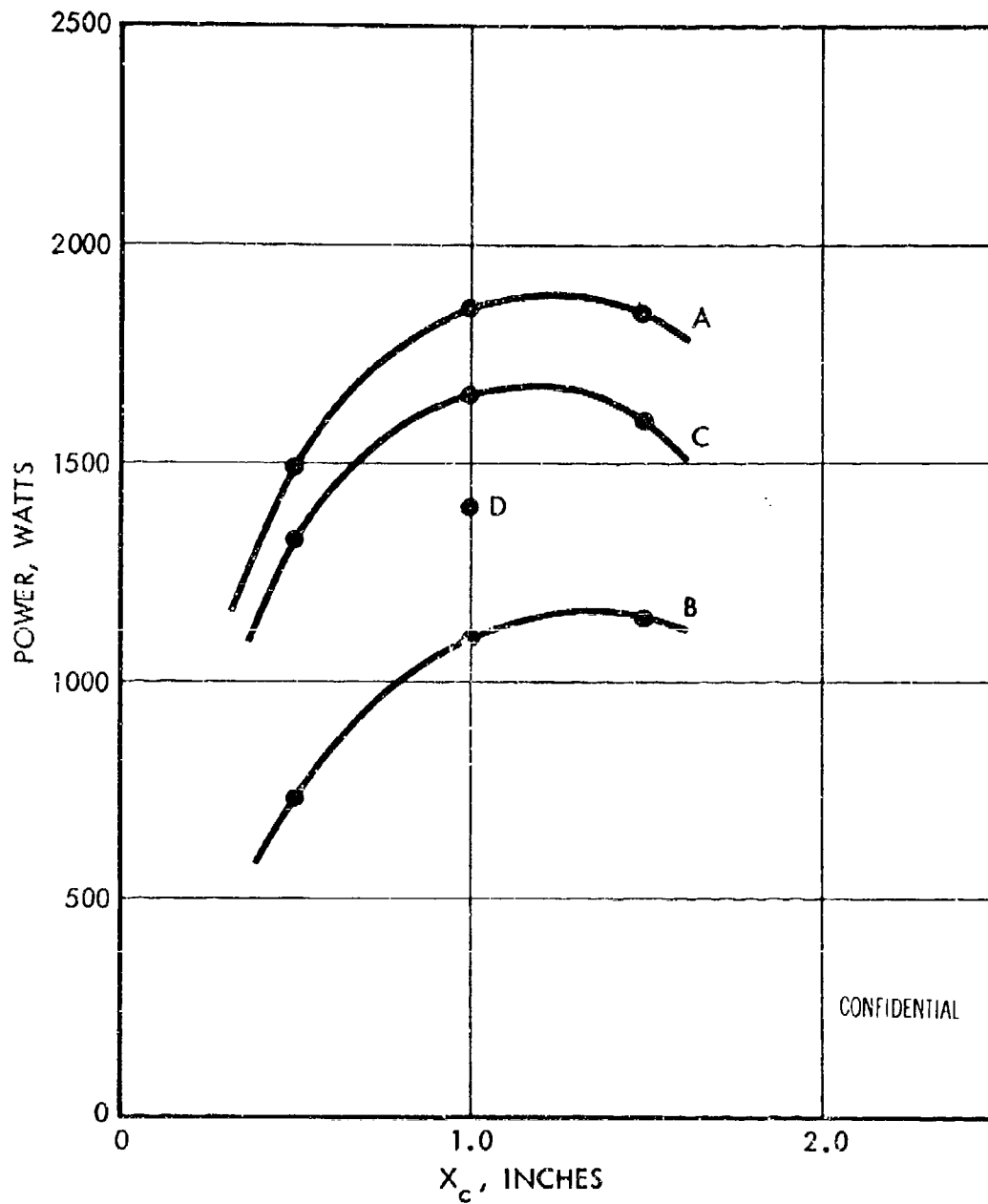


Figure 75. Closed Cavity Power X_c Scan for Test 097 (U)

CONFIDENTIAL

Table 14 is a foldout located on page 276.

CONFIDENTIAL

(C) Resultant data are presented in Figure 76 and Table 14.

(3) Tests 099A through 099E

(C) After selecting the optimum inlet temperature and He mole fraction, the H_2 flow was varied +100 and -50% from the baseline (4.3:1 molar ratio H_2/F), holding all nozzle inlet parameters constant.

(C) Target flow conditions (g/sec) for lasing were:

| <u>Test No.</u> | <u>99A</u> | <u>99B</u> | <u>99C</u> | <u>99D</u> | <u>99E</u> |
|-----------------|------------|------------|------------|------------|------------|
| $\dot{m}D_{2p}$ | 0.35 | 0.35 | 0.35 | 0.35 | 0.35 |
| $\dot{m}F_{2p}$ | 5.7 | 5.5 | 5.5 | 5.5 | 5.5 |
| $\dot{m}He_p$ | 2.05 | 2.0 | 2.0 | 2.0 | 2.0 |
| $\dot{m}H_{2C}$ | 1.0 | 1.0 | 0.5 | 1.5 | 2.0 |

(C) Resultant data are presented in Figure 77 and Table 14.

(4) Test 099F

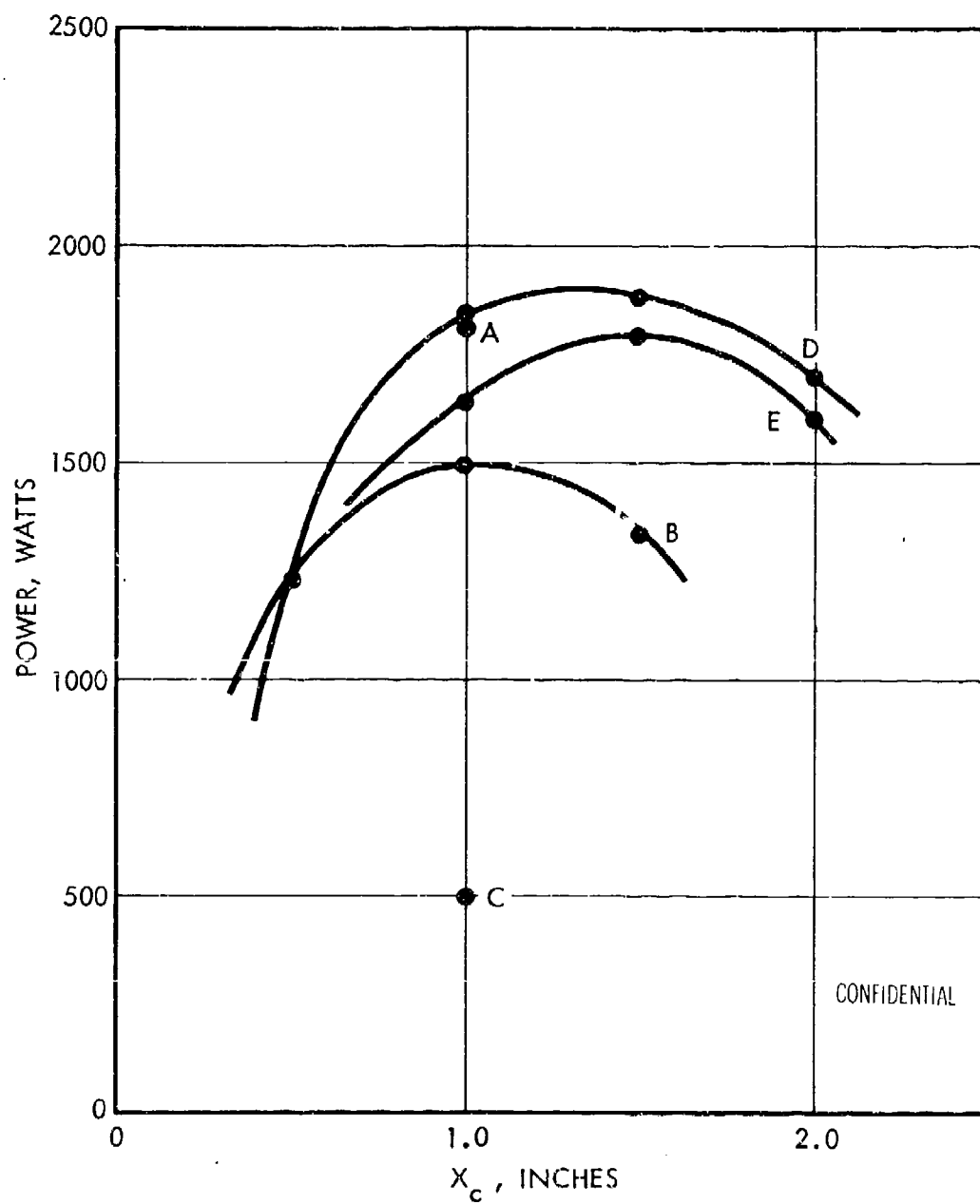
(C) This was a special test conducted to determine the effect of helium diluent distribution between the precombustor and optical cavity. Flow conditions were designed to give the same nozzle inlet temperature as for the nominal flow condition.

(C) Target flow conditions (g/sec) for lasing were:

| | |
|-----------------|------|
| $\dot{m}D_2$ | 0.31 |
| $\dot{m}F_{2p}$ | 5.2 |
| $\dot{m}He_p$ | 1.3 |
| $\dot{m}H_{2C}$ | 1.0 |
| $\dot{m}He_C$ | 0.7 |

(C) Reduced test data and specific power computations are tabulated in Table 14 and the data are presented by Figure 77.

CONFIDENTIAL

Figure 76. Closed Cavity Power X_c Scan for Test 098 (U)

CONFIDENTIAL

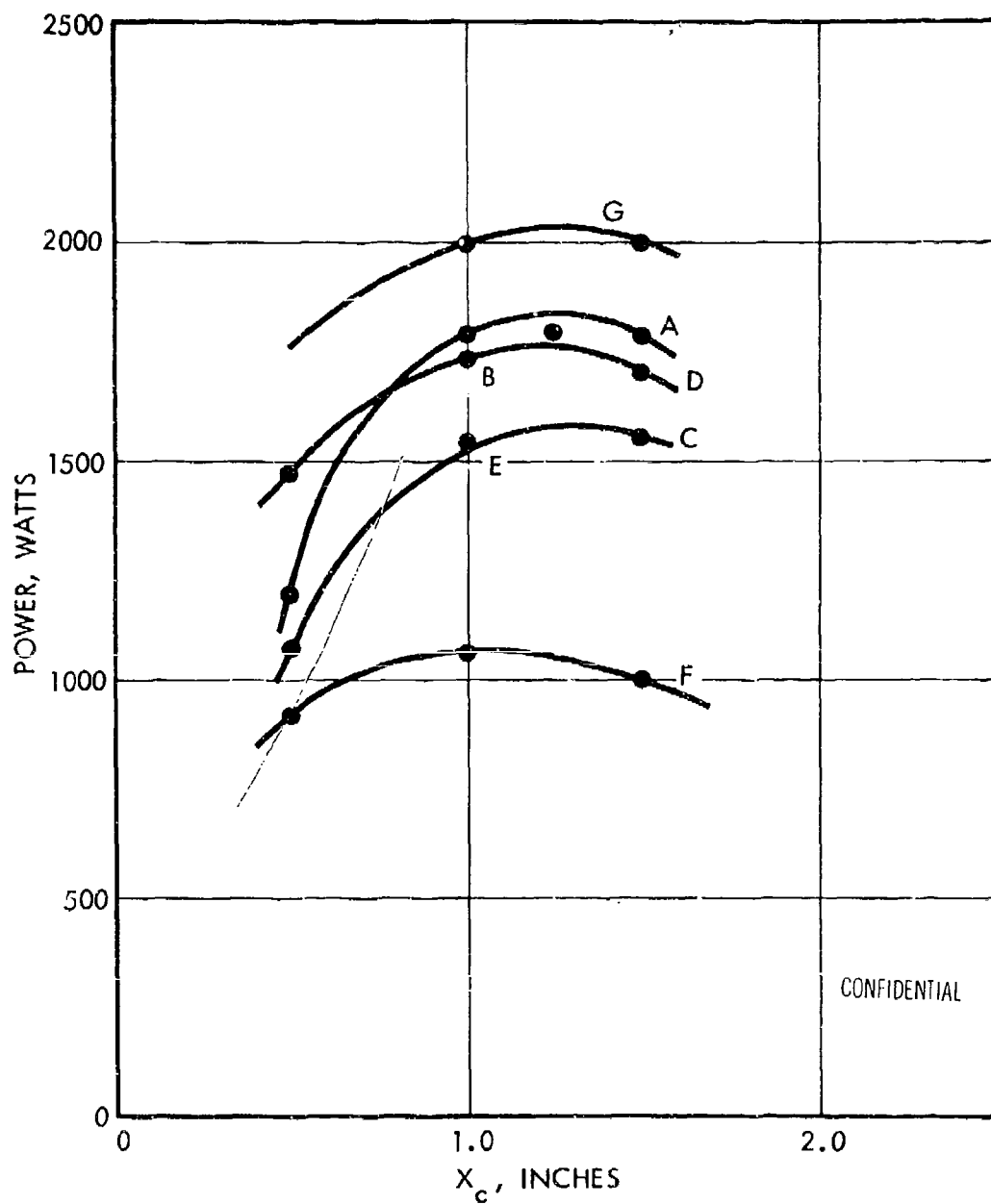


Figure 77. Closed Cavity Power X_c Scan for Test 099 (U)

(5) Tests 099G and H

(C) These tests were conducted to obtain an initial evaluation of increases of flow rates. Total reactant and diluent flow rates were increased in two 20% increments to obtain total and specific power data. It was noted that a flow increment of about 40% would be the maximum obtainable without a change in the flow-control orifices. Inasmuch as the probability of an abnormal heating condition was not high, the mirror extensions were not installed.

(C) Target flow conditions (g/sec) for lasing were:

| <u>Test No.</u> | <u>99G</u> | <u>99H</u> |
|-----------------|------------|------------|
| $\dot{m}F_{2p}$ | 6.6 | 7.7 |
| $\dot{m}D_{2p}$ | 0.42 | 0.49 |
| $\dot{m}He_p$ | 2.4 | 2.8 |
| $\dot{m}H_{2C}$ | 1.2 | 1.4 |

(C) Reduced data for these tests are tabulated in Table 14. As noted below, the laser power data for test 099H may be invalid but is reported as measured.

(6) Problems and Corrective Action

(C) No significant problems or failures of hardware or instrumentation were experienced during the test series until test HB5-099H. This test was aborted when it was observed that an abnormal mirror cooling water temperature rise was being experienced between the curved and flat mirrors. Post-test examination revealed that what appeared to be RTV sealant had extruded from back of the nozzle block, burned, and had become deposited on the curved mirror surface. It was also noted that the cavity cover plates were very hot relative to measurements made with previous higher than nominal flow rates.

(C) These mirrors were judged unsatisfactory for use as power calorimeters. First, their slow response to changes in power conditions necessitated long run durations causing excessive reactant and diluent consumption. Secondly, they were believed to yield erroneously low

to all power data. New improved mirrors were designed and made available before further power survey tests were conducted. Additionally, water-cooled cavity plates were designed and fabricated.

(7) Tests 100 and 101

(C) Tests No. 100 and 101 were performed utilizing a new set of TRW mirrors specifically designed for improved calorimetry. Several of the above described tests from series 097 to 099 were repeated to confirm power measurement corrections. Tests under the exact same conditions, using both the Aerospace Corporation and redesigned TRW mirrors, confirmed a 33% correction with a standard estimate of error of only 6%.

(8) Tests 100A - D

(C) These tests were conducted to confirm the results from test 097 and further investigate the effects of combustor temperature on specific power. Results are presented in Figure 78 and Table 14.

(9) Tests 101A - C

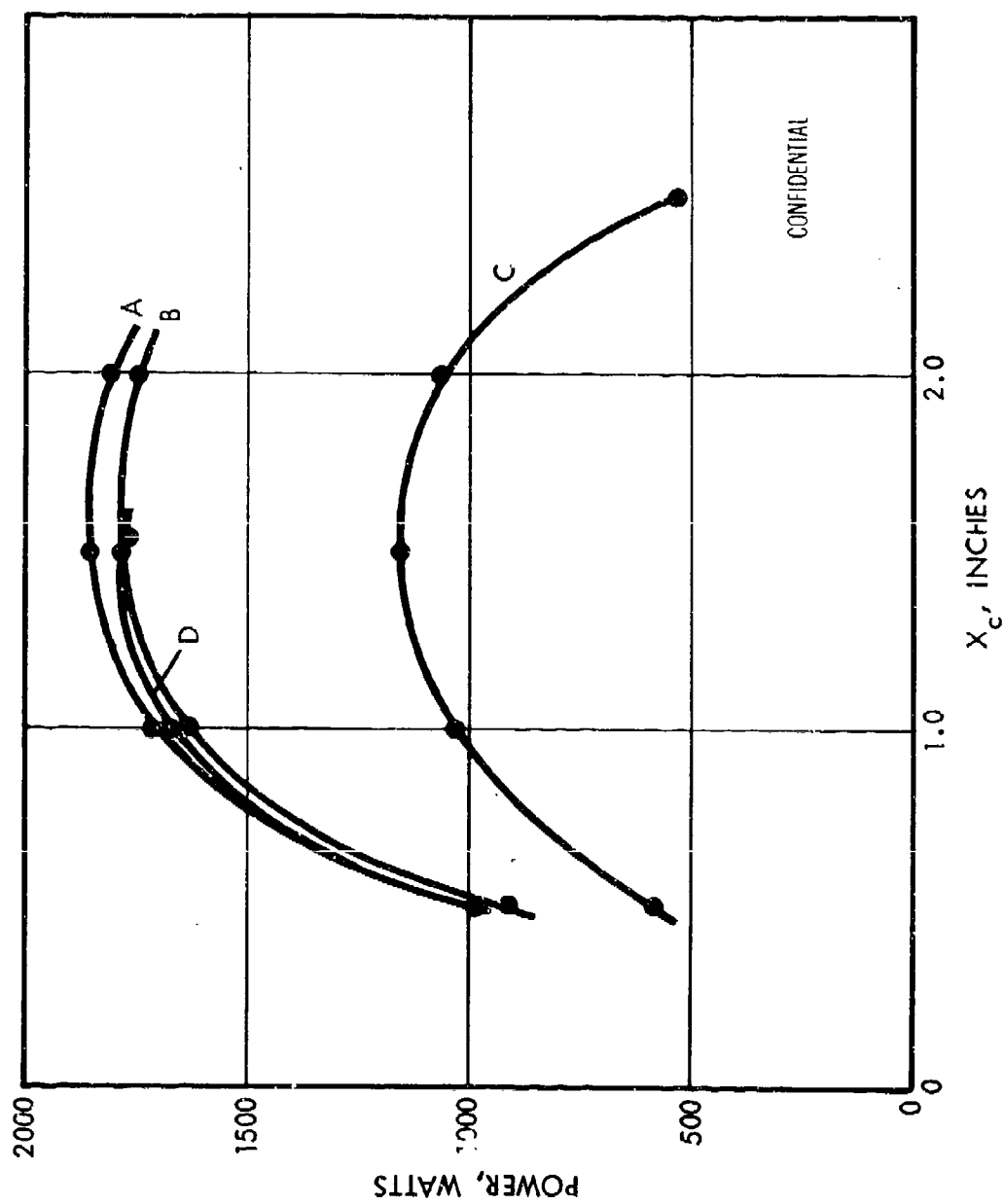
(C) These tests were conducted to confirm the results from test 099 and further investigate the effects of cavity H_2 flow. The tests were performed at increased mass flow and power. Results are presented in Figure 79 and Table 14.

(10) Tests 103 and 112

(C) These tests were performed to determine the effects of cavity pressure on the operating characteristics of the CL-II 1/2 x 7 inch nozzle. The redesigned TRW mirror calorimeters were used and no corrections to power data were required. Cavity pressures from 0.065 psia (3.2 torr) to 0.129 psia (6.5 torr) were evaluated. The results are presented in Figure 80 and Table 15. Test No. 100B is added as a baseline reference at a cavity pressure of 0.025 psia (≈ 1.2 torr).

(C) All subsequent tests of the 1/2 x 7 inch nozzle were concerned with diagnostic testing using the plane parallel resonator system. The results of these tests were inclusive and are discussed in the appendix.

CONFIDENTIAL

Figure 78. Closed Cavity Power X_c Scan for Test 100 (U)

CONFIDENTIAL

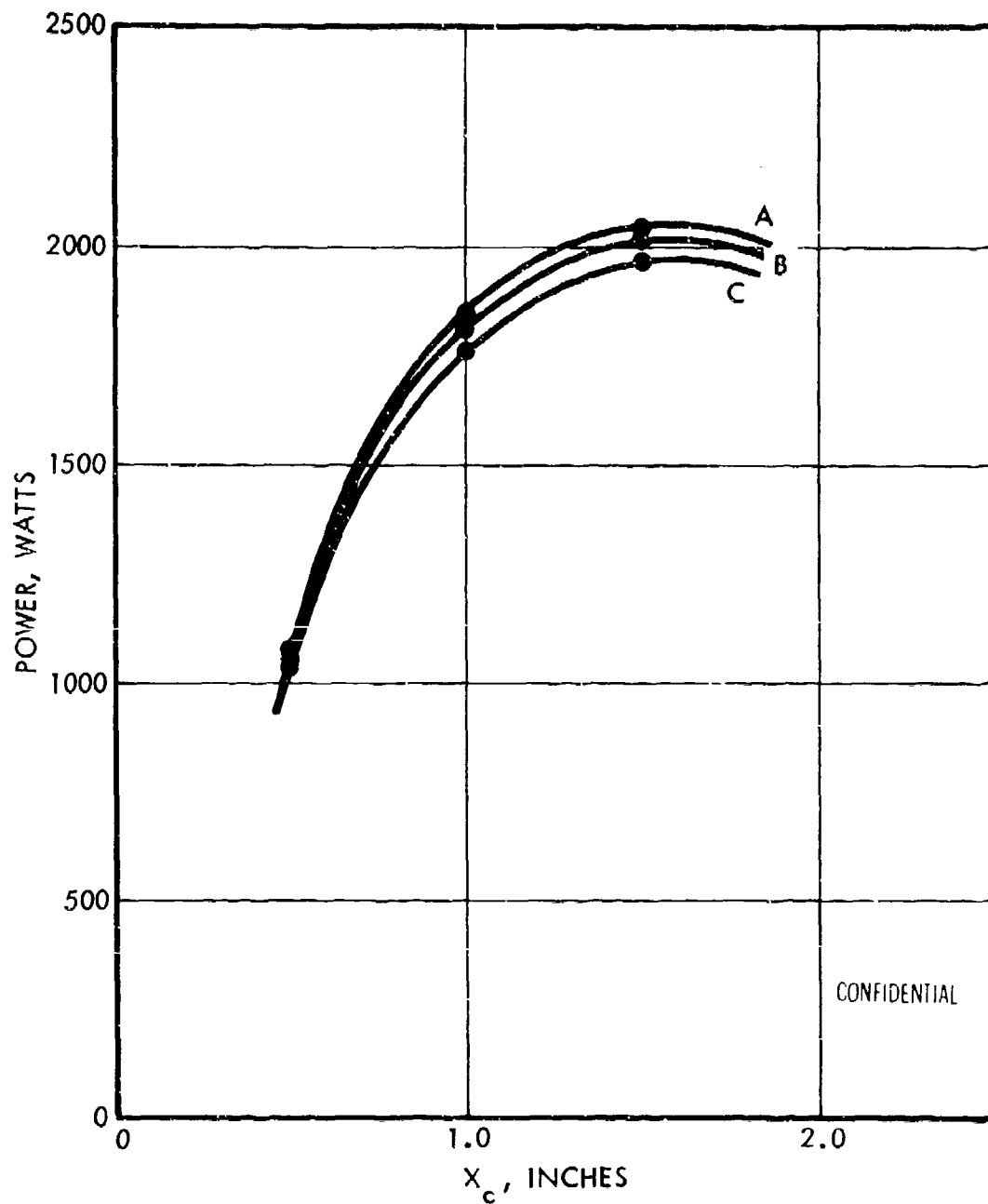
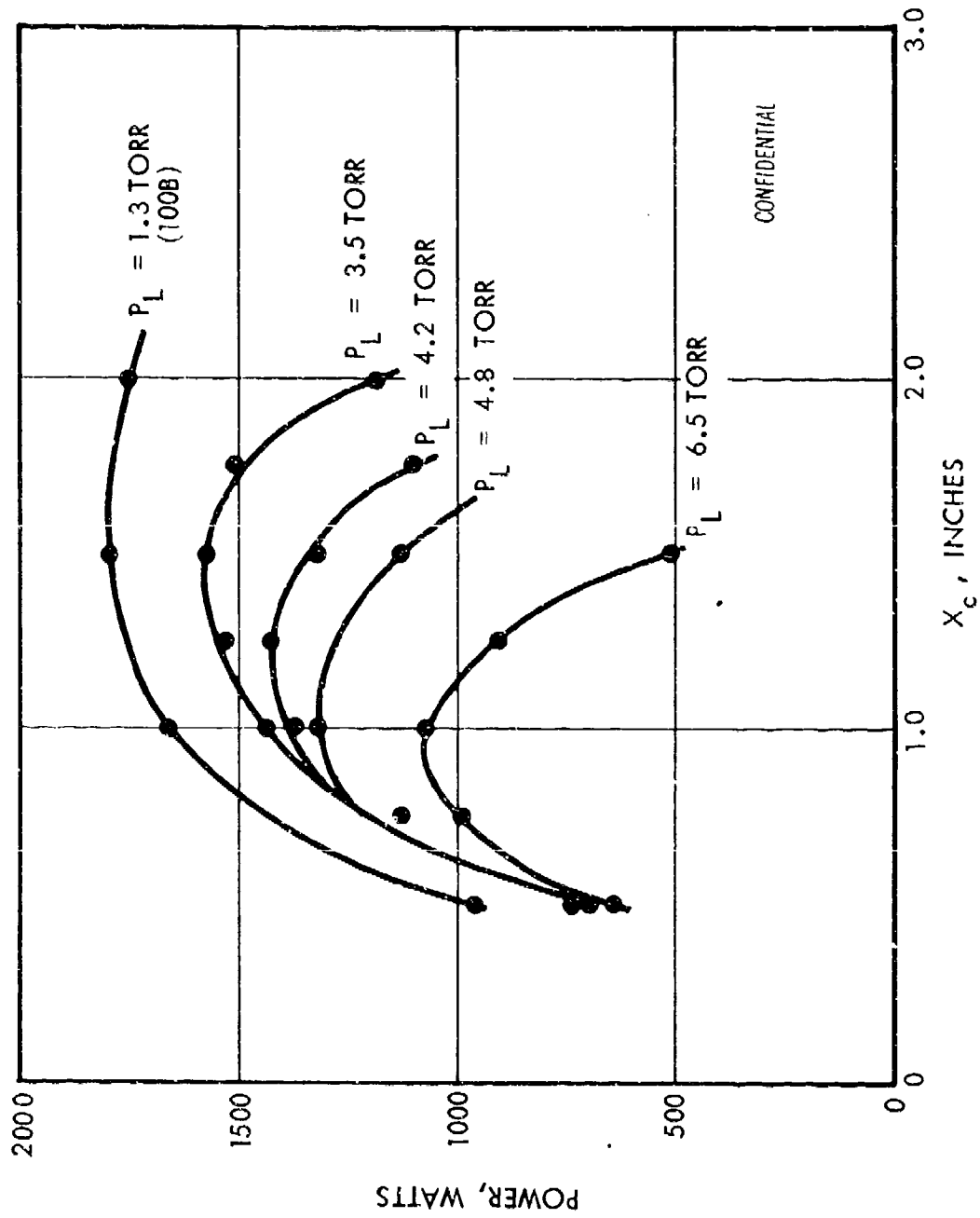


Figure 79. Closed Cavity Power X_c Scan for Test 101 (U)

Figure 80. Closed Cavity Power X_c Scan for Tests 103 and 112 (U)

CONFIDENTIAL

Table 15 is a foldout located on page 277.

CONFIDENTIAL
(This page is Unclassified)

b. Regression Analysis of 1/2 x 7 Inch Nozzle Data

(C) Before any correlation was possible, it was first necessary to evaluate differences between power level readings indicated by the Aerospace Corporation mirror system, the original TRW mirrors, and the new TRW mirror system. It was found, by reviewing tests conducted under the exact same conditions, that the Aerospace mirrors gave power readings 33 percent greater than the original TRW mirrors; the standard deviation was 6 percent. Therefore, all data were corrected to the power levels that would have been detected had the Aerospace mirrors been utilized on all tests. New TRW mirrors designed to correct earlier deficiencies, confirmed almost exactly the power level differences between the original TRW mirrors and the Aerospace mirrors.

(C) Next, it was necessary to establish a means of rapidly determining the maximum power point during a given mirror sweep conducted on each test. A second degree curve fit program was set up on a remote terminal, time shared computer to evaluate the various corrected mirror power levels and the corresponding X_c readings and to determine the location of the maximum power level and its corresponding X_c . For this regression analysis only the peak power was considered.

(C) Two laser systems were included in the data analysis; these were the CL-I and the CL-II systems. The CL-I system consisted of a combustor and divergent section; the latter was used as a mixer and inlet to a rectangular nozzle bank. The CL-II system eliminated the divergent section and combined both the precombustor and the mixer into one unit. The absence of the divergent section greatly reduced heat loss to the walls of the unit, allowing for a more nearly adiabatic reaction; the heat not rejected to the walls could be utilized to dissociate more fluorine; with a subsequent increase in laser specific energy. All regression analyses included one independent variable to account for first-order differences between the CL-I and CL-II laser configurations.

(C) Equilibrium conditions are assumed to exist within the mixer and inlet to the nozzle bank. Combustion temperature and atomic fluorine concentration for correlation analyses were determined by thermochemical

(C) equilibrium calculations in the combustor; the calculations include the contribution from the heat of reaction, and dissipation in the heat loss to the walls of the combustor, the heat of dissociation of the F_2 , and the heat capacity of the resulting gases. Furthermore, frozen conditions were assumed to exist through the nozzle bank, this is justified by the small transit time through the nozzles. The recombination of F in the nozzle boundary layers was neglected in these calculations. The effect of including this refinement would be to reduce the specific power levels discussed below by less than 10 percent.

(C) Probably the most significant result of the data analysis from scaling, operating, and design-criteria standpoint is presented in Figure 81 where specific power based on atomic fluorine flow is correlated with combustion temperature. This curve presents data from both the CL-I and CL-II 1/2 x 7 inch laser tests. Effects of cavity pressure, cavity fuel flow and helium diluent flow variations have been removed by regression analysis methods. The curve shows a linear dependence of specific power/gram of atomic fluorine injected into the cavity with combustion temperature. The standard error of estimate for this curve is $\pm 8\%$.

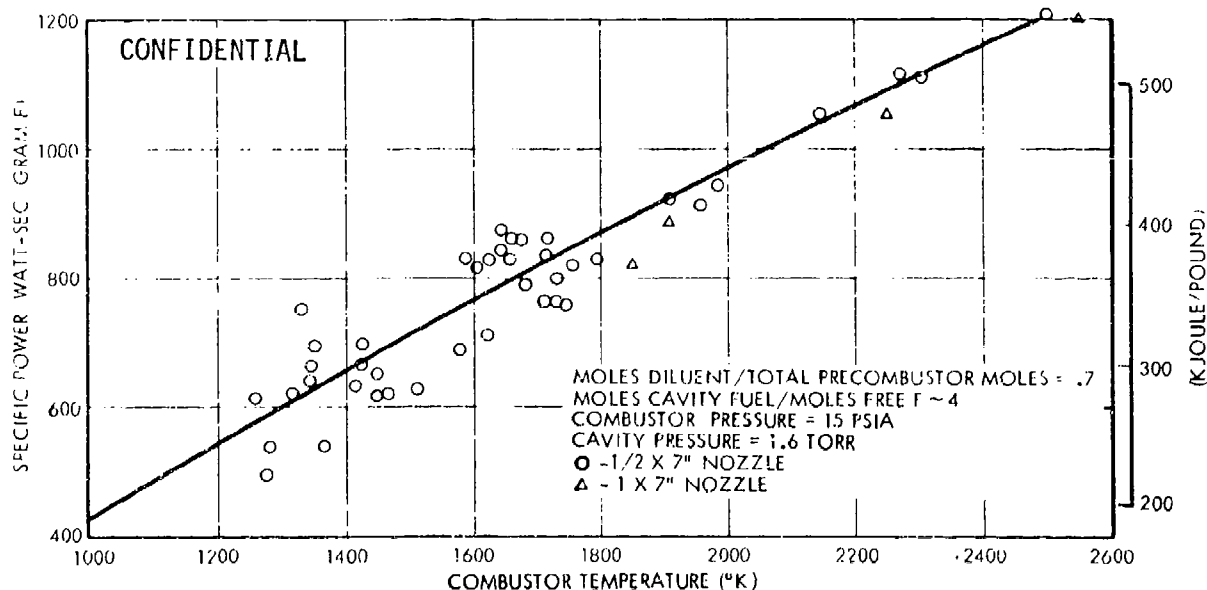


Figure 81. Specific Power vs Mixer Temperature for CL-I and CL-II Laser Tests (U)

(C) All the data presented in Figure 81 are corrected to the conditions stated, and as one can see, the correlation to F-atom concentrations is quite strong. The variation of the specific energy with the mixer temperature could be a fluid mechanical effect in that the velocity at the nozzle exit varies according to the square root of the absolute inlet temperature. In other words, higher velocity ratios of F to H_2 jets could possibly produce more efficient lasing conditions. Obviously, this effect, if fluid mechanical, cannot continue indefinitely. The range of our data is limited, but one would expect this curve to eventually have a maximum at some higher temperature. It is interesting to note that the curvature, although slight, is concave and downward, indicating this trend.

(C) The effect of incomplete dissociation of the cavity fluorine is shown by Figure 82. Specific power/gm of total cavity fluorine drops off markedly at combustor temperatures below $1400^\circ K$. Below $1400^\circ K$ the dissociation of excess fluorine is incomplete for the subject combustor pressure of 15 ± 3 psia. These results agree closely with the Aerospace Corporation results which also show that the cold reaction, $H_2 + F \rightarrow HF^* + H$, appears to be the primary source of usable laser power in this device. That is, fluorine, which is associated F_2 and available for the more energetic $H + F_2 \rightarrow HF^* + F$ reaction, is not contributing to laser power. The decrease in specific power beginning at $1400^\circ K$ is sometimes called the "break point." It is known that subtle interactions of chemistry and energy transfer processes give rise to the breakpoint.

(C) The functional relationship between specific power and cavity fuel flow is shown in Figure 83. It is apparent that the maximum specific energy/gram of total flow occurs at approximately a 3.5:1 mole ratio of cavity fuel flow to dissociated fluorine flow at the slit nozzle exit. Specific power/gram of total flow is not strongly influenced by variations over the range from 2.5:1 to 5:1 mole ratio.

(C) The effect of He diluent flow on specific power/gram of atomic fluorine and specific power/gram of total flow is shown in Figure 84. The optimum specific power/gram of total flow appears to be at a 0.69 mole fraction of He/total precombustor flow. Variation in He diluent mole fraction has a relatively strong influence on specific power.

CONFIDENTIAL

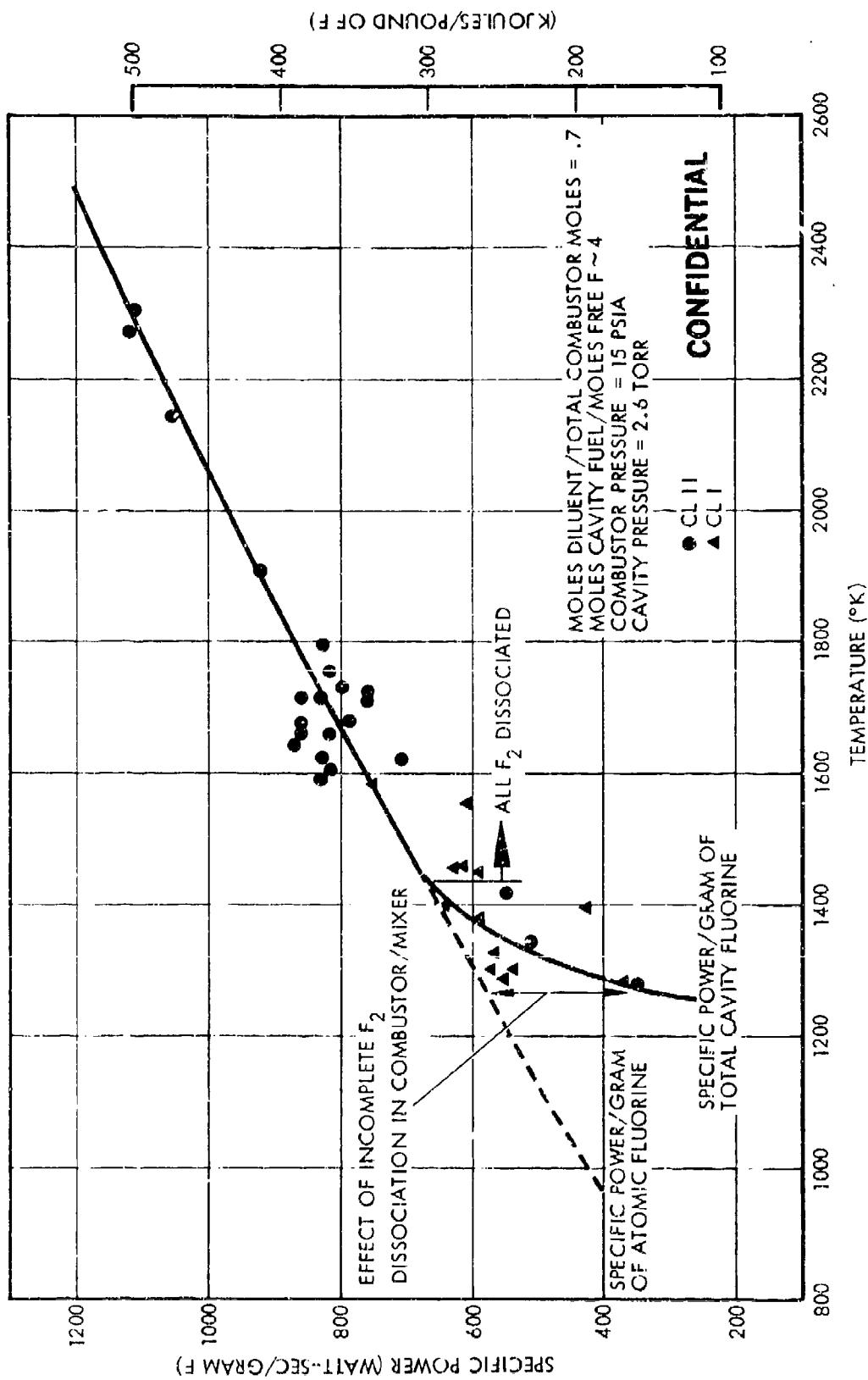


Figure 82. Effect of Incomplete Dissociation of Cavity Fluorine (U)

CONFIDENTIAL

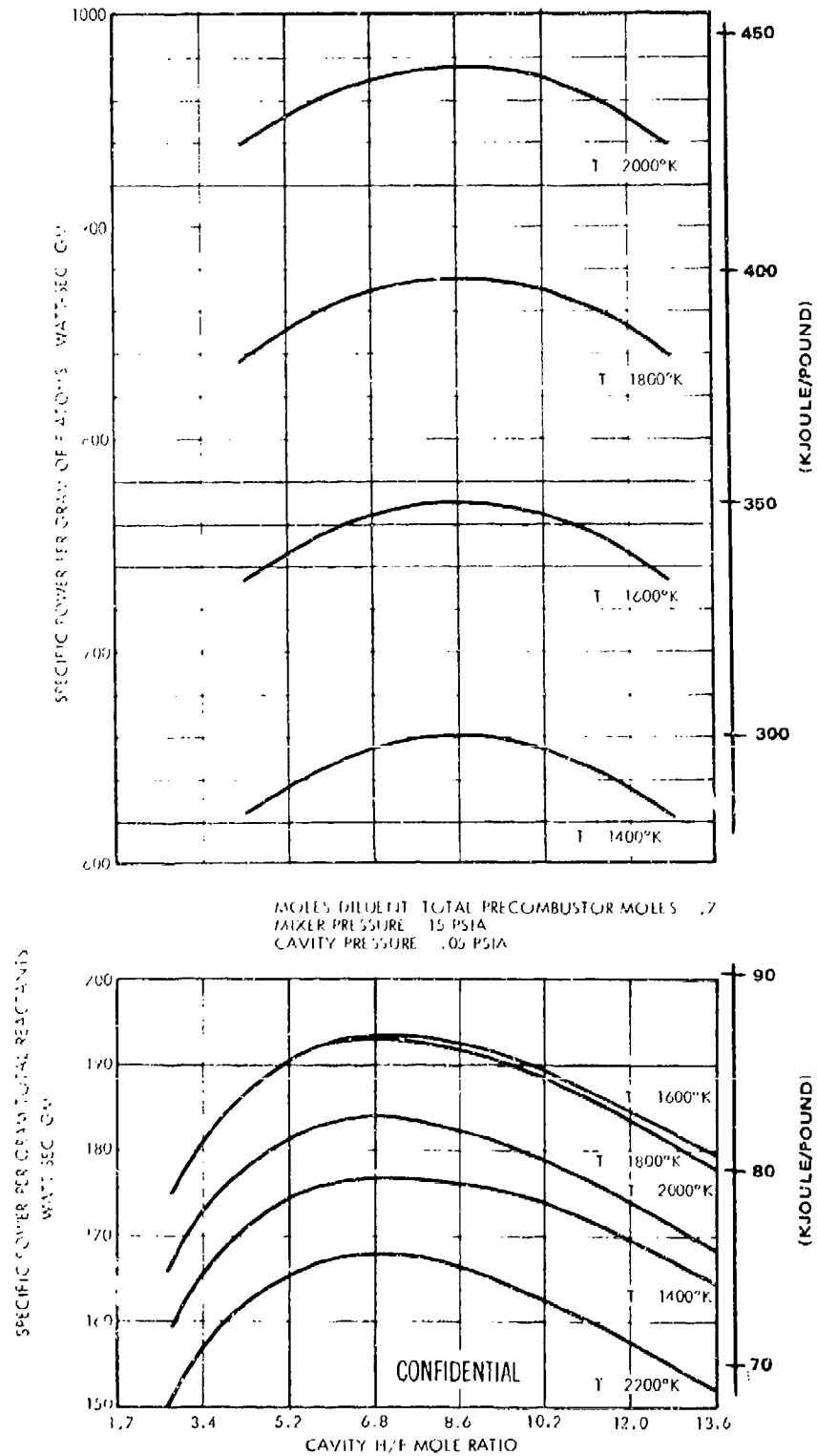


Figure 83. Functional Relationship Between Specific Power and Cavity Fuel Flow (U)

CONFIDENTIAL

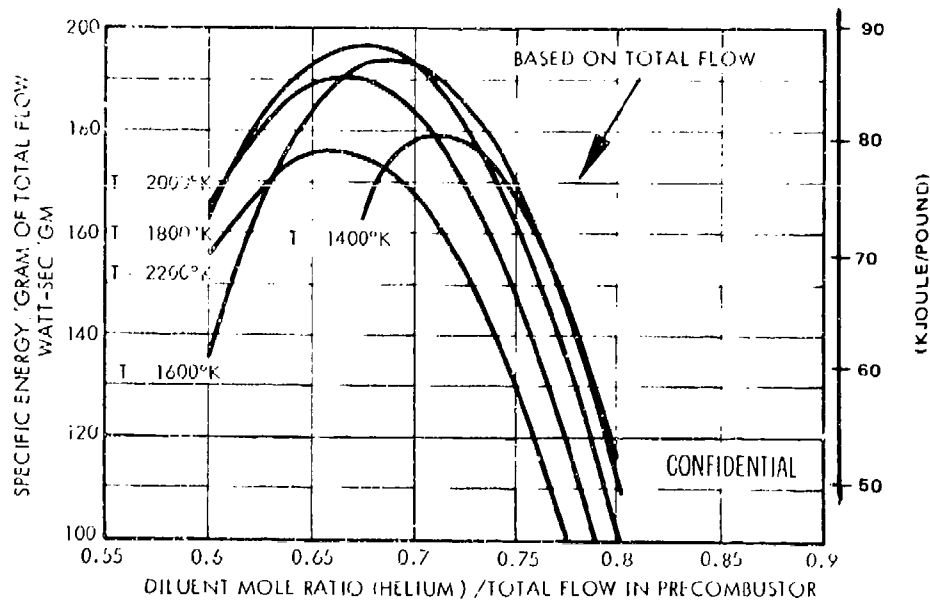
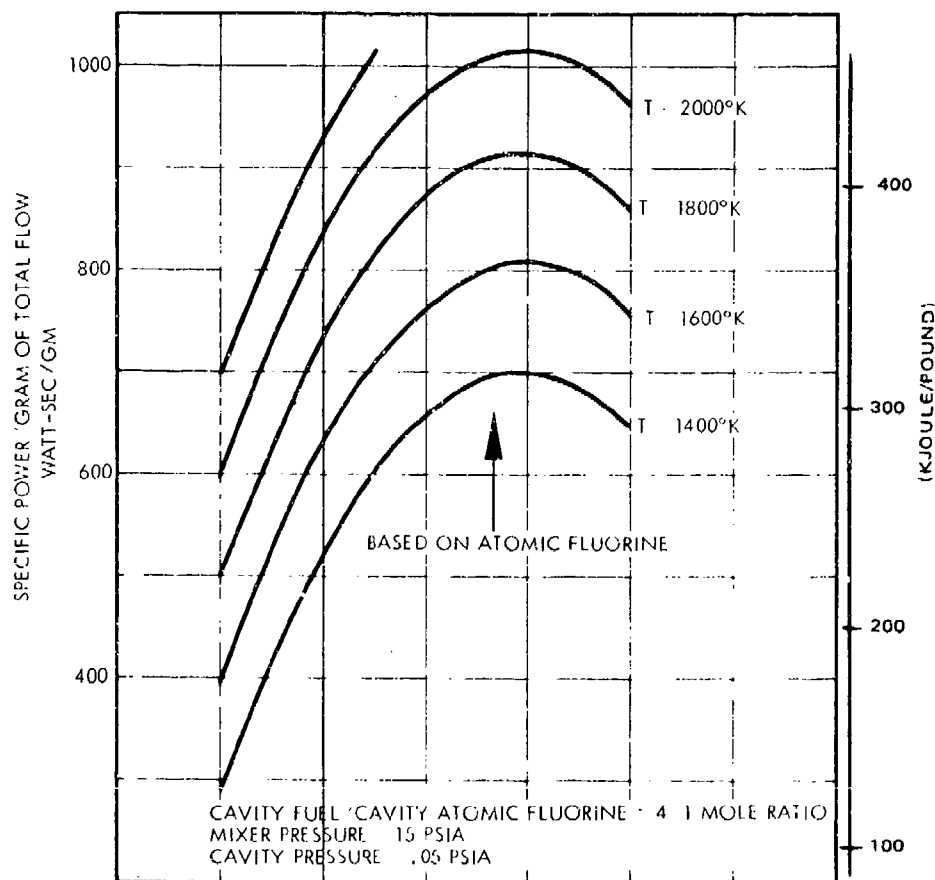


Figure 84. Effect of He Diluent Flow on Specific Power/Gram of Atomic Fluorine and Specific Power/Gram of Total Flow (U)

CONFIDENTIAL

(1) Combustor Heat Losses

(C) Figure 85 provides a summary comparison between the CL-I and CL-II combustor configurations, emphasizing the effects of the differences in precavity heat losses. Basically, the energy lost to the cooling jackets has to be supplied by flow of combustor reactants. Reduction of combustor heat losses, while maintaining the same combustor temperature, directly reduces the total flow required to produce a given atomic fluorine flow, and is therefore directly realized as an increase in specific power. In Figure 85 the increase in combustor mixture ratio indicates that proportionately more fluorine can be introduced, in excess of that required for combustion with reduced heat losses. The CL-II design reduced combustor heat losses by 30 to 35 percent from CL-I and showed an increase in average specific power from 165 to 195 watt-sec/gm of total flow. Extrapolation of this same effect to near adiabatic combustor design, as indicated in Figure 85 would provide over 300 watt-sec/gm of total flow.

(C) The curves shown in Figure 85 peak when the combustor temperature is near 1600°K . Below 1600°K , the effects of lower combustor temperature plus, at even lower temperatures, the effects of incomplete fluorine dissociation dominate. Above 1600°K more combustor reactant flows are being introduced without commensurate increase in free fluorine flow or the compensating temperature effect.

c. CL-II 1 x 7 Inch Nozzle Test Results

(C) The CL-II 1 x 7 inch nozzle assembly testing was initiated on May 25, 1971, beginning with test HB5-151. (See appendix for hardware description.) The objective of the initial test series, tests 151 through 161, was to determine the optimum operating conditions for the 1 x 7 inch nozzle, evaluate the effects of combustor operating temperature, helium diluent flow variations, cavity H_2 flow variations, and cavity pressure variations, and to select operating conditions for subsequent diagnostics.

CONFIDENTIAL

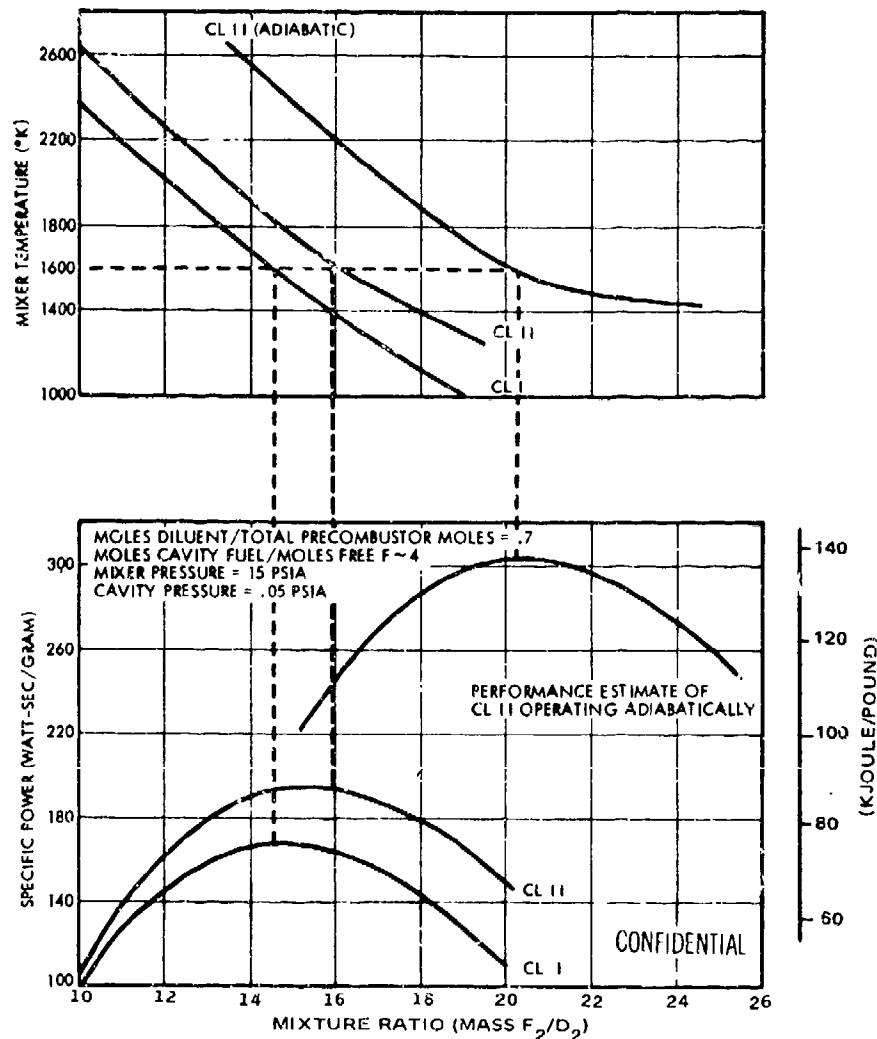


Figure 85. Summary Comparison Between CL-I and CL-II Combustor Configurations (U)

(1) Test 151

(C) Test 151B was conducted to evaluate the design nominal operating point of the 1 x 7 inch nozzle. Flow rates were established at exactly 2 times the 1/2 x 7 inch nozzle design flows. Figure 86 shows the power versus X_c plot for test 151B1 and the results of test 151B2 have been added to show the effect of 1 gm/sec of He added to the cavity H_2 flow. Table 16 contains the tabulation of all significant parameters for test 151.

CONFIDENTIAL

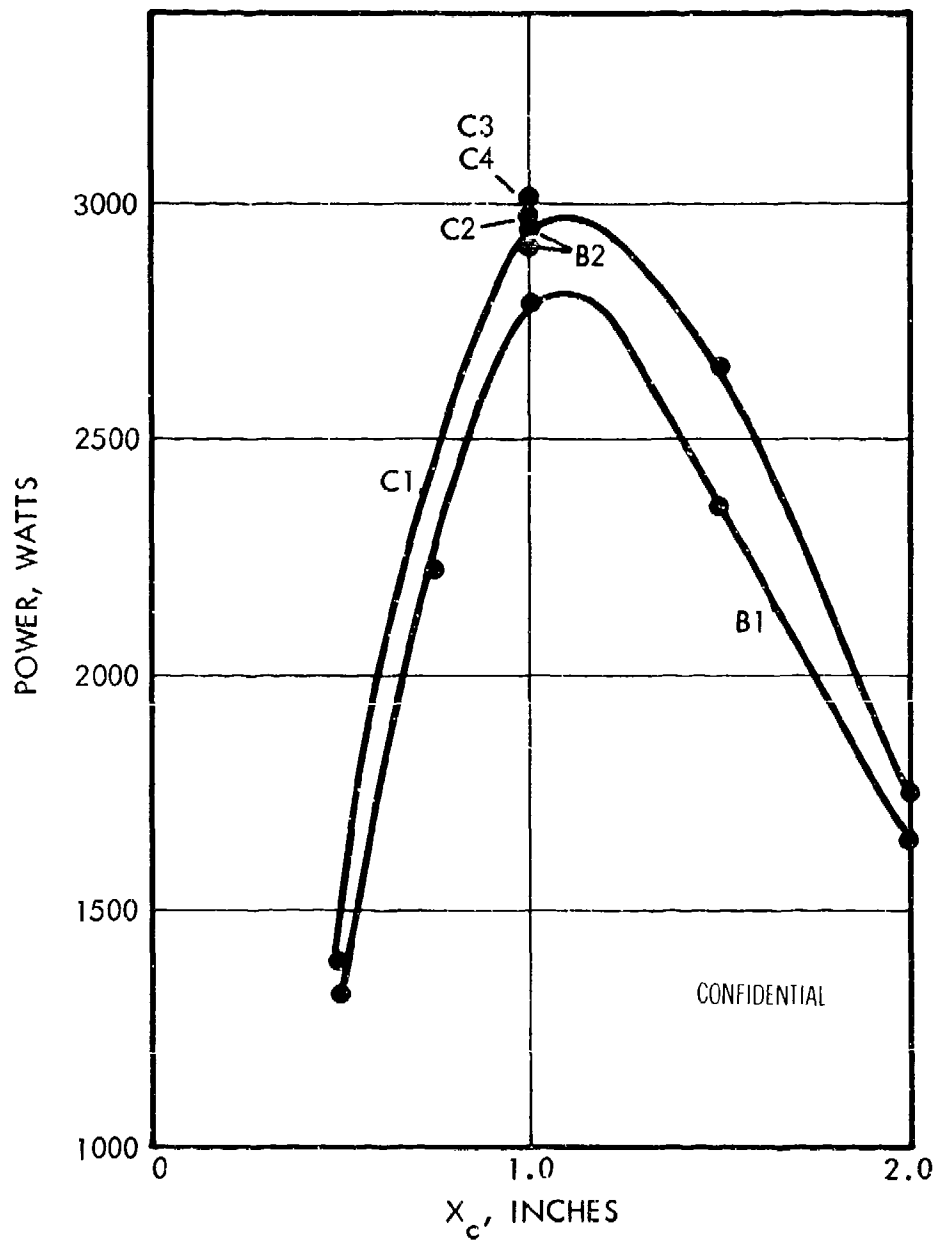


Figure 86. Closed Cavity Power X_c Scan for Test 151 (U)

CONFIDENTIAL

Table 16 is a foldout located on page 278.

CONFIDENTIAL
(This page is Unclassified)

(C) Test 151C1 was conducted at an increased total flow rate of 20%. Tests 151C2, C3, and C4 were run to show effects of continuing to increase the helium addition to the cavity H_2 injection. Specific values of these flows are presented in Table 16.

(2) Test 152

(C) Test 152 was a scan of the cavity fuel flow; test 152A at increased combustor temperature was performed at 1.5 times nominal cavity H_2 flow. Test 152B1 was performed at 25% of nominal cavity H_2 flow. For tests 152B2, B3, and B4 the cavity H_2 was replaced with He in increasing increments. Figure 87 presents the power versus X_c data and Table 16 is a summary of the significant parameters.

(C) The power versus X_c plots of tests 151 and 152 did not duplicate the shape of the power curves for the lower power $1/2 \times 7$ inch nozzle. A discontinuity appears between $X_c = 1$ and $X_c = 1.5$ in the power profiles. For this reason, the mirrors were replaced with a more refined water cooling design for subsequent tests beginning with test 153.

(3) Test 153

(C) Test 153B was a repeat of test 151B utilizing a more refined mirror cooling passage design. Figure 88 shows the resulting power versus X_c plot. The results indicate that a power loss occurs in the mirror calorimetry water circuits between the X_c position of 1.0 and 1.5, causing erroneous power measurements, particularly at higher power levels. This effect was attributed to the water passage design. The mirrors, with their redesigned and much refined water cooling passages, were used for all subsequent testing.

(4) Test 154

(C) Test 154 was a repeat of 153B. An adjustment was made in the diluent injection method in the combustor. As shown in Figure 89, no change in performance was noted.

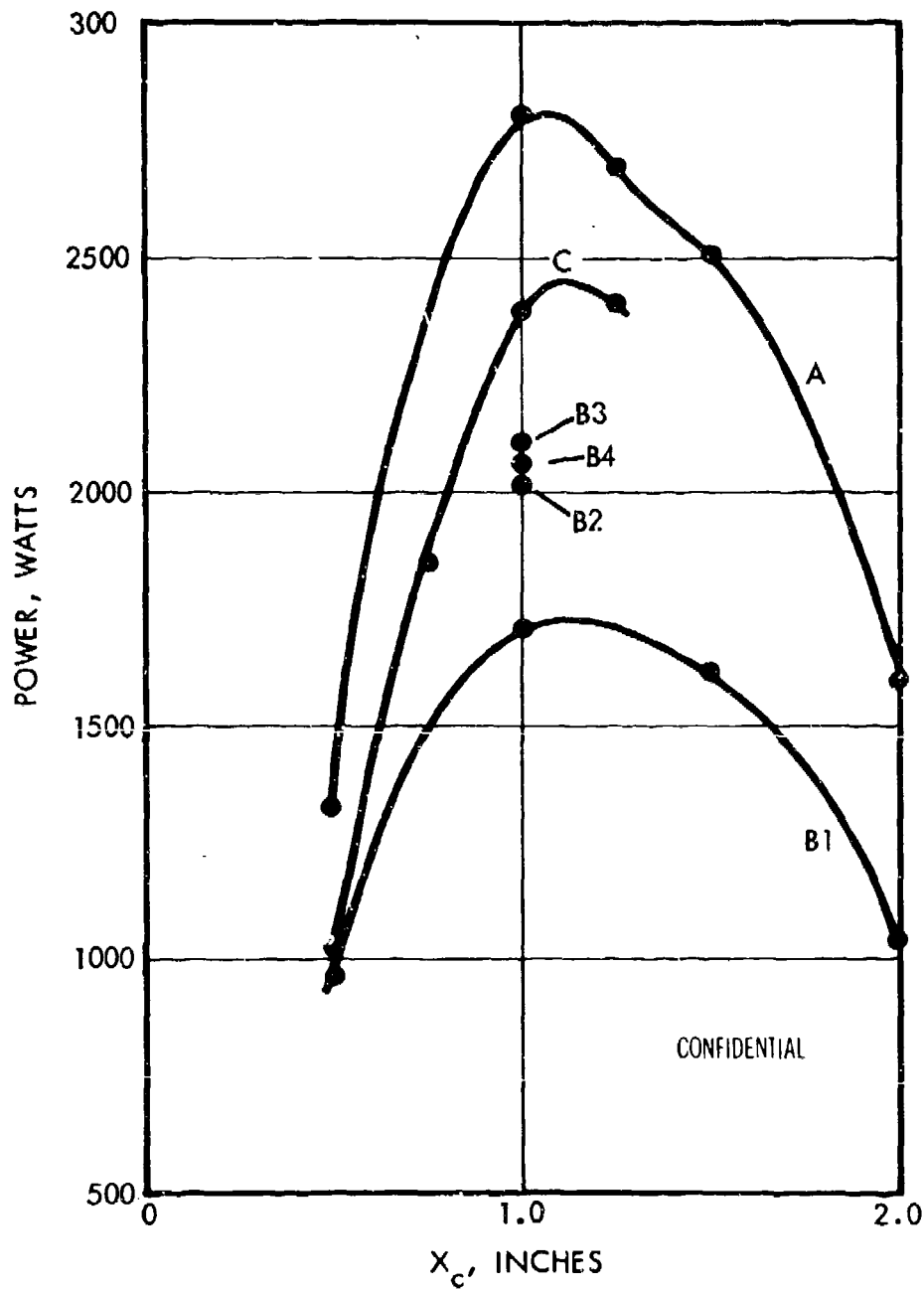
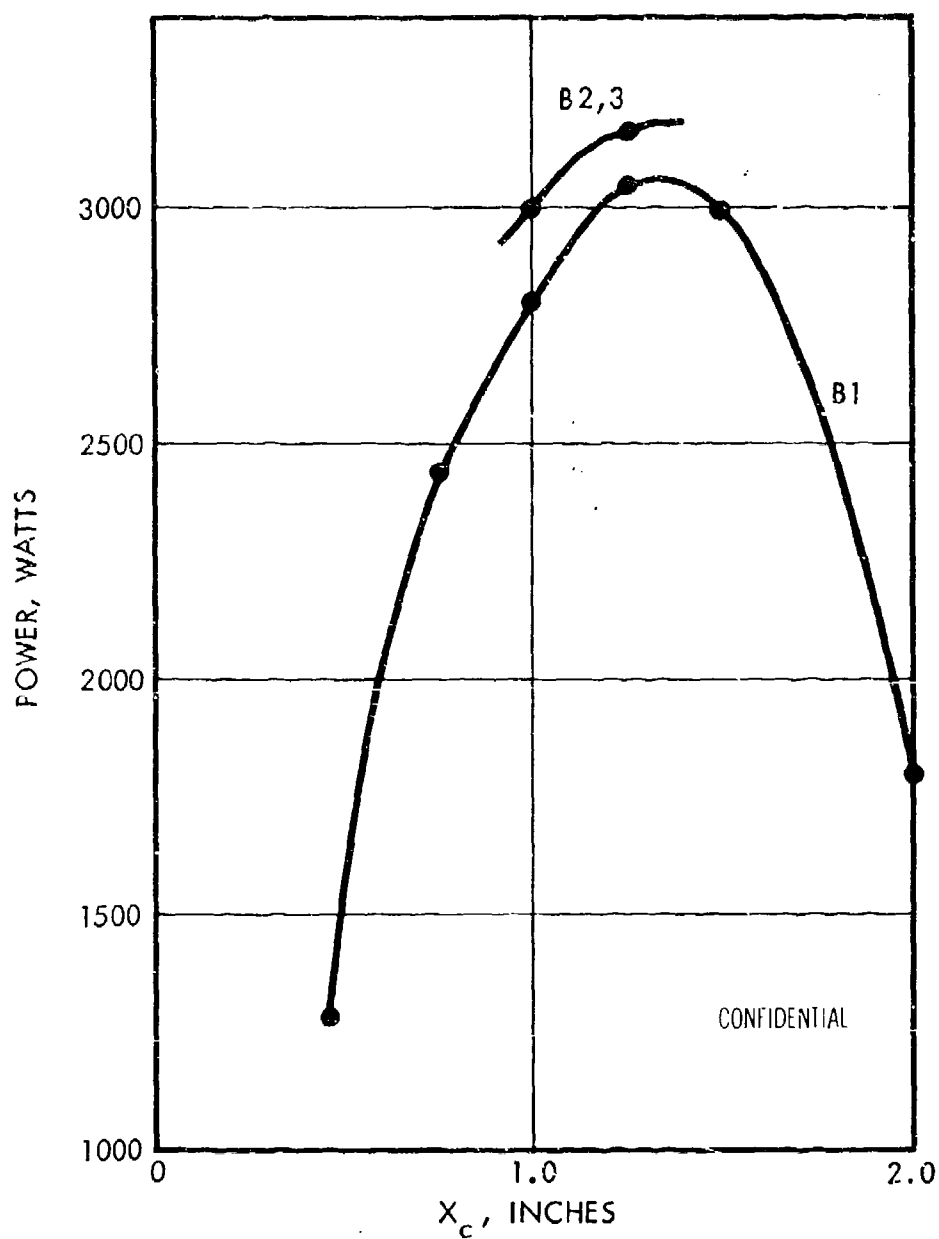


Figure 87. Closed Cavity Power X_c Scan for Test 152 (U)

CONFIDENTIAL

Figure 88. Closed Cavity Power X_c Scan for Test 153 (U)

CONFIDENTIAL

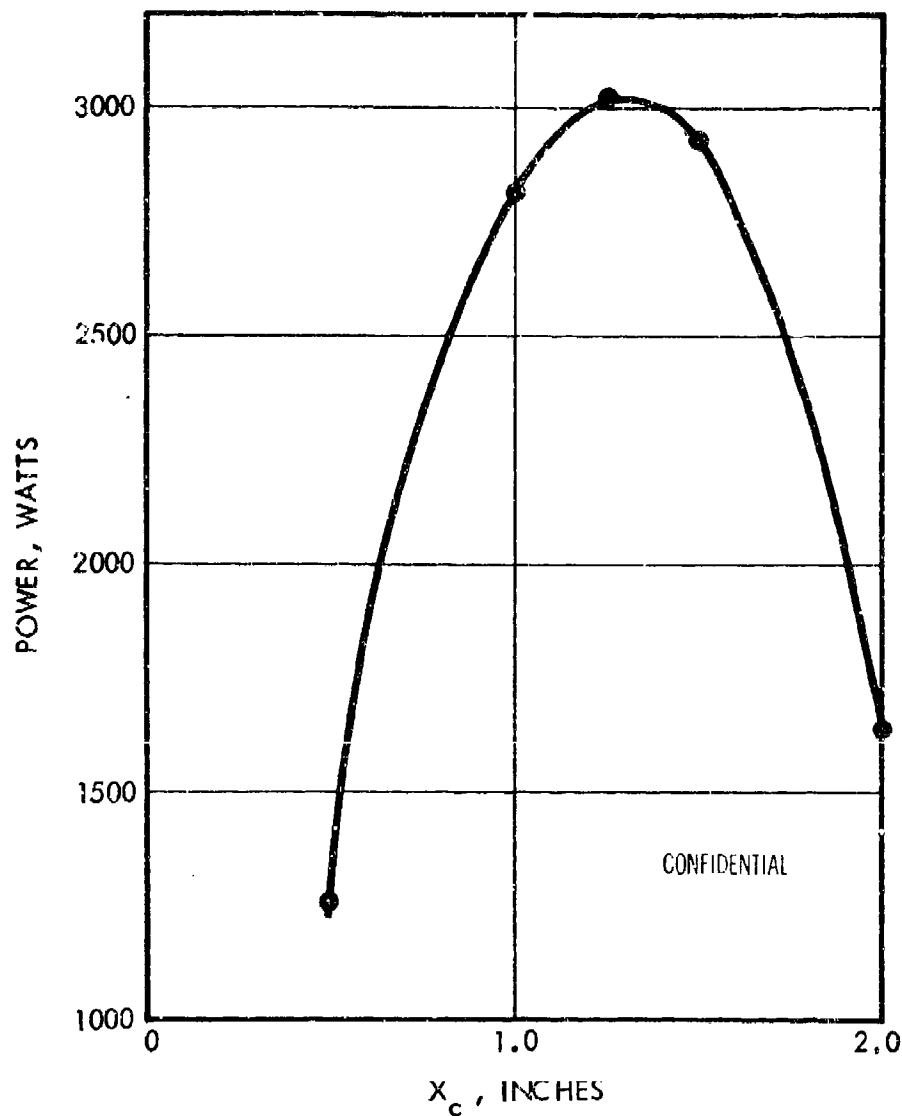


Figure 89. Closed Cavity Power X_c Scan for Test 154 (U)

(5) Tests 155 and 156

(C) Tests 155 and 156 were performed to survey the effect of combustor temperature on the performance of the 1 x 7 inch nozzle configuration. Test 155 was performed at 1976°K while the test 156 operating temperature was 1659°K. The power versus X_c results are presented in Figure 90 and Table 16.

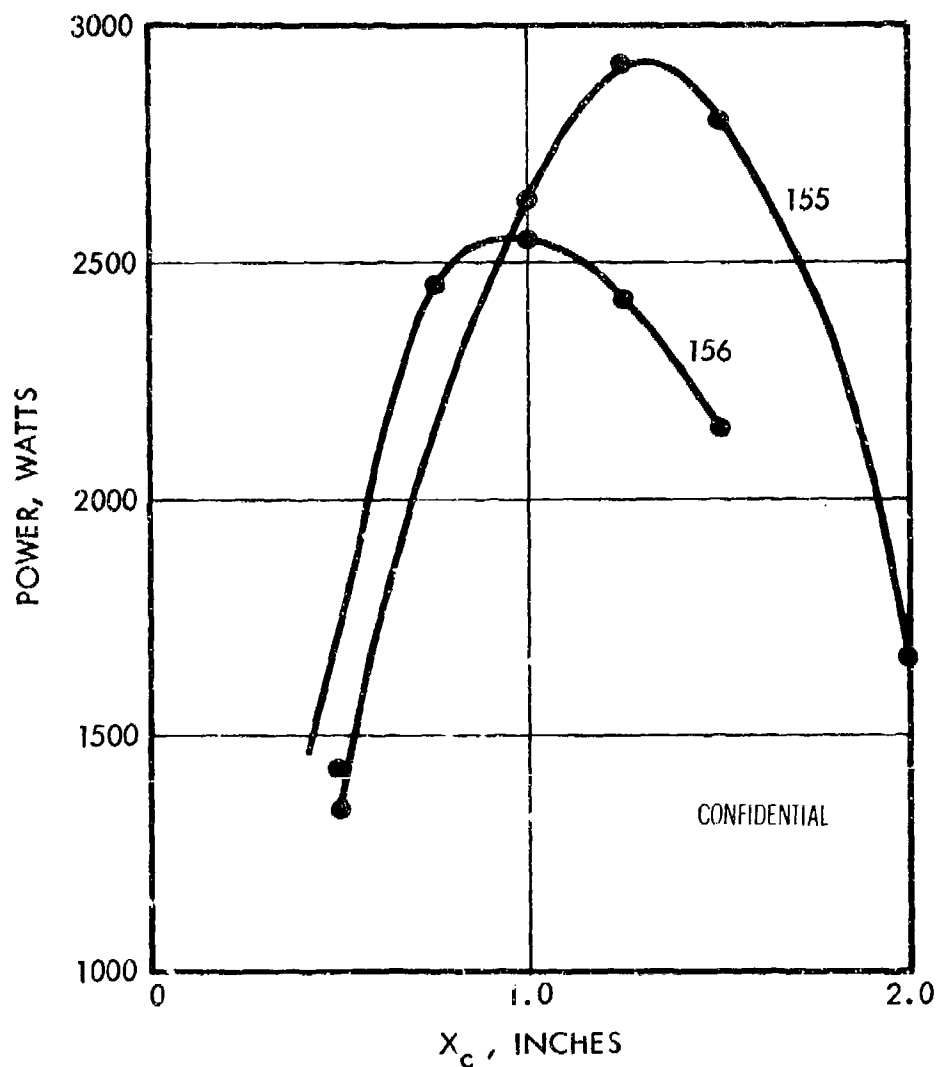


Figure 90. Closed Cavity Power X_c Scan for Tests 155 and 156 (U)

(6) Tests 157, 158 and 159

(C) The purpose of tests 157, 158 and 159 was to evaluate the effect of variations of the diluent flow. Excursions around the nominal diluent ratio, β (He/\dot{F}) of 4.3 were performed. For test 157, β was reduced to 2.4, a reduction of 1.2 gm/sec of helium from the combustor. During test 157B, 0.51 gm/sec of He was introduced with the cavity H_2 . For tests 157B and D, 1 gm/sec and 1.5 gm/sec, respectively, of

helium were added to the cavity H_2 . For test 158, β was increased to 3.3. A further increase to $\beta = 4.6$ was effected for test 159. Performance results are presented in Figures 91 through 93 and Table 16.

(7) Test 160

(C) The objective of test 160 was to evaluate the performance of the 1 x 7 inch nozzle at a 20% reduction of flow rate (total mass flow = 14 gm/sec). A second objective was to evaluate the effect of cavity pressure variations on nozzle performance. The specific power performance of the nozzle was improved significantly by operating at the 20% flow reduction, Figure 94. The 14 gm/sec case was redefined as the nominal case for subsequent tests. The effect of increasing cavity pressure on peak power and X_c profile is shown by Figure 95. Table 15 contains the test conditions corresponding to the curves.

(8) Tests 161 - 210

(C) Tests 161 through 210 were concerned with laser cavity diagnostics under conditions selected from review of the above data. Test results are reported in Section II.

(9) Test 210

(C) Test 210 was a nominal condition test ($\dot{W}_c = 14$ gm/sec). Orange glow photographs were obtained as well as closed cavity power. Results are presented in Figure 96 and Table 17.

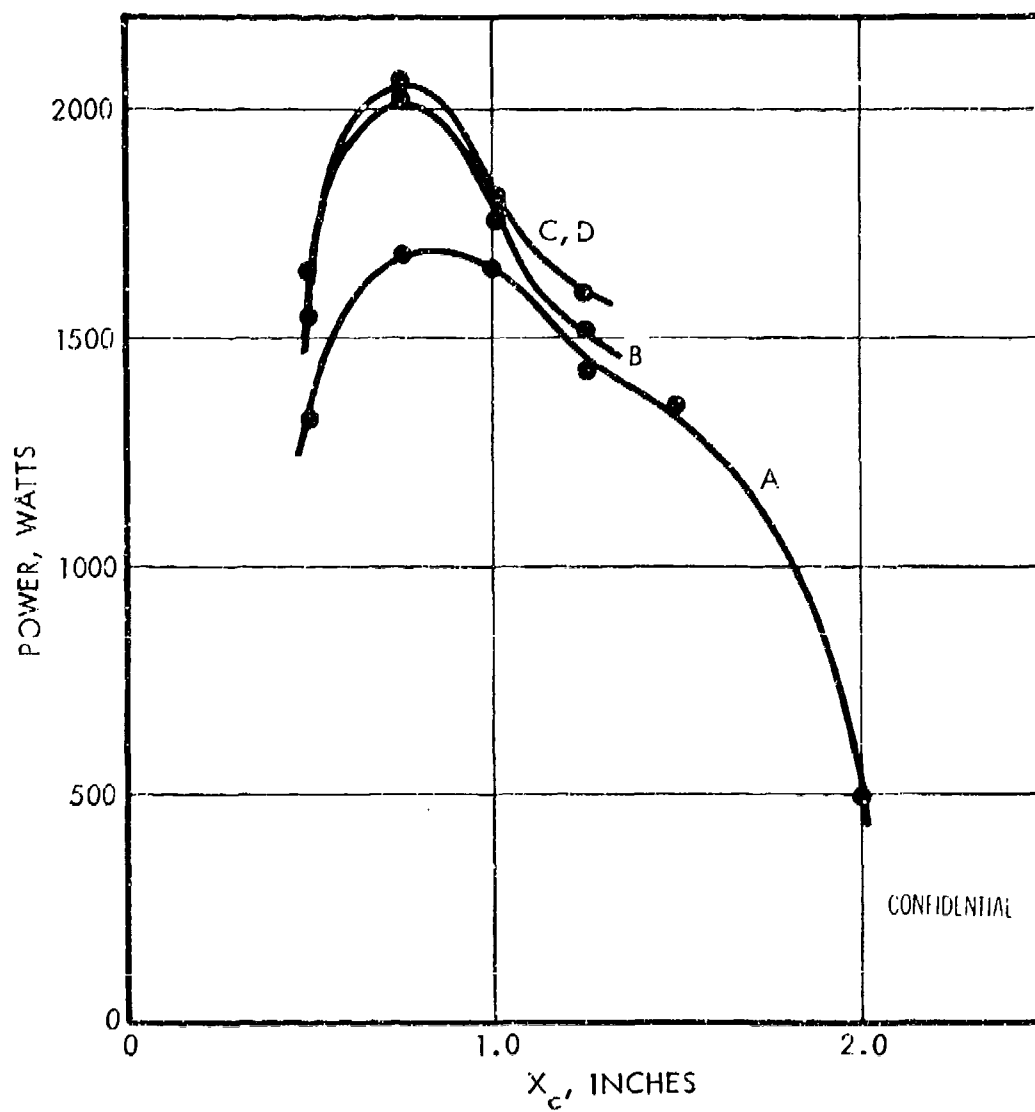
(10) Test 211

(C) A 50% reduction in cavity H_2 flow and replacement with helium on a mole basis yielded slightly improved power. Orange glow photographs were obtained. Results are presented in Figure 97 and Table 17.

(11) Tests 212 and 213

(C) Tests 212 and 213 were performed at combustor temperatures of 2263°K and 2554°K, respectively, while maintaining a nominal total flow of 14 gm/sec. At 2554°K, a specific energy/gram of free fluorine flow of 1203 joules/gm was achieved. Again, orange glow photographs were obtained. Results are presented in Figures 98 and 99 and Table 17.

CONFIDENTIAL

Figure 91. Closed Cavity Power X_c Scan for Test 157 (U)

CONFIDENTIAL

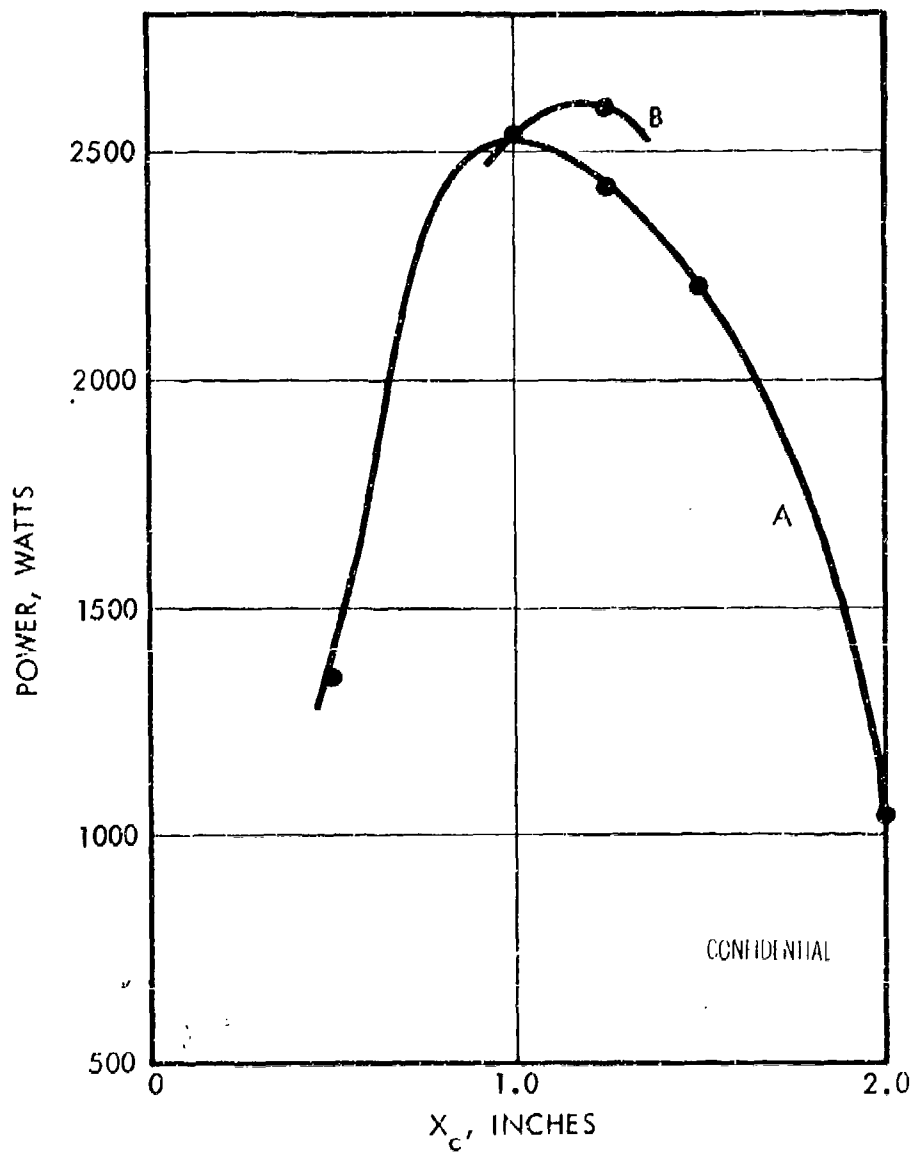
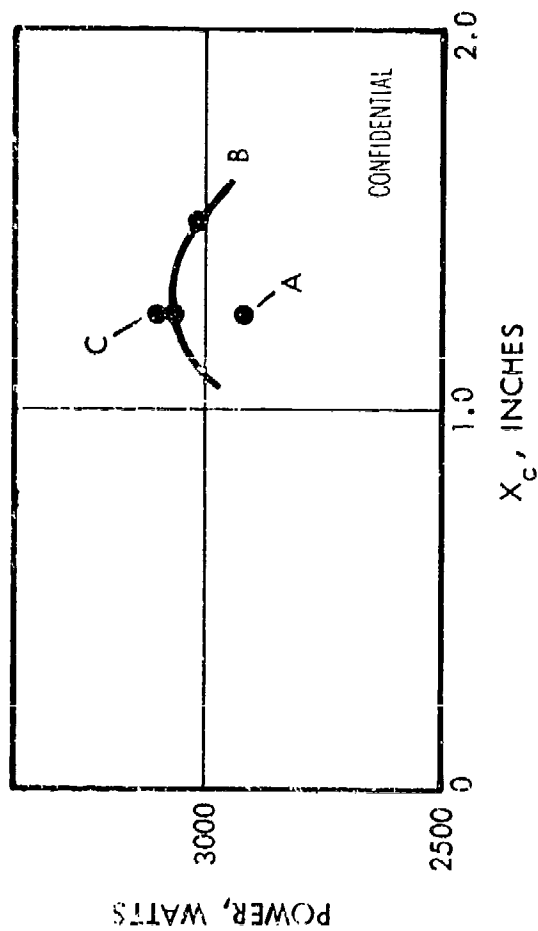


Figure 92. Closed Cavity Power X_c Scan for Test 158 (U)

Figure 93. Closed Cavity Power X_c Scan for Test 159 (U)

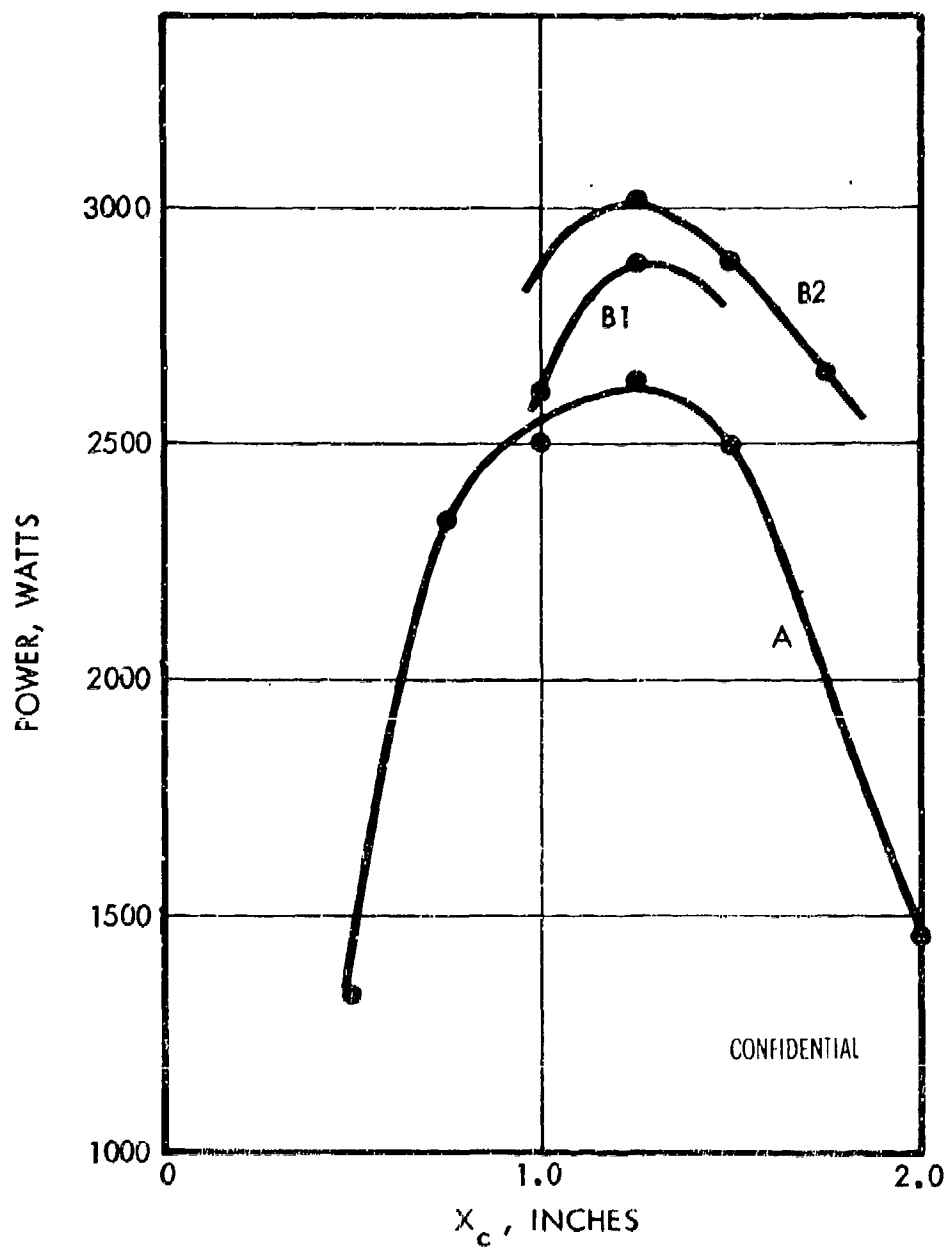
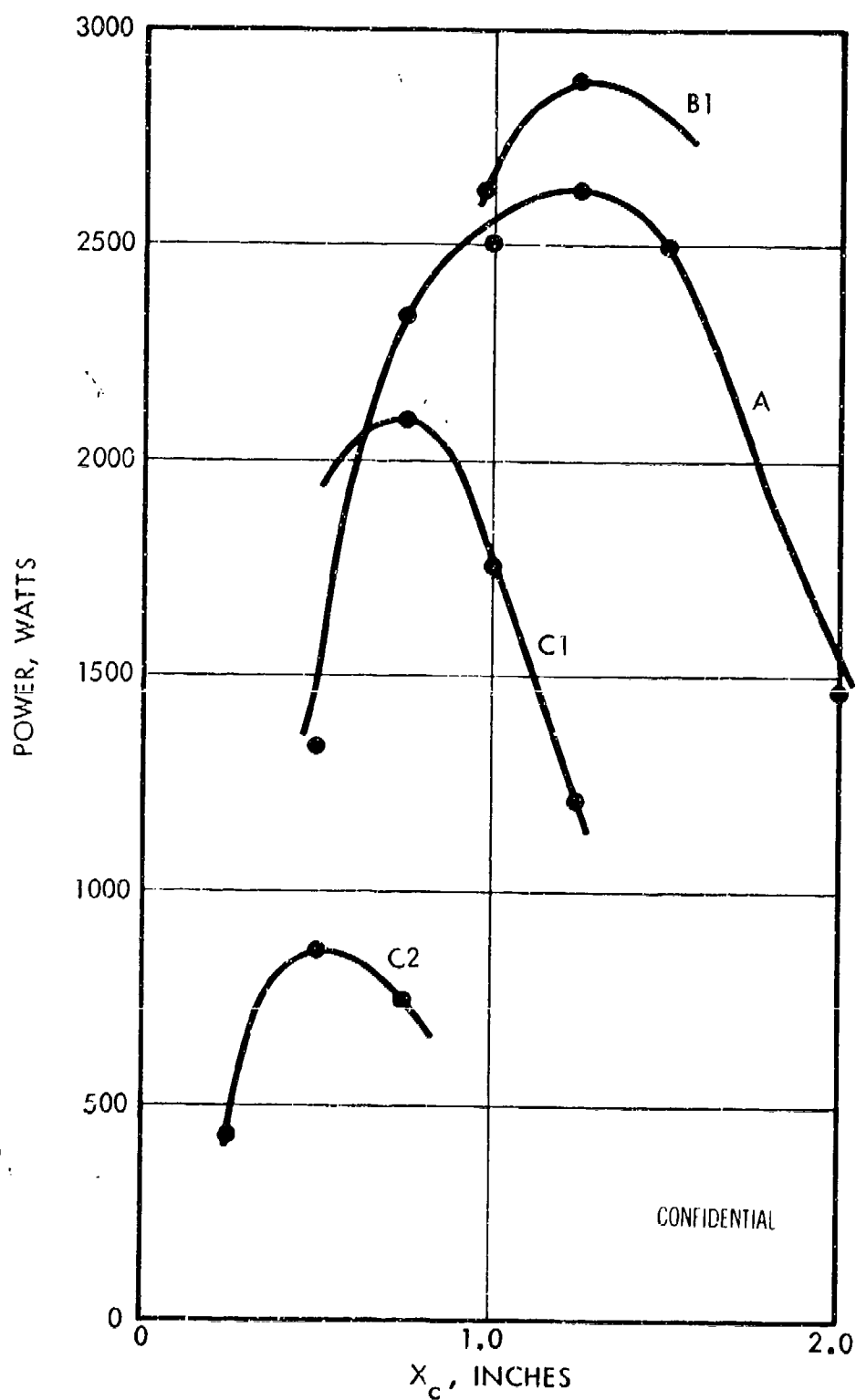


Figure 94. Closed Cavity Power X_c Scan for Test 160A and B (U)

CONFIDENTIAL

Figure 95. Closed Cavity Power X_c Scan for Test 160 (U)

CONFIDENTIAL

CONFIDENTIAL

AFWL-TR-72-28

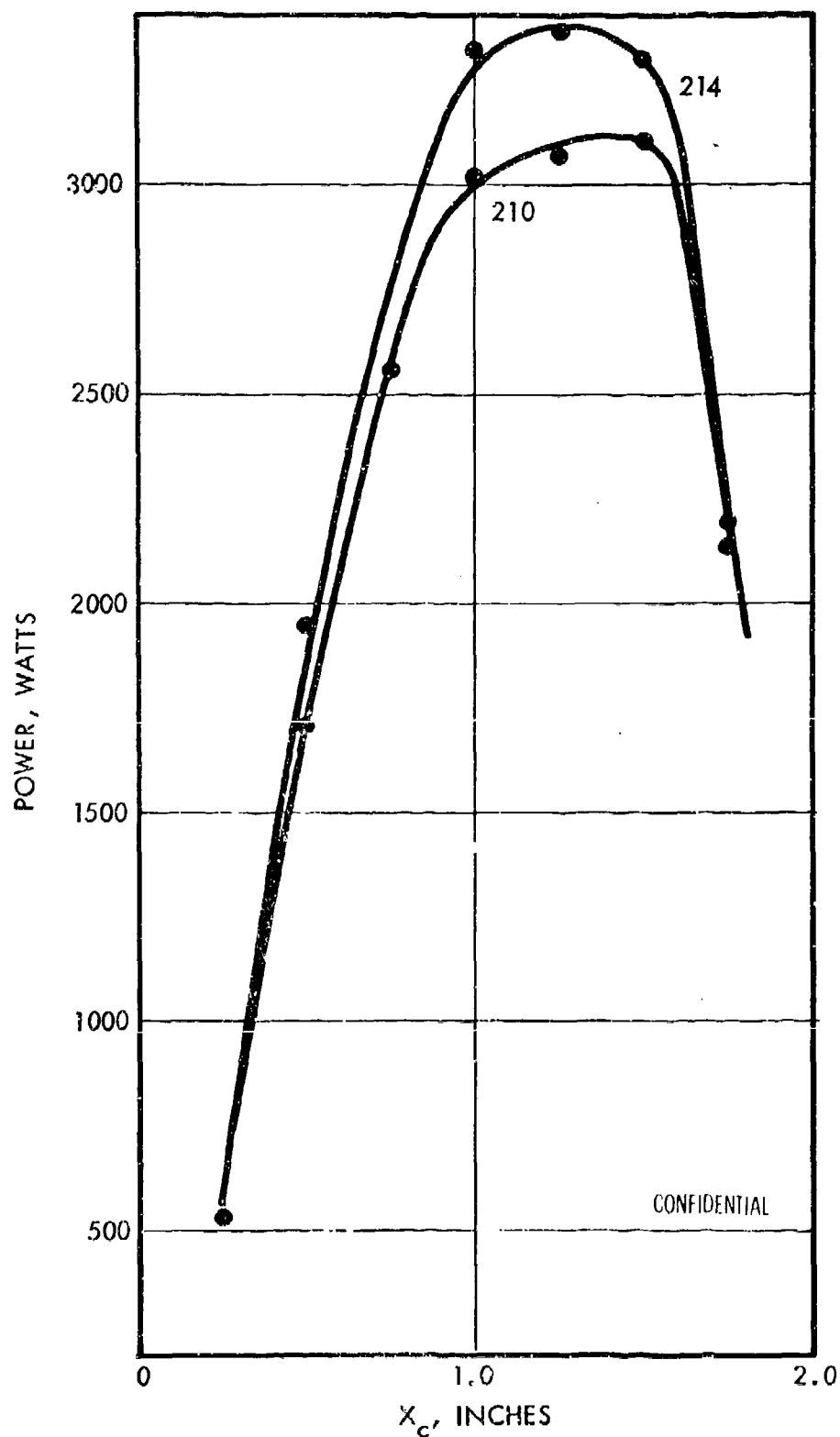


Figure 96. Closed Cavity Power X_c Scan for Tests 210 and 214 (U)

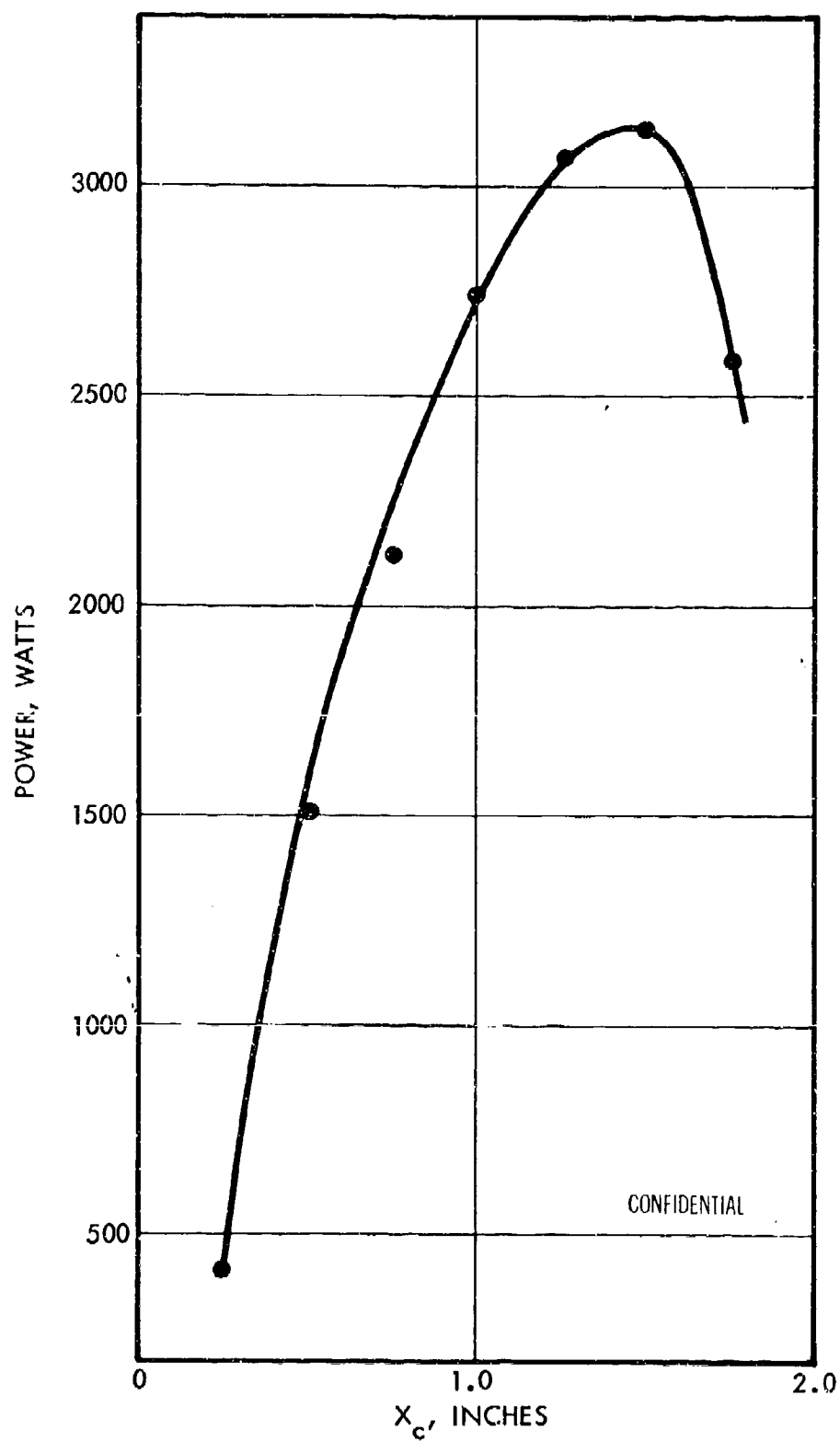
216
CONFIDENTIAL

CONFIDENTIAL

Table 17 is a foldout located on page 280.

CONFIDENTIAL
(This page is Unclassified)

CONFIDENTIAL

Figure 97. Closed Cavity Power X_c Scan for Test 211 (U)

CONFIDENTIAL

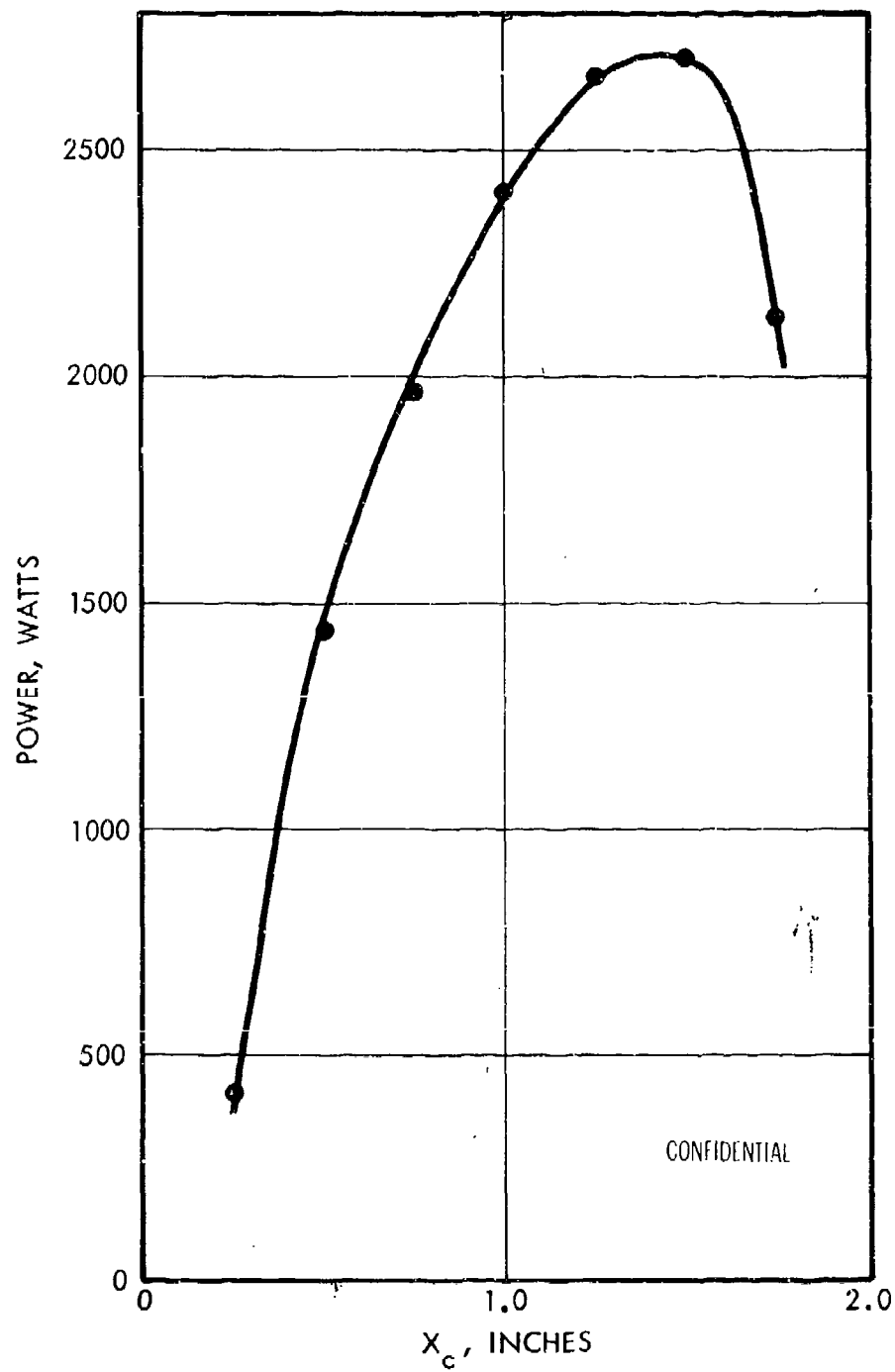


Figure 98. Closed Cavity Power X_c Scan for Test 212 (U)

CONFIDENTIAL

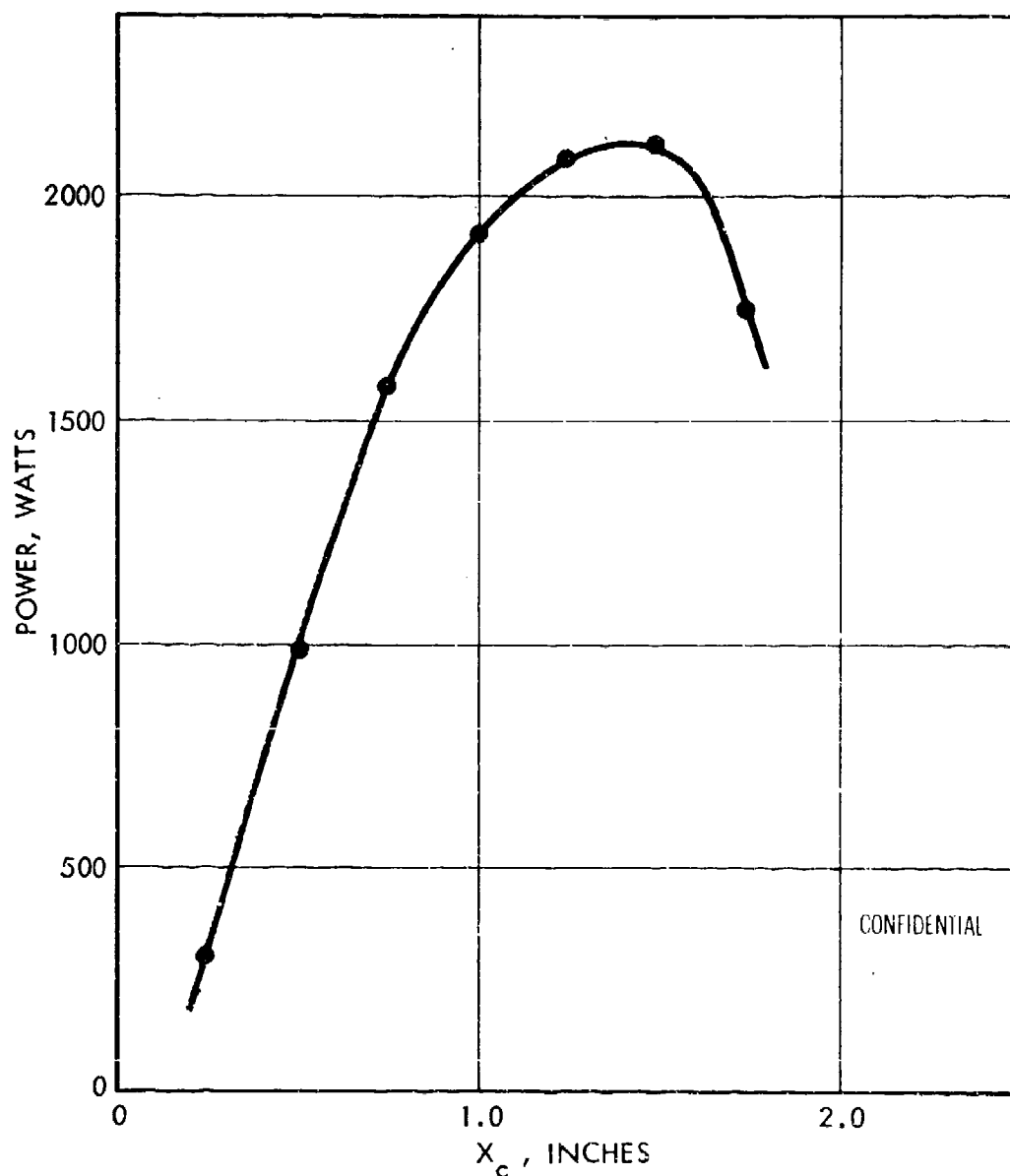


Figure 99. Closed Cavity Power X_c Scan for Test 213 (U)

(12) Test 214

(C) Test 214 was performed at 150% of nominal flow rate (21 gm/sec). Figure 96 presents the results superimposed on a baseline (14 gm/sec) X_c plot. It is noted that only a 10% increase in power was realized from the 50% increase in total flow. The exact cause of this failure to perform above the specific design point is as yet unexplained.

CONFIDENTIAL

(13) Tests 215, 216 and 217

(C) These tests were performed with N_2 diluent in the same molar proportions as He for previous tests. The total molar flow was held constant and as a result the combustor pressure and nozzle exit pressure were higher than the helium diluent tests. Specific powers were considerably reduced from the helium diluent case.

(C) The three tests were performed at combustor temperatures of 2227° , 1844° , and $1662^\circ K$, respectively. The best specific energy/gram of free fluorine for these tests was achieved at $2227^\circ K$ (644 joules/gm). Results are presented in Figure 100 and Table 17.

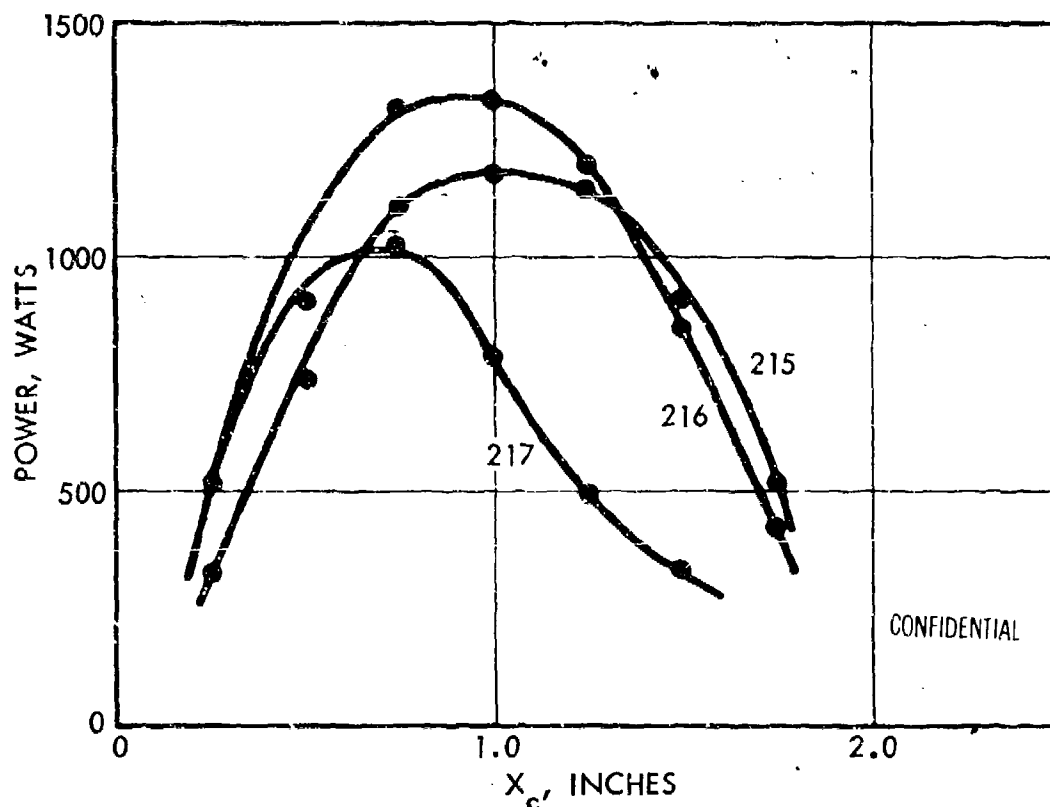


Figure 100. Closed Cavity Power X_c Scan for Tests 215, 216 and 217 (U)

(14) Tests 218, 219 and 220

(C) These tests were also performed with N_2 diluent. In this case, however, the total flow was reduced to reduce the combustor pressure to 14 psia and match the nozzle exit pressure to the cavity pressure. The three tests were performed at 1619° , 1907° , and $2156^\circ K$. The best specific energy recorded was achieved at $2156^\circ K$ (777 joules/gm). This compares to a value of approximately 970 joules/gm at the same temperature with helium diluent. Results are presented in Figure 101 and Table 17.

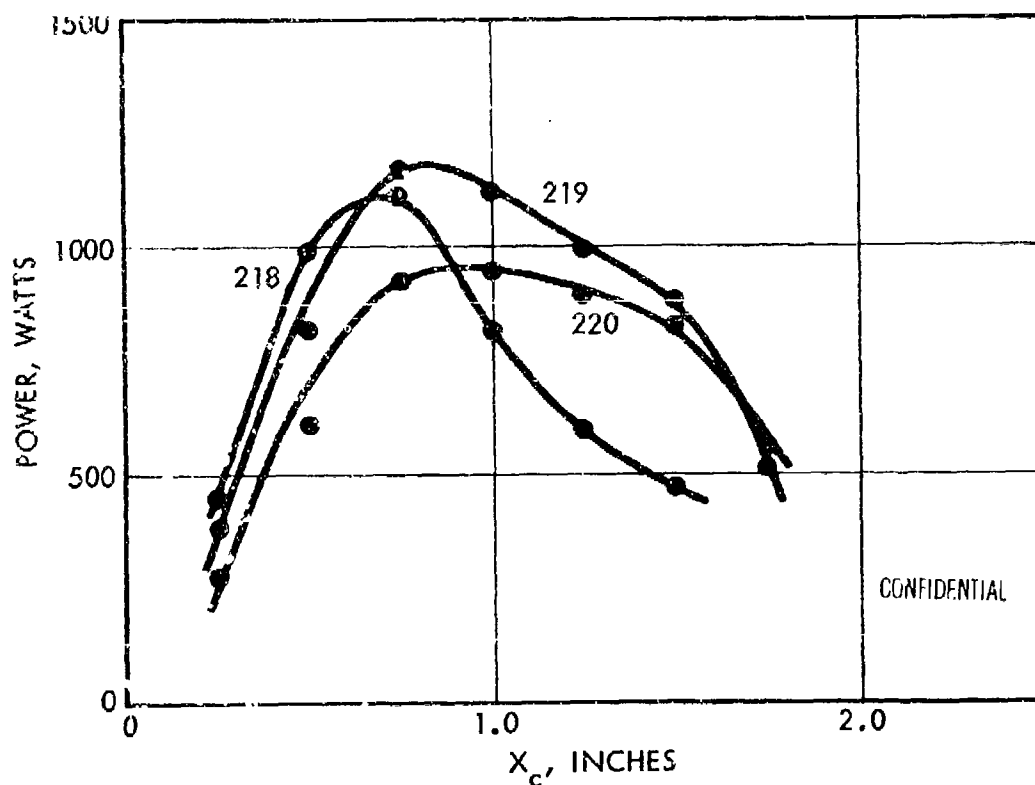


Figure 101. Closed Cavity Power X_c Scan for Tests 218, 219 and 220 (U)

d. Summary of Test Results

(C) The experimental evaluation of the two-dimensional multiple slit nozzle arrays (both 1/2 x 7 inch and 1 x 7 inch) with the TRW CL-II combustion-driven atomic fluorine generator laser device has resulted in a great body of engineering data defining the operating parameter trends and power limits of these cavity injector nozzle configurations. Among these results are:

- Peak closed-cavity power levels of approximately 1800 watts and approximately 3400 watts were demonstrated with the 1/2 x 7 inch and the 1 x 7 inch nozzle arrays, respectively.
- Best specific energy performance (power per unit flow rate) was obtained with helium as a diluent. At identical molar flow conditions, operation with nitrogen diluent reduced specific energy 20 percent relative to helium diluent performance.
- Overall performance in terms of power per gram of atomic fluorine correlates directly with combustor temperature and shows that the cold reaction ($H_2 + F \rightarrow HF^* + H$) appears to be the primary source of usable laser power.
- There are clearly determinable combustor diluent and cavity fuel molar ratios for optimum specific energy performance of either of the two cavity injector configurations. The optimum cavity fuel molar ratio is slightly hardware dependent, whereas the combustor diluent molar ratio appears to truly optimize at approximately 0.7.
- Heat losses in the combustor and nozzle bank hardware were shown to affect overall laser specific energy performance in a predictable manner. Reduction of combustor heat loss (while maintaining the same combustor temperature) directly reduces the total flow required to produce a given atomic fluorine flow, and is, therefore, directly realized as an increase in specific energy.
- The routine and reliable operation of a high power combustion-driven HF/DF chemical laser has been demonstrated as a practical engineering accomplishment. Over 24,000 seconds of cumulative HF lasing operation, with single lasing experiments running greater than 5000 seconds, were demonstrated during the subject program.

CONFIDENTIAL

SECTION V

CONCLUSIONS

(U) In the report we have presented detailed discussions of experimental data and shown the analyses which led us to certain important conclusions. We wish to pinpoint here the principal conclusions of the program.

- We conclude that entrainment of recirculating gases in the laser cavity is one of the major causes of performance decrease with increasing cavity pressure.
- Our data led us to conclude that the mixing of fuel and oxidizer jets in the laser cavity is governed by turbulent processes.
- We conclude that operation of chemical lasers in the cold reaction regime gives the maximum efficiency.
- We have demonstrated by extensive operation and performance evaluation that all-chemical, combustion-driven chemical laser is a viable device.
- We have established an engineering basis for fluorine-rich, chemical laser combustor design based on H_2/F_2 rocket technology.

CONFIDENTIAL

(This page is Unclassified)

APPENDIX I

TEST HARDWARE AND DATA REDUCTION PROCEDURES

1. EXPERIMENTAL LASER HARDWARE

(U) In a combustion driven chemical laser, the combustor and nozzles perform the basic function of reacting and mixing the laser working fluids and delivering them at specified conditions to the entrance plane of the optical cavity. These conditions include:

- Specific molar composition of reactants and diluents
- Mach number
- Pressure
- Kinetic temperature

(U) The combustor generates the desired atomic fluorine using the heat of reaction of deuterium and fluorine to dissociate the excess fluorine. Diluent is also added in an amount necessary to provide the desired molar ratio of diluent to reactant while precluding the recombination of atomic fluorine. The nozzle then accelerates the fluid to the high velocity, low temperature and pressure required in the optical cavity. The nozzles also serve as a fairing for the hydrogen injected at the cavity entrance.

(U) From a geometric sizing standpoint, the nozzle dimensions exert a primary influence over the combustor geometry and, to a slightly lesser extent, the optical cavity dimensions. Current HF/DF chemical laser nozzle exit geometries have width-to-height ratios in the range of 7 to 14. Expanding to either higher or lower exit Mach numbers would correspondingly raise or lower these width and height dimensions.

(U) In the design of a high efficiency HF laser it is desirable to minimize energy losses from the precavity components while maintaining tolerable material temperatures (from a hardware durability standpoint) and, at the same time, providing the desired degree of gas composition uniformity at the nozzle entrance plane. Basically, the technical disciplines (involving heat transfer, thermodynamics, fluid mechanics and engineering design) are identical to those successfully employed by TRW in the design and development of high energy propellant rocket engine hardware.

(U) A significant reduction in heat loss was achieved by the TRW CL-II laser combustor over the original CL-I configuration while the total chamber reactant flows for the two devices are basically the same. However, the CL-II combustor configuration is significantly different from that of the CL-I chamber/mixer combustor arrangement (Figure 102). The CL-I combustor consisted of a cylindrical chamber attached to a tapered two-dimensional mixing section. As a consequence, the large, cool, wall surface areas extracted much of the heat from the reactant flow. The cool wall area was reduced considerably in the CL-II device which was used exclusively in the HF Laser Technology Study Program.

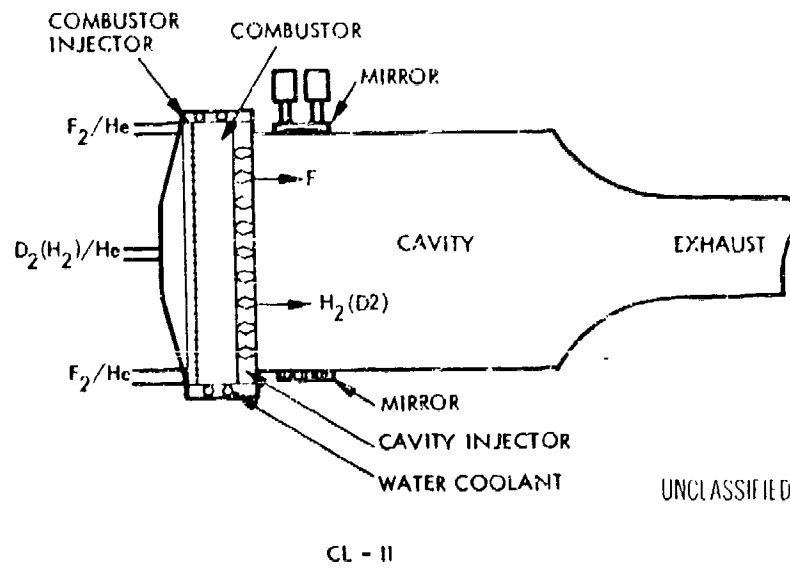
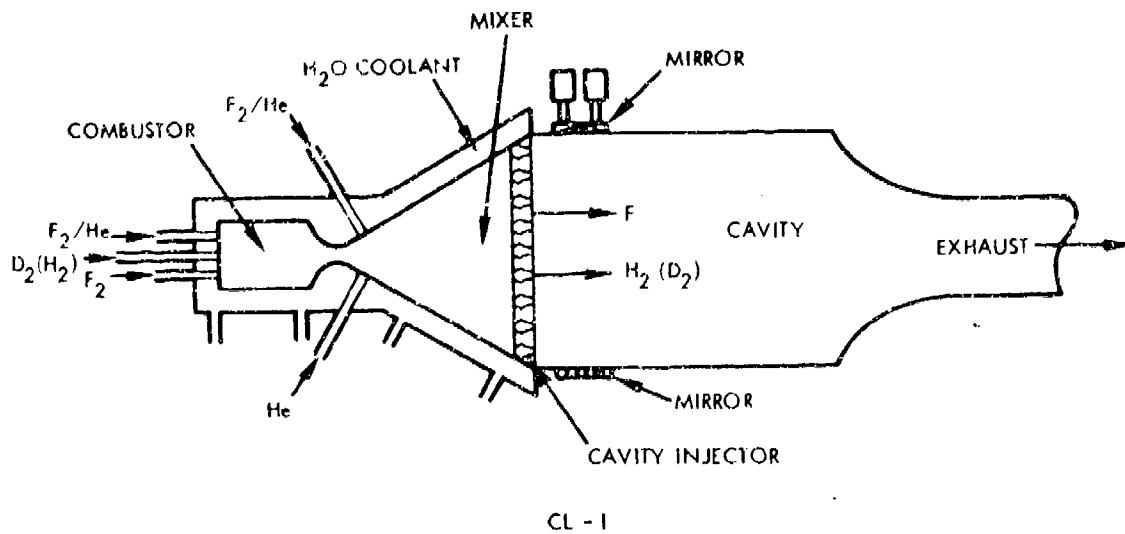
(U) The cavity injector nozzle bank employed with the CL-I configuration was also tested with the CL-II combustor configuration which provided directly comparable power efficiency data and verified the beneficial effects of reduced heat transfer losses. This nozzle consists of 37 two-dimensional slits with the throats 0.010 inch wide by 0.5 inch high expanding to an area ratio of 15:1. Each nozzle is water-cooled through internal manifolding that is fed from the mixing chamber. The nozzle is held in place by the hydrogen injector, which consists of 38 tubes that fit on the ends of the nozzles. Each tube has four orifices that inject the hydrogen into the cavity for mixing into the fluorine jets. This specific type of cavity injector nozzle configuration was also extensively evaluated in the Aerospace Corporation MESA device.

2. CL-II COMBUSTOR HARDWARE

(U) The CL-II combustor hardware is composed of the combustor injector and the combustor chamber which directly interfaces with the cavity injector nozzle assembly. The gas flow areas of all components are rectangular in shape with a 7-inch major dimension.

a. Combustor Injector

(U) The basic injector concepts which have been considered in the design of the TRW chemical laser for the gaseous reactants include shower-head, coaxial tube and impinging jet. These may be put together in a variety of geometries. In general, they all have similar basic fundamental characteristics. The showerhead and coaxial tube injectors cause mixing by shear flow interaction and eddy diffusion. The impinging jets



UNCLASSIFIED

Figure 102. CL-I and CL-II Combustor/Laser Schematics (U)

(U) promote mixing through increased eddy diffusion brought on by directed shearing action. In the unbounded flows, the gases expand and flow as jets. The limiting cases are axisymmetric and planar jets, each having its own characteristics. For all subject gaseous propellant work, the jet Reynolds numbers are sufficiently large so that the flow is essentially turbulent. The high injection velocities introduce recirculation effects which are much higher than normally encountered with liquid injectors; consequently, particular attention must be given to the injection geometry.

(U) Because of the compressible nature of the gaseous flows, it is necessary that the mixing zone be under dynamic control. For example, the lighter gas can escape around the field of impingement if the momentum ratios between the heavy and light gases are not controlled. Should this occur, then resultant gas uniformity may be expected to be adversely affected. On the other hand, if light gas velocities are too high, the reactant momentums will not be sufficient to penetrate the light gas jets and improper mixing will result. Consequently, attention must be given to the momentum mixing ratios.

(U) The injection of lightweight gases such as helium, deuterium, hydrogen or hydrogen-rich gases requires design provision for heat transfer effects on both injector faces as well as combustion chamber surfaces because of the high recirculation potential. These high levels of jet-induced recirculation are advantageous from a mixing/gas uniformity standpoint, but also have an adverse effect of producing high (localized) injector face heat transfer. TRW minimizes these undesirable injector heating effects in its CL-I and CL-II laser combustors by the use of the raised post injector design concept.

(U) Understanding the fundamental design parameters for gaseous propellant injectors is important to the subject laser reactant flow investigation since the combustor reactant injector is the controlling influence on mass and mixture ratio distribution. If proper mixing does not occur at the plenum injector head end, stratification of the products can result. If this occurs, the only forces available to redistribute the gases are those of molecular diffusion. This is normally relatively slow and requires fairly long combustion lengths to achieve high performance.

(U) Long combustion lengths in turn represent greater heat loss from the reacting gas stream.

(U) The CL-II combustor injector configuration selected for hardware implementation was a raised post showerhead design schematically illustrated in Figure 103. The fuel (deuterium or hydrogen) is injected through 45 equally spaced holes in the injector post. The fluorine is injected through two rows of 46 equally spaced holes (total of 92) to either side of the fuel orifices. Figure 104 presents an engineering drawing of the injector which also specifies the design parameters. Figure 105 shows a photograph of the completed assembly which is fabricated from Nickel 200.

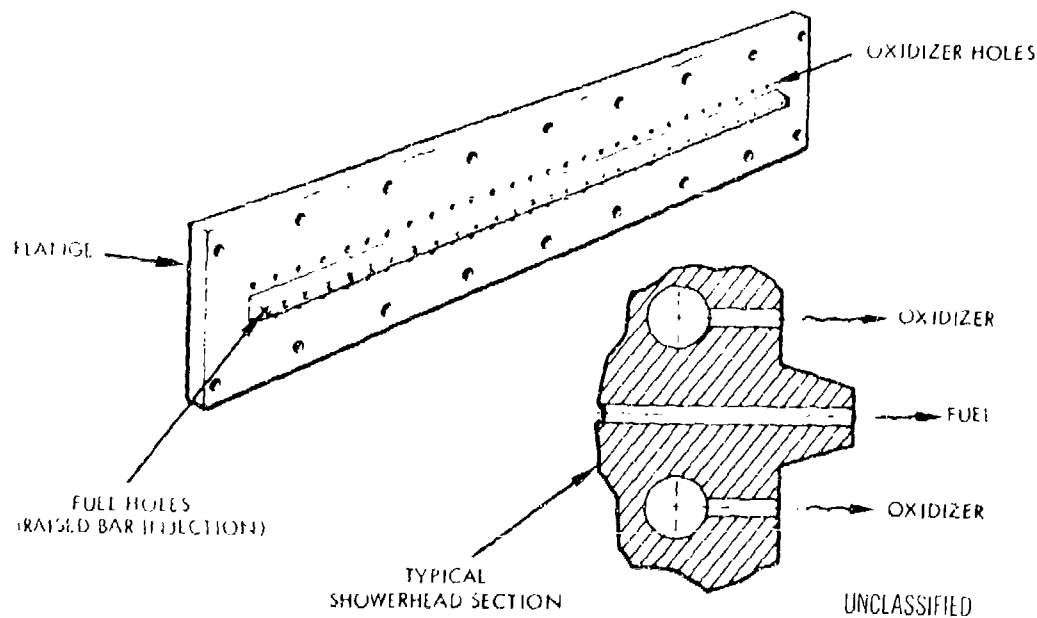
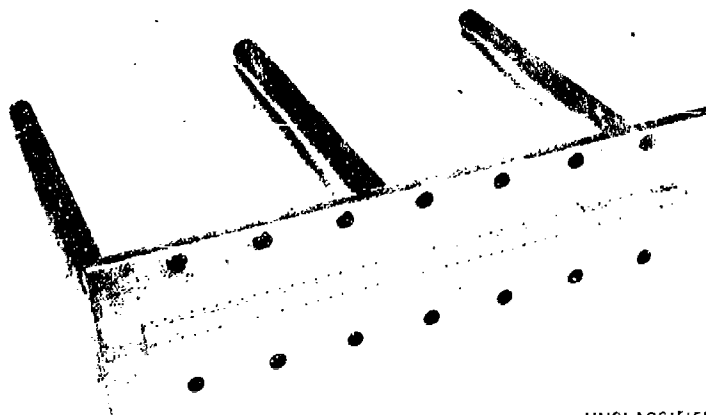


Figure 103. Combustor Injector Design Configuration (U)

Figure 104 is a foldout located on page 202.



UNCLASSIFIED

Figure 105. CL-II Pre-Cavity Combustor Injector (U)

b. Water-Cooled Combustor Chamber

(U) The function of the combustor chamber is to contain the atomic fluorine generating combustion process and permit adequate residence time to assure that the reactant mixing and combustion have been completed. The rectangular flow cross section dimensions were dictated by the cavity injector nozzles to nominally 1 inch by 7 inches. The length dimension (which determines residence time) was selected at 2 inches based upon prior experience with F_2/H_2 rocket engine combustors. This combustor length, when combined with the cavity injector nozzle inlet length (ignoring the contracting sections of the multiple nozzles, which would add equivalent length), resulted in a characteristic length (chamber volume divided by throat area) of 49 inches. From rocket engine standards a characteristic length, which is a measure of residence time, of 49 inches is more than adequate for F_2/H_2 combustion. For background, the characteristic length computation is made as follows:

$$\text{Combustor Volume, } 7.0 \times 1.0 \times 2.0 = 14 \text{ in}^3$$

$$\text{Nozzle Inlet Volume, } 7.0 \times 1.0 \times 0.5 = 3.5 \text{ in}^3$$

$$\underline{\underline{17.5 \text{ in}^3}}$$

(ignoring volume of contraction section
of nozzles)

(U) Nozzle Throat Area, $1.0 \times 0.01 = 0.01 \text{ in}^2$ per throat
 or 0.36 in^2 for 36 nozzles

$$\text{Characteristic Length,} = \frac{\text{Volume}}{\text{Throat Area}} = \frac{17.5 \text{ in}^3}{0.36 \text{ in}^2} \sim 49 \text{ in}$$

(U) Figure 106 presents an engineering drawing of the water-cooled combustor which is fabricated from OFHC copper. Figure 107 illustrates the installation of the combustor and injector into the test configuration.

c. Air Cooled Combustor Chamber

(U) The majority of TRW's chemical laser plenum devices employ water-cooled copper walls. However, an air-cooled nickel combustor was fabricated for use on the CL-II laser system. The design of this chamber is shown in Figures 108 and 109. The plenum walls can be cooled by forced air convection and considerable latitude in wall operating temperatures is provided by air flow control. Thus, the effects of wall temperature on F_2 recombination trends can be determined and controlled to the maximum permissible wall operating temperature that the fluorine environment will permit. At nominal flow conditions and a wall temperature of 810°K ($\sim 1000^\circ\text{F}$), the required cooling air flow is predicted to be approximately 400 scfm. As this device could not be introduced to test without a significant impact on schedule because of installation time and checkout thus compromising the major program objectives of diagnostic data acquisition, experimental verification was deferred.

(U) The anticipated heat loss rating for the cylindrical air-cooled plenum is compared to the CL-I and CL-II chambers in Table 18. From this table, it is seen that a 30 percent reduction in specific power loss is expected with the nickel plenum as compared to the water-cooled CL-II combustor. This reduction was made possible by allowing the wall temperature to increase and thereby lower the heat loss temperature driving potential. However, of considerably more importance is the ability of a hot wall plenum to suppress the amount of fluorine recombination in the wall gas boundary layer. Figure 110 illustrates the relative amount of atomic fluorine that can exist as a function of the gas temperature. Figure 111 shows the effect of both a "hot" wall and a "cold" wall plenum device. This figure shows the relative temperature profiles to be

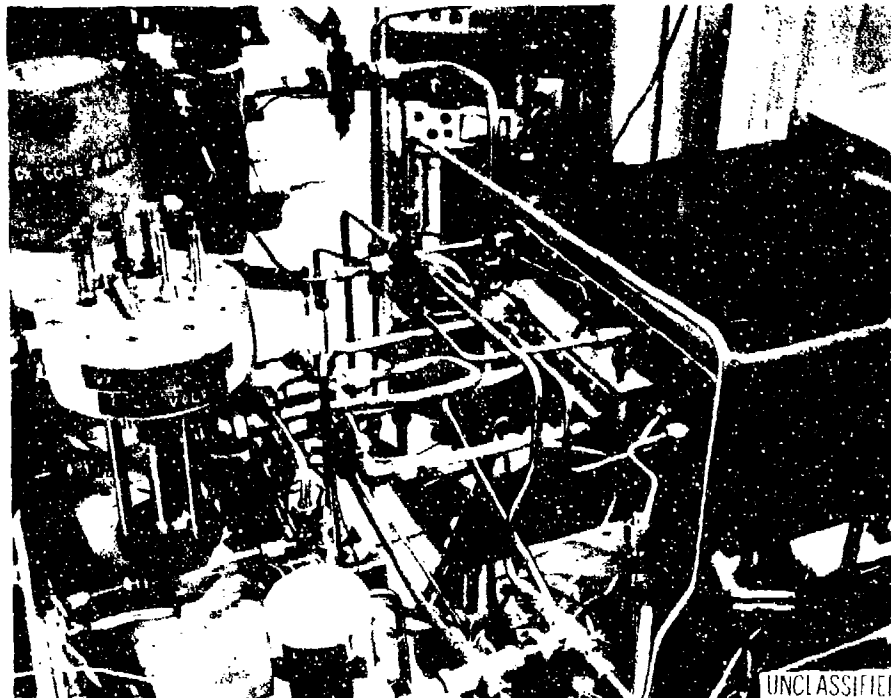


Figure 107. Installation of Combustor and Injector in Test Configuration (U)

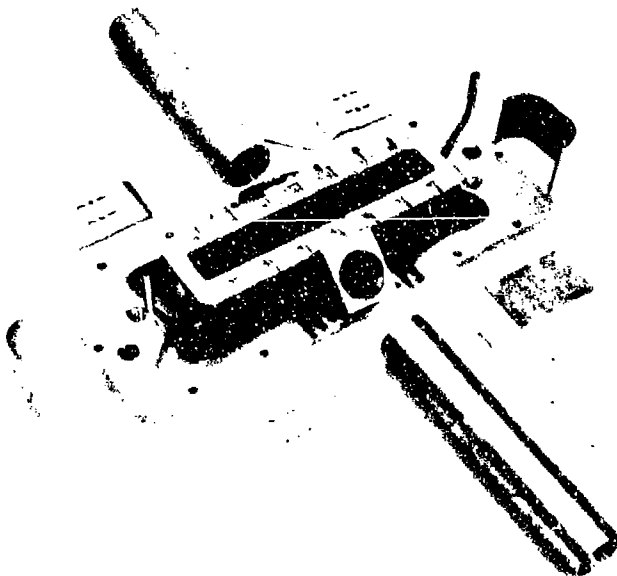


Figure 108. Exploded Assembly View of CL-II Gas Cooled Plenum (U)

Table 18. Specific Energy Losses to the Plenum Walls (U)

| Configuration | Q_L Heat Loss (Btu/sec) | wF Reactant Flow (g/sec) | PSPL Specific Power Loss (kw/g/sec) | Percent Change From CL-II Loss |
|----------------------------|---------------------------------|-----------------------------------|---|---|
| CL-I } Water-Cooled | 18 | 7.95 | 2.4 | +50 |
| CL-II } | 12 | 7.95 | 1.6 | 0 (Baseline) |
| Gas-Cooled CL-II Plenum | 8.5 | 7.95 | 1.1 | -30 |

$$\text{Specific Power Loss} = \frac{\text{Heat Loss}}{\text{Reactant Flow}} \times (1.055 \text{ kw/Btu/sec})$$

$$\text{Percent Change} = \frac{\text{CL-II Loss} - P_{\text{SPL}}}{\text{CL II Loss}} \times 100$$

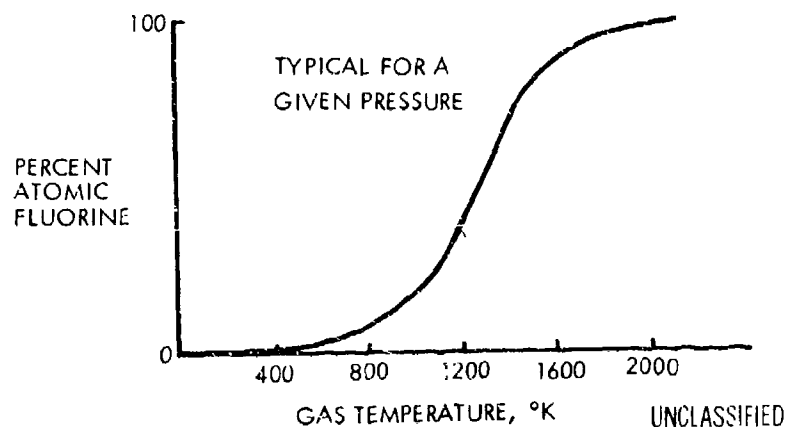


Figure 110. Atomic Fluorine Temperature Dependence (U)

(U) heat loss for the CL-II combustor was 12 Btu/sec for the same baseline reactant flows as the CL-I. This, however, still represents an appreciable percentage of the heat of reaction.

(U) Even further reductions in heat loss can be achieved with the gas-cooled plenum. An evaluation of the heat losses of the proposed chamber can be made by utilizing test data acquired from the CL-II laser combustor. The anticipated heat loss for the proposed combustor can then be calculated. Heat loss to the combustor wall is

$$Q_L = h_g A_s (T_g - T_w)$$

where

Q_L = heat loss, Btu/sec

h_g = gas convective coefficient, Btu/sec-in.²-°F

A_s = wall surface area, in.²

T_g = reactant gas temperature, °F

T_w = wall temperature, °F

The gas convective coefficient can be scaled by

$$h_g \propto \frac{(W_g/A_F)^{0.8}}{(D_H)^{0.2}}$$

for gas flow in ducts with negligible property changes where

W_g = gas flow rate, g/sec

A_F = gas flow area, in.²

D_H = duct hydraulic diameter, in.

(U) The CL-II baseline heat loss is utilized to generate a baseline precombustor hot gas convective coefficient as follows:

$$h_{g_{CL-II}} = \left[\frac{Q_L}{A_s (T_g - T_w)} \right]_{CL-II} \cong h_{g_{GC}}$$

However, the temperature driving potential is different for the gas-cooled plenum and the water-cooled CL-II combustor,

$$\left[T_g - T_w \right]_{CL-II} = 1700 - 425 = 1275^\circ K$$

$$\left[T_g - T_w \right]_{GC} = 1700 - 810 = 908^\circ K$$

(U) Then, the gas-cooled plenum would have the following heat loss:

$$\begin{aligned} \left[Q_L \right]_{GC} &= \left[Q_L \right]_{CL-II} \frac{\left[(T_g - T_w) \right]_{GC}}{\left[(T_g - T_w) \right]_{CL-II}} \\ &= 8.5 \text{ Btu/sec} \end{aligned}$$

(U) The specific power loss for the gas-cooled plenum is then only,

$$P_{SPL} = \frac{8.5}{7.95} (1.055) = 1.1 \text{ kw/g/sec}$$

(U) In the past, the evaluation of the effects of heat loss to the combustor walls was based, primarily, upon the reduction of delivered specific power of the laser caused by the heat loss magnitudes. It is anticipated that lower heat losses will be most directly achieved by allowing higher combustor wall operating temperatures. However, it is felt that an unfavorable tradeoff would ensue between minimizing heat loss and the complexity and reliability of controlling a higher wall temperature chamber. The most obvious and immediate benefits to be gained from higher wall temperatures are, in fact, a reduction in the amount of recombined fluorine in the gas boundary layer. Also, lowering heat losses to

(U) accomplish higher delivered specific laser power can be expected to provide rapidly diminishing returns as the absolute magnitude of the specific delivered power of the laser increases.

3. CAVITY INJECTOR NOZZLES

(U) The fundamental purpose of the chemical laser nozzle array is to deliver the dissociated fluorine through a sonic slit and expand it supersonically to be mixed with the fuel in the laser cavity, as shown in Figure 112. These nozzles must be cooled to the extent that material durability is not compromised.

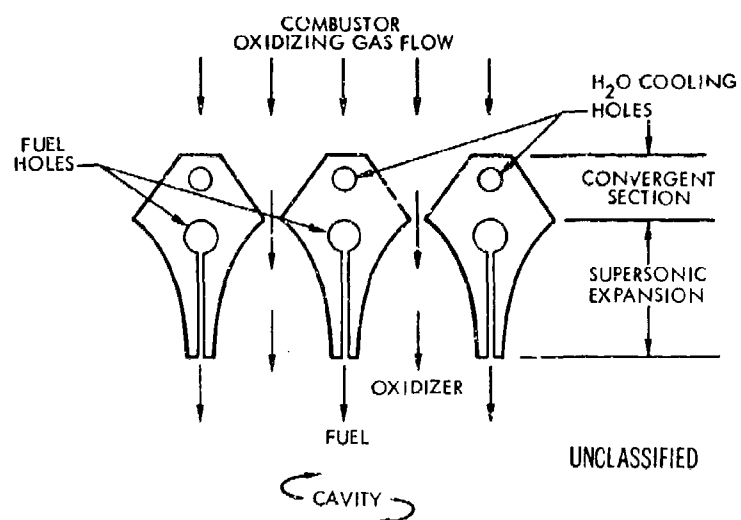
(U) Two basic cavity injector design configurations were evaluated under the Technology Program: 0.5-inch by 7-inch, two-dimensional slit (Figure 113) and the 1-inch by 7-inch, two-dimensional slit (Figure 114). Both nozzle configurations were utilized for emission power evaluations, however, the molecular and fluid mechanical diagnostic experiments employed the 1-inch by 7-inch nozzle array exclusively. A face-on view of the actual hardware is shown in Figure 115 and an engineering drawing of the 1-inch by 7-inch nozzle array is presented as Figure 116.

(U) Both nozzles are quite similar aerodynamically although one nozzle has twice the flow area of the other, however, there are also distinct differences as enumerated in Table 19.

Table 19. Comparison of Cavity Injector Design Characteristics (U)

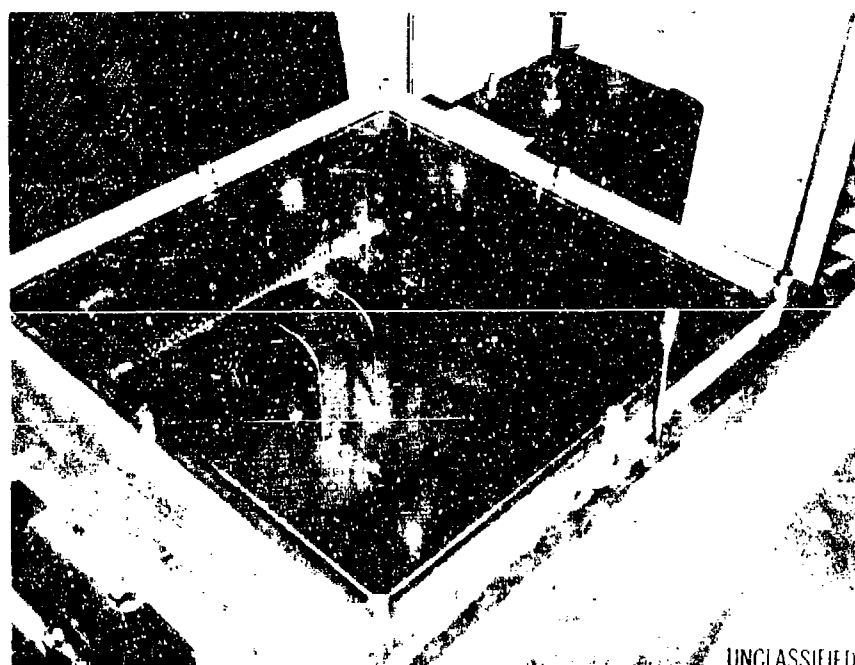
| General Designation | 0.5-inch by 7-inch, multiple-slit nozzle | 1-inch by 7-inch, multiple-slit nozzle |
|-----------------------------------|--|--|
| Number of Atomic Fluorine Nozzles | 36 | 36 |
| Nozzle Area Ratio | 15:1 | 15:1 |
| Throat Area (per nozzle) | 0.005 in ² (0.01 inch x 0.5 inch) | 0.01 in ² (0.01 inch x 1 inch) |
| Cavity Fuel Injection | Four drilled holes in tube adjacent to fluorine nozzle exit with fuel flow parallel to nozzle centerline | Continuous slot (0.006 inch x 1 inch) parallel with fluorine nozzle centerline |
| External Visual Access | Initial flow field obscured by injector body, nozzle exits recessed approximately 0.2 inch | Complete viewing access, nozzle exits flush with injector body |
| Experimental History | Identical to Aerospace MESA device. Tested on TRW CL-I and CL-II lasers | Designed, developed, and tested on TRW CL-II laser |

UNCLASSIFIED



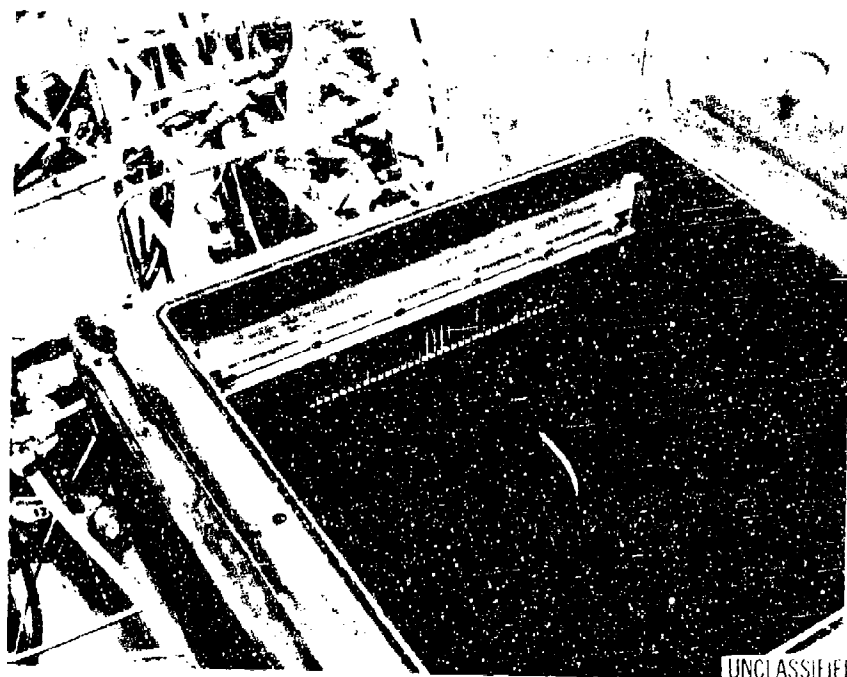
UNCLASSIFIED

Figure 112. Chemical Laser 1- by 7-Inch Nozzle Array (U)



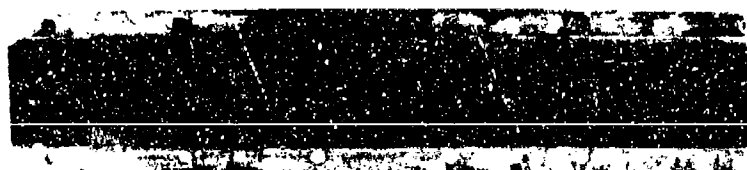
UNCLASSIFIED

Figure 113. Installation of 1/2- by 7-Inch Nozzle Array in CL-II Cavity Box (U)



UNCLASSIFIED

Figure 114. Installation of 1- by 7-Inch Nozzle Array in CL-II Cavity Box (U)



UNCLASSIFIED

Figure 115. Face-on View of CL-II 1- by 7-Inch Multiple Slot Array Cavity Injector (U)

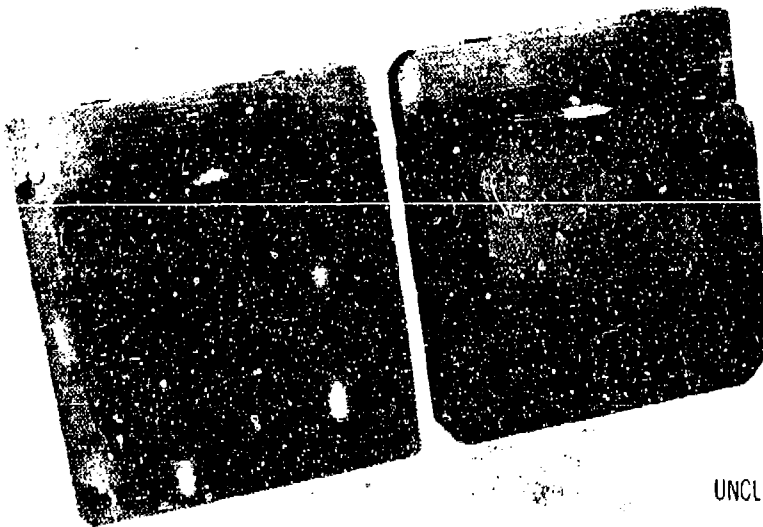
Figure 116 is a foldout located on page 283.

4. CAVITY OPTICS COMPONENTS

a. Water-Cooled Metal Mirrors

(U) During the course of the program, the major optical emission power diagnostic was the closed cavity measurement. These experiments determine the amount of energy deposited in the cavity end mirrors by the process of stimulated emission. The test is somewhat analogous to the short circuit testing of a generator or battery. The closed cavity measurements give only the maximum optical energy which could be withdrawn from the flow region since no concern is given to minimizing the beam spread or to the distribution of emitted power among the various possible vibrational-rotational states.

(U) The end mirrors shown in Figure 107 are a pair of water-cooled, polished, gold-coated reflectors. One reflector was slightly concave (10-foot radius of curvature), making the resonator stable. (The flat mirror has a small alignment hole at its center.) For convenience, the mirrors were mounted inside the lasing chamber. The two mirror surfaces were parallel to one another and parallel to the direction of gas flow.



UNCLASSIFIED

Figure 117. High Power Water-Cooled Laser Mirrors (U)

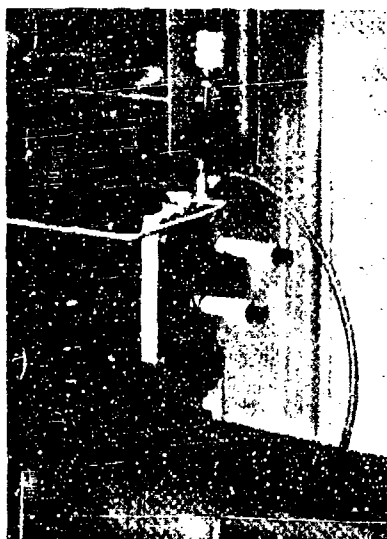
(U) The center line of the resonator's optical axis could be adjusted by means of micrometers on the mirror gimbal mounts as shown in Figures 118 and 119. The closed cavity measurements provide a means for simply and directly evaluating performance of different nozzle designs and mixing concepts. For example, the 1/2 by 7 inch slot nozzle originally developed by the Aerospace Corporation yielded a total closed cavity emission of 1800 watts using the TRW combustor. A larger 1 by 7 inch slot version produced an emission of approximately 3,500 watts.

(U) Figure 120 presents an engineering drawing of the water-cooled end mirrors which are fabricated from beryllium copper alloy 25. The cooling passages are drilled into the body of the mirror and then capped by brazing to force the water to flow in shuttle fashion behind the irradiated surface.

b. Plane-Parallel Externally Mounted Resonator

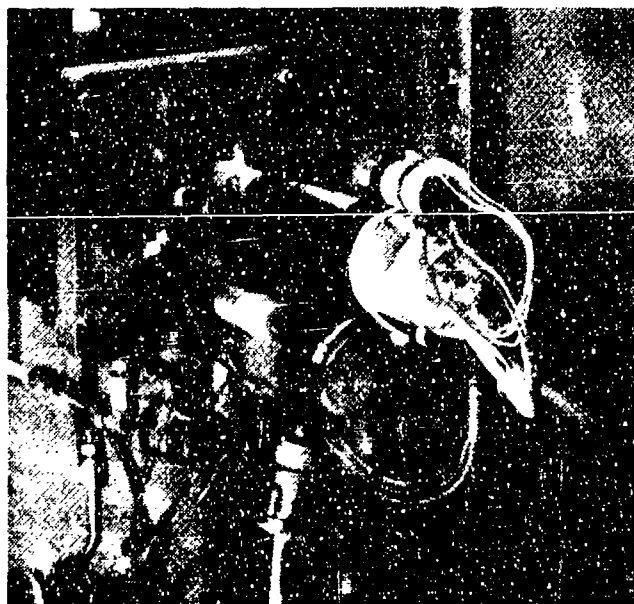
(U) Early in the program, a new resonator configuration was designed and introduced into the test program. Experimental evaluation was conducted with the 0.5-inch high by 7-inch long, multiple-slot cavity injector nozzle. The new configuration was intended to permit a wider variety of experiments; namely, to study the optimum outcoupling of the laser beam, to produce beams of low divergence, to find mirror reflectivities which optimize the output power, to generate output beams with partial reflecting end mirrors, and to test different resonator configurations.

(U) The resonator mount and associated hardware are shown schematically in Figure 121. In this design, the two cavity end mirrors are mounted independent of the lasing chamber. The mirrors are fastened to an independent frame thereby minimizing mirror misalignment. The ends of the frame are spaced by three Invar rods. One end mirror is outside the nozzle-vacuum envelope. The other is inside the vacuum environment. Mechanical isolation between the resonator frame and the vacuum nozzle manifold was achieved by connecting them through a pair of stainless steel double-acting bellows. The nozzle flow region was sealed against the atmosphere by two windows, one inside and one outside of the optical resonator.



UNCLASSIFIED

Figure 118. Manual Differential Micrometer Adjustments on CL-II Laser Mirrors (U)



UNCLASSIFIED

Figure 119. Remotely Operated Differential Micrometer Adjustments with Position Feedback on CL-II Laser Mirrors (U)



- 1 CLEAN ALL COMPONENTS PER PRG-2 LEVEL 1 PRIOR TO BURNING
- 2 BAKE IN A H_2 OR VACUUM ENVIRONMENT USING NI60 BRASSING ALLOY AT 1875 $^{\circ}F$ FOR 1 HOUR
- 3 POLISH SMOOTH & EN-1 TO MIRROR FINISH
- 4 COOPER / GOLD COAT IN EVAPORATOR - 18 $^{\circ}F$
- 5 ALL FILLET RADII .005 R MAX

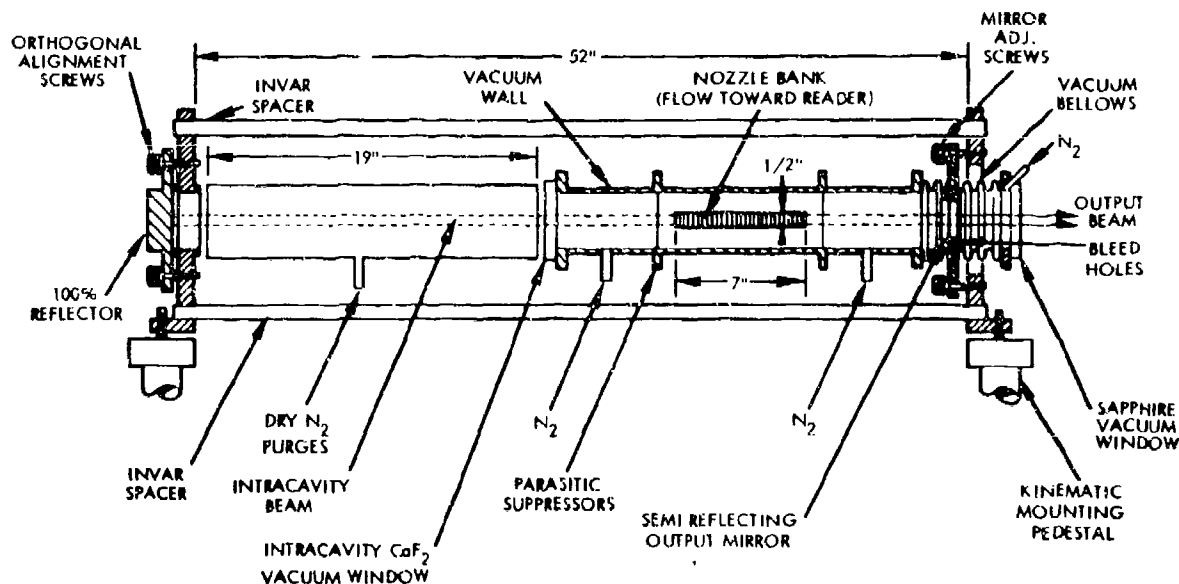
| QTY | UNIT | PART OR IDENTIFYING NO. | DESCRIPTION OR IDENTIFYING NO. | INTERNAL | DATE | TIME |
|-----|------|-------------------------|--------------------------------|-------------------|------|------|
| 2 | 1 | -5 | PLUG | CHRG EV BBD | | |
| 12 | 12 | -6 | PLUG | CHRG EV BBD | | |
| 1 | 1 | -3 | BODY | RECYCLING MACH 25 | | |
| - | - | -2 | MOTOR ASSY | | | |
| - | - | -1 | MOTOR ASSY | | | |
| 2 | 1 | | | | | |

Figure 120. Water-Cooled Mirror Assembly (U)

(U) Sapphire and calcium fluoride were chosen as candidate vacuum windows. Both have good transmission at the HF and DF laser emission wavelengths. Calcium fluoride was selected initially as the intracavity window insomuch as it had been used successfully as an outcoupling window in the earlier hole outcoupling experiments. Sapphire was used as the extracavity vacuum window. Neither window was antireflection coated.

(U) The external and internal cavity reflectors were separated by a distance of 52 inches. Maximum end mirror separation was chosen to decrease the wavelength interval between adjacent longitudinal cavity modes, and to decrease the geometrical beam divergence.

(U) The 52-inch end mirror separation design gives a calculated 0.03 Angstrom separation between neighboring longitudinal cavity modes for the 2.8 micron center wavelength of the HF transition. For the DF lasing transitions, the longitudinal modes are separated by 0.045 Angstrom. The room temperature line widths for these two gases are calculated to be 0.045 and 0.06 Å, respectively. Comparison between the cavity mode separation and the estimated line width shows that the 52-inch mirror separation is marginal for HF lasing, but may be too short for DF. In laser experiments, it is desirable to have the resonator long enough so



UNCLASSIFIED

Figure 121. Schematic of the TRW Chemical Laser Test Apparatus (U)

(U) that a longitudinal cavity mode is always under the peak of the gain curve for each laser transition. The 52-inch separation was chosen to approximate this criterion.

(U) The "long" cavity mirror separation was also chosen to decrease the divergence of the laser beam. For a 1-inch diameter output aperture, beam divergence can never be greater than the geometrical beam divergence; namely,

$$\alpha_{\text{GEOM}} = \frac{1}{52} \text{ radians} = 19 \text{ milliradians}$$

Based on experience with other high gain lasers, such as ruby and neodymium lasers, the process of stimulated emission narrows the beam divergence to 1/10 to 1/20 of the geometrical value. This was verified by laser tests with HL'.

(U) Photographs of the HEPTS laser system with the new resonator structure are shown in Figures 122 and 123. Figure 122 is a view looking toward the external cavity sapphire vacuum window (i. e., at the output end). The partial reflecting cavity end mirror is behind this window inside the vacuum system. One-half of the bellows assembly between the resonator frame and the vacuum plumbing can be seen from this view. As noted earlier, the bellows mechanically isolates this mirror mount from the vacuum system structure. The end window purge line can also be seen. The duct to the steam ejector vacuum pump is to the left. The reflecting surface of the "100 percent" rear cavity mirror can be seen in the background of Figure 122.

(U) Figure 123 is a side view of the laser looking at the external cavity end mirror mount. In this picture the space between the inner cavity calcium fluoride vacuum window and the external mirror is enclosed by a 19-inch long tube. A dry nitrogen supply was connected for the purpose of purging the atmospheric portion of the cavity of contaminant gases.

(U) A set of flat cavity output mirrors of various reflectivities was procured under the TRW IR&D program. These are 1-inch diameter,

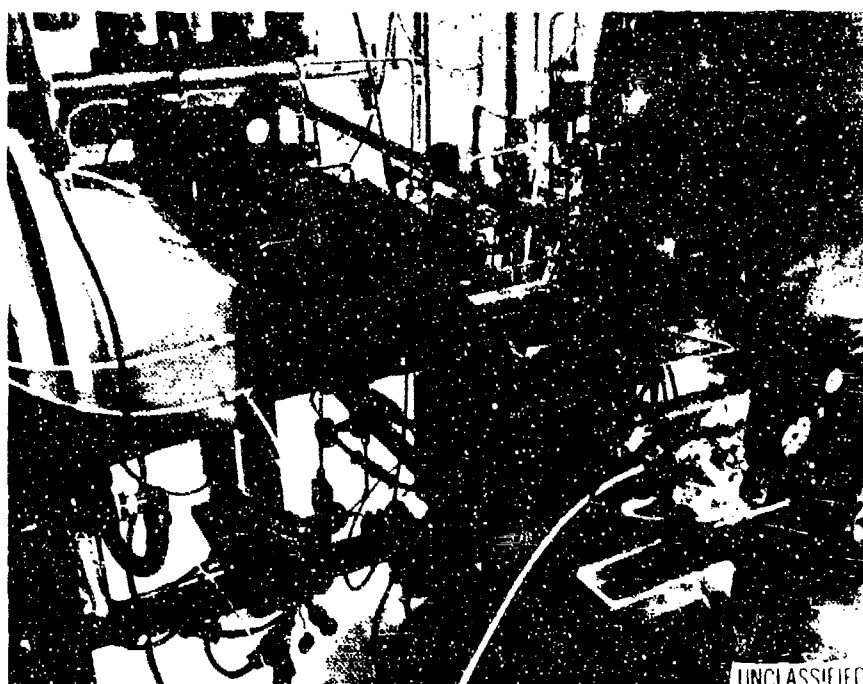


Figure 122. Photograph of the TRW HF/DF Chemical Laser System with New Resonator Mount. The output beam now passes through the sapphire vacuum window in the foreground. The rear reflector is visible in the background. Not seen is the intercavity vacuum window. A water calorimeter is located at the output window. (U)

(U) 1/8-inch thick sapphire substrates with different partial reflecting multilayer germanium-silicon monoxide coatings.* As noted earlier, sapphire substrates were selected because of good transmission at the HF and DF lasing wavelengths. One-inch sapphire blanks are readily available items and are commonly used as output reflectors for solid state ruby and neodymium lasers. The different multilayer coatings were produced for reflectivities of 40, 60, 80, 90, and 97 percent. Typical transmission curves for these reflectors are shown in Figure 124.

(U) The results from the earlier closed-cavity operation of the laser have tended to indicate that a region of high optical gain exists within approximately 0.5 inch from the face of the cavity injector. Accordingly, for the first series of tests, the output mirror was located far

*Product of Adolph Meller Company, Providence, Rhode Island. Coatings by Spectrum Systems, Mass.

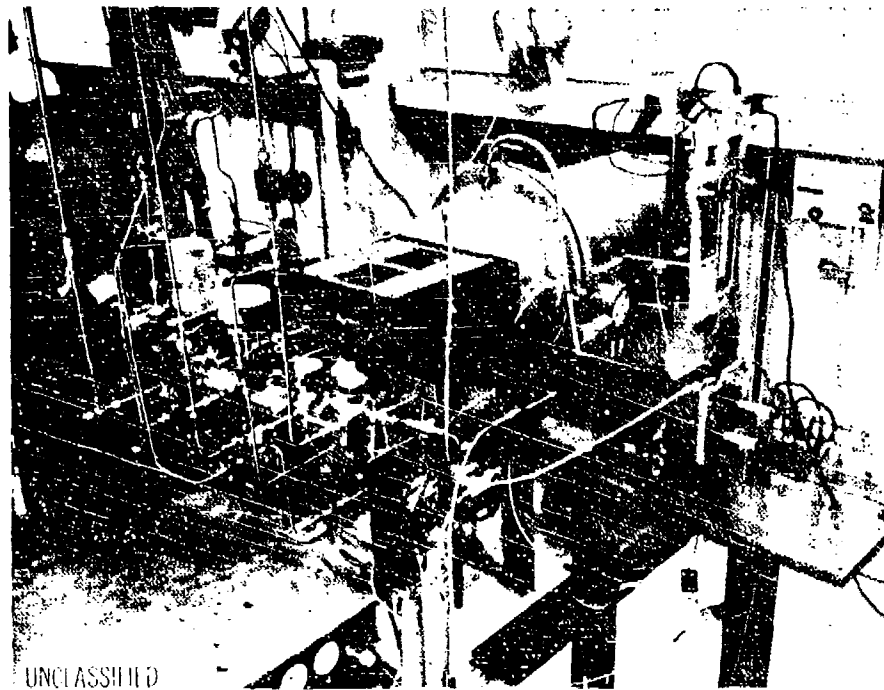


Figure 123. Photograph of the TRW HF/DF Chemical Laser viewed from the rear external mirror mount. In this view, the portion of the optical cavity at atmospheric pressure is enclosed by a duct and purged with dry nitrogen. (U)

(U) enough upstream (in the gas flow direction) to allow lasing to occur across the injector face. That this did indeed occur is shown in the sketch of the burn pattern, Figure 125. A Lucite block is placed about 4 inches from the laser output window. The outline of the injector is shown in profile. As one proceeds away from the injector face along the horizontal diameter of the beam, the power density increases rapidly to a maximum about 0.3 to 0.4 inch away from the injector face; it then decreases toward the opposite edge of the beam, as shown in the lower sketch in the figure.

(U) Using TRW's chemical laser at the Capistrano Test Site, beam signature burns were recorded at 5.5 inches and 152 inches from the output mirror. The laser resonator for this run consisted of the spherical mirror with a 120-inch radius of curvature and a flat dielectric output mirror. The cavity length was 52 inches.

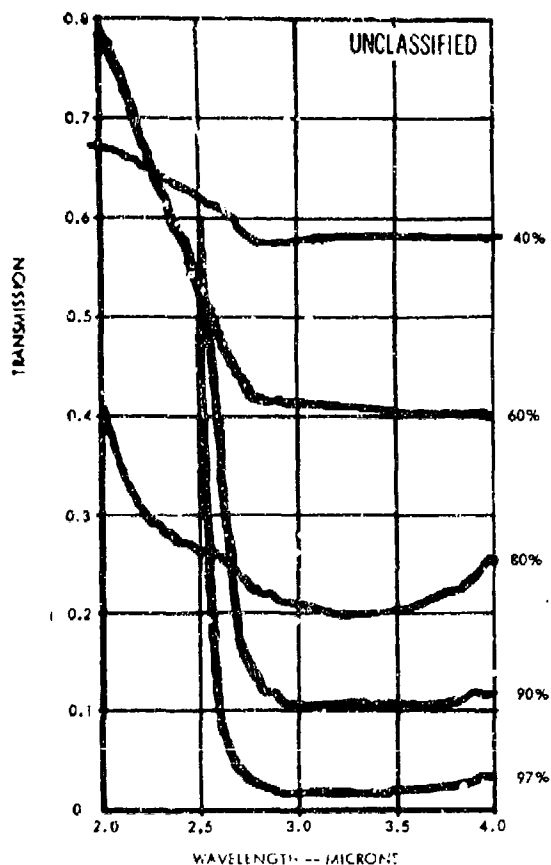


Figure 124.
Transmission Curves for
Sapphire Reflectors (U)

(U) The fact that one of the mirrors was spherical makes it possible to calculate mode diameters, estimate the total number of modes present, and compare the diameters of the two burn patterns to what would be produced by diffraction alone.

(U) One may first calculate the waist diameter of the dominant mode by assuming that the radius of curvature of the wavefront propagating from the waist to the curved mirror matches the radius of that mirror. Using the dimensions given above, the waist diameter is 0.090 inch. This mode would spread very little in propagating the 5.5 inches between the output mirror to the position at which the first burn was made. Since the burn was 0.8 inch in diameter, approximately 80 modes must have been oscillating.

(U) An accurate calculation of the beam spread would involve a superposition of radiation patterns from a long series of mode distributions

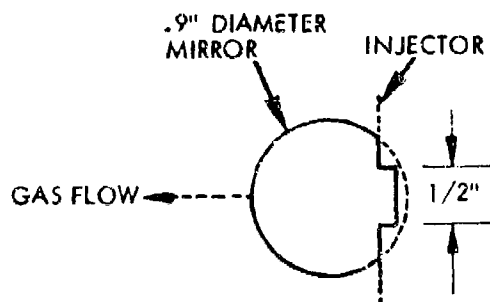


Figure 125.

Laser Burn Pattern Seen in Plexiglas Print; Note Projection of Nozzle Face (U)

UNCLASSIFIED



(U) described by high order Hermite polynomials, and would not be warranted in the present case. A rough estimate of diffraction spreading may be made, however, to see whether the observed increase in beam diameter can be accounted for. One may do this by estimating the number of phase reversals across the output beam, based on the wavelength, the diameter of the beam, and the length of the equivalent confocal cavity. This number is approximately 50. The size of the spot corresponding to the highest transverse spot is then approximately the beam diameter divided by 50. The diffraction spread of such spots, assuming a gaussian intensity distribution and uniform phase for each spot, is about 1.2 inches over the 152-inch distance to the position of the second burn. This diffraction spreading is enough to account roughly for the observed spread.

5. TEST FACILITY

a. Facility Description

(U) All the reactive tests conducted on this program were performed at the TRW Capistrano Test Site located near San Clemente, California, approximately 70 miles southeast of the main offices at Redondo Beach, California. The capistrano Test Site (CTS) has complete facilities for conducting experimental development and production testing of rocket engines, chemical processes, ordnance devices and chemical lasers.

(U) The current high energy chemical laser test facilities are located in the High Energy Propellant Test Stand (HEPTS) complex at CTS. The laser test position is located within a building specifically designed to house the laser and includes a laser effects laboratory immediately

(U) adjacent for conducting beam outcoupling experiments (Figure 126). In addition to the laser test building the HEPTS auxiliary support building has been partitioned to provide a clean work station for precision assembly, checkout, and storage of laser and optics equipment.

(U) High energy laser tests conducted at CTS are controlled from a centrally located blockhouse in the HEPTS complex (Figure 127). The control center also houses all the data acquisition and recording systems necessary for laser testing. Digital test data reduction is performed with a general purpose hybrid computer system located in the CTS Main Control Center.

(U) The chemical laser facility feed system is schematically illustrated in Figure 128. The feed system is designed for remote control and operation of all reactant and diluent flows from the laser test control console.

(U) The combustor oxidizer supply system is comprised of a liquid fluorine storage and supply tank, liquid-to-gas heat exchanger and gaseous fluorine storage bottle tank, hydraulically operated servo pressure regulator, sonic flow control orifices and remote control valves. When test duration requirements exceed the capacity of the gaseous fluorine storage bottle bank, the liquid storage tank is pressurized with helium and the heat exchanger provides a continuous temperature controlled gaseous fluorine flow through the combustor flow control system.

(U) The combustor fuel supply and feed system is designed for either gaseous hydrogen or deuterium flow the the combustor injector. Each fuel supply circuit includes a gaseous bottle storage, remote operating electric pressure regulator, and sonic flow control orifices feed to a solenoid-operated three-way select valve. Operation of this valve, together with the cavity fuel feed system described below, permits operating the laser alternately in either the HIF or DF mode. On-off control of the combustor fuel supply is provided by a solenoid-operated fire valve downstream of the H_2/D_2 select valve.

(U) Combustor diluent flow is supplied from gaseous storage bottles through a single remotely operated pressure regulator to separate sonic flow control orifices and on-off valves to the combustor fuel and oxidizer

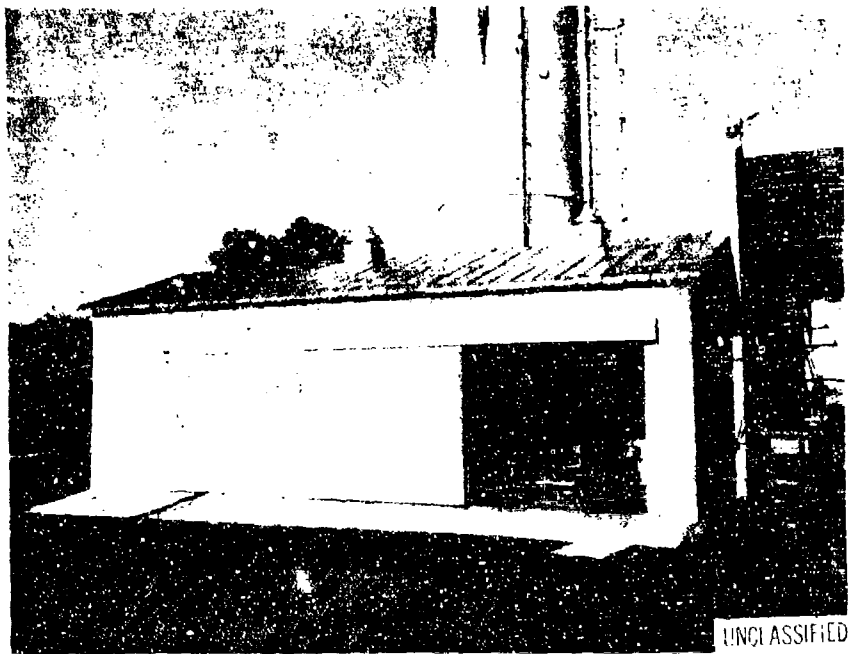


Figure 126. Laser Effects Laboratory (U)

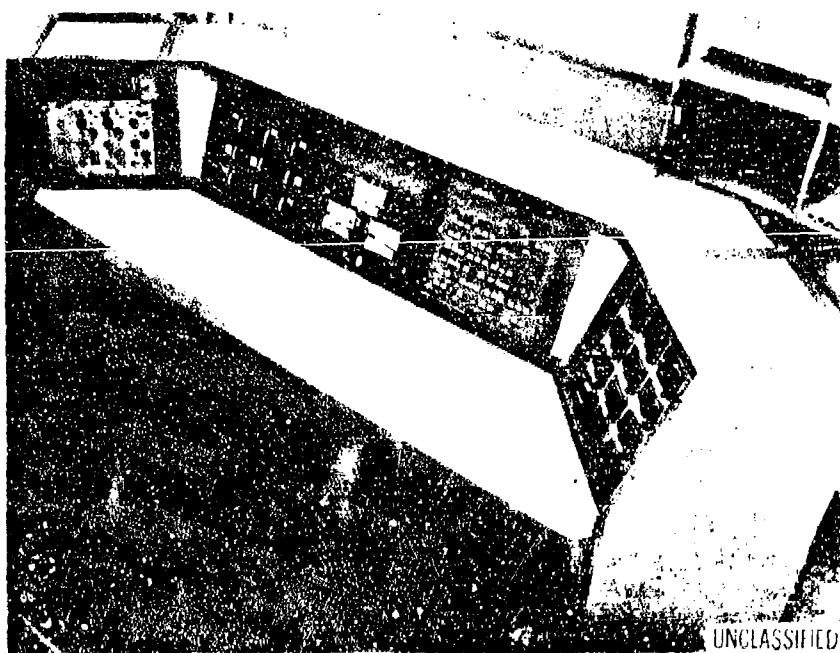
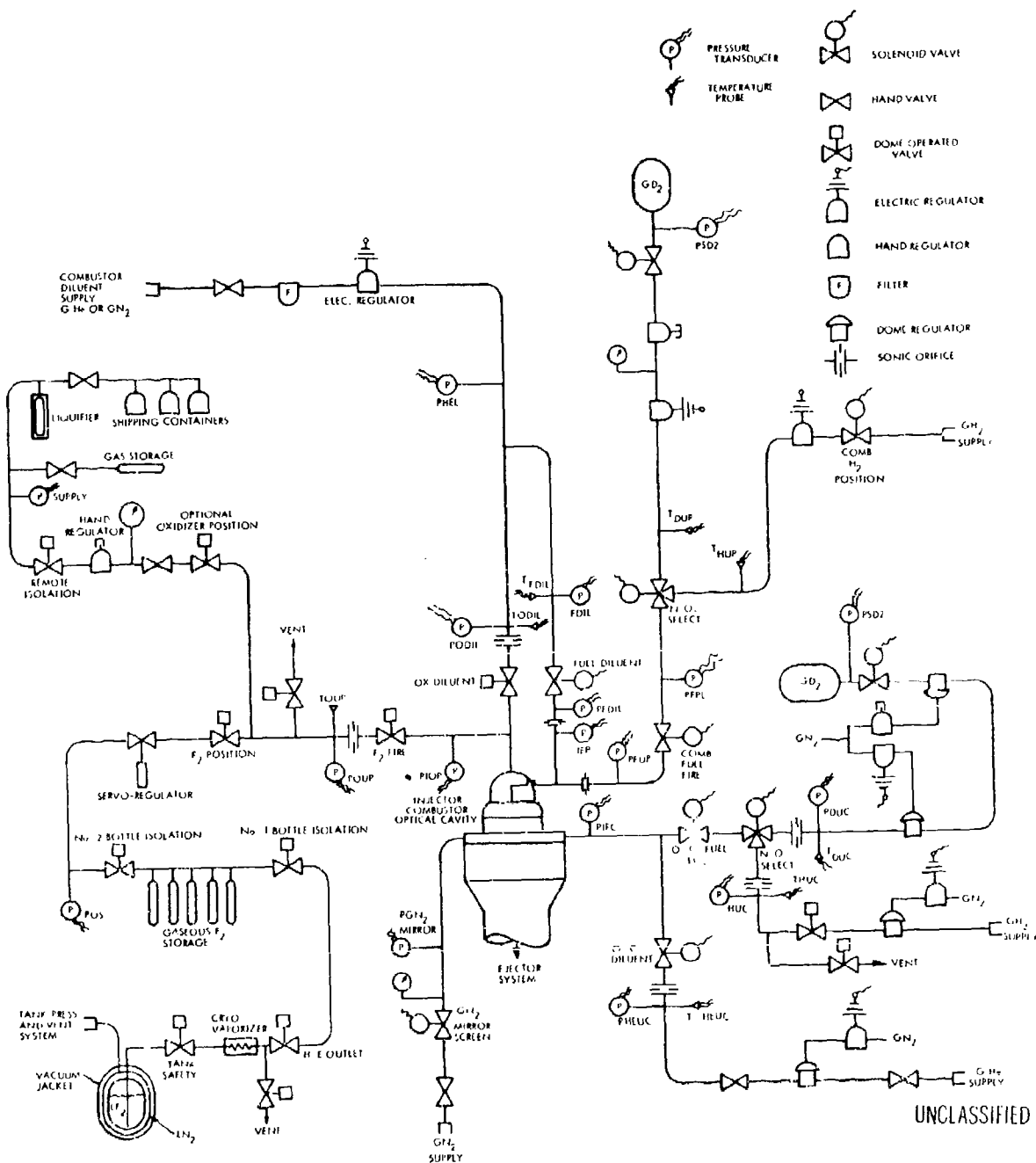


Figure 127. Laser Test Control Console (U)



UNCLASSIFIED

Figure 128. Chemical Laser Facility Feed System and Instrumentation Schematic (water cooling circuits omitted for clarity) (U)

(U) injector inlet manifolds. The diluents are premixed with the combustor oxidizer prior to injection through the combustor injector. Diluent distribution between the oxidizer and fuel circuits may be altered simply by changing the sonic orifices. Evaluation of other diluents is easily accomplished by changing gas bottle supply to the common pressure regulator.

(U) The cavity fuel and cavity diluent feed systems as shown in Figure 128 are similar to the combustor fuel and combustor diluent feed systems. The cavity may be fed with either gaseous hydrogen or deuterium from independently controlled pressure regulators and sonic control orifices to a select valve. A cavity fuel diluent supply system is also provided with remotely operated valves and a pressure control regulator for mixing, with the cavity fuel prior to injection into the laser cavity.

(U) The laser combustor and cavity box cooling is provided by a low pressure domestic water supply system with manual flow control valves and remote operating on-off control valves. The laser power meters, mirror-calorimeters, and cavity injector nozzles are cooled from a deionized water supply system with manual flow control valves and remotely operated on-off valves. The deionized water is supplied by a commercial water conditioner through an accumulator tank and feed supply pump.

(U) The laser test control console (Figure 127) is located in the test control and data acquisition center at the HEPTS complex. From this console all the valves and regulators for the laser feed and cooling system described previously may be controlled by a single console operator. Feed system supply pressures, upstream sonic orifice pressures, water cooling flow rates and temperatures, combustor and laser cavity pressures are all displayed on the console by meters and digital voltmeters. The test console also includes controls and feedback data displays of mirror gimbal position, laser closed cavity or outcoupled power, outcoupled beam central shutters, camera operation, etc.

(U) Test area surveillance is provided to the test conductor and console operator via a closed circuit television system which includes equipment for video and audio tape recording of test operations.

(U) The HEPTS altitude simulation system is used to pump the chemical laser effluents (Figure 129) and provide the required cavity vacuum environment. The pumping systems include two independently operable, continuously operating, three-stage steam ejectors with barometric intercondensers between stages. Both ejector systems are connected to a common header with 42-inch diameter vacuum isolation valves. The laser vacuum line is also connected to this header between the two isolation valves thereby permitting operation of the ejectors singly or in combination. The combined pumping capacity of the HEPTS ejector systems operating in parallel is approximately 1.3 lb/sec (30% non-condensables) free dry air equivalent flow at a section header pressure of 5 torr. The vacuum line from the laser test position includes a remotely operable vacuum isolation valve that can be throttled during test operations to provide controlled cavity pressure variations.

b. Instrumentation and Data Acquisition

(U) The instrumentation and data acquisition system used for chemical laser testing at CTS is all located within the HEPTS complex. The primary data acquisition system used for laser tests is the digital data

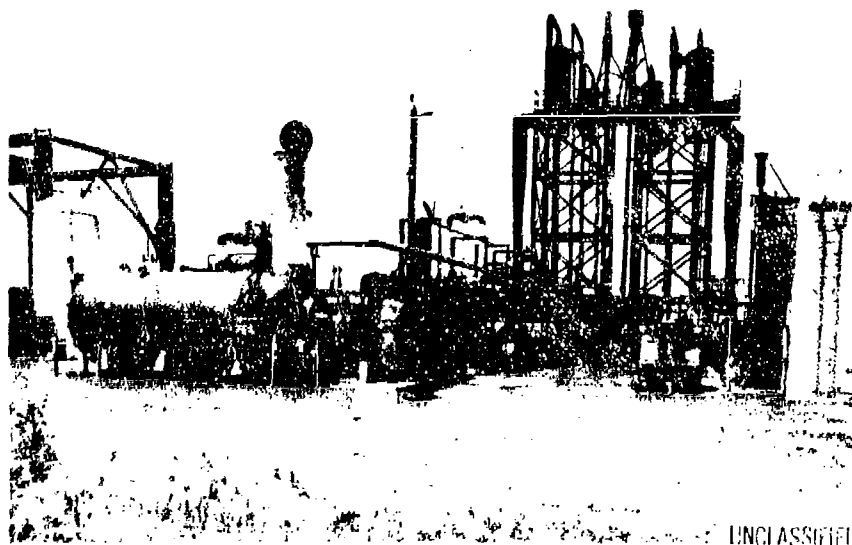


Figure 129. HEPTS Steam Ejector Pumping System (U)

(U) recorder system. All instrumentation parameters for computation of laser flow rates, power, heat loss, pressures, temperatures, etc. are required on the digital tape recorder. Redundant data recording is made of selected parameters on strip chart recorders for test monitoring and quick look test data results. Table 20 lists the data acquisition and recording equipment available at HEPTS.

(U) A typical instrumentation list for a chemical laser test series at HEPTS will have 50 to 60 measurements, including 25 to 30 pressures, 15 to 20 temperatures, 10 voltage command signals, five water flows, position potentiometers, etc. The feed system schematic, Figure 128, shows the instrumentation location of many of the test parameters recorded.

(U) Post-test digital data reduction is performed utilizing an Adage Ambilog 200 general purpose hybrid computer system located in the CTS Main Control Center. This computer uses both analog and digital circuits in computing arithmetic and logic operations in a single program step. The computer system has a 30-bit word length, 32 multiplexer channels under program control, 16K bytes of core memory, 10 priority interrupt channels, an oscilloscope display, a 600 line per minute line printer, a 120 ips magnetic tape drive and a teletype for program instruction.

(U) This section presents the results of an error analysis conducted on the measurement system used to obtain data from the laser technology experiments. The ground rules for this study were that (1) only available calibration data be used, and (2) for uncertainties not available because of lack of calibration or special test data, the best estimate based on a referenceable source be used. This report presents the results of the analysis for these primary laser measurements; individual gas feed flow rates, power, feed gas temperature and pressure, calorimeter water flow rate, and calorimeter water temperature.

(U) The approach used to develop each uncertainty estimate was to first determine if any calibration data were available. If calibration data existed, they were used to develop precision estimates. The precision estimates, together with accuracy estimates established by NBS (National Bureau of Standards), were to be combined to obtain the total

Table 20. HEPTS Data Acquisition and Recording Equipment (U)

| <u>Acquisition and Signal Conditioning Equipment</u> | <u>Recording Equipment</u> |
|--|--|
| • 72 strain gauge bridge channels | • 1 digital data acquisition system with a 72 multiplexer capability at total throughput of 20 kHz |
| • 96 thermocouple channels | • 1 Ampex FR-1200, 14 track, FM or direct record analog tape recorder |
| • 12 turbine flowmeter channels | • 1 Ampex FR-1800, 14 track, FM or direct record analog tape recorder |
| • 12 resistance temperature channels | • 2, CEC 36-channel oscillographs |
| • 16 voltage channels | • 1 Honeywell, 24-channel oscillograph |
| • 6 charge amplifiers | • 1 Honeywell, 36-channel oscillograph |
| • 128 data acquisition amplifiers | • 30 L and N strip chart recorders |

UNCLASSIFIED

(U) measurement uncertainty. If no calibration data existed for a given instrument type, but previous error analyses had been conducted at TRW, then previous analyses results were to be used. Failing the above, the estimate for uncertainty was to be based on the maximum quoted by either the ISA (Instrument Society of America) or NBS for the given type of measurement.

(U) The measurement of gas feed flow rate is made by the use of a sonic orifice and the upstream temperature and pressure measurements. In order to develop the uncertainty of the gas flow measurement, it is necessary to first examine the calibration of the orifice device. A review of the availability of calibration data of sonic orifice flowmeters (sonics) resulted in the conclusion that only the calibrations made using the Quantum Dynamics gas flowmeter could be used for estimating uncertainties. These calibration data included replicate runs on some of the sonic orifices. An estimate of the calibration precision was obtained (0.36% - 3 sigma) across all the sonics by using the data from replicate runs. The minimum flow rate limitation of the reference gas flowmeter (Quantum Dynamics) requires that the smaller sonic orifices be calibrated differently from the larger sonics. The smaller sonic orifices (i.e., throat diameters less than 0.03 inch) are calibrated by the difference of two runs, one with the test sonic and one with only the reference sonic and therefore the precision estimate for the smaller sonics was multiplied by the square root of two to obtain the final precision estimate (0.51% - 3 sigma). The accuracy of the Quantum Dynamics gas flowmeter calibration device is established by NBS to be 0.25%.

(U) The additional measurements that are necessary to develop the gas feed flows (i.e., gas pressure and temperature upstream of the sonic orifice) are provided by Taber transducers and Chromel-Alumel thermocouples. The uncertainty in gas pressure was obtained from a previous error analysis conducted at TRW Systems and for precision and accuracy, respectively, are 0.43 percent (3 sigma) and 0.17 percent (Reference 26). No previous error analysis has been conducted on the Chromel-Alumel thermocouples and therefore the precision estimate (2 percent - 3 sigma) was based on the maximum quoted by the Instrument Society of America (ISA). The root sum squaring (RSS) of the precision components and

(U) addition of the accuracy components results in estimates of 2.40 percent for large sonics and 2.44 percent for the small sonics.

(U) The measurement of power is made by the unit conversion of the closed cavity heat loss which in turn is determined from the measurement of the calorimeter water flow rate and associated temperature drop. These measurements, calorimeter water flow rate and temperature drop, are obtained from a 1 gpm turbine meter and a CU-CON thermocouple. Reference values for these measurements were obtained from the ISA and, in the case of the turbine meter, manufacturers specifications. These measurement uncertainty estimates (0.5 to 0.8 percent for the turbine meter and 2 percent for the thermocouple) were then combined by root sum squaring (RSS) to obtain the estimate of uncertainty in power. Note, that since the total heat loss (i. e. , power) is obtained from the sum of two independent water flow streams and temperature measurements, the uncertainty is multiplied by the square root of two.

(U) A summary of the measurement uncertainties is presented in Table 21. The run-to-run precision of each flow rate was developed from the laser technology testing for the nominal base case tests. A comparison of these run-to-run precision estimates to the total uncertainty estimates indicates a very good agreement supports the validity of the measurement uncertainty estimates.

d. Data Reduction Procedures for the Chemical Laser Test Facility

(1) Summary

(U) This section outlines the general data reduction and analysis procedures for the chemical laser test data. Presently, the data reduction system uses hand summaries of engineering test data with the calculations for the engineering parameters being done on the TRW remote TSS. Data storage is presently on punch cards and it is anticipated that as data volume and flow increases, this retrieval system will be converted to magnetic tape.

Table 2i. Laser Technology Experiments Summary of Measurement Uncertainty (U)

| Measurement Type | Nominal Value | Units | Run-to-Run Repeatability $\pm 3\sigma$ (%) / df | Total Measurement Uncertainty % Nominal |
|------------------------------------|---------------|-------|---|---|
| Flow rates (gas) | | | | |
| F ₂ (combustor chamber) | 8.8 | g/sec | 2.5/13 | 2.40 |
| He (combustor chamber) | 3.2 | g/sec | 4.7/13 | 2.40 |
| D ₂ (combustor chamber) | 0.56 | g/sec | 3.7/13 | 2.44 |
| H ₂ (optical cavity) | 0.8 | g/sec | 3.4/13 | 2.44 |
| He (optical cavity) | 1.6 | g/sec | N/A | 2.40 |
| Flow rate (liquid) | | | | |
| H ₂ O (calorimeter) | 1.0 | gpm | N/A | (0.5 to 0.8) |
| Pressure (gas) | 700 | psia | - | 0.6 |
| Temperatures (the rmocouples) | | | | |
| CR-AL (gas) | 70 | °F | - | 2.0 |
| CU-CON (liquid) | 40 | °F | - | 2.0 |
| Power* | N/A | watts | - | (2.9 to 3.03) UNCLASSIFIED |

*Uncertainty in power developed from the water flow measurement uncertainty and the (CU-CON) thermocouple temperature measurement uncertainty.

(2) Discussion

(U) The equations presently used to refine raw test data follow.

(a) Test Data Input

 m_i = mas flow rates (g/sec)

| <u>i</u> | <u>Description</u> |
|----------|---------------------------------|
| 1 | Combustor F_2 |
| 2 | Combustor D_2 |
| 3 | Combustor diluent |
| 4 | Combustor H_2 |
| 5 | Cavity D_2 |
| 6 | Cavity H_2 |
| 7 | Cavity Diluent |
| 8 | Combustor water jacket |
| 9 | Mirror calorimeter water jacket |

 P_i = system pressures (psia)

| <u>i</u> | <u>Description</u> |
|----------|--------------------|
| 1 | Combustor static |
| 2 | Cavity static |

 T_i = cooling system temperature ($^{\circ}\text{F}$)

| <u>i</u> | <u>Description</u> |
|----------|---|
| 1 | Combustor water jacket temperature change |
| 2 | Mirror calorimeter temperature change |

(U)

M_{w_i} = molecular wts

| i | Description |
|---|-------------------|
| 1 | Combustor F_2 |
| 2 | Combustor D_2 |
| 3 | Combustor diluent |
| 4 | Combustor H_2 |
| 5 | Cavity D_2 |
| 6 | Cavity H_2 |
| 7 | Cavity diluent |

(b) Gross Closed Cavity Power (watts)

$$S = C_1 \dot{m}_9 T_2$$

(c) Net Closed Cavity Power (no convection) (watts)

$$W = S - S'$$

where S' is the power level during a null test
(i. e. , cavity fuel = combustor fuel)

(d) Combustor heat loss (Btu/sec)

$$\dot{Q}_p = C_2 \dot{m}_8 T_1$$

(e) Total mass flow (g/sec)

$$\dot{m}_t = \sum_{i=1}^7 \dot{m}_i$$

(f) Combustor oxidizer-to-fuel molar ratio (diml)

$$R_C = (\dot{m}_1/4)/(\dot{m}_2/38)$$

- (U) (g) Moles of diluent/total combustor moles (diml)

$$R_d = (\dot{m}_3/Mw_3) / \sum_{i=1}^4 (\dot{m}_i/Mw_i)$$

- (h) Combustor mass flow (g/sec)

$$\dot{m} = \sum_{i=1}^4 \dot{m}_i$$

- (i) Combustor specific heat loss (Btu/g)

$$Q_p = q/\dot{m}_p$$

- (j) Combustor temperature (
- $^{\circ}$
- K)

$$T_p = f_1(p_1, R_d, Q_p) \text{ (second order Taylor Series expansion)}$$

- (k) Total mass flow (gram/sec)

$$\dot{m}_t = \sum_{i=1}^7 \dot{m}_i$$

- (l) Excess fluorine (both
- F_2
- and
- F
-) over stoichiometric (g/sec)

$$\dot{F}_2 = \dot{m}_1 - C_j \dot{m}_j$$

where:

$$C_j = \begin{cases} 19 & \text{for } j = 4 \text{ (D}_2\text{)} \\ 9.5 & \text{for } j = 2 \text{ (H}_2\text{)} \end{cases}$$

- (m) Partial pressure of
- $F_2 \rightleftharpoons 2F$
- system (psia)

$$P = P_1 \cdot V / (V + \sum_{i=2}^3 \dot{m}_i / Mw_1)$$

(U)

where:

$$V = (\dot{f} + \dot{F}_2)/38$$

$$\dot{f} = \text{flow rate of dissociated } F_2 \text{ (g/sec)} \\ \text{(see Equation (p))}$$

(n) Fluorine Dissociation Constant

$$K = \exp(f_2(P_p, T_p)) \quad \text{(argument is a second order Taylor Series expansion)}$$

(o) Molar Concentration of free F (to free F + F₂)

$$\lambda = (-K + \sqrt{K^2 + 4K})/2$$

(p) Mass Flow Rate of dissociated Fluorine (g/sec)

$$\dot{f} = \dot{F}_2 / (1 - \lambda)$$

(q) Combustor products mole flow (mole/sec)

$$\dot{n}_p = V + \sum_{i=1}^2 \dot{m}_i / Mw_i$$

(r) Cavity Reactant Mole Flow (mole/sec)

$$\dot{n}_c = \dot{n}_p + \sum_{i=4}^7 \dot{m}_i / Mw_i$$

(s) Laser Specific Energy Based on Total Consumption

$$\sigma = W / \dot{m}_t \text{ (joule/gram) or } 0.454 W / \dot{m}_t \text{ (Kjoule/lb)}$$

(t) Laser Specific Energy Based on Free Fluorine

$$\sigma_f = W / \dot{f} \text{ (joule/gram) or } 0.454 W / \dot{f} \text{ (Kjoule/lb)}$$

(u) Fluorine Dissociation Ratio (diml)

$$\alpha = \dot{f}_2 / \dot{F}_2$$

(U) (v) (Moles HF + moles dil)/(moles free fluorine as all F_2)

$$\dot{\Psi} = (\dot{m}_2/Mw_2 + \dot{m}_3/Mw_3)/(\dot{f}/Mw_1)$$

(w) Diluent/Fluorine Molar Ratio

$$\beta = (\dot{m}_3/Mw_3)/(\dot{f}/Mw_1)$$

(x) Moles Cavity Fuel/Moles Free F

$$R_3 = (\dot{m}_i/Mw_i)/(2 \dot{f}/Mw_1)$$

$$i = 5 \text{ or } 6$$

(y) Moles Cavity Fuel/Mole Excess F_2

$$R_L = (\dot{m}_i/Mw_i)/(\dot{F}_2/Mw_1)$$

$$i = 5 \text{ or } 6$$

APPENDIX II

CHEMILUMINESCENT SPECTRUM REDUCTION PROGRAM

(U) Our program I0219 reduces HF vibration-rotation spectra generated from the chemiluminescent experiment to absolute vibration-rotation line intensities and to upper excited state population number densities integrated along the respective line-of-sight. The chemiluminescent experiment output consists of IR detected output signals (volts) recorded on magnetic tape. The tape also contains two wavelength markers to indicate the start and end of an individual spectral scan. The first task of the computer is to identify each HF spectral line by determining its wavelength position and comparing it with input information. The next step is to read the line signal level (microvolts) and to compute absolute line intensity. Computed absolute vibration-rotation line intensities are then used as inputs in a final computational routine for calculating excited state number densities using Equation (1). (For these latter steps a calibration curve and molecular constants are provided as input data.) A brief description of the program is given below. The printed computer output is hand plotted for further detailed data analysis.

Laser Spectral Program Description

Input

Parameters

Punched card input includes control parameters such as:

LAMDA0 - Starting value of lambda in microns

DELTA - Tolerance for fit in the peak lambda table

MULT-BIAS - Calibration factors if no cal files are available

- (U) Tables of the following values are input for each branch
(P and R) and for each transition within the branch:

PLAM - RLAM - Peak values of lambda

PW - RW - Responsivity

PWAT - RWAT - $\nu^{-4} \cdot S$

Tape

The magnetic tape is generated on the PDP-11 from the laser analog tape. The recorded counts represent a measurement of relative module density.

Method

(U) Counts are converted to millivolts using the multiplier (MULT) and bias (BIAS) computed from the calibration files. If no calibration files are available, MULT and BIAS must be input.

(U) Peaks are determined by finding a positive and negative slope on each side of a point (five points on each side).

(U) After the peaks have been determined and wavelength for each peak computed, the program goes into the tables to pick up J' and responsivity.

Equations

$$I = p * W$$

where:

p = peak microvolts

W = responsivity

$$(\text{number of molecules/cm}^2) = \frac{1 \cdot 10^{-7}}{|m| \{ \nu^{-4} \cdot S \} \frac{16\pi^3}{3} (3 \times 10^{10})}$$

$$\text{where: } S = \left| \langle \nu' j' | M(r) | \nu'' j'' \rangle \right|^2$$

$$|m| = j' + 1 = j'' \text{ (P branch)}$$

$$|m| = j' = j'' + 1 \text{ (R branch)}$$

Output

(U) Output consists of tabulated listings of input as well as computed values. There is a separate listing for each transition of each branch (P and R). The values output include wavelength, responsivity, peak microvolts, $\nu^4 \cdot S_j (J'+1)$, and number of molecules/cm².

1. IR-SCANNER DATA PERSPECTIVE PLOT PROGRAM

(U) The purpose of the IR scanner data perspective plot program is to generate a display of the IR scanner experimental output data suitable for visual perception of flow field IR emission structure. The data have been recorded on analog tape and available data are contained in two FM recorded functions. One function is the IR detector output signals while scanning the laser cavity as described in Section 4. b. The other FM recorded function is a switch indicating the start of each horizontal scan in the forward direction.

(U) The perspective plot program works with a digitized tape generated from the analog tape by the Data Reduction Center (DRC). Utilizing the start of scan signal, the program locates the start of data for successive horizontal sweeps of the cavity window, extracts, calibrates and plots a predetermined interval of the IR detector output signal. The calibration for the most part is arbitrary, but was incorporated to provide a means of controlling individual scan resolution.

(U) Appropriate vertical and horizontal adjustments are made to the data from each sweep in order to achieve a perspective orientation in the final plot. The vertical adjustment increment chosen is such that an even vertical distribution of all the scans over the plot surface is achieved. The horizontal adjustment increment is small and just sufficient to distinguish between parallel scan lines.

(a) Input

(U) Input to the IR scanner data perspective plot program is the analog tape generated from the IR scanner experiment. Input to the perspective plot program is the DRC digital tape.

(U) Digitizing of the IR detector signal is at 30,000 samples per record while the start of scan status is sensed with analog methods (Schmidt trigger) and flag bits are appropriately set to indicate its on-off status.

(U) The data tape is the standard tape written by the DRC for CDC 6500 computer processing. Certain program control parameters pertaining to scan rates data resolution, and plot formats are also input

(b) Output

(U) The output of the perspective plot program is a Cal Comp zip mode plot tape. Each plot picture contains all of the scan lines recorded for a complete traverse of the cavity window. The X axis of each plot is proportionate to horizontal sensor position, while the distribution of the scan lines along the Y axis scale is arbitrary and a function of plot resolution desired.

2. IR-SCANNER DATA INTENSITY CONTOUR MAP PROGRAM

(U) Program I0218 was designed to produce contour plots of the IR scanner signals from the laser cavity. The IR scanner output signals are recorded on analog tape which is at a later time converted (digitized) to a digital format compatible with TRW's CDC 6500 computer. Each scan line contains several hundred digital data points. The program reads the input magnetic tape, performs calibrations to convert the data from digital counts to engineering units (volts), searches the data for relative maxima and minima. These data are output onto a contour format tape and a CEFØRM data tape for further reference.

(a) Input

(U) Modes of input are magnetic tape and cards. The magnetic tape is a Data Reduction Center (DRC) tape generated on the PDP-11 computer, and contains data digitized from the IR-scanner analog tape. The punched card input contains control parameters and specification data necessary to perform the data reduction and contouring processes.

(b) Operation

(U) The usual way to run the program is to run the contour program, CALCOMP GPCP, in the Batch Mode, immediately following program I0218. Program GPCP reads the control cards produced by I0218, reads the contour data tape, and generates a plot tape containing a contour map of the data. Program GPCP may be run separately, utilizing the data on the contour tape and cards which may or may not have been generated by I0218, depending on the required results.

(c) Equations

(U) Calibration equations generated by least squares

$$p = \theta(C) = a_1 + a_2 C + a_3 C^2$$

where p = percent bandwidth

C = digital counts (averaged from calibration files on tape or read from cards)

$$e = \psi(p) = b_1 + b_2 p + b_3 p^2$$

where e = engineering units

p = percent bandwidth

(U) Given the above transformations, there exists a third: $e = \theta(C) = \psi[\theta(C)]$ which converts directly from counts to engineering units. This transformation is used, eliminating the need for two consecutive polynomial evaluations to convert from counts to engineering units.

Method of Establishing Maxima/Minima

(U) The data are examined in samples of several points at a time (usually five points). A quadratic polynomial is fit to each sample, and the sign of the second derivative is established. If the second derivative is positive, the function is concave upward, and a search is made for a relative minimum. If negative, it is concave downward, and a relative maximum is established. Thus, peaks in the data are retained as close together as the distance spanned by twice the sample size, usually 10 points, which is generally the maximum resolution criterion.

Contouring Equations

(U) A complete formulation of contouring equations used may be obtained from reading the CALCOMP GPCP Manual, published by CALCOMP Inc., particularly Section 2. A detailed description is beyond the scope of this document.

(d) Output

(U) Modes of output are a listing, punched cards, magnetic tape, and plots. The listing contains a general synopsis of what occurs during execution. Control cards for input to the GPCP contour program are punched for future use. Magnetic tapes written include a GEFØRM general-purpose tape containing (X, Y, Z) data generated by the data reduction process, an input tape to the contour program GPCP, containing (X, Y, Z) data in a BCD format, and a plot tape generated by program GPCP. The plots generated are contour plots of laser cavity intensity read by the IR-scanner.

REFERENCES

1. Spencer, D.J., Jacobs, T.A., Mirels, H., and Gross, R.W.F., "Continuous-Wave Chemical Laser," J. Chem. Kinet, 1, p. 493, 1969.
2. Spencer, D.J., Mirels, H., Jacobs, T.A., and Gross, R.W.F., "Preliminary Performance of a CW Chemical Laser," Appl. Phys. Letters, 16 p. 235, 1970.
3. Spencer, D.J., Mirels, H., and Jacobs, T.A., "Comparison of HF and DF Continuous Chemical Lasers: I. Power," Appl. Phys. Letters, 16, p. 384, 1970.
4. Spencer, D.J., Mirels, H., and Jacobs, T.A., "Initial Performance of a CW Chemical Laser," Opto-Electronics, 2, pp. 155-160, 1970.
5. Spencer, D.J., Durran, D.A., and Bisler, H.A., "Continuous-Chemical-Laser Cavity Studies," Appl. Phys. Letters, 20, p. 164, 1972.
6. Project MESA Data Summary - 1970, Aerospace Report No. TR-0172(2779)-3, 1971.
7. Emanuel, G., Cohen, N., and Jacobs, T.A., Theoretical Performance of an HF Chemical CW Laser, Aerospace Report No. TR-0172(2776)-2, 1971.
8. High Energy Laser Technology (U), TRW Proposal Number 18273.000, 31 October, 1970 (Confidential)
9. Lynds, L., Chemiluminescence Emission Study, TRW Internal Report No. 70.4214-240, October 9, 1970.
10. Cornell, P.H., and Pimentel, G.C., "Hydrogen-Chlorine Explosion Laser II. DC2," J. Chem. Phys., 49 (3), pp. 1379-1386, 1968.
11. Cool, T.A., Stephens, R.R., and Shirley, J.A., "HCl, HF, and DF Partially Inverted CW Chemical Lasers," J. of Applied Physics, 41, pp. 4038-4050, 1970.
12. Meredith and Smith, F.G., Investigations of Fundamental Laser Processes, Vol. II - Computation of Electric Dipole Matrix Elements for Hydrogen Fluoride and Deuterium Fluoride, Willow Run Laboratories, University of Michigan, Report No. 84130-39-T (II), November 1971.
13. Valiant, W., Birang, B., and MacLean, D.I., Measurement of Fluorine Atom Concentrations and Combination Rates by ESR Spectroscopy, Contract No. N00014-69-A-0453 to ONR from Boston College, Chestnut Hill, Massachusetts, October 1971.

14. Parker, J.H. and Pimentel, J.C., "Vibrational Energy Distribution Through Chemical Laser Studies I. Fluorine Atom Plus Hydrogen or Methane," J. Chem. Phys., 51, pp. 91-96, 1969.
15. Pilanyi, J.C. and Tardy, D.C., "Energy Distribution in the Exothermic Reaction $F + H_2$ and the Endothermic Reaction $HF + H^*$," J. Chem. Phys., 51, pp. 5717-5719, 1969.
16. Jonathan, N., Melliar-Smith, C.M., and Slater, D.H., Initial Vibrational Energy Distributions Determined by Infrared Chemiluminescence: Part I. The Reaction of Fluorine Atoms with Hydrogen and Methane, Chemistry Department, The University of Southampton, Report Contract F60152-69-C-0032, 1970.
17. Bittner, J.W. and Gregorek, G.M., An Investigation of Planar Free Jets, Aerospace Research Labs., USAF, Contract AF 33 (657) - 11060, Project 7065, March 1966.
18. Demetriades, A. and Doughman, E.L., Mean Flow Measurements in a Self-Preserving Turbulent Plasma Jet, Technical Report SAMSO TR 68-166, Philco-Ford Corp., Newport Beach, Calif., Feb. 1968.
19. Page, R.H. and Hill, W.G., Jr., "Location of Transition in a Free Jet Region" AIAA Jour., Vol. 4, No. 5, p. 944, May 1966.
20. Mirels, H. and Spencer, D.J., "Power and Efficiency of a Continuous HF Chemical Laser," IEEE Jour. of Quantum Electronics, Vol. QE-7, No. 11, Nov. 1971.
21. Miles, J.B. and Slick, J., "Similarity Parameter for Two-Stream Turbulent Jet-Mixing Region," AIAA Jour. No. 6, pp. 1429-1430, 1968.
22. Cohen, C.B., and Reshotko, E., Similar Solutions for the Compressible Laminar Boundary Layer with Heat Transfer and Pressure Gradient, NACA Report 1293.
23. Beckwith, I.E., and Cohen, N.B., Application of Similar Solutions to Calculations of Laminar Heat Transfer on Bodies with Yaw and Large Pressure Gradient in High Speed Flow, NASA TN D-625, January 1961.
24. "Theory of Laminar Flows," F.K. Moore, Ed., Vol. IV, High Speed Aerodynamics and Jet Propulsion, Princeton University Press, 1964.
5. Talbot, L., A Mach 3.106 Two-Dimensional Adjustable Nozzle for Low Density Flow, Technical Report No. HE-150-120, University of California, Institute of Engineering Research, Berkeley, February 1954.
26. Oki, C.H. and Verner, C.E., LMDE Instrumentation Error, TRW Report 01827-6002-R000, 31 August 1966.

CONFID

Table 13. Target Diagnosis

| Test Conditions | | Combustion Chamber | | | | Or |
|-----------------|---|--------------------------------|------------------------------|------------------------------|-----------------------------|----|
| | | \dot{m}_{Total} (gms/sec) | \dot{m}_{F_2} (gms/sec) | \dot{m}_{D_2} (gms/sec) | \dot{m}_{He} (gms/sec) | |
| Ia | o Nominal Flows (Baseline Conditions) | 14.2 | 8.8 | 0.56 | 3.2 | 1 |
| Ib | o Nominal Flows With 2 Times Baseline Cavity Pressure | 14.2 | 8.8 | 0.56 | 3.2 | 1 |
| Ic | o Nominal Flows With 4 Times Baseline Cavity Pressure | 14.2 | 8.8 | 0.56 | 3.2 | 1 |
| Id | o Nominal Flows With 6 Times Baseline Cavity Pressure | 14.2 | 8.8 | 0.56 | 3.2 | 1 |
| II | o 1.5 Times Nominal Flows | 21.2 | 13.2 | 0.84 | 4.8 | 2 |
| III | o Nominal Combustor Flows With 50 Percent of Cavity Hydrogen Replacement with Equivalent Molar Flow of Helium | 15.0 | 8.8 | 0.56 | 3.2 | 0 |
| IV | o Nominal Total Flows With Increased Combustor Temperature | 14.2 | 8.7 | 0.65 | 3.6 | 1 |

(This page is Un

CONF

Diagnostic Test Conditions (U)

| Optical Cavity | | | | | | | | | |
|----------------|------------------------------|-----------------------------|----------------------------|--|--|---------------------------------------|------------------------------------|--------------------------------|----------------------------------|
| He (sec) | \dot{m}_{H_2} (gms/sec) | \dot{m}_{He} (gms/sec) | Re Combustor Mass MR | Rd Moles <u>Combustor He</u> <u>Combustor Total</u> Combustor Flow | R3 Moles <u>H₂ Cavity</u> <u>Moles F</u> | P _c Combustor (psia) | P _L Cavity (torr) | P _c /P _L | Combustor Temperature (°K) |
| 2 | 1.6 | 0 | 15.7 | 0.7 | 4.4 | 12.5 | 1.4 | 480 | 1900 |
| 1 | 1.6 | 0 | 15.7 | 0.7 | 4.4 | 12.5 | 2.8 | 240 | 1900 |
| 2 | 1.6 | 0 | 15.7 | 0.7 | 4.4 | 12.5 | 5.4 | 125 | 1900 |
| 2 | 1.6 | 0 | 15.7 | 0.7 | 4.4 | 12.5 | 7.8 | 83 | 1900 |
| 8 | 2.4 | 0 | 15.7 | 0.7 | 4.4 | 19.4 | 1.9 | 525 | 1900 |
| 2 | 0.8 | 1.6 | 15.7 | 0.7 | 2.2 | 12.5 | 1.4 | 480 | 1900 |
| 6 | 1.2 | 0 | 13.4 | 0.7 | 4.4 | 13.7 | 1.4 | 525 | 2300 |

UNCLASSIFIED

UNCLASSIFIED

CONFIDENTIAL

Table 14. Data Summary for Runs 97 Th

| Test No. | \dot{m}_{F_2} (g/sec) | \dot{m}_{D_2} (g/sec) | \dot{m}_{He} (g/sec) | \dot{m}_{H_2} (g/sec) | Laser Power (watts) | PC (psia) | Cavity Press. PL (torr) | Q (btu/sec) | XC (in) |
|----------|----------------------------|----------------------------|---------------------------|----------------------------|---------------------------|--------------|-------------------------------|----------------|------------|
| HB5-97A | 5.538 | .345 | 1.998 | 1.020 | 1882 | 15.5 | 1.34 | 12.0 | 1.26 |
| HB5-97B | 4.478 | .346 | 1.593 | .593 | 1165 | 13.8 | 1.09 | 13.0 | 1.32 |
| HB5-97C | 6.491 | .335 | 2.260 | 1.446 | 1693 | 16.5 | 1.91 | 11.8 | 1.16 |
| HB5-97D | 7.212 | .341 | 2.680 | 1.818 | 1388 | 18.1 | 2.28 | 11.0 | |
| HB5-98B | 5.441 | .340 | 1.980 | 1.016 | 1494 | 15.2 | 1.40 | 12.2 | 1.07 |
| HB5-98C | 5.000 | .286 | .994 | 1.004 | 514 | 11.8 | 1.50 | 8.9 | |
| HB5-98D | 5.780 | .371 | 2.402 | 1.005 | 1887 | 17.1 | 1.45 | 13.3 | 1.38 |
| HB5-98E | 5.883 | .400 | 2.889 | 1.002 | 1791 | 19.0 | 1.40 | 13.8 | 1.48 |
| HB5-99A | 5.630 | .350 | 2.048 | .978 | 1833 | 16.0 | 1.40 | 12.3 | 1.28 |
| HB5-99B | 5.456 | .347 | 1.988 | .970 | 1790 | 15.6 | 1.34 | 12.2 | |
| HB5-99C | 5.370 | .346 | 1.991 | .480 | 1587 | 15.6 | 1.24 | 12.4 | 1.30 |
| HB5-99D | 5.389 | .346 | 1.998 | 1.473 | 1751 | 15.6 | 1.45 | 12.6 | 1.20 |
| HB5-99E | 5.355 | .347 | 1.990 | 1.987 | 1520 | 15.7 | 1.55 | 12.1 | |
| HB5-99F | 5.133 | .302 | 1.274 | .984 | 1064 | 13.2 | 1.60 | 9.9 | 1.15 |
| HB5-99G | 6.320 | .409 | 2.346 | 1.201 | 1960 | 18.6 | 1.45 | 14.2 | |
| HB5-99H | 7.492 | .474 | 2.777 | 1.387 | 1655 | 22.0 | 1.65 | 15.2 | |
| HB5-100A | 5.716 | .350 | 2.040 | 1.002 | 1878 | 16.0 | 1.29 | 11.3 | 1.60 |
| HB5-100B | 5.598 | .353 | 2.007 | .989 | 1840 | 16.0 | 1.24 | 11.5 | 1.61 |
| HB5-100C | 4.469 | .352 | 1.622 | .593 | 1173 | 14.2 | 0.10 | 11.9 | 1.48 |
| HB5-100D | 6.538 | .350 | 2.339 | 1.423 | 1806 | 17.2 | 1.71 | 10.8 | 1.36 |
| HB5-101A | 6.619 | .422 | 2.395 | 1.213 | 2045 | 19.3 | 1.40 | 13.4 | 1.44 |
| HB5-101B | 6.674 | .420 | 2.385 | .998 | 2025 | 19.2 | 1.34 | 13.4 | 1.42 |
| HB5-101C | 6.673 | .421 | 2.386 | .795 | 1929 | 19.2 | 1.34 | 13.5 | 1.41 |

| Test No. | Rd Moles Diluent/ Total Com- bustor Moles | Combustor Tempera- ture (°K) | F ₂ Dissoci- ation α | Excess F Flow Rate (g/sec) | Flow Rate Free F (g/sec) | σ , Specific Energy - Total Flow | | σ_f |
|----------|--|---------------------------------------|---|-------------------------------------|-----------------------------------|--|-------------|------------|
| | | | | | | (joule/g) | (Kjoule/lb) | (joule/g) |
| HB5-97A | .683 | 1643 | .992 | 2.261 | 2.242 | 211.4 | 96.0 | 81 |
| HB5-97B | .660 | 2147 | 1.000 | 1.191 | 1.191 | 166.2 | 75.5 | 91 |
| HB5-97C | .689 | 1343 | .827 | 3.309 | 2.736 | 160.7 | 73.0 | 61 |
| HB5-97D | .709 | 1276 | .689 | 3.972 | 2.736 | 115.2 | 52.3 | 51 |
| HB5-98B | .685 | 1621 | .997 | 2.211 | 2.204 | 170.2 | 77.3 | 61 |
| HB5-98C | .549 | 1907 | 1.000 | 2.283 | 2.283 | 70.6 | 32.1 | 22 |
| HB5-98D | .711 | 1489 | .986 | 2.255 | 2.223 | 197.4 | 89.6 | 84 |
| HB5-98E | .739 | 1589 | 1.000 | 2.083 | 2.083 | 176.0 | 79.9 | 85 |
| HB5-99A | .685 | 1625 | .997 | 2.305 | 2.299 | 203.5 | 92.4 | 79 |
| HB5-99B | .684 | 1677 | 1.000 | 2.159 | 2.159 | 204.3 | 92.8 | 82 |
| HB5-99C | .686 | 1683 | 1.000 | 2.083 | 2.083 | 193.8 | 88.0 | 76 |
| HB5-99D | .686 | 1661 | 1.000 | 2.102 | 2.102 | 190.4 | 86.4 | 83 |
| HB5-99E | .687 | 1712 | 1.000 | 2.058 | 2.058 | 157.0 | 71.3 | 73 |
| HB5-99F | .603 | 1797 | 1.000 | 2.264 | 2.264 | 138.3 | 62.8 | 47 |
| HB5-99G | .687 | 1716 | .999 | 2.434 | 2.432 | 190.7 | 86.6 | 80 |
| HB5-99H | .687 | 1715 | .998 | 2.989 | 2.983 | 136.4 | 61.9 | 55 |
| HB5-100A | .682 | 1659 | .997 | 2.391 | 2.383 | 206.2 | 93.6 | 78 |
| HB5-100B | .681 | 1718 | 1.000 | 2.245 | 2.245 | 205.7 | 93.4 | 81 |
| HB5-100C | .663 | 2272 | 1.000 | 1.125 | 1.125 | 166.7 | 75.7 | 104 |
| HB5-100D | .693 | 1416 | .910 | 3.213 | 2.924 | 169.6 | 77.0 | 61 |
| HB5-101A | .682 | 1756 | 1.000 | 2.610 | 2.610 | 192.0 | 87.2 | 78 |
| HB5-101B | .680 | 1733 | 1.000 | 2.684 | 2.684 | 193.3 | 87.8 | 79 |
| HB5-101C | .680 | 1728 | 1.000 | 2.674 | 2.674 | 187.7 | 85.2 | 72 |

CONFIDENTIAL

CONFIDENTIAL

AFWL-TR-72-28

Runs 87 Through 101 (U)

| Q (btu/sec) | XC (in) | Total Mass Flow (g/sec) | Cavity Mole Flow (m/sec) | Combustor Mass Flow (g/sec) | Combustor Mole Flow (m/sec) | RC Combustor Molar Ratio |
|----------------|------------|-------------------------------|--------------------------------|-----------------------------------|-----------------------------------|--------------------------------|
| 12.0 | 1.26 | 8.901 | .510 | 7.881 | .731 | 1.690 |
| 13.0 | 1.32 | 7.010 | .296 | 6.417 | .603 | 1.362 |
| 11.8 | 1.16 | 10.532 | .723 | 9.086 | .820 | 2.040 |
| 11.0 | | 12.051 | .909 | 10.233 | .945 | 2.226 |
| 12.2 | 1.07 | 8.777 | .508 | 7.761 | .723 | 1.685 |
| 8.9 | | 7.284 | .502 | 6.280 | .452 | 1.840 |
| 13.3 | 1.38 | 9.558 | .503 | 8.553 | .845 | 1.640 |
| 13.8 | 1.48 | 10.174 | .501 | 9.172 | .977 | 1.548 |
| 12.3 | 1.28 | 9.006 | .489 | 8.028 | .748 | 1.693 |
| 12.2 | | 8.761 | .485 | 7.791 | .727 | 1.655 |
| 12.4 | 1.30 | 8.187 | .240 | 7.707 | .726 | 1.634 |
| 12.6 | 1.20 | 9.196 | .736 | 7.723 | .725 | 1.639 |
| 12.1 | | 9.679 | .994 | 7.692 | .725 | 1.624 |
| 9.9 | 1.15 | 7.693 | .492 | 6.709 | .529 | 1.789 |
| 14.2 | | 10.276 | .601 | 9.075 | .855 | 1.627 |
| 15.2 | | 12.130 | .694 | 10.743 | 1.010 | 1.664 |
| 11.3 | 1.60 | 9.108 | .501 | 8.106 | .748 | 1.719 |
| 11.5 | 1.61 | 8.947 | .495 | 7.958 | .737 | 1.669 |
| 11.9 | 1.48 | 7.036 | .296 | 6.443 | .611 | 1.336 |
| 10.8 | 1.36 | 10.650 | .712 | 9.227 | .844 | 1.996 |
| 13.4 | 1.44 | 10.649 | .607 | 9.436 | .878 | 1.651 |
| 13.4 | 1.42 | 10.477 | .499 | 9.479 | .877 | 1.673 |
| 13.5 | 1.41 | 10.275 | .398 | 9.480 | .877 | 1.668 |

| Specific Energy - Total Flow (Kjoule/lb) | σ_f , Specific Energy - Free F (joule/g) | σ_f , Specific Energy - Free F (Kjoule/lb) | ψ Combustor Diluent Ratio | β Combustor Diluent Ratio | R_3 Mole Ratio Cavity Fuel to Free F | R_L Cavity Molar Ratio |
|--|---|---|---|--|---|-----------------------------------|
| 96.0 | 839.4 | 381.1 | 11.390 | 8.458 | 4.322 | 8.644 |
| 75.5 | 978.2 | 444.1 | 18.265 | 12.716 | 4.722 | 9.444 |
| 73.0 | 618.8 | 280.9 | 10.389 | 7.847 | 5.021 | 10.042 |
| 52.3 | 507.3 | 230.3 | 12.125 | 9.306 | 6.312 | 12.625 |
| 77.3 | 677.9 | 307.8 | 11.466 | 8.535 | 4.380 | 8.759 |
| 32.1 | 225.1 | 102.2 | 6.521 | 4.127 | 4.178 | 8.356 |
| 89.6 | 848.9 | 385.4 | 13.444 | 10.274 | 4.299 | 8.598 |
| 79.9 | 859.8 | 390.3 | 16.829 | 13.175 | 4.570 | 9.140 |
| 92.4 | 797.3 | 361.9 | 11.364 | 8.463 | 4.041 | 8.083 |
| 92.8 | 828.9 | 376.3 | 11.799 | 9.014 | 4.268 | 8.536 |
| 88.0 | 761.9 | 345.9 | 12.248 | 9.088 | 2.189 | 4.378 |
| 86.4 | 833.0 | 378.2 | 12.110 | 8.987 | 6.652 | 13.305 |
| 71.3 | 738.4 | 335.2 | 12.377 | 9.188 | 9.177 | 18.354 |
| 62.8 | 470.0 | 213.4 | 8.446 | 5.696 | 4.129 | 8.258 |
| 86.6 | 805.9 | 365.9 | 12.359 | 9.172 | 4.695 | 9.391 |
| 61.9 | 554.8 | 251.9 | 11.866 | 8.841 | 4.488 | 8.976 |
| 93.6 | 788.1 | 357.8 | 10.930 | 8.134 | 3.994 | 7.989 |
| 93.4 | 819.8 | 372.2 | 11.470 | 8.494 | 4.189 | 8.379 |
| 75.7 | 1042.7 | 473.4 | 19.642 | 13.682 | 4.999 | 9.998 |
| 77.0 | 617.6 | 280.4 | 9.975 | 7.607 | 4.626 | 9.253 |
| 87.2 | 783.5 | 355.7 | 11.780 | 8.719 | 4.419 | 8.838 |
| 87.8 | 754.5 | 342.5 | 11.422 | 8.442 | 3.532 | 7.065 |
| 85.2 | 721.5 | 327.6 | 11.457 | 8.466 | 2.828 | 5.656 |

CONFIDENTIAL

CONFIDENTIAL

CONFIDENTIAL

Table 15. Data Summary for Runs

| Test No. | \dot{m}_{F_2} (g/sec) | \dot{m}_{D_2} (g/sec) | \dot{m}_{H_e} (g/sec) | \dot{m}_{H_2} (g/sec) | Laser Power (watts) | PC (psia) | Cavity Press. PL (torr) | (btu) |
|-----------|----------------------------|----------------------------|----------------------------|----------------------------|---------------------------|--------------|-------------------------------|-------|
| HB5-103B | 5.491 | .360 | 2.061 | .978 | 1562 | 15.8 | 3.47 | 12 |
| HB5-103C1 | 5.596 | .351 | 2.017 | .996 | 1672 | 15.6 | 3.36 | 11 |
| HB5-103C2 | 5.555 | .350 | 2.015 | .995 | 1454 | 15.5 | 4.60 | 11 |
| HB5-103C3 | 5.536 | .350 | 2.014 | .996 | 873 | 15.5 | 6.62 | 11 |
| HB5-103C4 | 5.497 | .349 | 2.012 | .996 | 1080 | 15.4 | 6.67 | 11 |
| HB5-103D | 5.716 | .357 | 2.046 | 1.010 | 1355 | 15.8 | 5.02 | 11 |
| HB5-112B | 5.416 | .352 | 2.035 | .993 | 1583 | 16.0 | 3.21 | 12 |
| HB5-112C1 | 5.489 | .352 | 2.034 | .996 | 1398 | 16.1 | 4.29 | 12 |
| HB5-112C2 | 5.487 | .352 | 2.028 | .999 | 1025 | 16.1 | 6.46 | 12 |

| Test No. | R_d Moles Diluent/ Total Com- bustor Moles | Combustor Tempera- ture (°K) | F_2 Dissoci- ation α | Excess F Flow Rate (g/sec) | Flow Rate Free F (g/sec) | σ , Specific En Total Flo (joule/g) (Kj) |
|-----------|---|---------------------------------------|--|-------------------------------------|-----------------------------------|---|
| HB5-103B | .687 | 1705 | 1.000 | 2.075 | 2.179 | 175.7 |
| HB5-103C1 | .682 | 1679 | 1.000 | 2.261 | 2.271 | 186.6 |
| HB5-103C2 | .684 | 1678 | 1.000 | 2.230 | 2.234 | 163.1 |
| HB5-103C3 | .682 | 1689 | 1.000 | 2.211 | 2.211 | 98.1 |
| HB5-103C4 | .684 | 1685 | 1.000 | 2.181 | 2.190 | 122.0 |
| HB5-103D | .682 | 1693 | 1.000 | 2.325 | 2.328 | 148.4 |
| HB5-112B | .687 | 1715 | 1.000 | 2.072 | 2.080 | 180.0 |
| HB5-112C1 | .689 | 1696 | 1.000 | 2.145 | 2.147 | 157.6 |
| HB5-112C2 | .686 | 1679 | 1.000 | 2.143 | 2.146 | 115.6 |

CONFIDENTIAL

Summary for Runs 103 Through 112 (U)

| Y Press. PL (orr) | Q (btu/sec) | XC (in) | Total Mass Flow (g/sec) | Cavity Mole Flow (m/sec) | Combustor Mass Flow (g/sec) | Combustor Mole Flow (m/sec) | RC Combustor Molar Ratio |
|-------------------------|----------------|------------|-------------------------------|--------------------------------|-----------------------------------|-----------------------------------|--------------------------------|
| .47 | 12.5 | 1.43 | 8.890 | .489 | 7.912 | .750 | 1.606 |
| .36 | 11.7 | 1.25 | 8.960 | .498 | 7.964 | .739 | 1.678 |
| .60 | 11.9 | 1.16 | 8.915 | .498 | 7.920 | .737 | 1.671 |
| .62 | 11.9 | .97 | 8.896 | .498 | 7.900 | .737 | 1.665 |
| .67 | 11.9 | .96 | 8.854 | .498 | 7.858 | .735 | 1.658 |
| .02 | 11.7 | 1.12 | 9.129 | .505 | 8.119 | .751 | 1.685 |
| .21 | 12.2 | 1.46 | 8.796 | .496 | 7.803 | .739 | 1.620 |
| .29 | 12.2 | 1.19 | 8.871 | .498 | 7.875 | .741 | 1.641 |
| .46 | 12.5 | .93 | 8.866 | .499 | 7.867 | .739 | 1.641 |

| σ , Specific Energy - Total Flow | | σ_f , Specific Energy - Free F | | ψ Combustor Diluent Ratio | β Combustor Diluent Ratio | R_3 Mole Ratio Cavity Fuel to Free F | R_L Cavity Molar Ratio |
|--|-------------|--|-------------|---|--|---|-----------------------------------|
| (joule/g) | (Kjoule/lb) | (joule/g) | (Kjoule/lb) | | | | |
| 175.7 | 79.8 | 716.8 | 325.4 | 12.089 | 8.988 | 4.264 | 8.528 |
| 186.6 | 84.7 | 736.2 | 334.2 | 11.358 | 8.428 | 4.166 | 8.333 |
| 163.1 | 74.1 | 650.9 | 295.5 | 11.534 | 8.571 | 4.235 | 8.471 |
| 98.1 | 44.5 | 394.8 | 179.2 | 11.663 | 8.643 | 4.280 | 8.559 |
| 122.0 | 55.4 | 493.2 | 223.9 | 11.760 | 8.733 | 4.320 | 8.641 |
| 148.4 | 67.4 | 582.0 | 264.2 | 11.251 | 8.352 | 4.121 | 8.243 |
| 180.0 | 81.7 | 761.1 | 345.5 | 12.510 | 9.305 | 4.530 | 9.061 |
| 157.6 | 71.6 | 651.1 | 295.6 | 12.115 | 9.009 | 4.407 | 8.814 |
| 115.6 | 52.5 | 477.6 | 216.8 | 12.080 | 8.973 | 4.418 | 8.836 |

CONFIDENTIAL

CONFIDENTIAL

Table 16. Data Summary for Runs 151 Through 160 (U)

| Test Number | Description | \dot{m}_{F_2} (g/sec) | \dot{m}_{D_2} (g/sec) | \dot{m}_{He} (g/sec) | \dot{m}_{H_2} (g/sec) | $\dot{m}_{He_{cav}}$ (g/sec) | Laser Power (watts) | P_C (psia) | Cavity Pressure P_L (torr) | Q (Btu/sec) | X_C | Total Mass Flow (g/sec) | Ca M Fl (m/ |
|-------------|--|----------------------------|----------------------------|---------------------------|----------------------------|---------------------------------|------------------------|-----------------|---------------------------------|------------------|-------|----------------------------|----------------|
| HB5-151B1 | MAX POWER MIRROR SWEEP, NOMINAL BASE CASE | 11.064 | .690 | 3.961 | 1.972 | .000 | 2726 | 16.0 | 3.72 | 15.9 | 1.28 | 17.687 | 2.1 |
| HB5-151B2 | REPEAT $X_C=1$ POINT CAV DIL INJ | 11.078 | .691 | 3.948 | 1.966 | 1.032 | 2874* | 16.0 | 3.93 | 16.3 | 1.0 | 18.715 | 2.1 |
| HB5-151C1 | 20 PCNT FLOW INC AT NOM TEMP, MAX POWER | 13.124 | .830 | 4.755 | 2.388 | .000 | 2948 | 19.5 | 4.03 | 18.2 | 1.28 | 21.097 | 2.1 |
| HB5-151C2 | CAV DIL INJ AT $X_C=1$ | 13.124 | .831 | 4.736 | 2.370 | 1.080 | 2973* | 19.4 | 4.24 | 18.2 | 1.0 | 22.141 | 3.1 |
| HB5-151C3 | CAV DIL INJ AT $X_C=1$ | 13.120 | .831 | 4.734 | 2.370 | 1.956 | 3020* | 19.4 | 4.45 | 18.2 | 1.0 | 23.011 | 3.1 |
| HB5-151C4 | CAV DIL IN AT $X_C=1$ | 13.119 | .829 | 4.734 | 2.369 | 2.877 | 3021* | 19.4 | 3.93 | 18.2 | 1.0 | 23.928 | 3.1 |
| HB5-152A | CAV FUEL SCAN | 11.007 | .690 | 3.926 | 3.195 | .000 | 2664 | 18.8 | 3.93 | 15.8 | 1.30 | 18.818 | 2.1 |
| HB5-152B1 | CAV FUEL SCAN NOM TEMP | 10.932 | .696 | 3.963 | .434 | .000 | 1761 | 16.0 | 3.10 | 15.0 | 1.26 | 16.025 | 1.6 |
| HB5-152B2 | CAV FUEL SCAN WITH CAV DIL INJ | 10.932 | .696 | 3.963 | .434 | 1.014 | 2027* | 16.0 | 3.26 | 15.0 | 1.0 | 17.039 | 1.6 |
| HB5-152B3 | CAV FUEL SCAN WITH CAV DIL INJ | 10.932 | .696 | 3.963 | .434 | 1.923 | 2108* | 15.9 | 3.41 | 15.0 | 1.0 | 17.948 | 2.0 |
| HB5-152B4 | CAV FUEL SCAN WITH CAV DIL INJ | 10.932 | .696 | 3.963 | .434 | 2.919 | 2074* | 15.9 | 3.57 | 15.0 | 1.0 | 18.944 | 2.3 |
| HB5-152C | HIGH TEMP MAX POWER SCAN | 9.605 | .695 | 3.709 | 1.316 | .000 | 2460 | 15.1 | 3.05 | 16.4 | 1.13 | 15.325 | 1.9 |
| HB5-153B1 | TEMP SCAN | 11.040 | .720 | 4.070 | 2.030 | .000 | 3087 | 16.1 | 3.83 | 17.0 | 1.32 | 17.860 | 2.4 |
| HB5-153B2 | TEMP SCAN, NOM TEMP, REDUCED GN2 MIRR PURGE | 11.040 | .720 | 4.070 | 2.030 | .000 | 2900* | 16.1 | 2.59 | 17.0 | 1.0 | 17.860 | 2.4 |
| HB5-153B3 | TEMP SCAN, NOM TEMP, REDUCED GN2 MIRR PURGE | 11.040 | .720 | 4.070 | 2.030 | .000 | 3173* | 16.1 | 2.59 | 17.0 | 1.0 | 17.860 | 2.4 |
| HB5-154 | REPEAT OF 153B1, NO OX DIL. QUICK LOOK DATA ONLY | 11.000 | .700 | 4.000 | 2.000 | .000 | 3051 | 16.7 | 3.75 | 16.0 | 1.31 | 17.700 | 2.4 |
| HB5-155 | TEMP SCAN | 10.370 | .682 | 3.750 | 1.710 | .000 | 2899 | 15.1 | 3.57 | 16.5 | 1.29 | 16.512 | 2.1 |
| HB5-156 | TEMP SCAN | 12.080 | .663 | 4.000 | 2.610 | .000 | 2561 | 15.9 | 4.34 | 15.3 | 0.99 | 19.353 | 2.7 |
| HB5-157A | DIL MOLE RATIO SCAN | 11.480 | .647 | 2.700 | 2.390 | .000 | 1678 | 13.8 | 4.09 | 17.5 | 1.00 | 17.217 | 2.3 |
| HB5-157B | DIL MOLE RATIO SCAN | 11.420 | .641 | 2.680 | 2.380 | .510 | 2044 | 13.7 | 4.19 | 17.0 | 0.84 | 17.631 | 2.4 |
| HB5-157C1 | DIL MOLE RATIO SCAN | 11.450 | .643 | 2.690 | 2.360 | 1.000 | 1965 | 13.8 | 4.29 | 17.1 | 0.87 | 18.143 | 2.5 |
| HB5-157C2 | DIL MOLE RATION SCAN, NO CAV DIL. | 11.450 | .643 | 2.690 | 2.360 | .000 | 1650* | 13.8 | 4.29 | 17.1 | 0.75 | 17.143 | 2.2 |
| HB5-157D | DIL MOLE RATIO SCAN | 11.410 | .641 | 2.690 | 2.420 | 1.500 | 1979 | 13.7 | 4.50 | 17.3 | 0.87 | 18.661 | 2.6 |
| HB5-158A | DIL MOLE RATIO SCAN | 10.900 | .660 | 3.200 | 2.080 | .000 | 2420 | 14.5 | 3.88 | 16.6 | 1.21 | 16.840 | 2.2 |
| HB5-158B | DIL MOLE RATIO SCAN, CAV DIL INJ | 10.900 | .660 | 3.200 | 2.080 | 1.000 | 2608* | 14.5 | 4.09 | 16.6 | 1.25 | 17.840 | 2.4 |
| HB5-159A | DIL MOLE RATIO SCAN | 10.300 | .676 | 3.770 | 1.700 | .000 | 2913* | 15.3 | 3.57 | 16.0 | 1.25 | 16.446 | 2.1 |
| HB5-159B | DIL MOLE RATIO SCAN, CAV DIL INJ | 10.300 | .676 | 3.770 | 1.700 | 1.000 | 3073* | 15.3 | 3.72 | 16.0 | 1.25 | 17.446 | 2.4 |
| HB5-159C | DIL MOLE RATIO SCAN, CAV DIL INJ | 10.300 | .676 | 3.770 | 1.700 | 1.470 | 3092* | 15.3 | 3.83 | 16.0 | 1.25 | 17.916 | 2.53 |
| HB5-160A | CAV PRESS SCAN, -20% FLOW, NO GN2 MIRR PURGE | 8.820 | .560 | 3.170 | 1.600 | .000 | 2640 | 12.5 | 3.46 | 13.6 | 1.27 | 14.150 | 1.91 |
| HB5-160B1 | CAV PRESS SCAN, -20% FLOW NO GN2 MIRR PURGE | 8.850 | .552 | 3.130 | 1.604 | .000 | 2916 | 12.5 | 2.30 | 13.5 | 1.39 | 14.136 | 1.91 |
| HB5-160B2 | -20% FLOW, NO MIRR PURGE, CAV DIL INJ | 8.850 | .552 | 3.130 | 1.604 | 1.010 | 3012* | 12.5 | 2.53 | 13.5 | 1.25 | 15.146 | 2.16 |
| HB5-160C1 | CAV PRESS SCAN, -20% FLOW | 8.850 | .551 | 3.100 | 1.560 | .000 | 2137 | 12.5 | 6.31 | 13.8 | 0.81 | 14.061 | 1.88 |
| HB5-160C2 | CAV PRESS SCAN, -20% FLOW | 8.850 | .551 | 3.100 | 1.560 | .000 | 890 | 12.5 | 9.52 | 13.8 | 0.57 | 14.061 | 1.88 |

* No Mirror Sweep

AFWL-TR-72-28

gh 160 (U)

| No. | Total Mass Flow (g/sec) | Cavity Mole Flow (m/sec) | Combustor Mass Flow (g/sec) | Combustor Mole Flow (m/sec) | RC Combustor Molar Ratio |
|------|----------------------------------|-----------------------------------|-----------------------------------|-----------------------------------|-----------------------------------|
| 1.28 | 17.687 | 2.389 | 15.715 | 1.399 | 1.688 |
| 1.0 | 18.715 | 2.638 | 15.717 | 1.397 | 1.688 |
| 1.28 | 21.097 | 2.865 | 18.709 | 1.671 | 1.664 |
| 1.0 | 22.141 | 3.121 | 18.691 | 1.666 | 1.662 |
| 1.0 | 23.011 | 3.339 | 18.685 | 1.666 | 1.662 |
| 1.0 | 23.928 | 3.570 | 18.682 | 1.666 | 1.666 |
| 1.30 | 18.818 | 2.985 | 15.623 | 1.388 | 1.679 |
| 1.26 | 16.025 | 1.609 | 15.591 | 1.391 | 1.653 |
| 1.0 | 17.039 | 1.862 | 15.391 | 1.392 | 1.653 |
| 1.0 | 17.948 | 2.089 | 15.591 | 1.392 | 1.653 |
| 1.0 | 18.944 | 2.339 | 15.591 | 1.392 | 1.653 |
| 1.13 | 15.325 | 1.917 | 14.009 | 1.259 | 1.455 |
| 1.32 | 17.860 | 2.433 | 15.830 | 1.418 | 1.614 |
| 1.0 | 17.860 | 2.433 | 15.830 | 1.418 | 1.614 |
| 1.0 | 17.860 | 2.433 | 15.830 | 1.418 | 1.614 |
| 1.31 | 17.700 | 2.404 | 15.700 | 1.404 | 1.654 |
| 1.29 | 16.512 | 2.168 | 14.802 | 1.313 | 1.601 |
| 0.99 | 19.353 | 2.774 | 16.743 | 1.469 | 1.918 |
| 1.00 | 17.217 | 2.312 | 14.827 | 1.117 | 1.868 |
| 0.84 | 17.631 | 2.428 | 14.741 | 1.110 | 1.875 |
| 0.87 | 18.143 | 2.544 | 14.783 | 1.114 | 1.874 |
| 0.75 | 17.143 | 2.294 | 14.783 | 1.114 | 1.874 |
| 0.87 | 18.661 | 2.697 | 14.741 | 1.112 | 1.874 |
| 1.21 | 16.840 | 2.248 | 14.760 | 1.208 | 1.738 |
| 1.25 | 17.840 | 2.498 | 14.760 | 1.208 | 1.738 |
| 1.25 | 16.446 | 2.165 | 14.746 | 1.315 | 1.604 |
| 1.25 | 17.446 | 2.415 | 14.746 | 1.315 | 1.604 |
| 1.25 | 17.916 | 2.533 | 14.746 | 1.315 | 1.604 |
| 1.27 | 14.150 | 1.917 | 12.550 | 1.117 | 1.658 |
| 1.39 | 14.136 | 1.912 | 12.532 | 1.110 | 1.688 |
| 1.25 | 15.146 | 2.165 | 12.532 | 1.110 | 1.688 |
| 0.81 | 14.961 | 1.883 | 12.501 | 1.103 | 1.691 |
| 0.87 | 14.961 | 1.883 | 12.501 | 1.103 | 1.691 |

CONFIDENTIAL

Table 16. Data Summary for Runs 151 Throu

| Test No. | R _d Moles Diluent/ Total Com- bustor moles | Combustor Tempera- ture (°K) | F ₂ Dissoci- ation α | Excess F Flow Rate (g/sec) | Flow Rate Free F (g/sec) | σ Specific Energy - Total Flow (joule/g) (Kjoule/lb) | |
|-----------|--|---------------------------------------|---|-------------------------------------|--------------------------------|---|------|
| HB5-151B1 | .6811 | 1874 | .99809 | 4.509 | 4.492 | 154.1 | 70.0 |
| HB5-151B2 | .6800 | 1868 | .99808 | 4.514 | 4.496 | 153.5 | 69.7 |
| HB5-151C1 | .6826 | 1918 | .99757 | 5.239 | 5.214 | 139.7 | 63.4 |
| HB5-151C2 | .6816 | 1924 | .99758 | 5.229 | 5.204 | 134.3 | 61.0 |
| HB5-151C3 | .6815 | 1925 | .99759 | 5.226 | 5.200 | 131.2 | 59.6 |
| HB5-151C4 | .6817 | 1919 | .99758 | 5.244 | 5.218 | 126.3 | 57.3 |
| HB5-152A | .6799 | 1893 | .99761 | 4.452 | 4.431 | 141.6 | 64.3 |
| HB5-152B1 | .6821 | 1936 | .99823 | 4.320 | 4.305 | 109.4 | 49.7 |
| HB5-152B2 | .6821 | 1936 | .99823 | 4.320 | 4.305 | 119.0 | 54.0 |
| HB5-152B3 | .6821 | 1936 | .99824 | 4.320 | 4.305 | 117.4 | 53.3 |
| HB5-152B4 | .6821 | 1936 | .99824 | 4.320 | 4.305 | 116.1 | 52.7 |
| HB5-152C | .6849 | 2128 | .99831 | 3.003 | 2.992 | 160.5 | 72.9 |
| HB5-153B1 | .6838 | 1938 | .99833 | 4.200 | 4.186 | 172.8 | 78.5 |
| HB5-153B2 | .6838 | 1938 | .99833 | 4.200 | 4.186 | 172.4 | 73.7 |
| HB5-153B3 | .6838 | 1938 | .99833 | 4.200 | 4.186 | 177.7 | 80.7 |
| HB5-154 | .6828 | 1909 | .99812 | 4.350 | 4.334 | 172.4 | 78.3 |
| HB5-155 | .6789 | 1961 | .99847 | 3.891 | 3.879 | 175.0 | 79.7 |
| HB5-156 | .6740 | 1660 | .99505 | 5.782 | 5.725 | 152.4 | 60.1 |
| HB5-157A | .5927 | 1883 | .99726 | 5.334 | 5.304 | 97.4 | 44.2 |
| HB5-157B | .5925 | 1885 | .99727 | 5.330 | 5.301 | 115.9 | 52.6 |
| HB5-157C1 | .5927 | 1884 | .99724 | 5.342 | 5.312 | 108.3 | 49.2 |
| HB5-157C2 | .5927 | 1884 | .99724 | 5.342 | 5.312 | 96.3 | 43.7 |
| HB5-157D | .5936 | 1875 | .99726 | 5.320 | 5.292 | 106.1 | 48.2 |
| HB5-158A | .6391 | 1926 | .99790 | 4.630 | 4.611 | 143.7 | 65.2 |
| HB5-158B | .6391 | 1926 | .99790 | 4.630 | 4.611 | 146.2 | 66.4 |
| HB5-159A | .6817 | 1956 | .99845 | 3.878 | 3.866 | 177.1 | 80.4 |
| HB5-159B | .6817 | 1956 | .99845 | 3.878 | 3.866 | 176.1 | 80.0 |
| HB5-159C | .6817 | 1956 | .99845 | 3.878 | 3.866 | 172.5 | 78.3 |
| HB5-160A | .6805 | 1885 | .99876 | 3.500 | 3.491 | 186.6 | 84.7 |
| HB5-160B1 | .6784 | 1856 | .99865 | 3.606 | 3.596 | 206.2 | 93.6 |
| HB5-160B2 | .6784 | 1856 | .99865 | 3.606 | 3.596 | 198.8 | 90.3 |
| HB5-160C1 | .6764 | 1849 | .99862 | 3.616 | 3.606 | 152.0 | 69.0 |
| HB5-160C2 | .6764 | 1849 | .99862 | 3.616 | 3.606 | 63.3 | 28.7 |

CONFIDENTIAL

or Runs 151 Through 160 (Continued) (U)

| Specific Energy - σ_f Total Flow | | Specific Energy - Free F | | ψ Combustor Diluent Ratio | β Combustor Diluent Ratio | R_3 Mole Ratio Cavity Fuel to Free F | R_L Cavity Molar Ratio |
|---|-----------------------|--------------------------|-----------------------|---|--|---|-----------------------------------|
| (joule/g) (Kjoule/lb) | (joule/g) (Kjoule/lb) | (joule/g) (Kjoule/lb) | (joule/g) (Kjoule/lb) | | | | |
| 154.1 | 70.0 | 606.9 | 275.5 | 11.253 | 8.345 | 8.309 | 16.619 |
| 153.5 | 69.7 | 639.2 | 290.2 | 11.218 | 8.309 | 8.276 | 16.552 |
| 139.7 | 63.4 | 565.4 | 256.7 | 11.632 | 8.622 | 8.660 | 17.231 |
| 134.3 | 61.0 | 571.3 | 259.4 | 11.623 | 8.603 | 8.611 | 17.221 |
| 131.2 | 59.6 | 580.8 | 263.7 | 11.628 | 8.606 | 8.617 | 17.235 |
| 126.3 | 57.3 | 579.0 | 262.9 | 11.581 | 8.578 | 8.585 | 17.170 |
| 141.6 | 64.3 | 601.2 | 272.9 | 11.322 | 7.113 | 11.577 | 23.154 |
| 109.4 | 49.7 | 409.1 | 185.7 | 11.776 | 8.457 | 1.852 | 3.704 |
| 119.0 | 54.0 | 470.8 | 213.7 | 11.776 | 8.715 | 1.909 | 3.818 |
| 117.4 | 53.3 | 489.7 | 222.3 | 11.776 | 8.715 | 1.909 | 3.818 |
| 116.1 | 52.7 | 495.5 | 224.9 | 11.776 | 8.715 | 1.909 | 3.818 |
| 160.5 | 72.9 | 822.2 | 373.3 | 16.133 | 8.156 | 5.788 | 11.576 |
| 172.8 | 78.5 | 737.5 | 334.8 | 12.463 | 8.950 | 8.928 | 17.856 |
| 162.4 | 73.7 | 692.8 | 314.5 | 12.463 | 12.878 | 12.846 | 25.692 |
| 177.7 | 80.7 | 758.0 | 344.1 | 12.463 | 9.206 | 9.183 | 18.367 |
| 172.4 | 78.3 | 704.0 | 319.6 | 11.793 | 8.736 | 8.736 | 17.471 |
| 175.6 | 79.7 | 747.4 | 339.3 | 12.486 | 9.156 | 8.350 | 16.700 |
| 132.4 | 60.1 | 447.3 | 302.1 | 8.752 | 6.573 | 8.577 | 17.155 |
| 97.4 | 44.2 | 316.4 | 143.6 | 7.114 | 4.809 | 8.514 | 17.028 |
| 115.9 | 52.6 | 385.6 | 175.1 | 7.061 | 4.776 | 8.483 | 16.967 |
| 108.3 | 49.2 | 369.9 | 167.2 | 7.071 | 4.784 | 8.395 | 16.789 |
| 96.3 | 43.7 | 310.6 | 141.0 | 7.071 | 4.784 | 8.395 | 16.789 |
| 106.1 | 48.2 | 374.0 | 169.8 | 7.092 | 4.784 | 8.608 | 17.216 |
| 143.7 | 65.2 | 524.9 | 238.3 | 9.274 | 5.714 | 7.428 | 14.856 |
| 146.2 | 66.4 | 565.7 | 256.8 | 9.274 | 6.566 | 8.536 | 17.071 |
| 177.1 | 80.4 | 753.5 | 342.1 | 12.547 | 7.735 | 6.976 | 13.952 |
| 176.1 | 80.0 | 794.9 | 360.9 | 12.547 | 9.235 | 8.329 | 16.658 |
| 172.5 | 78.3 | 799.8 | 363.1 | 12.547 | 9.235 | 8.329 | 16.658 |
| 186.6 | 84.7 | 756.2 | 343.3 | 11.644 | 7.766 | 7.839 | 15.678 |
| 206.2 | 93.6 | 810.9 | 368.1 | 11.154 | 8.496 | 8.707 | 17.415 |
| 198.8 | 90.3 | 837.6 | 380.3 | 11.154 | 8.246 | 8.451 | 16.903 |
| 152.0 | 69.0 | 592.6 | 269.0 | 11.041 | 8.145 | 8.198 | 16.396 |
| 63.3 | 28.7 | 246.8 | 112.0 | 11.041 | 8.145 | 8.198 | 16.396 |

CONFIDENTIAL

CONFIDENTIAL

CONFIDENTIAL

Table 17. Data Summary for Runs 210 Through 220

| Test No. | Description | \dot{m}_{F_2} (g/sec) | \dot{m}_{D_2} (g/sec) | \dot{m}_{He} (g/sec) | \dot{m}_{H_2} (g/sec) | $\dot{m}_{He_{cav}}$ (g/sec) | Laser Power (watts) | p_c (psia) | Cavity Pressure P_L (torr) | Q_p (Btu/sec) |
|----------|---|----------------------------|----------------------------|---------------------------|----------------------------|---------------------------------|------------------------|-----------------|---------------------------------|--------------------|
| HBS-210B | NOM W1, ORANGE GLO PHOTO AT NC 1.48 | 8,975 | 1,573 | 3,313 | 1,642 | 0 | 533 | 12.6 | 1.86 | 12.4 |
| HBS-210C | NOM W1, ORANGE GLO PHOTO AT NC 1.48 | 8,975 | 1,573 | 3,313 | 1,642 | 0 | 1700 | 12.6 | 1.86 | 12.4 |
| HBS-210D | NOM W1, ORANGE GLO PHOTO AT NC 1.48 | 8,975 | 1,573 | 3,313 | 1,642 | 0 | 2562 | 12.6 | 1.86 | 12.4 |
| HBS-210E | NOM W1, ORANGE GLO PHOTO AT NC 1.48 | 8,975 | 1,573 | 3,313 | 1,642 | 0 | 3027 | 12.6 | 1.86 | 12.4 |
| HBS-210F | NOM W1, ORANGE GLO PHOTO AT NC 1.48 | 8,975 | 1,573 | 3,313 | 1,642 | 0 | 3079 | 12.6 | 1.86 | 12.4 |
| HBS-210G | NOM W1, ORANGE GLO PHOTO AT NC 1.48 | 8,975 | 1,573 | 3,313 | 1,642 | 0 | 3196 | 12.6 | 1.86 | 12.4 |
| HBS-210H | NOM W1, ORANGE GLO PHOTO AT NC 1.48 | 8,975 | 1,573 | 3,313 | 1,642 | 0 | 2192 | 12.6 | 1.86 | 12.4 |
| HBS-210I | NOM W1, ORANGE GLO PHOTO AT NC 1.48 | 8,975 | 1,573 | 3,313 | 1,642 | 0 | 620 | 12.6 | 1.86 | 12.4 |
| HBS-210J | NOM W1, RED CAV 12 - ILL. ORANGE GLO PHOTO NC 1.73 | 8,946 | 1,572 | 3,324 | 1,821 | 1.6 | 434 | 12.6 | 1.97 | 11 |
| HBS-210K | NOM W1, RED CAV 12 - ILL. ORANGE GLO PHOTO NC 1.73 | 8,946 | 1,572 | 3,324 | 1,821 | 1.6 | 1511 | 12.6 | 1.97 | 11 |
| HBS-210L | NOM W1, RED CAV 12 - ILL. ORANGE GLO PHOTO NC 1.73 | 8,946 | 1,572 | 3,324 | 1,821 | 1.6 | 2129 | 12.6 | 1.97 | 11 |
| HBS-210M | NOM W1, RED CAV 12 - ILL. ORANGE GLO PHOTO NC 1.73 | 8,946 | 1,572 | 3,324 | 1,821 | 1.6 | 2751 | 12.6 | 1.97 | 11 |
| HBS-210N | NOM W1, RED CAV 12 - ILL. ORANGE GLO PHOTO NC 1.73 | 8,946 | 1,572 | 3,324 | 1,821 | 1.6 | 3075 | 12.6 | 1.97 | 11 |
| HBS-210O | NOM W1, RED CAV 12 - ILL. ORANGE GLO PHOTO NC 1.73 | 8,946 | 1,572 | 3,324 | 1,821 | 1.6 | 3118 | 12.6 | 1.97 | 11 |
| HBS-210P | NOM W1, RED CAV 12 - ILL. ORANGE GLO PHOTO NC 1.73 | 8,946 | 1,572 | 3,324 | 1,821 | 1.6 | 2587 | 12.6 | 1.97 | 11 |
| HBS-210Q | NOM W1, RED CAV 12 - ILL. ORANGE GLO PHOTO NC 1.73 | 8,946 | 1,572 | 3,324 | 1,821 | 1.6 | 1109 | 12.6 | 1.97 | 11 |
| HBS-210R | NOM W1, HI TEMP COMB, ORANGE GLO PHOTO NC 1.50 | 8,888 | 1,661 | 3,406 | 1,214 | 0 | 415 | 13.9 | 1.69 | 13 |
| HBS-210S | NOM W1, HI TEMP COMB, ORANGE GLO PHOTO NC 1.50 | 8,888 | 1,661 | 3,406 | 1,214 | 0 | 1438 | 13.9 | 1.69 | 13 |
| HBS-210T | NOM W1, HI TEMP COMB, ORANGE GLO PHOTO NC 1.50 | 8,888 | 1,661 | 3,406 | 1,214 | 0 | 1965 | 13.9 | 1.69 | 13 |
| HBS-210U | NOM W1, HI TEMP COMB, ORANGE GLO PHOTO NC 1.50 | 8,888 | 1,661 | 3,406 | 1,214 | 0 | 2428 | 13.9 | 1.69 | 13 |
| HBS-210V | NOM W1, HI TEMP COMB, ORANGE GLO PHOTO NC 1.50 | 8,888 | 1,661 | 3,406 | 1,214 | 0 | 2671 | 13.9 | 1.69 | 13 |
| HBS-210W | NOM W1, HI TEMP COMB, ORANGE GLO PHOTO NC 1.50 | 8,888 | 1,661 | 3,406 | 1,214 | 0 | 2714 | 13.9 | 1.69 | 13 |
| HBS-210X | NOM W1, HI TEMP COMB, ORANGE GLO PHOTO NC 1.50 | 8,888 | 1,661 | 3,406 | 1,214 | 0 | 2137 | 13.9 | 1.69 | 13 |
| HBS-210Y | NOM W1, HI TEMP COMB, ORANGE GLO PHOTO NC 1.50 | 8,888 | 1,661 | 3,406 | 1,214 | 0 | 841 | 13.9 | 1.69 | 13 |
| HBS-210Z | NOM W1, HI TEMP COMB, ORANGE GLO PHOTO NC 1.48 | 8,782 | 1,739 | 3,414 | 1,223 | 0 | 20 | 14.4 | 1.4 | 15 |
| HBS-211A | NOM W1, HI TEMP COMB, ORANGE GLO PHOTO NC 1.48 | 8,782 | 1,739 | 3,414 | 1,223 | 0 | 566 | 14.4 | 1.4 | 15 |
| HBS-211B | NOM W1, HI TEMP COMB, ORANGE GLO PHOTO NC 1.48 | 8,782 | 1,739 | 3,414 | 1,223 | 0 | 1584 | 14.4 | 1.4 | 15 |
| HBS-211C | NOM W1, HI TEMP COMB, ORANGE GLO PHOTO NC 1.48 | 8,782 | 1,739 | 3,414 | 1,223 | 0 | 1925 | 14.4 | 1.4 | 15 |
| HBS-211D | NOM W1, HI TEMP COMB, ORANGE GLO PHOTO NC 1.48 | 8,782 | 1,739 | 3,414 | 1,223 | 0 | 2088 | 14.4 | 1.35 | 15 |
| HBS-211E | NOM W1, HI TEMP COMB, ORANGE GLO PHOTO NC 1.48 | 8,782 | 1,739 | 3,414 | 1,223 | 0 | 2118 | 14.4 | 1.4 | 15 |
| HBS-211F | NOM W1, HI TEMP COMB, ORANGE GLO PHOTO NC 1.48 | 8,782 | 1,739 | 3,414 | 1,223 | 0 | 1754 | 14.4 | 1.4 | 15 |
| HBS-211G | NOM W1, HI TEMP COMB, ORANGE GLO PHOTO NC 1.48 | 8,782 | 1,739 | 3,414 | 1,223 | 0 | 828 | 14.4 | 1.4 | 15 |
| HBS-211H | 1.5 NOM W1, TOP VIEW ORANGE GLO PHOTO AT NC 1.74 | 13,331 | 1,846 | 4,783 | 2,394 | 0 | 549 | 19 | 2.28 | 16.2 |
| HBS-211I | 1.5 NOM W1, TOP VIEW ORANGE GLO PHOTO AT NC 1.74 | 13,331 | 1,846 | 4,783 | 2,394 | 0 | 1946 | 19 | 2.28 | 16.2 |
| HBS-211J | 1.5 NOM W1, TOP VIEW ORANGE GLO PHOTO AT NC 1.74 | 13,331 | 1,846 | 4,783 | 2,394 | 0 | 2543 | 19 | 2.28 | 16.2 |
| HBS-211K | 1.5 NOM W1, TOP VIEW ORANGE GLO PHOTO AT NC 1.74 | 13,331 | 1,846 | 4,783 | 2,394 | 0 | 3327 | 19 | 2.28 | 16.2 |
| HBS-211L | 1.5 NOM W1, TOP VIEW ORANGE GLO PHOTO AT NC 1.74 | 13,331 | 1,846 | 4,783 | 2,394 | 0 | 3375 | 19 | 2.28 | 16.2 |
| HBS-211M | 1.5 NOM W1, TOP VIEW ORANGE GLO PHOTO AT NC 1.74 | 13,331 | 1,846 | 4,783 | 2,394 | 0 | 329 | 19 | 2.28 | 16.2 |
| HBS-211N | 1.5 NOM W1, TOP VIEW ORANGE GLO PHOTO AT NC 1.74 | 13,331 | 1,846 | 4,783 | 2,394 | 0 | 2178 | 19 | 2.28 | 16.2 |
| HBS-211O | 1.5 NOM W1, TOP VIEW ORANGE GLO PHOTO AT NC 1.74 | 13,331 | 1,846 | 4,783 | 2,394 | 0 | 483 | 19 | 2.28 | 16.2 |
| HBS-211P | N2 DIL, HI TEMP COMB, ORANGE GLO TOP PHOTO AT 1.48, 1.74 | 8,798 | 1,738 | 23,274 | 1,214 | 0 | 330 | 23.6 | 1.69 | 11.6 |
| HBS-211Q | N2 DIL, HI TEMP COMB, ORANGE GLO TOP PHOTO AT 1.48, 1.74 | 8,798 | 1,738 | 23,274 | 1,214 | 0 | 742 | 23.6 | 1.69 | 11.6 |
| HBS-211R | N2 DIL, HI TEMP COMB, ORANGE GLO TOP PHOTO AT 1.48, 1.74 | 8,798 | 1,738 | 23,274 | 1,214 | 0 | 1115 | 23.6 | 1.69 | 11.6 |
| HBS-211S | N2 DIL, HI TEMP COMB, ORANGE GLO TOP PHOTO AT 1.48, 1.74 | 8,798 | 1,738 | 23,274 | 1,214 | 0 | 1184 | 23.6 | 1.69 | 11.6 |
| HBS-211T | N2 DIL, HI TEMP COMB, ORANGE GLO TOP PHOTO AT 1.48, 1.74 | 8,798 | 1,738 | 23,274 | 1,214 | 0 | 1153 | 23.6 | 1.69 | 11.6 |
| HBS-211U | N2 DIL, HI TEMP COMB, ORANGE GLO TOP PHOTO AT 1.48, 1.74 | 8,798 | 1,738 | 23,274 | 1,214 | 0 | 911 | 23.6 | 1.69 | 11.6 |
| HBS-211V | N2 DIL, HI TEMP COMB, ORANGE GLO TOP PHOTO AT 1.48, 1.74 | 8,798 | 1,738 | 23,274 | 1,214 | 0 | 519 | 23.6 | 1.69 | 11.6 |
| HBS-211W | N2 DIL, HI TEMP COMB, ORANGE GLO TOP PHOTO AT 1.48, 1.74 | 8,798 | 1,738 | 23,274 | 1,214 | 0 | 137 | 23.6 | 1.69 | 11.6 |
| HBS-211X | N2 DIL, MED TEMP COMB, ORANGE GLO TOP PHOTO AT 1.76, 2.25 | 8,904 | 1,648 | 25,144 | 1,215 | 0 | 513 | 23 | 1.89 | 10 |
| HBS-211Y | N2 DIL, MED TEMP COMB, ORANGE GLO TOP PHOTO AT 1.76, 2.25 | 8,904 | 1,648 | 25,144 | 1,215 | 0 | 903 | 23 | 1.89 | 10 |
| HBS-211Z | N2 DIL, MED TEMP COMB, ORANGE GLO TOP PHOTO AT 1.76, 2.25 | 8,904 | 1,648 | 25,144 | 1,215 | 0 | 1329 | 23 | 1.89 | 10 |
| HBS-212A | N2 DIL, MED TEMP COMB, ORANGE GLO TOP PHOTO AT 1.76, 2.25 | 8,904 | 1,648 | 25,144 | 1,215 | 0 | 1340 | 23 | 1.89 | 10 |
| HBS-212B | N2 DIL, MED TEMP COMB, ORANGE GLO TOP PHOTO AT 1.76, 2.25 | 8,904 | 1,648 | 25,144 | 1,215 | 0 | 1098 | 23 | 1.89 | 10 |
| HBS-212C | N2 DIL, MED TEMP COMB, ORANGE GLO TOP PHOTO AT 1.76, 2.25 | 8,904 | 1,648 | 25,144 | 1,215 | 0 | 863 | 23 | 1.89 | 10 |
| HBS-212D | N2 DIL, MED TEMP COMB, ORANGE GLO TOP PHOTO AT 1.76, 2.25 | 8,904 | 1,648 | 25,144 | 1,215 | 0 | 429 | 23 | 1.89 | 10 |
| HBS-212E | N2 DIL, MED TEMP COMB, ORANGE GLO TOP PHOTO AT 1.76, 2.25 | 8,904 | 1,648 | 25,144 | 1,215 | 0 | 94 | 23 | 1.89 | 10 |
| HBS-212F | N2 DIL, LO TEMP COMB, ORANGE GLO PHOTO AT 1.48, 1.74 | 8,998 | 1,565 | 22,303 | 1,219 | 0 | 510 | 19.9 | 2.07 | 8.6 |
| HBS-212G | N2 DIL, LO TEMP COMB, ORANGE GLO PHOTO AT 1.48, 1.74 | 8,998 | 1,565 | 22,303 | 1,219 | 0 | 1034 | 19.9 | 2.07 | 8.6 |
| HBS-212H | N2 DIL, LO TEMP COMB, ORANGE GLO PHOTO AT 1.48, 1.74 | 8,998 | 1,565 | 22,303 | 1,219 | 0 | 1031 | 19.9 | 2.07 | 8.6 |
| HBS-212I | N2 DIL, LO TEMP COMB, ORANGE GLO PHOTO AT 1.48, 1.74 | 8,998 | 1,565 | 22,303 | 1,219 | 0 | 793 | 19.9 | 2.07 | 8.6 |
| HBS-212J | N2 DIL, LO TEMP COMB, ORANGE GLO PHOTO AT 1.48, 1.74 | 8,998 | 1,565 | 22,303 | 1,219 | 0 | 497 | 19.9 | 2.07 | 8.6 |
| HBS-212K | N2 DIL, LO TEMP COMB, ORANGE GLO PHOTO AT 1.48, 1.74 | 8,998 | 1,565 | 22,303 | 1,219 | 0 | 351 | 19.9 | 2.07 | 8.6 |
| HBS-212L | N2 DIL, LO TEMP COMB, ORANGE GLO PHOTO AT 1.48, 1.74 | 8,998 | 1,565 | 22,303 | 1,219 | 0 | 153 | 19.9 | 2.07 | 8.6 |
| HBS-212M | N2 DIL, LO TEMP COMB, ORANGE GLO PHOTO AT 1.48, 1.74 | 8,998 | 1,565 | 22,303 | 1,219 | 0 | 18 | 19.9 | 2.07 | 8.6 |
| HBS-212N | N2 DIL, RED W1, LO TEMP COMB, ORANGE GLO TOP PHOTO | 5,432 | 1,339 | 13,356 | 1,773 | 0 | 439 | 11.6 | 1.81 | 6 |
| HBS-212O | N2 DIL, RED W1, LO TEMP COMB, ORANGE GLO TOP PHOTO | 5,432 | 1,339 | 13,356 | 1,773 | 0 | 984 | 11.6 | 1.81 | 6 |
| HBS-212P | N2 DIL, RED W1, LO TEMP COMB, ORANGE GLO TOP PHOTO | 5,432 | 1,339 | 13,356 | 1,773 | 0 | 1114 | 11.6 | 1.81 | 6 |
| HBS-212Q | N2 DIL, RED W1, LO TEMP COMB, ORANGE GLO TOP PHOTO | 5,432 | 1,339 | 13,356 | 1,773 | 0 | 813 | 11.6 | 1.81 | 6 |
| HBS-212R | N2 DIL, RED W1, LO TEMP COMB, ORANGE GLO TOP PHOTO | 5,432 | 1,339 | 13,356 | 1,773 | 0 | 598 | 11.6 | 1.81 | 6 |
| HBS-212S | N2 DIL, RED W1, LO TEMP COMB, ORANGE GLO TOP PHOTO | 5,432 | 1,339 | 13,356 | 1,773 | 0 | 474 | 11.6 | 1.81 | 6 |
| HBS-212T | N2 DIL, RED W1, MED TEMP COMB, ORANGE GLO TOP | 5,393 | 1,381 | 13,273 | 1,73 | 0 | 378 | 12.4 | 1.69 | 6 |
| HBS-212U | N2 DIL, RED W1, MED TEMP COMB, ORANGE GLO TOP | 5,393 | 1,381 | 13,273 | 1,73 | 0 | 814 | 12.4 | 1.69 | 6 |
| HBS-212V | N2 DIL, RED W1, MED TEMP COMB, ORANGE GLO TOP | 5,393 | 1,381 | 13,273 | 1,73 | 0 | 1177 | 12.4 | 1.69 | 6 |
| HBS-212W | N2 DIL, RED W1, MED TEMP COMB, ORANGE GLO TOP | 5,393 | 1,381 | 13,273 | 1,73 | 0 | 1120 | 12.4 | 1.69 | 6 |
| HBS-212X | N2 DIL, RED W1, MED TEMP COMB, ORANGE GLO TOP | 5,393 | 1,381 | 13,273 | 1,73 | 0 | 989 | 12.4 | 1.69 | 6 |
| HBS-212Y | N2 DIL, RED W1, MED TEMP COMB, ORANGE GLO TOP | 5,393 | 1,381 | 13,273 | 1,73 | 0 | 881 | 12.4 | 1.69 | 6 |
| HBS-212Z | N2 DIL, RED W1, MED TEMP COMB, ORANGE GLO TOP | 5,393 | 1,381 | 13,273 | 1,73 | 0 | 505 | 12.4 | 1.69 | 6 |
| HBS-213A | N2 DIL, RED W1, MED TEMP COMB, ORANGE GLO TOP | 5,393 | 1,381 | 13,273 | 1,73 | 0 | 92 | 12.4 | 1.69 | 6 |
| HBS-213B | N2 DIL, RED W1, HI TEMP COMB, ORANGE GLO TOP | 5,322 | 1,436 | 14,388 | 1,73 | 0 | 273 | 13.8 | 1.50 | 6.6 |
| HBS-213C | N2 DIL, RED W1, HI TEMP COMB, ORANGE GLO TOP | 5,322 | 1,436 | 14,388 | 1,73 | 0 | 607 | 13.8 | 1.50 | 6.6 |
| HBS-213D | N2 DIL, RED W1, HI TEMP COMB, ORANGE GLO TOP | 5,322 | 1,436 | 14,388 | 1,73 | 0 | 939 | 13.8 | 1.50 | 6.6 |
| HBS-213E | N2 DIL, RED W1, HI TEMP COMB, ORANGE GLO TOP | 5,322 | 1,436 | 14,388 | 1,73 | 0 | 940 | 13.8 | 1.50 | 6.6 |
| HBS-213F | N2 DIL, RED W1, HI TEMP COMB, ORANGE GLO TOP | 5,322 | 1,436 | 14,388 | 1,73 | 0 | 891 | 13.8 | 1.50 | 6.6 |
| HBS-213G | N2 DIL, RED W1, HI TEMP COMB, ORANGE GLO TOP | 5,322 | 1,436 | 14,388 | 1,73 | 0 | 824 | 13.8 | 1.50 | 6.6 |
| HBS-213H | N2 DIL, RED W1, HI TEMP COMB, ORANGE GLO TOP | 5,322 | 1,436 | 14,388 | 1,73 | 0 | 525 | 13.8 | 1.50 | 6.6 |
| HBS-213I | N2 DIL, RED W1, HI TEMP COMB, ORANGE GLO TOP | 5,322 | 1,436 | 14,388 | 1,73 | 0 | 110 | 13.8 | 1.50 | 6.6 |

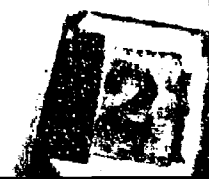
CONFIDENTIAL

AFWL-TR-72-28

Through 220 (U)

| PC (in) | Cavity Flow P _c (atm) | Q _p (Btu/sec) | SC (in) | Total Mass Flow (g/sec) | Cavity Mole Flow (m/sec) | Combustor Mass Flow (g/sec) | Combustor Mole Flow (m/sec) | R _c Combustor Molar Ratio |
|------------|--|-----------------------------|------------|-------------------------------|--------------------------------|-----------------------------------|-----------------------------------|--|
| 2.6 | 1.86 | 12.4 | 1.24 | 14,603 | 1,978 | 12,861 | 1,157 | 1,649 |
| 2.6 | 1.86 | 12.4 | 1.5 | 14,603 | 1,978 | 12,861 | 1,157 | 1,649 |
| 2.6 | 1.86 | 12.4 | 1.73 | 14,603 | 1,978 | 12,861 | 1,157 | 1,649 |
| 2.6 | 1.86 | 12.4 | 1.01 | 14,603 | 1,978 | 12,861 | 1,157 | 1,649 |
| 2.6 | 1.86 | 12.4 | 1.24 | 14,603 | 1,978 | 12,861 | 1,157 | 1,649 |
| 2.6 | 1.86 | 12.4 | 1.5 | 14,603 | 1,978 | 12,861 | 1,157 | 1,649 |
| 2.6 | 1.86 | 12.4 | 1.75 | 14,603 | 1,978 | 12,861 | 1,157 | 1,649 |
| 2.6 | 1.86 | 12.4 | 2.28 | 14,603 | 1,978 | 12,861 | 1,157 | 1,649 |
| 2.6 | 1.97 | 11 | 1.25 | 15,263 | 1,969 | 12,842 | 1,159 | 1,646 |
| 2.6 | 1.97 | 11 | 1.48 | 15,263 | 1,969 | 12,842 | 1,159 | 1,646 |
| 2.6 | 1.97 | 11 | 1.75 | 15,263 | 1,969 | 12,842 | 1,159 | 1,646 |
| 2.6 | 1.97 | 11 | 1.99 | 15,263 | 1,969 | 12,842 | 1,159 | 1,646 |
| 2.6 | 1.97 | 11 | 1.24 | 15,263 | 1,969 | 12,842 | 1,159 | 1,646 |
| 2.6 | 1.97 | 11 | 1.5 | 15,263 | 1,969 | 12,842 | 1,159 | 1,646 |
| 2.6 | 1.97 | 11 | 1.75 | 15,263 | 1,969 | 12,842 | 1,159 | 1,646 |
| 2.6 | 1.97 | 11 | 2.28 | 15,263 | 1,969 | 12,842 | 1,159 | 1,646 |
| 3.9 | 1.60 | 13 | 1.25 | 14,258 | 1,783 | 13,041 | 1,176 | 1,415 |
| 3.9 | 1.60 | 13 | 1.49 | 14,258 | 1,783 | 13,041 | 1,176 | 1,415 |
| 3.9 | 1.60 | 13 | 1.74 | 14,258 | 1,783 | 13,041 | 1,176 | 1,415 |
| 3.9 | 1.60 | 13 | 1.0 | 14,258 | 1,783 | 13,041 | 1,176 | 1,415 |
| 3.9 | 1.60 | 13 | 1.24 | 14,258 | 1,783 | 13,041 | 1,176 | 1,415 |
| 3.9 | 1.60 | 13 | 1.51 | 14,258 | 1,783 | 13,041 | 1,176 | 1,415 |
| 3.9 | 1.60 | 13 | 1.77 | 14,258 | 1,783 | 13,041 | 1,176 | 1,415 |
| 3.9 | 1.60 | 13 | 2.27 | 14,258 | 1,783 | 13,041 | 1,176 | 1,415 |
| 4.4 | 1.45 | 15 | 1.23 | 14,158 | 1,747 | 12,935 | 1,131 | 1,251 |
| 4.4 | 1.45 | 15 | 1.49 | 14,158 | 1,747 | 12,935 | 1,131 | 1,251 |
| 4.4 | 1.45 | 15 | 1.75 | 14,158 | 1,747 | 12,935 | 1,131 | 1,251 |
| 4.4 | 1.45 | 15 | 1.98 | 14,158 | 1,747 | 12,935 | 1,131 | 1,251 |
| 4.4 | 1.45 | 15 | 1.25 | 14,158 | 1,747 | 12,935 | 1,131 | 1,251 |
| 4.4 | 1.45 | 15 | 1.5 | 14,158 | 1,747 | 12,935 | 1,131 | 1,251 |
| 4.4 | 1.45 | 15 | 1.74 | 14,158 | 1,747 | 12,935 | 1,131 | 1,251 |
| 4.4 | 1.45 | 15 | 2.26 | 14,158 | 1,747 | 12,935 | 1,131 | 1,251 |
| 5.9 | 1.28 | 16.2 | 1.25 | 21,354 | 2,882 | 18,96 | 1,685 | 1,659 |
| 5.9 | 1.28 | 16.2 | 1.49 | 21,354 | 2,882 | 18,96 | 1,685 | 1,659 |
| 5.9 | 1.28 | 16.2 | 1.75 | 21,354 | 2,882 | 18,96 | 1,685 | 1,659 |
| 5.9 | 1.28 | 16.2 | 1.0 | 21,354 | 2,882 | 18,96 | 1,685 | 1,659 |
| 5.9 | 1.28 | 16.2 | 1.25 | 21,354 | 2,882 | 18,96 | 1,685 | 1,659 |
| 5.9 | 1.28 | 16.2 | 1.51 | 21,354 | 2,882 | 18,96 | 1,685 | 1,659 |
| 5.9 | 1.28 | 16.2 | 1.75 | 21,354 | 2,882 | 18,96 | 1,685 | 1,659 |
| 5.9 | 1.28 | 16.2 | 2.26 | 21,354 | 2,882 | 18,96 | 1,685 | 1,659 |
| 3.6 | 1.66 | 11.6 | 1.24 | 34,024 | 32,81 | | | 1,255 |
| 3.6 | 1.66 | 11.6 | 1.49 | 34,024 | 32,81 | | | 1,255 |
| 3.6 | 1.66 | 11.6 | 1.74 | 34,024 | 32,81 | | | 1,255 |
| 3.6 | 1.66 | 11.6 | 1.99 | 34,024 | 32,81 | | | 1,255 |
| 3.6 | 1.66 | 11.6 | 1.24 | 34,024 | 32,81 | | | 1,255 |
| 3.6 | 1.66 | 11.6 | 1.51 | 34,024 | 32,81 | | | 1,255 |
| 3.6 | 1.66 | 11.6 | 1.74 | 34,024 | 32,81 | | | 1,255 |
| 3.6 | 1.66 | 11.6 | 2.27 | 34,024 | 32,81 | | | 1,255 |
| 3.1 | 1.86 | 10 | 1.25 | 35,911 | 34,696 | | | 1,446 |
| 3.1 | 1.86 | 10 | 1.49 | 35,911 | 34,696 | | | 1,446 |
| 3.1 | 1.86 | 10 | 1.73 | 35,911 | 34,696 | | | 1,446 |
| 3.1 | 1.86 | 10 | 1.0 | 35,911 | 34,696 | | | 1,446 |
| 3.1 | 1.86 | 10 | 1.25 | 35,911 | 34,696 | | | 1,446 |
| 3.1 | 1.86 | 10 | 1.51 | 35,911 | 34,696 | | | 1,446 |
| 3.1 | 1.86 | 10 | 1.74 | 35,911 | 34,696 | | | 1,446 |
| 3.1 | 1.86 | 10 | 2.28 | 35,911 | 34,696 | | | 1,446 |
| 9.9 | 2.07 | 8.6 | 1.23 | 33,085 | 31,866 | | | 1,676 |
| 9.9 | 2.07 | 8.6 | 1.49 | 33,085 | 31,866 | | | 1,676 |
| 9.9 | 2.07 | 8.6 | 1.72 | 33,085 | 31,866 | | | 1,676 |
| 9.9 | 2.07 | 8.6 | 1.99 | 33,085 | 31,866 | | | 1,676 |
| 9.9 | 2.07 | 8.6 | 1.23 | 33,085 | 31,866 | | | 1,676 |
| 9.9 | 2.07 | 8.6 | 1.49 | 33,085 | 31,866 | | | 1,676 |
| 9.9 | 2.07 | 8.6 | 1.75 | 33,085 | 31,866 | | | 1,676 |
| 9.9 | 2.07 | 8.6 | 2.26 | 33,085 | 31,866 | | | 1,676 |
| 11.6 | 1.81 | 6 | 1.25 | 19,9 | 19,127 | | | 1,686 |
| 11.6 | 1.81 | 6 | 1.49 | 19,9 | 19,127 | | | 1,686 |
| 11.6 | 1.81 | 6 | 1.73 | 19,9 | 19,127 | | | 1,686 |
| 11.6 | 1.81 | 6 | 1.99 | 19,9 | 19,127 | | | 1,686 |
| 11.6 | 1.81 | 6 | 1.22 | 19,9 | 19,127 | | | 1,686 |
| 11.6 | 1.81 | 6 | 1.49 | 19,9 | 19,127 | | | 1,686 |
| 11.6 | 1.81 | 6 | 1.24 | 19,777 | 19,047 | | | 1,489 |
| 12.4 | 1.60 | 6 | 1.48 | 19,777 | 19,047 | | | 1,489 |
| 12.4 | 1.60 | 6 | 1.75 | 19,777 | 19,047 | | | 1,489 |
| 12.4 | 1.60 | 6 | 1.99 | 19,777 | 19,047 | | | 1,489 |
| 12.4 | 1.60 | 6 | 1.23 | 19,777 | 19,047 | | | 1,489 |
| 12.4 | 1.60 | 6 | 1.5 | 19,777 | 19,047 | | | 1,489 |
| 12.4 | 1.60 | 6 | 1.74 | 19,777 | 19,047 | | | 1,489 |
| 12.4 | 1.60 | 6 | 2.28 | 19,777 | 19,047 | | | 1,489 |
| 13.9 | 1.50 | 6.6 | 1.25 | 20,876 | 20,146 | | | 1,285 |
| 13.9 | 1.50 | 6.6 | 1.48 | 20,876 | 20,146 | | | 1,285 |
| 13.9 | 1.50 | 6.6 | 1.53 | 20,876 | 20,146 | | | 1,285 |
| 13.9 | 1.50 | 6.6 | 1.0 | 20,876 | 20,146 | | | 1,285 |
| 13.9 | 1.50 | 6.6 | 1.23 | 20,876 | 20,146 | | | 1,285 |
| 13.9 | 1.50 | 6.6 | 1.51 | 20,876 | 20,146 | | | 1,285 |
| 13.9 | 1.50 | 6.6 | 1.74 | 20,876 | 20,146 | | | 1,285 |
| 13.9 | 1.50 | 6.6 | 2.26 | 20,876 | 20,146 | | | 1,285 |

CONFIDENTIAL



CONFIDENTIAL

Table 17. Data Summary for Runs 210 Through 220 (Continued) (U)

| Test No | R _d Moles Diluent/ Total Com- bustor moles | Combus- tor Tempera- ture (°K) | F ₂ Dissoci- ation σ | Excess F Flow Rate (g/sec) | Flow Rate Free F (g/sec) | σ Specific Energy - Total Flow (joule/g) (Kjoule/lb) | σ _f Specific Energy - Free F (joule/g) (Kjoule/lb) | σ Combus- tor Diluent Ratio | σ Combus- tor Diluent Ratio | R _d Mole Ratio Cavity Fuel to Free F | σ Cav- ity Fuel to Free F Ratio | | |
|----------|--|--|--|-------------------------------------|--------------------------------|--|---|---|---|--|---|--------|--------|
| HB5-210P | .6858 | 1923 | .9988 | 3.5315 | 3.523 | 36.8 | 16.7 | 151.3 | 68.7 | 11.995 | 8.912 | 8.834 | 17.668 |
| HB5-210C | .6858 | 1923 | .9988 | 3.5315 | 3.523 | 117.2 | 53.2 | 492.5 | 219.1 | 11.995 | 8.912 | 8.834 | 17.668 |
| HB5-210D | .6858 | 1923 | .9988 | 3.5315 | 3.523 | 176.7 | 80.2 | 727.2 | 330.2 | 11.995 | 8.912 | 8.834 | 17.668 |
| HB5-210E | .6858 | 1923 | .9988 | 3.5315 | 3.523 | 208.7 | 94.8 | 859.2 | 390.1 | 11.995 | 8.912 | 8.834 | 17.668 |
| HB5-210F | .6858 | 1923 | .9988 | 3.5315 | 3.523 | 212.3 | 96.3 | 873.9 | 396.8 | 11.995 | 8.912 | 8.834 | 17.668 |
| HB5-210G | .6858 | 1923 | .9988 | 3.5315 | 3.523 | 214.1 | 97.2 | 881.6 | 400.3 | 11.995 | 8.912 | 8.834 | 17.668 |
| HB5-210H | .6858 | 1923 | .9988 | 3.5315 | 3.523 | 151.1 | 68.6 | 622.2 | 282.5 | 11.995 | 8.912 | 8.834 | 17.668 |
| HB5-210I | .6858 | 1923 | .9988 | 3.5315 | 3.523 | 42.8 | 19.4 | 176.0 | 79.9 | 11.995 | 8.912 | 8.834 | 17.668 |
| HB5-211P | .6871 | 1966 | .9988 | 3.512 | 3.504 | 28.4 | 12.9 | 123.9 | 56.2 | 12.086 | 8.991 | 4.442 | 8.883 |
| HB5-211C | .6871 | 1966 | .9988 | 3.512 | 3.504 | 99.0 | 44.9 | 431.3 | 195.8 | 12.086 | 8.991 | 4.442 | 8.883 |
| HB5-211D | .6871 | 1966 | .9988 | 3.512 | 3.504 | 139.5 | 63.3 | 607.7 | 275.9 | 12.086 | 8.991 | 4.442 | 8.883 |
| HB5-211E | .6871 | 1966 | .9988 | 3.512 | 3.504 | 180.2 | 81.8 | 785.2 | 356.5 | 12.086 | 8.991 | 4.442 | 8.883 |
| HB5-211F | .6871 | 1966 | .9988 | 3.512 | 3.504 | 201.5 | 91.5 | 877.7 | 398.5 | 12.086 | 8.991 | 4.442 | 8.883 |
| HB5-211G | .6871 | 1966 | .9988 | 3.512 | 3.504 | 206.3 | 93.6 | 808.5 | 407.9 | 12.086 | 8.991 | 4.442 | 8.883 |
| HB5-211H | .6871 | 1966 | .9988 | 3.512 | 3.504 | 169.5 | 77.0 | 738.4 | 335.2 | 12.086 | 8.991 | 4.442 | 8.883 |
| HB5-211I | .6871 | 1966 | .9988 | 3.512 | 3.504 | 72.7 | 33.0 | 316.5 | 143.7 | 12.086 | 8.991 | 4.442 | 8.883 |
| HB5-212P | .6864 | 2263 | .9972 | 2.6085 | 2.594 | 29.1 | 13.2 | 160.0 | 72.6 | 17.543 | 12.729 | 8.843 | 17.685 |
| HB5-212C | .6864 | 2263 | .9972 | 2.6085 | 2.594 | 100.9 | 46.8 | 554.4 | 251.7 | 17.543 | 12.729 | 8.843 | 17.685 |
| HB5-212D | .6864 | 2263 | .9972 | 2.6085 | 2.594 | 137.8 | 62.6 | 757.6 | 344.0 | 17.543 | 12.729 | 8.843 | 17.685 |
| HB5-212E | .6864 | 2263 | .9972 | 2.6085 | 2.594 | 170.3 | 77.3 | 934.1 | 425.6 | 17.543 | 12.729 | 8.843 | 17.685 |
| HB5-212F | .6864 | 2263 | .9972 | 2.6085 | 2.594 | 187.3 | 85.1 | 1029.8 | 467.5 | 17.543 | 12.729 | 8.843 | 17.685 |
| HB5-212G | .6864 | 2263 | .9972 | 2.6085 | 2.594 | 190.4 | 86.4 | 1046.4 | 475.1 | 17.543 | 12.729 | 8.843 | 17.685 |
| HB5-212H | .6864 | 2263 | .9972 | 2.6085 | 2.594 | 149.9 | 68.0 | 803.9 | 374.1 | 17.543 | 12.729 | 8.843 | 17.685 |
| HB5-212I | .6864 | 2263 | .9972 | 2.6085 | 2.594 | 58.9 | 26.8 | 324.3 | 147.2 | 17.543 | 12.729 | 8.843 | 17.685 |
| HB5-213P | .6724 | 2554 | .9997 | 1.7615 | 1.760 | 21.1 | 9.6 | 109.8 | 77.1 | 26.383 | 18.412 | 13.132 | 26.383 |
| HB5-213C | .6724 | 2554 | .9997 | 1.7615 | 1.760 | 69.6 | 31.6 | 360.1 | 254.3 | 26.383 | 18.412 | 13.132 | 26.383 |
| HB5-213D | .6724 | 2554 | .9997 | 1.7615 | 1.760 | 111.5 | 50.8 | 509.7 | 408.5 | 26.383 | 18.412 | 13.132 | 26.383 |
| HB5-213E | .6724 | 2554 | .9997 | 1.7615 | 1.760 | 135.9 | 61.7 | 1095.4 | 496.4 | 26.383 | 18.412 | 13.132 | 26.383 |
| HB5-213F | .6724 | 2554 | .9997 | 1.7615 | 1.760 | 147.5 | 66.9 | 1186.0 | 538.5 | 26.383 | 18.412 | 13.132 | 26.383 |
| HB5-213G | .6724 | 2554 | .9997 | 1.7615 | 1.760 | 149.6 | 67.9 | 1203.1 | 546.2 | 26.383 | 18.412 | 13.132 | 26.383 |
| HB5-213H | .6724 | 2554 | .9997 | 1.7615 | 1.760 | 123.9 | 56.2 | 946.3 | 452.3 | 26.383 | 18.412 | 13.132 | 26.383 |
| HB5-213I | .6724 | 2554 | .9997 | 1.7615 | 1.760 | 58.5 | 26.6 | 426.3 | 213.5 | 26.383 | 18.412 | 13.132 | 26.383 |
| HB5-214P | .6801 | 1986 | .9975 | 5.294 | 5.268 | 25.7 | 11.7 | 114.0 | 47.2 | 11.619 | 8.583 | 8.592 | 17.184 |
| HB5-214C | .6801 | 1986 | .9975 | 5.294 | 5.268 | 91.1 | 41.4 | 519.4 | 167.7 | 11.619 | 8.583 | 8.592 | 17.184 |
| HB5-214D | .6801 | 1986 | .9975 | 5.294 | 5.268 | 118.6 | 53.9 | 580.8 | 218.3 | 11.619 | 8.583 | 8.592 | 17.184 |
| HB5-214E | .6801 | 1986 | .9975 | 5.294 | 5.268 | 155.8 | 70.7 | 631.6 | 286.7 | 11.619 | 8.583 | 8.592 | 17.184 |
| HB5-214F | .6801 | 1986 | .9975 | 5.294 | 5.268 | 157.9 | 71.7 | 639.9 | 290.5 | 11.619 | 8.583 | 8.592 | 17.184 |
| HB5-214G | .6801 | 1986 | .9975 | 5.294 | 5.268 | 154.4 | 70.0 | 625.7 | 284.1 | 11.619 | 8.583 | 8.592 | 17.184 |
| HB5-214H | .6801 | 1986 | .9975 | 5.294 | 5.268 | 99.7 | 45.2 | 403.9 | 183.4 | 11.619 | 8.583 | 8.592 | 17.184 |
| HB5-214I | .6801 | 1986 | .9975 | 5.294 | 5.268 | 22.6 | 10.3 | 91.7 | 41.6 | 11.619 | 8.583 | 8.592 | 17.184 |
| HB5-215P | 4.665 | 2227 | .9997 | 1.787 | 1.836 | 9.3 | 4.2 | 172.0 | 78.9 | - | - | - | - |
| HB5-215C | 4.665 | 2227 | .9997 | 1.787 | 1.836 | 21.8 | 9.9 | 554.9 | 252.6 | - | - | - | - |
| HB5-215D | 4.665 | 2227 | .9997 | 1.787 | 1.836 | 32.8 | 14.9 | 667.0 | 275.0 | - | - | - | - |
| HB5-215E | 4.665 | 2227 | .9997 | 1.787 | 1.836 | 34.8 | 15.8 | 684.6 | 292.0 | - | - | - | - |
| HB5-215F | 4.665 | 2227 | .9997 | 1.787 | 1.836 | 33.9 | 15.4 | 627.0 | 285.0 | - | - | - | - |
| HB5-215G | 4.665 | 2227 | .9997 | 1.787 | 1.836 | 26.8 | 12.2 | 494.0 | 225.0 | - | - | - | - |
| HB5-215H | 4.665 | 2227 | .9997 | 1.787 | 1.836 | 15.3 | 6.9 | 282.0 | 128.0 | - | - | - | - |
| HB5-215I | 4.665 | 2227 | .9997 | 1.787 | 1.836 | 4.0 | 1.8 | 78.0 | 34.0 | - | - | - | - |
| HB5-216P | 4.856 | 1844 | .9965 | 2.748 | 2.780 | 14.8 | 6.7 | 151.0 | 86.0 | - | - | - | - |
| HB5-216C | 4.856 | 1844 | .9965 | 2.748 | 2.780 | 25.2 | 11.4 | 524.0 | 147.0 | - | - | - | - |
| HB5-216D | 4.856 | 1844 | .9965 | 2.748 | 2.780 | 36.8 | 16.7 | 425.0 | 216.0 | - | - | - | - |
| HB5-216E | 4.856 | 1844 | .9965 | 2.748 | 2.780 | 37.3 | 17.0 | 482.0 | 219.0 | - | - | - | - |
| HB5-216F | 4.856 | 1844 | .9965 | 2.748 | 2.780 | 30.6 | 13.9 | 398.0 | 178.0 | - | - | - | - |
| HB5-216G | 4.856 | 1844 | .9965 | 2.748 | 2.780 | 24.0 | 10.9 | 310.0 | 141.0 | - | - | - | - |
| HB5-216H | 4.856 | 1844 | .9965 | 2.748 | 2.780 | 11.9 | 5.4 | 154.0 | 70.0 | - | - | - | - |
| HB5-216I | 4.856 | 1844 | .9965 | 2.748 | 2.780 | 2.6 | 1.2 | 34.0 | 15.0 | - | - | - | - |
| HB5-217P | 4.747 | 1662 | .9860 | 3.6305 | 3.617 | 15.4 | 7.0 | 141.0 | 64.0 | - | - | - | - |
| HB5-217C | 4.747 | 1662 | .9860 | 3.6305 | 3.617 | 31.3 | 14.2 | 286.0 | 130.0 | - | - | - | - |
| HB5-217D | 4.747 | 1662 | .9860 | 3.6305 | 3.617 | 31.2 | 14.1 | 285.0 | 129.0 | - | - | - | - |
| HB5-217E | 4.747 | 1662 | .9860 | 3.6305 | 3.617 | 24.0 | 10.9 | 219.0 | 99.0 | - | - | - | - |
| HB5-217F | 4.747 | 1662 | .9860 | 3.6305 | 3.617 | 15.0 | 6.8 | 157.0 | 62.0 | - | - | - | - |
| HB5-217G | 4.747 | 1662 | .9860 | 3.6305 | 3.617 | 10.6 | 4.8 | 97.0 | 44.0 | - | - | - | - |
| HB5-217H | 4.747 | 1662 | .9860 | 3.6305 | 3.617 | 4.6 | 2.1 | 42.0 | 19.0 | - | - | - | - |
| HB5-217I | 4.747 | 1662 | .9860 | 3.6305 | 3.617 | .5 | .2 | - | - | - | - | - | - |
| HB5-218P | 4.738 | 1619 | .9886 | 2.2115 | 2.209 | 22.1 | 10.0 | 199.0 | 90.0 | - | - | - | - |
| HB5-218C | 4.738 | 1619 | .9886 | 2.2115 | 2.209 | 49.5 | 22.4 | 445.0 | 202.0 | - | - | - | - |
| HB5-218D | 4.738 | 1619 | .9886 | 2.2115 | 2.209 | 56.0 | 25.3 | 504.0 | 229.0 | - | - | - | - |
| HB5-218E | 4.738 | 1619 | .9886 | 2.2115 | 2.209 | 40.9 | 18.6 | 368.0 | 167.0 | - | - | - | - |
| HB5-218F | 4.738 | 1619 | .9886 | 2.2115 | 2.209 | 30.1 | 13.6 | 271.0 | 123.0 | - | - | - | - |
| HB5-218G | 4.738 | 1619 | .9886 | 2.2115 | 2.209 | 23.8 | 10.8 | 214.0 | 97.0 | - | - | - | - |
| HB5-219P | 4.666 | 1907 | .9985 | 1.7735 | 1.796 | 19.1 | 8.7 | 210.0 | 96.0 | - | - | - | - |
| HB5-219C | 4.666 | 1907 | .9985 | 1.7735 | 1.796 | 41.2 | 18.7 | 452.0 | 205.0 | - | - | - | - |
| HB5-219D | 4.666 | 1907 | .9985 | 1.7735 | 1.796 | 59.5 | 27.0 | 653.0 | 296.0 | - | - | - | - |
| HB5-219E | 4.666 | 1907 | .9985 | 1.7735 | 1.796 | 56.6 | 25.7 | 622.0 | 282.0 | - | - | - | - |
| HB5-219F | 4.666 | 1907 | .9985 | 1.7735 | 1.796 | 50.0 | 22.7 | 549.0 | 259.0 | - | - | - | - |
| HB5-219G | 4.666 | 1907 | .9985 | 1.7735 | 1.796 | 44.6 | 20.2 | 489.0 | 222.0 | - | - | - | - |
| HB5-219H | 4.666 | 1907 | .9985 | 1.7735 | 1.796 | 25.5 | 11.6 | 280.0 | 127.0 | - | - | - | - |
| HB5-219I | 4.666 | 1907 | .9 | | | | | | | | | | |

CONFIDENTIAL

CONFIDENTIAL

"PRECEDING PAGE BLANK-NOT FILMED."

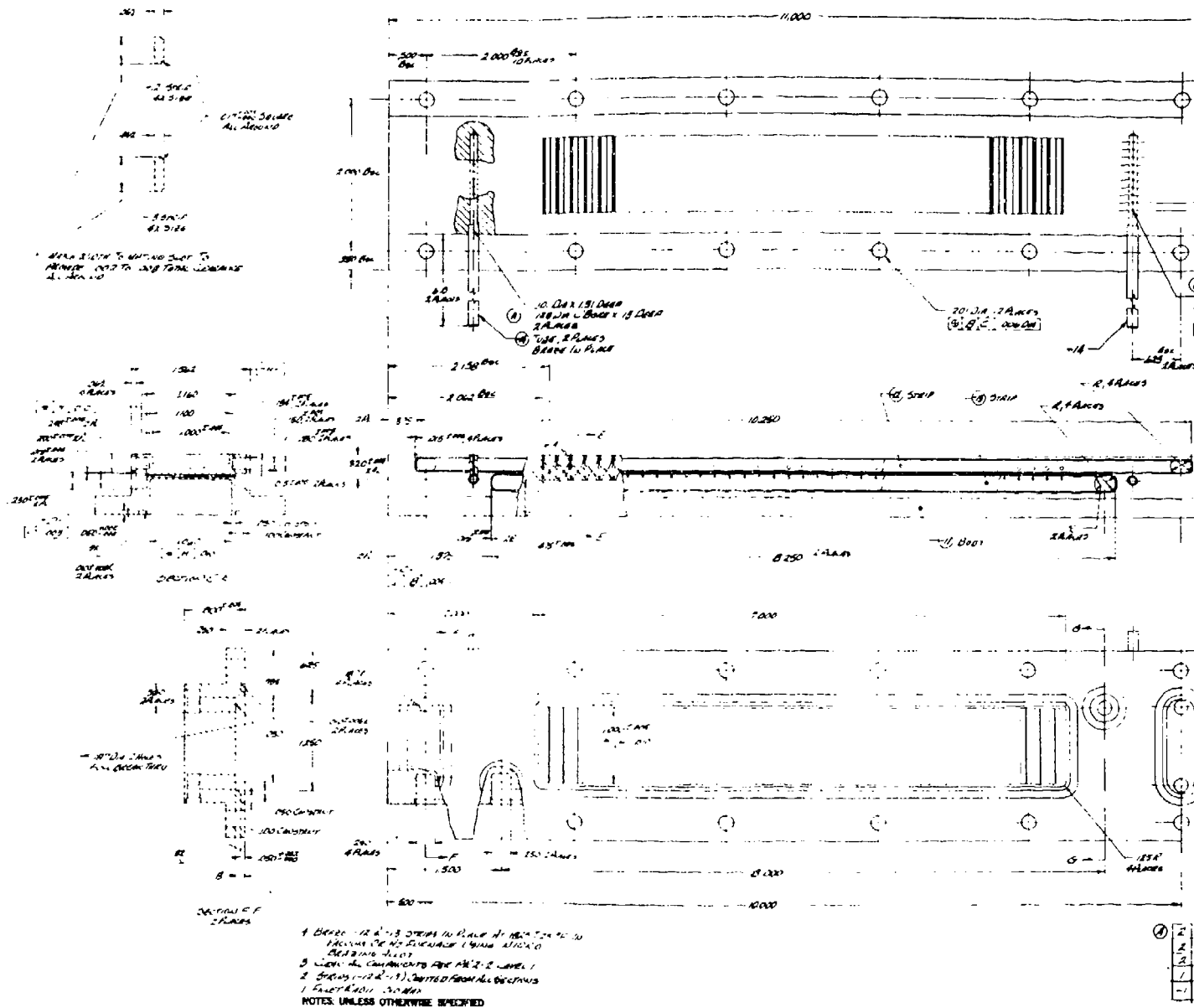


Figure 116. 1- by 7-Inch 2D Slit Nozzle (U)

CONFIDENTIAL

UNCLASSIFIED
Security Classification

| DOCUMENT CONTROL DATA - R & D | | |
|---|---|--|
| (Security classification of title, body of abstract and indexing annotation must be entered when the overall report is classified) | | |
| 1. ORIGINATING ACTIVITY (Corporate author) TRW Systems Group One Space Park Redondo Beach, California 90278 | | 2a. REPORT SECURITY CLASSIFICATION CONFIDENTIAL |
| | | 2b. REPORT NUMBER XGDS-3 |
| 3. REPORT TITLE (U) HYDROGEN FLUORIDE LASER TECHNOLOGY STUDY | | |
| 4. DESCRIPTIVE NOTES (Type of report and inclusive dates) 22 March 1971 through 22 October 1971 | | |
| 5. AUTHOR(S) (First name, middle initial, last name) F. Mastrup, E. Broadwell, J. Miller, T. A. Jacobs | | |
| 6. REPORT DATE October 1972 | 7a. TOTAL NO. OF PAGES 304 | 7b. NO. OF REFS 26 |
| 8a. CONTRACT OR GRANT NO. F29601-71-C-0070 | 9a. ORIGINATOR'S REPORT NUMBER(S) AFWL-TR-72-28 | |
| b. PROJECT NO. 1256 | | |
| c. | 9b. OTHER REPORT NO(S) (Any other numbers that may be assigned this report) | |
| d. | | |
| 10. DISTRIBUTION STATEMENT Distribution limited to US Government agencies only because of test and evaluation (Oct 1972). Other requests for this document must be referred to AFWL (LRT), Kirtland AFB, NM 87117. | | |
| 11. SUPPLEMENTARY NOTES | | 12. SPONSORING MILITARY ACTIVITY AFWL (LRT) Kirtland AFB, NM 87117 |
| 13. ABSTRACT (Distribution Limitation Statement B) This report presents an in-depth discussion of performance and diagnostic testing of the TRW versions of all-chemical, combustion driven hydrogen-fluorine lasers. Emphasis is placed on engineering principles of combustor/injector operation and design; performance testing; spectroscopic measurements and infrared mapping of excited and ground-state molecular concentrations in the laser cavity flow field; and fluid mechanical observations of the flow field. The exceptionally high quality of the data has permitted several distinct and significant conclusions concerning the nature of the flow field and has indicated the direction for future chemical laser research. A sufficiently in-depth discussion is presented which may serve as a point of departure for future chemical laser technology efforts. | | |

CONFIDENTIAL

DD FORM 1 NOV 61 1473

UNCLASSIFIED
Security Classification

(This page is unclassified)

~~UNCLASSIFIED~~
~~Security Classification~~

CONFIDENTIAL

(This page is unclassified)

~~UNCLASSIFIED~~
Security Classification